

DATA-DRIVEN AND HYBRID METHODS FOR POWER MAGNETICS DESIGN

HAORAN LI

A DISSERTATION
PRESENTED TO THE FACULTY
OF PRINCETON UNIVERSITY
IN CANDIDACY FOR THE DEGREE
OF DOCTOR OF PHILOSOPHY

RECOMMENDED FOR ACCEPTANCE
BY THE DEPARTMENT OF
ELECTRICAL AND COMPUTER ENGINEERING
ADVISER: PROFESSOR MINJIE CHEN

SEPTEMBER 2025

© Copyright by Haoran Li, 2025.

All rights reserved.

Abstract

The growing demand for high-performance power delivery spans across a wide range of domains, including data centers, artificial intelligence infrastructure, transportation electrification, and renewable energy systems. These applications require power electronics that are not only highly efficient but also extremely compact, often operating under tight thermal and spatial constraints. Among the key components in these systems, power magnetics frequently become a bottleneck due to their bulky form factor, considerable core losses, and complex, nonlinear behavior. Their characteristics vary significantly with factors such as frequency, temperature, and dc bias, making accurate modeling and efficient design particularly difficult using traditional methods based on empirical formulas and datasheet curves.

This thesis proposes a hybrid method that combines data-driven and model-driven approaches to better understand and improve magnetic modeling and design. A major contribution of this work is the creation of the MagNet database – a large-scale open-source collection of power magnetic data measured under diverse operating conditions. The database was built from scratch with carefully controlled data quality and comprehensive coverage of excitation and material conditions. The fundamental complexity of magnetic materials was investigated using the MagNet database. To capture the high-dimensional and nonlinear relationships in power magnetics modeling, we develop neural network models including LSTM and Transformer architectures. These models serve as intelligent surrogates for traditional datasheets, offering accurate, fast, flexible predictions that can be used for material comparison, component design, simulation, and system optimization. Based on the MagNet database, we also launched the MagNet Challenge, a community-driven and worldwide open competition that promotes collaboration and advances in data-driven magnetics modeling.

Building on this modeling foundation, the thesis explores two independent design directions for magnetic components in high-density power applications. The first focuses on via-winding magnetics for multiphase coupled inductors design in vertical power delivery applications, where a hybrid design approach combining finite-element simulations and data-guided parameter optimization is used to create compact structures with high current-handling capability. The second presents the Air-LEGO architecture, a magnetic-free design based on air-core coupling, which eliminates core losses and temperature sensitivity while supporting ultra-thin, high-current regulation.

Together, these methods demonstrate how combining machine learning with physical modeling and innovative design can help overcome long-standing limitations in power magnetics, enabling more compact, efficient, and reliable power electronics systems for a wide range of next-generation applications – from advanced computing infrastructure to electrified mobility and renewable energy.

Acknowledgements

I would like to express my deepest gratitude to my advisor, Professor Minjie Chen. Thank you for your consistent guidance, encouragement, and support throughout my Ph.D. journey. From the very beginning, you placed your trust in me and offered both the clear direction and the freedom for me to explore ideas and grow as a researcher. Your technical insight and vision have shaped how I approach problems, design systems, communicate ideas, and work toward achieving meaningful goals. The many lessons I've learned from you – technical and non-technical, within and beyond engineering – will stay with me far beyond this dissertation.

I am deeply thankful to the faculty members who have supported me throughout my academic journey. To my general exam and FPO committee members – Professors Niraj Jha, Barry Rand, and Yuxin Chen – thank you for your time, thoughtful feedback, and valuable guidance. I would also like to thank my thesis reader, Professor Mike Ranjram from Arizona State University, for generously reviewing my dissertation and offering thoughtful suggestions that strengthened this work. Special thanks go to Professor Charles Sullivan from Dartmouth College. From early on in my Ph.D. study, his expertise in magnetics and high standards for rigor and clarity have been instrumental to my research and development. His constructive feedback greatly shaped both the technical depth and quality of this dissertation.

To all past and present members of our PU PowerLab – Ming, Yenan, Jaeil, Diego, Yufei, Jing, Ping, Youssef, Daniel, Mian, Tanuj, Hsin, Shukai, Wenliang, Gyeong-Gu, Hyukjae, Davit, Elias, Konstantinos, and many others. Thank you for the friendship, collaboration, and inspiration. It has been a pleasure learning and growing alongside you all. You have made this journey not only intellectually rewarding but also genuinely enjoyable. I feel truly fortunate to have been part of such a supportive and talented team.

Finally, to my parents – thank you for your unconditional love, support, and encouragement over the years, even from halfway across the world. Your belief in me gave me strength during the times I struggled, and your constant presence has been my foundation. To my wife, Rong – thank you for being my greatest source of support and joy. Your unwavering companionship made the difficult times bearable and the good times even better. While pursuing your own demanding DMA degree, you still found the grace to stand by me with warmth and strength. I'm endlessly proud of your journey and grateful to be walking mine beside you. And to all of my family – thank you for the ever-present care and concern.

This dissertation marks the end of a long and meaningful journey, and it would not have been possible without the many people who walked beside me. Thank you all from the bottom of my heart.

To the journey
and those beside me.

Contents

Abstract	3
Acknowledgements	4
List of Tables	10
List of Figures	11
1 Introduction	28
1.1 Power Magnetics in Modern Energy Systems	28
1.1.1 Emerging Demands and Vertical Power Delivery	29
1.1.2 Role of Power Magnetics	31
1.1.3 Challenges in Magnetics Modeling and Designing	34
1.2 Contributions and Thesis Organization	37
2 MagNet: Machine Learning Framework for Modeling Power Magnetic Material	40
2.1 Background and Motivation	40
2.2 Automated Data Acquisition System	44
2.3 Data Quality Control	49
2.4 Database Construction	52
2.5 Neural Network Models for Power Magnetics Modeling	59
2.5.1 Encoder-Projector-Decoder Architecture	60
2.5.2 LSTM Neural Network Models	62
2.5.3 Transformer Neural Network Models	64

2.6	Data Processing and Augmentation	67
2.6.1	Single-Cycle Interpolation	70
2.6.2	Phase-Shifting Augmentation	71
2.6.3	Multi-Cycle Augmentation	73
2.7	Model Training and Testing Results	74
2.7.1	Hysteresis <i>B-H</i> Loop Prediction	75
2.7.2	Core Loss Prediction	77
2.7.3	Comparison and Discussion	79
2.8	Applications of Neural Network Models	81
2.8.1	MagNet-AI: A NN-aided Smart Datasheet	81
2.8.2	NN-aided Material Recommendation	87
2.8.3	Online Smartsheet Platform	90
2.9	Transfer Learning for Data Size Reduction	93
2.9.1	Material-to-Material Transfer Learning	94
2.9.2	Temperature-to-Temperature Transfer Learning	98
2.10	Chapter Summary	101
3	Via-Winding Magnetics: Ultra-Thin Multiphase Pinwheel Coupled Inductors	106
3.1	Background and Motivation	106
3.2	Modeling and Optimization Framework	111
3.2.1	Principles of Multiphase Coupling	111
3.2.2	Optimization Framework	113
3.3	Design Examples and Implementation of Pinwheel Coupled Inductors	115
3.3.1	Design #1: Pinwheel Coupled Inductor	117
3.3.2	Design #2: Extended Pinwheel Coupled Inductor	125
3.4	Experimental Verification	135
3.4.1	Four-Phase Buck Voltage Regulator Design	135

3.4.2	Converter Efficiency	137
3.4.3	Converter Transient Performance	143
3.4.4	Tolerance to Dc Current Imbalance	145
3.5	Chapter Summary	148
3.5.1	Performance Benchmarking	148
3.5.2	Conclusion	151
4	Air-LEGO: Air-Coupled Inductors for Ultra-thin Power Delivery	152
4.1	Background and Motivation	152
4.2	LEGO Architecture and Operation Principles	155
4.3	Air-Coupled Inductor Design	158
4.4	Experimental Results	164
4.5	Chapter Summary	170
5	Conclusion	172
5.1	Conclusion	172
5.2	Future Work	174
A	Detailed Implementation of Automated Data Acquisition System	177
A.1	Excitation	177
A.2	Device Under Test	180
A.3	Measurement and Acquisition	181
A.4	Temperature Control	182
A.5	Software System	183
A.6	Range of Measurement	184
B	Data Quality Control of Large-Scale Measurement	187
B.1	Equipment Evaluation and Calibration	187
B.2	Model-driven Method for Quantifying the Error	189

CONTENTS

B.3 Data-driven Methods for Data Quality Control	193
C MagNet Challenge for Data-Driven Power Magnetics Modeling	196
C.1 Background and Motivation	196
C.2 Goals, Task Setup, and Evaluation Criteria	202
C.3 Final Evaluation Results	206
C.4 Conclusion and Future Roadmap	208
Bibliography	212

List of Tables

1.1	Number of Parameters used by Core Loss Models	34
2.1	Number of Data Points Currently in the MagNet Dataset	55
2.2	Comparison of the LSTM and Transformer implementation of the encoder-projector-decoder architecture.	80
2.3	Comparison of the theoretical computational cost between the LSTM and the self-attention (transformer).	81
3.1	Electrical Parameters and Constraints	117
3.2	Geometric Parameters of Designed Pinwheel Inductor	120
3.3	Geometric Parameters of Designed Pinwheel Inductor	128
3.4	Bill-of-Materials for Four-Phase Buck VRM	137
3.5	Performance Comparison between Coupled and Discrete VRM Implementation (Operating Condition: 4 V-to-1 V, and $f_s = 2$ MHz) . . .	148
3.6	Comparison of the Pinwheel Coupled Inductor Against Other Magnetics Solutions for VRMs	149
4.1	Comparison of PCB-winding inductor and Litz-wire inductor.	163

List of Figures

1.1	Vertically stacked in-package VRM with capacitor, semiconductor, and magnetic layers enabling high-density power delivery.	31
1.2	Examples of measured B - H loops for ferrite materials under different conditions.	33
1.3	Concept of neural network as datasheet.	36
2.1	Examples of B - H loops measured with N87 ferrite material under 50% duty ratio triangular excitations. The reference loop (blue) is measured at 200 kHz, 25 °C, and 0 A/m dc bias. Each of the three figures shows the variation of B - H loop at different frequencies, temperatures, and dc biases, respectively. The B (only ac) waveform is extracted from voltage measurement, and the H (both ac and dc) waveform is extracted from current measurement.	41
2.2	Overview of the MagNet framework: from data engineering, model development, to magnetics design tool.	42
2.3	Overview of the automated data acquisition system of MagNet. . . .	45
2.4	Experiment setup and circuit configuration of the magnetic core loss data acquisition system of MagNet.	46
2.5	Example measured voltage, current, and power waveform of TDK N87 ferrite material at 100 kHz.	51

2.6 Example voltage and current waveforms of sinusoidal, triangular, symmetric trapezoidal, and asymmetric trapezoidal excitations.	53
2.7 Data format of the MagNet database with four different types of contents.	54
2.8 Data visualization of the measured core losses under triangular excitation for N87 material: (a) core loss versus peak flux density with frequency at 200 kHz; (b) core loss versus frequency with peak flux density around 120 mT;	56
2.9 Data visualization of the measured core losses under triangular excitation for N87 material: (a) core loss versus duty ratios at different flux density level with frequency at 200 kHz; (b) core loss versus peak flux density at different temperature with frequency at 200 kHz and duty ratio at 0.5.	57
2.10 Three example ways of modeling the behavior of magnetic materials with neural networks: (a) scalar-to-scalar, (b) sequence-to-scalar, and (c) sequence-to-sequence.	58
2.11 Architecture and data flow of the encoder-projector-decoder neural network architecture.	61
2.12 Neural network structure of the LSTM-based encoder-projector-decoder architecture. Temperature (T), frequency (f), and dc bias (H_{dc}) information are mixed with the waveform information in the FNN projector after the encoder and before the decoder.	62

2.13 Network structure of the transformer-based encoder-projector-decoder architecture. $B(t)$ waveform is the sequence input of the encoder. T , f and H_{dc} are the scalar inputs of the projector. During the model training, the targeting $H(t)$ is directly fed to the decoder as a reference input. During the model inference, the predicted sequence is fed back to the decoder, generating the entire output sequence in an auto-regressive manner.	65
2.14 Examples of the full-length waveforms measured with N87 ferrite material under varying frequency, temperature, and dc bias conditions: (a) sinusoidal wave; (b) triangular wave; (c) trapezoidal wave.	68
2.15 Examples of the single-cycle waveforms with a sequence length of 128, corresponding to the full-length waveforms shown in Fig. 2.14.	70
2.16 A set of example $B(t)$ waveforms of N87 ferrite before and after the phase-shifting augmentation. The waveforms are measured under sinusoidal excitations at 100 kHz, 25°C, and zero dc bias.	72
2.17 Examples of multi-cycle data augmentation: (a) the original single-cycle waveform at 125 kHz; (b) the augmented two-cycle waveform at an effective frequency of 62.5 kHz. A well-designed and well-trained neural network should be able to predict similar results for both cases.	73
2.18 Prediction results of the $H(t)$ waveform and the $B-H$ loop of an example testing point (trapezoidal, 140 kHz, 90°C, 30 A/m dc bias) at different stages of the training. The mismatch decreases progressively as the training advances, eventually achieving a close match between the predicted and measured waveforms.	74
2.19 Relative error distributions of the predicted $H(t)$ sequence generated by the LSTM-based and transformer-based neural network models.	76

2.20	Relative error distributions of the predicted core loss generated by the LSTM-based and transformer-based neural network models.	78
2.21	Examples of the predicted B - H loops under different frequency, temperature, and dc bias conditions, with multiple waveform shapes. Both the LSTM-based and the transformer-based models accurately predict the majority part of the B - H loops, while the sharp corners are better captured by the transformer-based model.	79
2.22	Flowchart of the neural network-aided smart datasheet. Users can specify the excitation waveform and the operating conditions through the user interface as the inputs to the neural network model. The model inference is executed to predict the response waveform. After post-processing, the prediction results, such as the hysteresis loop, core loss, and permeability, are visualized and provided to users.	81
2.23	Predicted B - H loops with the manually generated model inputs using 50% duty ratio pure triangular waves, where the amplitude of flux density is swept from 30 mT to 240 mT. The frequency, temperature, and dc bias are fixed at 100 kHz, 25°C, and 0 A/m, respectively.	82
2.24	Predicted B - H loops with the manually generated model inputs using pure sinusoidal waves, where the fundamental frequency is swept from 100 kHz to 400 kHz. The amplitude, temperature, and dc bias are fixed at 45 mT, 25°C, and 0 A/m, respectively.	83
2.25	Predicted B - H loops with the manually generated model inputs using pure sinusoidal waves, where the dc bias is swept from 0 A/m to 30 A/m. The amplitude, frequency, and temperature are fixed at 30 mT, 200 kHz, and 25°C, respectively.	85

2.26 Predicted core loss curves with the manually generated model inputs, where the duty ratio of the triangular wave is swept from 10% to 90%. The amplitude, frequency, temperature, and dc bias are fixed at 43.5 mT, 315 kHz, 25°C, and 0 A/m, respectively.	86
2.27 Predicted core loss curves with the manually generated model inputs, where the flux density is fixed at 35 mT, 70 mT, and 140 mT, and the temperature is swept from 25°C to 90°C. The frequency and dc bias are fixed at 100 kHz and 0 A/m, respectively.	87
2.28 Material ranking map at different levels of dc bias across a wide range of flux density amplitude and frequency.	88
2.29 Material ranking map across a wide range of flux density amplitude and temperature.	89
2.30 Core loss curve comparisons at different levels of flux density amplitude and temperatures.	89
2.31 The website architecture and information flow of the MagNet webpage platform, which provides users with access to download and visualize the measured data in the MagNet core loss database, as well as analyze and simulate the magnetic behaviors with the deployed neural network models and the PLECS simulation engine.	91
2.32 An example screenshot of the MagNet-AI webpage-based magnetics analysis and prediction platform: (a) smartsheet session; (b) simulation session. MagNet-AI is available at: https://mag-net.princeton.edu , and open-sourced at: https://github.com/PrincetonUniversity/magnet	92
2.33 The core concept of transfer learning for magnetic core loss modeling.	94
2.34 Network training process of the material-to-material transfer learning.	95

2.35 Prediction results: (a) applying a pre-trained model to the new material without re-training; (b) applying a pre-trained model to the new material after re-training with very few data points (100 randomly selected); (c) applying a randomly initialized model trained with very few data points (100 randomly selected); (d) applying a randomly initialized model trained with a large amount of data (100 data points).	96
2.36 Error distribution of the prediction results: (a) using a randomly initialized model trained with only 100 data points from N87 (normal training); (b) using a pre-trained model from 4 existing materials re-trained with 100 data points from N87 (transfer learning). The data shown is a subset with a duty ratio of 0.5.	97
2.37 Testing average relative error rates after training a normal FNN and re-training a pre-trained FNN with varying amounts of data.	98
2.38 Training process of temperature-to-temperature transfer learning. Pre-training and fine-tuning can significantly reduce the data requirements for modeling magnetic core loss at different temperatures.	99
2.39 Prediction results: (a) applying a pre-trained 25 °C model to 90 °C data points without re-training; (b) applying a pre-trained 25 °C model to 90 °C data points after re-training with very few data points (10 randomly selected); (c) applying a randomly initialized model trained with very few data points (10 randomly selected); (d) applying a randomly initialized model trained with a large amount of data (800 data points).	100
2.40 Error distribution of prediction results: (a) applying a randomly initialized model trained with 10 randomly selected 90 °C data points (normal training); (b) applying a pre-trained 25 °C model to the 90 °C data after re-training with 10 data points (transfer learning).	101

2.41 Testing average relative error rates of normal training and transfer learning as the number of data points increases.	102
3.1 The vision of power-via magnetics. The power vias in packaging are surrounded by a pinwheel patterned magnetic layer as the substrate for minimizing the power distribution network (PDN) impedance, and connected with power vias in silicon to enable end-to-end vertical power delivery.	107
3.2 Rendering of the concept of pinwheel magnetics. The magnetic core forms a 3D structure that effectively contorts itself around vertical windings to achieve multiphase coupling with low resistance and height.	109
3.3 Assembly procedure for a four-phase pinwheel inductor. Two identical core pieces are used, with the top piece rotated 180° in the x-axis and placed on top of the bottom piece. Four vertical windings are inserted through the core assembly.	110
3.4 Generalized lumped reluctance model of an M -phase coupled inductor. The model captures the geometric structure with M leg reluctances representing the flux paths around each winding and a central reluctance representing the middle air gap. This formulation aligns closely with physical dimensions, allowing calculation of flux distribution and enabling evaluation of key design constraints such as inductance, coupling coefficient, and maximum flux density during optimization.	112

3.5 Flowchart of the optimization process for a multiphase coupled inductor. Given the system operating conditions and geometric parameters, the algorithm estimates the reluctance of each magnetic path and the winding resistance, then computes coupled inductor characteristics. The optimization minimizes the total loss of inductors while satisfying constraints on geometric limitations, coupled inductor performance, peak current and flux density.	114
3.6 (a) 3D view of the four-phase pinwheel coupled inductor, illustrating the flux path associated with winding 1. The dc flux generated by this winding wraps around the winding and circulates from the top core piece to the bottom, with most of the flux continuing to the leg posts of the other three windings, while a small amount of the flux travels through the middle air gap, completing the magnetic path. (b) Parameterization of the pinwheel inductor geometry. The top view defines the key in-plane dimensions s_{inner} , s_{outer} , and l_{leg} , which determine the allocation of ferrite material for each leg and the central region, as well as the designated copper winding space. The side view illustrates the z -dimension parameters: core plate thickness h_g and air gap height h_p , and total assembled height. These geometric parameters serve as the basis for structural optimization and magnetic modeling.	118
3.7 Pareto front of the pinwheel coupled inductor optimization. The “knee” of the curve, where the height is minimized while maintaining low loss, is at 1.8 mm. The design at 1.8 mm is selected for fabrication.	119

3.8 ANSYS Maxwell 3D dc flux density distribution with balanced phase currents of 25 A per phase (left) and a dc current mismatch where $I_{DC,1-3} = 24.5$ A and $I_{DC,4} = 27$ A (right). The maximum flux density in the core is 360 mT when all phases have balanced currents. For the dc current mismatch condition, the inductance of winding four drops by 20% of its zero dc bias inductance value, still providing sufficient inductance during full load unbalanced operation.	121
3.9 Photographs of the fabricated pinwheel core pieces and the fully assembled four-phase coupled inductor. The identical top and bottom core halves are shown alongside the final stacked assembly.	122
3.10 Simulated inductor current waveforms using the inductance matrix obtained from Ansys Maxwell 3D for a four-phase buck converter with $V_{in} = 4$ V, $V_{out} = 1$ V, and $f_s = 2$ MHz. The peak-to-peak current ripple is 1.52 A.	123
3.11 Plot of the steady-state inductance (L_{pss}) vs. duty cycle for the pinwheel coupled inductor assembly. At $D = 0.25$, $L_{pss} = 243$ nH, exceeding L_S by a factor of 1.3 and exceeding L_{ptr} by a factor of 7. . . .	124
3.12 Plot of the peak-to-peak phase current ripple for the four-phase buck VRM when $V_{in} = 4$ V and $f_s = 2$ MHz compared to if four discrete inductors with values $L_{disc} = L_S$ and $L_{disc} = L_{ptr}$ were used. The peak-to-peak phase current ripple at $D = 0.25$ is 1.54 A for the coupled inductor, 1.98 A for the discrete inductor case where $L_{disc} = L_S$, and 14.13 A for the discrete inductor case where $L_{disc} = L_{ptr}$	124
3.13 (a) 3D rendering of the extended pinwheel inductor, showing vertical current conduction and flux circulation paths. (b) Geometry parameterization highlighting key variables a , b , x , s , l_{side} , h_p , and h_g , which are used in modeling and optimization.	126

3.14 ANSYS Maxwell 3D simulation of dc flux density distribution in the extended pinwheel inductor under (left) balanced phase currents of 40 A and (right) a 10% dc current mismatch where $I_{DC,1-3} = 40$ A and $I_{DC,4} = 44$ A. The maximum flux density reaches 400 mT under balanced conditions. With the imbalance, localized flux increases are observed and the self-inductance of winding four decreases by 15%, while remaining sufficient for full-load operation.	129
3.15 Three variants of the extended pinwheel coupled inductor design. (a) Variant #1 is fabricated based on the original extended pinwheel geometry, where two core halves with interleaved structures are assembled at 45° corner joints, resulting in unintended air gaps due to manufacturing limitations. (b) Variant #2 modifies the corner geometry to form complementary 90° angled faces, allowing easier machining and improved alignment. (c) Variant #3 introduces a horizontal split along the z -axis, forming two equal-thickness core halves with all contact surfaces lying in a single plane, enabling tighter assembly and reduced variation across phases.	130
3.16 Conceptual manufacturing process of magnetic components with customized geometries, provided by ITG Electronics. The carving precision determines how closely the fabricated shape matches the intended design. During sintering, dimensional shrinkage occurs and must be accounted. The effectiveness of grinding directly impacts the flatness and quality of contact surfaces, which are critical for achieving tight assembly and minimizing unintended air gaps.	131
3.17 Steady-state inductance (L_{pss}) and leakage inductance (L_ℓ) vs. duty cycle, extracted from the measured inductance matrix. At $D = 0.25$, $L_{pss} = 160.9$ nH.	134

3.18 Comparison of peak-to-peak phase current ripple at $V_{in} = 4$ V, $f_s = 2$ MHz, $D = 0.25$ for three inductor configurations: coupled inductor, discrete inductor with L_S , and discrete inductor with L_{ptr}	135
3.19 Top-layer layout of the four-phase buck converter power stage, highlighting the symmetrical placement of each MP86936 DrMOS device and associated passive components. Switch nodes are routed vertically through vias for direct connection to the coupled inductor.	136
3.20 3D view of the fully assembled power stage. The vertically coupled inductor is mounted by soldering its through-windings to the via pads of both the power stage PCB and the motherboard. Power connectors on the baseboard supply input voltage and ground return paths.	137
3.21 Test fixture setup for the four-phase buck VRM. The power stage evaluation board contains the four-phase buck power stage, including the pinwheel coupled inductor, as well as the base motherboard which hosts the input and output power terminals. A TMS320F28388D microcontroller is connected to a signal board, which generates the PWM signals, provides the gate drive power, and houses test points. System cooling is provided by a 36 CFM dc fan.	138
3.22 Power stage of the four-phase buck VRM in Fig. 3.19, assembled with the pinwheel coupled inductor design #1 (left) and four discrete Coilcraft SLR4040 inductors (right). The pinwheel-based assembly achieves a total system height of 3.4 mm, reducing the height by over 2 mm compared to the 5.6 mm height of the system using discrete inductors.	139

3.23 Measured system efficiency of the four-phase buck VRM using the pinwheel coupled inductor (design 1), extended pinwheel inductor (design 2), and Coilcraft SLR4040 discrete inductors with 22 nH and 100 nH values. All data points correspond to DrMOS junction temperatures below 100°C. Design 1 achieves a peak efficiency of 91.5%, while design 2 reaches 93.5%. Both coupled inductor configurations outperform the 22 nH discrete inductors by a large margin, which offer comparable transient performance. Compared to the 100 nH discrete inductors, design 1 exhibits slightly lower peak efficiency, whereas design 2 matches or exceeds efficiency across the full load range.	140
3.24 Loss breakdown for the four-phase buck VRM with the pinwheel coupled inductor (design 1). Measured and calculated values are compared. DrMOS switching and conduction losses dominate the total system loss, while inductor losses remain minimal due to low dc resistance and vertically integrated layout.	142
3.25 Output voltage response to a common-mode duty cycle step from 10% to 25% at $V_{in} = 4$ V and $f_s = 2$ MHz. From top to bottom: the pinwheel coupled inductor (design #1) settles within 200 ns; the extended pinwheel coupled inductor (design #2) settles within 400 ns; the VRM with 100 nH discrete inductors requires approximately 1600 ns to reach its new steady state.	144

3.26 Current waveforms and corresponding switch node voltages for the four-phase buck VRM under intentional duty cycle mismatch. Phase 4 operates at a duty ratio of 25.4% with a measured dc current of 21.1 A, while the other three phases operate at nominal 25% duty ratio with approximately 18.5 A dc current. Despite an approximately 13% current imbalance, all four phases exhibit clean, undistorted current waveforms, indicating that the magnetic core remains unsaturated and maintains linear behavior.	146
4.1 Ultra-thin Air-LEGO VRM embedded into a CPU or GPU package for compact in-package integration. The air-coupled inductor enables a system height under 3 mm while mitigating thermal constraints. . .	153
4.2 Principles of LEGO architecture, consisting of three series-stacked switched-capacitor submodules and three paralleled multi-phase buck submodules with coupled inductors. LEGO architecture provides large voltage conversion ratio and high current capacity with reduced switch stress for high current VRM applications.	156
4.3 Theoretical gate drive modulation strategy of LEGO architecture. The switched-capacitor unit is driven by low frequency 50% duty ratio square waves with 180° phase difference. The two-phase buck unit is driven by a higher frequency sequence with desired duty ratio, where two phases are 180° interleaved. Soft-charging of capacitors, zero-current switching of SC unit, and phase current balancing through phase rotation are achieved.	157
4.4 Basic geometry of the two-phase air-coupled inductor. Three parameters need to be determined, where the coupling factor between two phases is mostly determined by l_2 and l_3 , while l_1 provides additional self-inductance.	159

4.5 Simulation results with parameter sweeping for different l_1 and l_2 combinations: (a) self inductance per phase; (b) coupling coefficient between phases; and (c) Dc resistance per phase.	160
4.6 Simulated current density distributions for interleaved structure (top) and non-interleaved structure (bottom), where interleaving greatly mitigates the skin effect and proximity effect, and reduces the winding ac resistance.	161
4.7 Simulated flux density distributions for interleaved structure (top) and non-interleaved structure (bottom), where interleaving effectively minimizes fringing flux and confines it around the winding plane.	162
4.8 The interleaved winding structure in this design, where each phase contains two sets of parallel windings, and the two phases are fully interleaved in an 8-layer PCB stack.	162
4.9 Pictures of the air-coupled inductors: (a) PCB traces as windings; (b) Litz-wire as windings.	163
4.10 Pictures of the Air-LEGO prototype (with PCB-trace inductors) from front, back, and side views, achieving a low profile of 3 mm.	164
4.11 Pictures of the testing platform, including dc power supplies, electronic loads, digital multimeters with current shunts for power measurement, and an oscilloscope.	165
4.12 Key experimental waveforms of the Air-LEGO prototype: (a) switched-capacitor stage 400 kHz gate drive signals, with 50% duty ratio and 180° phase shift; 2 MHz two-phase gate drive signals for one of the buck submodules, with 180° phase interleaving. (b) 4 V intermediate bus voltage, two-phase interleaved buck stage switch node voltage, and 1 V output voltage.	166

4.13 Thermal image of the Air-LEGO prototype with PCB windings at 24-to-1 V operation and 120 A output current. The DrMOS modules in the buck stage shows the highest temperature.	167
4.14 Measured efficiency of the Air-LEGO prototype with either the Litz-wire inductors or PCB winding inductors, at different input voltages and different buck stage switching frequencies, excluding consumption of gate drives. Prototype with Litz-wire air-coupled inductors demonstrates higher efficiency.	168
4.15 Calculated loss breakdown of the Air-LEGO prototype during 24 V-to-1 V operation at 2 MHz with PCB-winding inductors. The switched capacitor stage loss is split into switching and conduction losses due to the switches, losses due to the capacitors. In the buck stage, the loss is divided into the device switching and conduction losses and the winding from the air-coupled inductors.	169
A.1 Circuit schematic of the power stage for generating the excitations and measuring the magnetic component behaviors in the data acquisition system of MagNet.	178
A.2 Circuit schematic of the auxiliary dc-bias current injection circuitry for the measurements under dc-bias conditions.	178
A.3 Range of measurement for the flux density amplitude and the frequency.	184
B.1 Workflow of the virtual measurement simulation. The virtual measurement setup numerically simulates the impact of various sources of measurement error. The virtually measured waveform is compared against the ideal waveform to estimate the measurement accuracy. . .	189

B.2 Example simulation results for TDK N87 material with the virtual measurement setup and Monte Carlo experiments, where the measurement uncertainties introduced by the probe and scope are taken into consideration. Colors depict the discrepancy between the virtually measured core loss and the expected core loss.	191
B.3 Error distribution of an example point (300 kHz, 50 mT, 50% duty ratio triangular wave with zero dc bias measured at 25°C), where the measurement uncertainties introduced by the circuit parasitics, scope and probe, temperature variation, and geometry variations are considered. Both the systematic error and the statistical error are less than 4% for the majority of trials in the Monte Carlo experiments. The spread of systematic error is larger than that of statistical error. . . .	192
B.4 Example distribution of the defined weight of closeness for a specific considered data point. The local Steinmetz will be performed within the local range that is close enough to the considered data point. . . .	195
B.5 Example of outlier data points in a dataset for the material N87 under sinusoidal excitation. For each point, data up to 0.1 decades far in terms of flux density and frequency are used to generate the local Steinmetz parameters. The data points discarded because the error compared to the estimation is above $\pm 4\%$ are marked as solid stars. .	195
C.1 The vision and mission of the MagNet Challenge in 2023. The open-source initiative aims at developing less complex, more versatile, and more accurate data-driven power magnetics models.	198
C.2 The 1-year timeline of the MagNet Challenge in 2023, spanning from February 2023 to February 2024.	201

C.3 Average 95 th percentile error across the 5 materials, and average model number of parameters (size) of the 24 final submissions, together with the state-of-the-art (SOTA) Pareto fronts before and after the MagNet Challenge, estimated using the results reported in [80] as a benchmark. The minimum average 95 th percentile error reaches 7 %, and the smallest model parameter size reaches 60. Both the model sizes and average errors are greatly reduced as a result of the community effort in the MagNet Challenge.	207
C.4 Roadmap of the MagNet challenge with addressed topics marked in red boxes, and example future topics marked in white boxes.	209

Chapter 1

Introduction

1.1 Power Magnetics in Modern Energy Systems

Power electronics form the backbone of modern energy systems, enabling the efficient conversion, regulation, and distribution of electrical power across a vast array of applications. From renewable energy and electric vehicles to industrial automation and advanced computing, nearly every domain of modern technology relies on power electronic converters to bridge different voltage levels, power domains, and load requirements. As society progresses toward electrification, miniaturization, and digitalization, the demand for compact, efficient, and high-performance power delivery systems continues to escalate.

This demand is especially evident in high-density electronic systems, where enormous amounts of power must be delivered within tight spatial and thermal constraints. Examples include data centers, modular energy storage systems, high-power optical systems, and, most prominently, the computing industry. Modern microprocessors, particularly those designed for artificial intelligence and high-performance computing, now require power levels approaching kilowatts, with localized current densities exceeding 1000 A within a few square centimeters of silicon area. These extreme power

requirements push the limits of conventional converter architectures, calling for new approaches that can deliver high current quickly, efficiently, and reliably.

Among all components in power electronics systems, magnetic elements – inductors and transformers – play indispensable roles in energy transfer, voltage regulation, filtering, and isolation. However, they also constitute a primary bottleneck. Magnetic components are typically the largest in physical volume, the most difficult to scale, and a significant source of power loss. Their non-ideal behavior under complex excitation conditions, strong dependence on environmental factors, and the lack of accurate, generalizable models make their design both critical and challenging.

To meet the evolving needs of high-density power electronics systems, fundamental innovations are needed not only in circuit topologies and semiconductor technologies, but also in the modeling, design, and integration of magnetic components. A holistic rethinking of magnetics – from material behavior and geometric design to data-driven modeling and vertical integration – is essential for unlocking the next generation of high-efficiency, high-density, and scalable power delivery systems.

1.1.1 Emerging Demands and Vertical Power Delivery

The escalating performance of high-end computing platforms – particularly CPUs, GPUs, and AI accelerators – has pushed the boundaries of power delivery infrastructure. These devices operate at low voltages (often below 1 V) but demand increasingly high currents (surpassing 1000 A), requiring voltage regulation modules (VRMs) that can support both high efficiency and extreme current density within confined footprints. As power consumption continues to rise in high-density computing environments, such as data centers, edge AI servers, and advanced mobile systems, traditional power delivery solutions are straining to meet performance, thermal, and spatial constraints.

Conventional VRMs are typically implemented at the printed circuit board (PCB) level and rely on lateral routing to distribute power to the processor. This approach introduces substantial parasitic impedance due to the long interconnect paths and multiple interfaces across the power delivery network (PDN). The resulting I^2R losses not only reduce overall energy efficiency but also exacerbate thermal management and electromagnetic interference (EMI) challenges. Additionally, the bulky nature of PCB-level magnetics and passives limits miniaturization and complicates signal routing, particularly for high-speed interconnects coexisting on the same substrate.

In response to these challenges, the industry has been transitioning toward more integrated, high-efficiency packaging solutions, most notably vertical power delivery (VPD) architectures. VPD approaches fundamentally alter the spatial configuration of power flow, replacing lateral distribution with vertically stacked modules that deliver current directly from the package substrate to the die. Such architectures leverage advances in 3D integration, including micro-bumps, through-silicon vias (TSVs), and wafer-level packaging techniques, to enable a high-density, low-impedance path between the VRM and the load.

A representative VPD implementation is illustrated in Fig. 1.1, which shows an in-packaging vertically stacked VRM architecture designed to optimize current area density. Power flows vertically through three tightly integrated functional layers: a capacitor layer for energy buffering and charge transfer, a semiconductor layer for high-frequency switching, and a magnetic layer for current filtering and modulation. This stratified organization enables significant improvements in transient response, thermal spreading, and PDN efficiency, while also freeing up lateral space for high-speed signal routing.

Among these layers, the magnetic layer presents the most substantial bottleneck for further miniaturization and integration. Unlike capacitors and semiconductor switches, which benefit from continuous scaling in advanced fabrication processes,

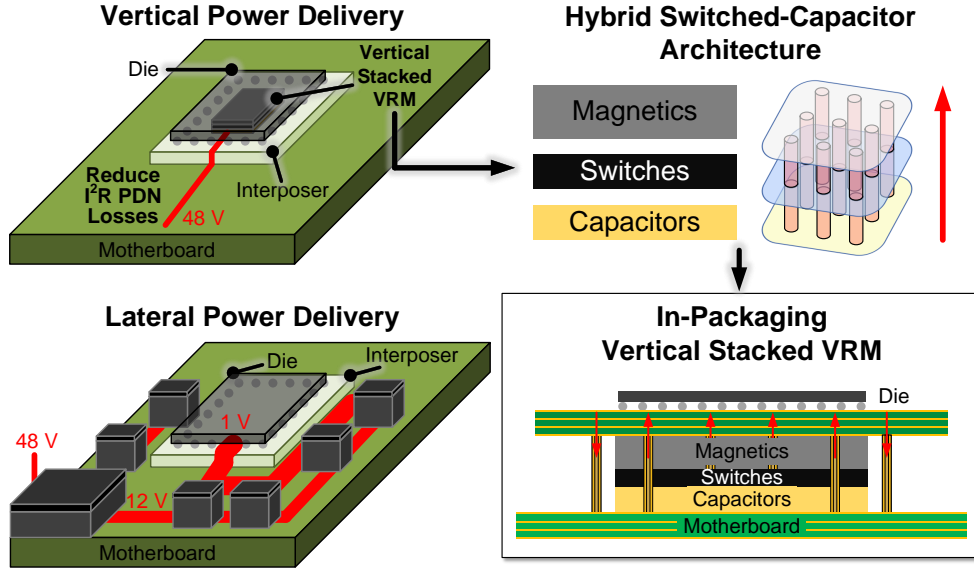


Figure 1.1: Vertically stacked in-package VRM with capacitor, semiconductor, and magnetic layers enabling high-density power delivery.

magnetic components remain bulky, lossy, and difficult to integrate into thin vertical stacks. Their design and optimization are also hindered by limited modeling fidelity, material variability, and a lack of design tools that account for multi-physics, multi-dimensional operating conditions.

Thus, vertical power delivery systems bring not only new opportunities but also new constraints, shifting the burden of performance and integration heavily onto the design of compact, efficient magnetics. Overcoming these challenges is critical for enabling the next generation of high-performance, power-dense computing systems.

1.1.2 Role of Power Magnetics

Magnetic components – including inductors, coupled inductors, and transformers – are essential in virtually all power electronic converters. They regulate current, provide energy buffering, ensure voltage stability, and support soft-switching or resonant operation. In applications such as vertical voltage regulation modules (VRMs) for high-performance computing, where extremely high current densities must be deliv-

ered through compact form factors, magnetics become even more critical. However, these components also represent the most significant bottlenecks in system miniaturization, efficiency, and design complexity.

One major challenge is size: magnetics are typically the bulkiest components in a converter. In vertically stacked VRM architectures, for instance, the magnetic layer often dominates the total system height, as illustrated in Fig. 1.1. The miniaturization of magnetic components is fundamentally limited by material saturation, required inductance, and thermal constraints – factors that are increasingly difficult to balance as current densities rise.

Another key challenge lies in loss mechanisms. Magnetic components introduce both core losses and copper losses, with core loss being especially sensitive to operating conditions. Unlike semiconductors, whose behaviors are modeled with well-established physics, magnetic materials exhibit highly nonlinear, hysteretic responses that vary drastically with factors such as frequency, flux density, temperature, and dc bias. This makes modeling and prediction extremely difficult.

Figure 1.2 shows representative examples of measured B - H hysteresis loops under different conditions for ferrite materials. These loops illustrate how drastically the magnetic behavior can change depending on frequency, excitation amplitude, waveform shape, temperature, and dc bias. Each subfigure isolates a single variable while holding others roughly constant. Even under controlled laboratory settings, the material characteristics shift in complex ways, demonstrating the multi-dimensional and intertwined nature of the influencing factors. In real-world applications, these conditions often co-exist and vary simultaneously, making it impractical to use static models or isolated measurements for accurate design.

Conventional modeling approaches, such as the Steinmetz Equation and its variants (e.g., iGSE, i^2 GSE) shown in Table 1.1, can capture loss trends for simple waveforms under limited conditions, but they fail to account for waveform distortion,

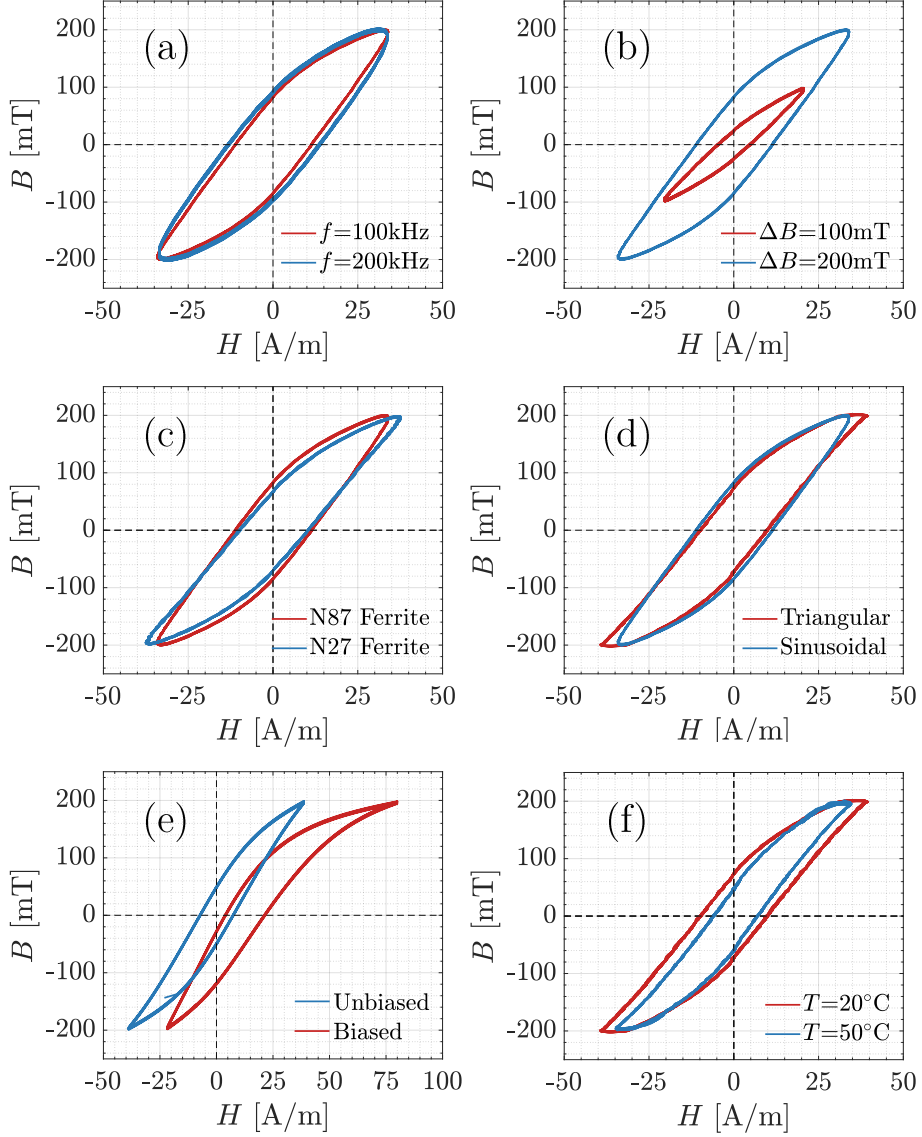


Figure 1.2: Examples of measured B - H loops for ferrite materials under different conditions.

temperature effects, or history-dependent behavior. These empirical models also lack the flexibility to generalize across multiple devices, materials, and operating regimes.

In summary, the fundamental importance of magnetics is accompanied by deep-rooted challenges: physical constraints on miniaturization, significant and condition-sensitive losses, and a lack of accurate, generalizable models. These challenges have slowed progress in developing compact, efficient, and high-speed power delivery solu-

Table 1.1: Number of Parameters used by Core Loss Models

Method	Core Loss (P_V)	#Param.
SE	$k f^\alpha \hat{B}^\beta$	3
iGSE	$\frac{1}{T} \int_0^T k_i \frac{dB}{dt} ^\alpha (\Delta B)^{\beta-\alpha} dt$	3
i^2 GSE	$\frac{1}{T} \int_0^T k_i \frac{dB}{dt} ^\alpha (\Delta B)^{\beta-\alpha} dt + \sum_{l=1}^n Q_{rl} P_{rl}$	8
ML	Neural Network	$\gg 100$

tions. In the next section, we examine the limitations of current modeling techniques in more detail and explore why a new modeling paradigm is urgently needed.

1.1.3 Challenges in Magnetics Modeling and Designing

The modeling and design of magnetic components have long been recognized as one of the most intricate and underdeveloped areas in power electronics. Unlike semiconductors – whose behaviors can be described by relatively complete physical models – magnetic materials exhibit complex, nonlinear, and history-dependent responses that defy simple analytic descriptions. This complexity significantly impedes accurate prediction and efficient design.

Traditional design workflows for power magnetics heavily rely on manufacturer datasheets, which typically provide only a limited set of parameters under narrow operating conditions. These datasheets might include static B - H loops, low-frequency permeability curves, or loss charts for sinusoidal waveforms at select temperatures. However, in real applications, waveforms are often non-sinusoidal (e.g., triangular or trapezoidal), and devices operate under varying temperatures, flux densities, and dc biases. These interdependent factors can drastically affect both permeability and core loss behavior, but are seldom captured comprehensively in datasheets. As a result, designers must either rely on coarse safety margins – leading to oversized and inefficient designs – or engage in repeated prototyping and empirical tuning, which is time-consuming and costly.

Empirical models, such as the Steinmetz Equation (SE) and its variants (e.g., iGSE, i^2 GSE), offer modest improvements over static datasheets by estimating losses under more complex waveforms. Yet, these models are still built upon fitting limited datasets, often with fixed assumptions and oversimplified dependencies. They lack generalizability across materials and operating regimes, and provide little insight into parameter sensitivity or model reliability. Their inability to systematically incorporate multi-dimensional dependencies like temperature, waveform shape, and dc bias remains a major barrier.

Another critical limitation in this field is the scarcity of standardized, high-quality, and large-scale datasets for magnetic materials. Most existing models are developed on proprietary or unpublished data, making it difficult to reproduce results, compare methodologies, or drive innovation. This lack of open, diverse datasets hampers the development of robust and generalizable modeling frameworks, and stifles the application of modern data-driven techniques.

In recent years, the rise of machine learning – especially neural networks – has opened up a transformative opportunity. These models are capable of capturing highly nonlinear, multi-variable relationships by learning directly from data, without the need for rigid analytic expressions. In the context of magnetic modeling, neural networks offer the potential to unify the effects of waveform shape, amplitude, frequency, temperature, and dc bias within a single framework. They can interpolate across observed conditions and, with sufficient data and structure, even extrapolate to unseen ones.

Figure 1.3 illustrates the emerging concept of a “neural network as datasheet” – a trained neural network that replaces traditional loss charts and lookup tables. Such a model can store and retrieve B - H behavior under arbitrary conditions, providing designers with real-time feedback and enabling advanced optimization and co-design flows. In contrast to empirical models with fixed form and limited adaptability,

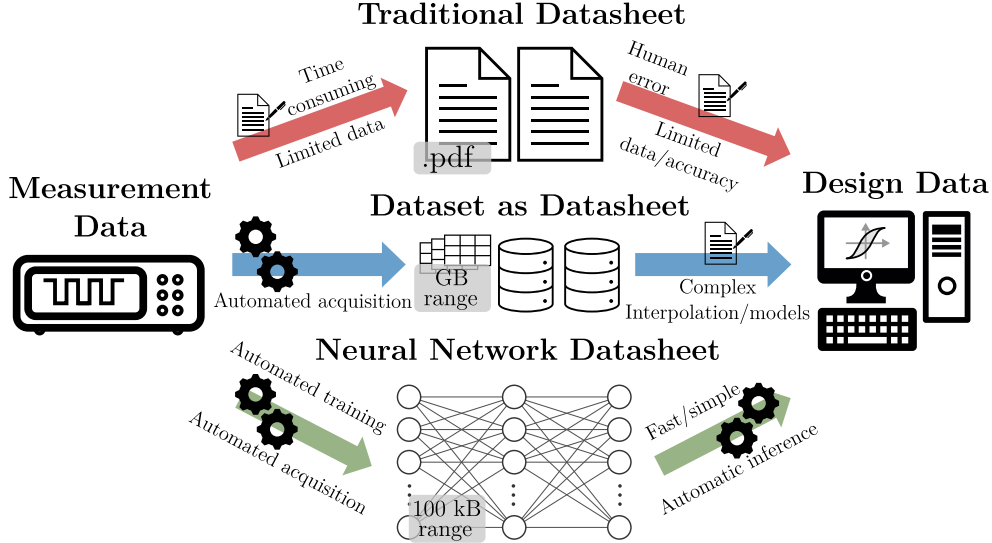


Figure 1.3: Concept of neural network as datasheet.

neural networks can evolve with new data, improve prediction accuracy, and offer unprecedented modeling flexibility.

Nonetheless, data-driven modeling also brings new challenges. Acquiring large and diverse datasets with reliable ground truth requires extensive measurement infrastructure and calibration. Model interpretability, consistency with physical laws, generalization, and integration into design tools are all active areas of research. Yet, despite these hurdles, the direction is clear: machine learning is poised to become a central pillar in next-generation power magnetics design.

In this work, we build upon this paradigm by developing hybrid modeling approaches that combine domain knowledge with machine learning, and demonstrate their application to real-world magnetic design challenges. From fundamental modeling to component optimization, data-driven methods offer a pathway to close the long-standing gap between magnetic theory and practical design.

1.2 Contributions and Thesis Organization

The continual evolution of high-performance computing systems has created unprecedented demands for efficient, compact, and scalable power delivery. Meeting these demands requires not only architectural innovations such as vertically integrated VRMs, but also fundamental breakthroughs in the modeling and design of magnetic components. This thesis addresses these challenges through a data-driven and hybrid approach to magnetic modeling and component design, with contributions spanning three major areas.

Chapter 2 investigates data-driven methods for power magnetics modeling. Contributions include:

- A fully automated magnetic measurement and data acquisition platform is developed, enabling the generation of a large, diverse, and high-quality database
 - MagNet – comprising over 500,000 experimental datapoints across various magnetic materials and excitation conditions.
- Data quality control and dataset structuring methods are introduced to ensure the reliability and representativeness of the collected measurements.
- Multiple neural network-based modeling frameworks are proposed, including LSTM and Transformer architectures, to capture nonlinear magnetic behaviors such as B - H loops and core losses across wide operating ranges with high accuracy.
- Transfer learning techniques are applied to reduce the data requirement for new materials while maintaining high model fidelity, promoting model generalization and reuse.
- The “Neural Network as Datasheet” paradigm is demonstrated via the MagNet-AI online platform, which supports rapid material prediction, comparison, and

selection, laying the foundation for integrating learned models into future design workflows.

Chapter 3 presents design methodologies for ultra-thin, multiphase coupled inductors tailored for vertical power delivery. Contributions are summarized as:

- A novel via-winding structure is proposed to achieve low interconnect impedance and efficient vertical current conduction in tightly stacked packages.
- A systematic design and optimization framework is introduced to co-optimize core shape, winding path, and phase arrangement under compact packaging constraints.
- Two practical prototypes with pinwheel magnetic cores and up to 160 A total current capacity are designed and fabricated, achieving power densities of up to 3,960 W/in³ and efficiency exceeding 93% at 2 MHz.
- Experimental validation is performed in a four-phase buck VRM module, demonstrating the feasibility of high-density, low-loss magnetics for next-generation 3D-integrated converters.

Chapter 4 explores the design and implementation of magnetic-free, air-coupled inductors for modular VRM systems. Contributions include:

- Air-core coupled inductors are designed and implemented using both PCB and Litz-wire windings, offering EMI-friendly packaging, relaxed thermal design, and magnetic-free integration.
- Experimental comparison of different winding technologies is conducted, validating the performance and trade-offs of air-coupled designs.
- A complete Air-LEGO VRM prototype is developed and tested, demonstrating the viability of magnet-free packaging for future high-current, low-profile applications.

Finally, Chapter 5 summarizes the thesis and discusses future research directions. These contributions collectively aim to bridge the longstanding gap between magnetic component modeling and power electronics system integration by leveraging data-driven techniques, hybrid design methodologies, and practical prototyping.

Chapter 2

MagNet: Machine Learning Framework for Modeling Power Magnetic Material

2.1 Background and Motivation

Magnetic components such as inductors and transformers are indispensable in nearly all power electronics systems. However, these components often represent a bottleneck in achieving higher power density and efficiency, primarily due to their substantial physical volume and significant power loss. Although the field has witnessed rapid progress in power semiconductor devices and converter architectures, the modeling and design methodologies for power magnetic components and materials have not kept pace [1–5].

A critical barrier in magnetic component design is the challenge of accurately modeling magnetic material behavior, especially under real-world operating conditions that involve complex, non-sinusoidal excitations. Hysteresis behavior in magnetic cores arises from highly nonlinear and history-dependent excitation-response mechanisms, influenced by multiple factors including frequency, temperature, dc bias, and magnetic memory effects, as depicted in Figure 1.2 and detailed in 2.1. These interacting influences are difficult to model accurately using existing analytical or physics-based techniques [6]. Although empirical models like the Steinmetz Equa-

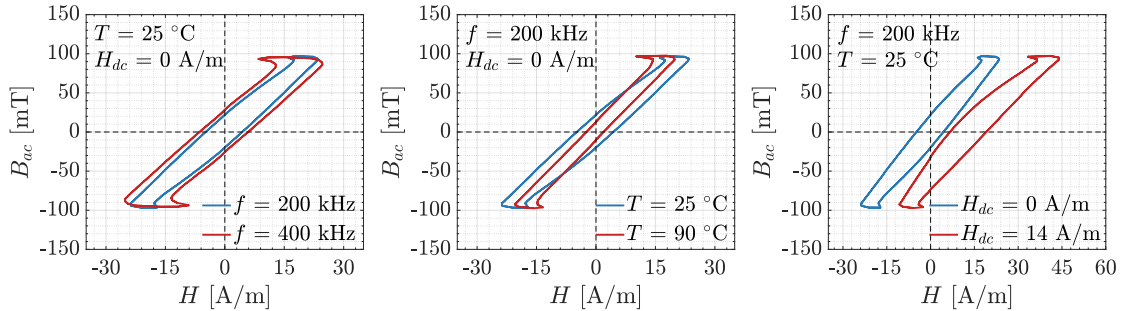


Figure 2.1: Examples of B - H loops measured with N87 ferrite material under 50% duty ratio triangular excitations. The reference loop (blue) is measured at 200 kHz, 25 °C, and 0 A/m dc bias. Each of the three figures shows the variation of B - H loop at different frequencies, temperatures, and dc biases, respectively. The B (only ac) waveform is extracted from voltage measurement, and the H (both ac and dc) waveform is extracted from current measurement.

tion and its extensions [7–9] or physics-informed models such as the Jiles-Atherton model [10] have been widely used, they typically make strong assumptions (e.g., sinusoidal waveforms, fixed temperatures) that limit their general applicability and accuracy.

In practice, designers often rely on manufacturer-provided datasheets or interpolated loss maps, which are based on limited datasets and constrained operating conditions. These datasheets are typically valid only for specific excitation types (e.g., sinusoidal) and do not provide sufficient information for predicting performance under realistic operating conditions encountered in power converter applications. Even online datasets provided by vendors, while more comprehensive, grow exponentially in size with the number of influencing parameters and are difficult to incorporate into modeling tools due to their unstructured format and complexity in extraction.

Recent developments in data-driven modeling – particularly neural networks and other machine learning techniques – offer a promising solution to these challenges. Neural networks have proven effective in capturing nonlinear, multivariable dependencies across a range of disciplines [11–14], and have also been explored in the context of magnetic hysteresis modeling [15–23]. However, most of these studies have used

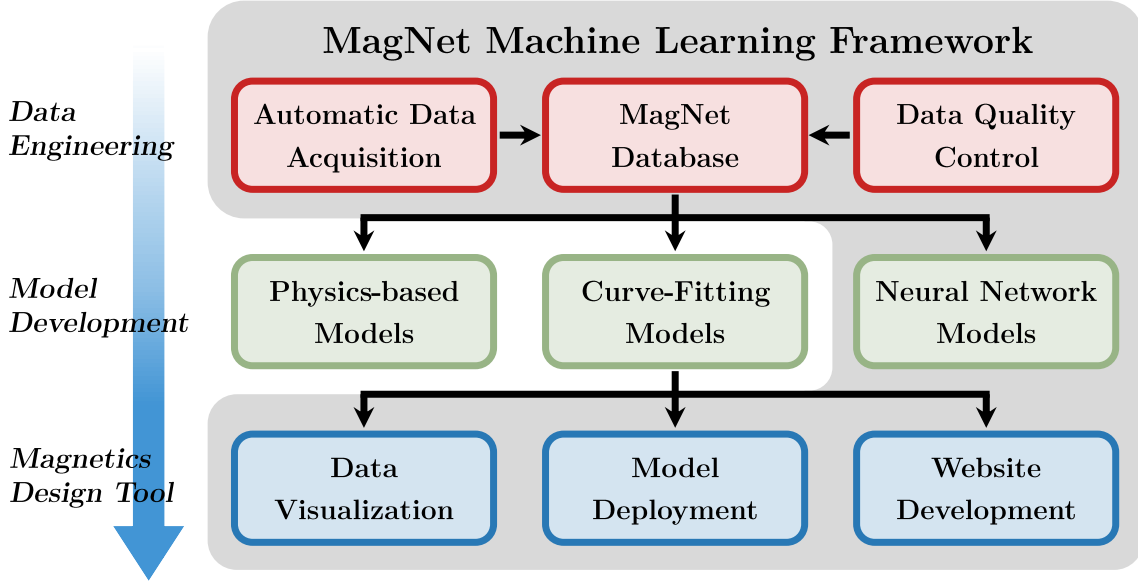


Figure 2.2: Overview of the MagNet framework: from data engineering, model development, to magnetics design tool.

limited datasets, simplistic network architectures (e.g., simple feedforward neural networks, FNNs), or lacked robust evaluation on diverse operating conditions.

This chapter presents a systematic approach toward data-driven modeling and design of power magnetics, emphasizing neural network-based hysteresis modeling. Figure 1.3 illustrates the core concept: rather than relying on traditional static datasheets, a neural network can effectively serve as a dynamic, high-resolution “datasheet” by learning to predict the B - H hysteresis behavior across a wide range of conditions. This approach allows magnetic components to be characterized as a function of multiple variables – such as amplitude, frequency, temperature, and dc bias – thereby enabling accurate and efficient design decisions.

To enable this modeling approach at scale, we propose the MagNet framework – an open-source, large-scale data infrastructure and modeling pipeline for power magnetics. Figure 2.2 shows an overview of this framework, encompassing data collection, preprocessing, neural network training, and integration with magnetics design workflows. The goal of MagNet is to provide a common ground for evaluating different

magnetic materials, modeling techniques, and design tools – much like how *ImageNet* has propelled progress in computer vision [14]. Both equation-based and data-driven models rely fundamentally on the quality and breadth of underlying datasets. By standardizing and expanding this foundation, MagNet seeks to advance the design and optimization of magnetic components for next-generation power electronics systems. The major contributions are summarized as follows:

- MagNet Platform Development: We introduce MagNet, an open-source, large-scale data acquisition and modeling platform tailored for power magnetics research. The system includes detailed hardware-software integration for automatic hysteresis loop and core loss measurement, along with robust data quality evaluation and control mechanisms.
- Unified Machine Learning Workflow: An end-to-end data-driven workflow is developed to model magnetic material behavior under various excitation and environmental conditions. This includes scalar-to-scalar core loss modeling, sequence-to-sequence hysteresis loop prediction, and sequence-to-scalar mappings, which unify the effects of waveform shape, amplitude, frequency, temperature, and dc bias.
- Neural Network as Datasheet: We propose the concept of using neural networks as dynamic, high-resolution datasheets for magnetic materials. Compared to traditional datasheets or tabulated datasets, neural networks enable more accurate, compact, and interpretable material characterization for component design and optimization.
- Advanced Training Techniques: Several techniques are introduced to improve modeling efficiency and generalization capability. These include systematic data augmentation, transfer learning to reduce the required dataset size, and archi-

tectural exploration across different neural network topologies to balance accuracy and computational cost.

- Online Platform and Material Recommendation: The MagNet-AI platform is demonstrated as a web-accessible research tool, supporting neural-network-aided material recommendation for rapid magnetic design prototyping. This validates the applicability of learned models in real-world design workflows.

2.2 Automated Data Acquisition System

High-quality, large-scale datasets are essential to the success of machine learning and data-driven modeling frameworks, as the performance and generalizability of the resulting models are fundamentally limited by the data used for training. In the context of power magnetics, this requirement becomes especially challenging due to the wide range of parameters that influence magnetic behavior. Characteristics such as core loss and hysteresis loop shape are highly sensitive to a number of interrelated factors, including excitation frequency, peak flux density, waveform shape, dc bias, and ambient temperature. The multidimensional nature of these inputs creates an expansive parameter space that must be explored in order to obtain sufficiently representative data.

To meet this need, a fully automated measurement system is required – one that can reliably characterize magnetic behavior across the full span of operating conditions while maintaining high repeatability and accuracy. Automating the measurement process not only accelerates data collection, but also minimizes errors introduced by human operation, which is particularly important for the consistency of time-domain waveforms and derived loss metrics.

A widely used approach for characterizing magnetic materials is the two-winding or voltamperometric method [24–26], which we adopt in this work. This method

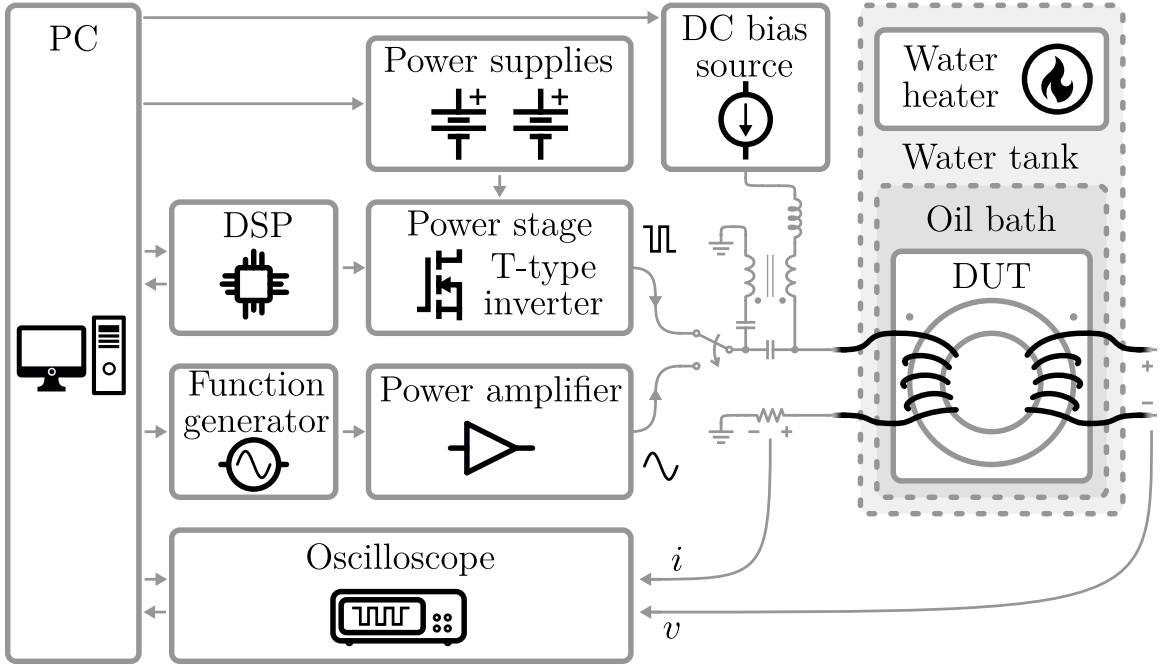


Figure 2.3: Overview of the automated data acquisition system of MagNet.

utilizes two separated windings on the magnetic core: an excitation winding and a sensing winding. The excitation current applied to the primary winding is used to compute the magnetic field strength H , while the voltage induced in the secondary winding is used to determine the magnetic flux density B . Since the secondary winding is isolated from the resistance and leakage inductance of the primary, this setup ensures accurate measurement of B under high-frequency excitations [25].

Figure 2.3 provides an overview of the developed automated data acquisition system. The system consists of a programmable power stage capable of synthesizing a wide range of excitation waveforms, a test fixture for the device under test (DUT), voltage and current sensing paths, an auxiliary dc-bias injection stage, and a thermal control unit. These subsystems are integrated into a software-controlled measurement pipeline, enabling large-scale, multi-condition testing with minimal user intervention.

The physical implementation of the testbench is shown in Fig. 2.4, which captures both the experimental station and the circuit configuration used for magnetic core

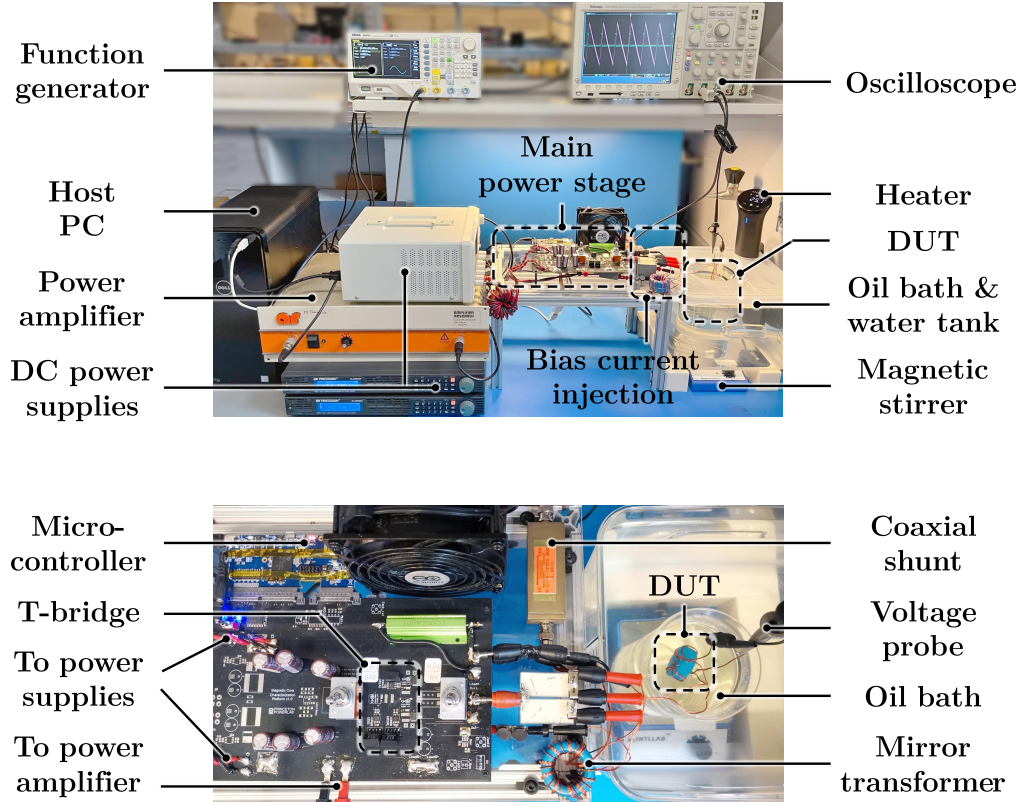


Figure 2.4: Experiment setup and circuit configuration of the magnetic core loss data acquisition system of MagNet.

characterization. The design supports waveform customization, rapid DUT swapping, and temperature variation, forming the basis for scalable and repeatable data generation.

In the implemented MagNet system, the excitation applied to the magnetic core is synthesized and generated using two methods depending on the desired waveform shape. For non-sinusoidal excitations – such as triangular, trapezoidal, or arbitrary periodic waveforms – a T-type inverter is employed in the power stage to enable flexible and accurate waveform generation across a broad frequency range. For purely sinusoidal excitation, a power amplifier driven by a function generator is used to ensure high-fidelity low-distortion waveforms suitable for frequency-domain characterization.

The core responses are captured by measuring both the voltage across the secondary winding and the current through the primary winding. Voltage sensing is performed directly across the secondary, while current sensing utilizes a wide-band coaxial shunt resistor placed in the primary path to ensure accurate current measurements even under high-frequency excitation. To explore the behavior of magnetic materials under dc-biased conditions, an optional bias injection circuit is implemented to superimpose a dc current onto the ac excitation. Only the dc component of the magnetic field strength, H_{dc} , is recorded during this operation.

To support temperature-dependent studies, the setup integrates a thermal control subsystem consisting of an external water heater, a water tank, and an oil bath enclosure. This enables controlled heating of the DUT and allows measurements to be conducted over a wide temperature range.

A host PC runs a dedicated software suite to coordinate the entire measurement process. This system handles waveform generation, device control, data acquisition, and logging, enabling fully automated execution of parameter sweeps across frequency, amplitude, bias level, and temperature. More detailed descriptions of the system hardware, instrumentation, and software control structure are provided in Appendix A.

Once the experiment is triggered, the system automatically applies the programmed excitation waveforms and records the voltage and current signals. The key magnetic characteristics – namely, the B - H loop and the core loss – are extracted based on the classical voltamperometric method [24, 27–29]. The core loss per unit time is calculated using the instantaneous power integration:

$$P_{loss} = \frac{1}{NT} \int_{t_0}^{t_0+NT} v_L(t) \cdot i_L(t), dt \quad (2.1)$$

The magnetic flux density $B(t)$ is reconstructed from the secondary-side voltage by time integration:

$$B(t) = \frac{1}{A_e \cdot n_2} \int v_L(t), dt \quad (2.2)$$

The magnetic field strength $H(t)$ is obtained from the measured excitation current:

$$H(t) = \frac{n_1}{l_e} \cdot i_L(t) \quad (2.3)$$

where $v_L(t)$ and $i_L(t)$ are the measured secondary voltage and primary current, respectively; n_1 and n_2 are the number of turns in the primary and secondary windings; A_e is the effective cross-sectional area, and l_e is the effective magnetic path length of the core, which can be acquired from the component datasheet. The measurement duration NT is selected to ensure that a complete number of waveform periods is captured, eliminating transient artifacts and enabling precise loss and loop shape calculations.

With the described system, each measurement cycle takes approximately 1.5 seconds to complete. Although the actual waveform duration used for measurement is only 100 μ s, additional time is allocated for control commands, hardware communication, and allowing the magnetic material to reach electrical steady state. This deliberate pacing also helps avoid unintended self-heating of the core, which could otherwise compromise measurement consistency. As a result, the system is capable of autonomously collecting up to 2,400 data points per hour without human intervention. A full characterization sweep for a single magnetic material typically takes several hours to complete.

For some magnetic materials, however, additional precautions may be necessary. Certain materials exhibit strong magnetic memory or thermal relaxation behavior, which requires extended time between consecutive excitations, as well as tailored waveform ramp-up and ramp-down procedures to restore the core to a demagnetized or repeatable initial state. In such cases, measurement throughput may be reduced.

Therefore, it is essential to pre-characterize and understand the behavior of the target material to determine appropriate measurement intervals before initiating large-scale data collection.

While the two-winding voltamperometric method was adopted in this work due to its speed, flexibility, and ease of automation, other methods exist for core loss measurement with potentially higher accuracy. For instance, the calorimetric method [30] measures thermal energy dissipation directly and provides highly accurate loss characterization, especially at high frequencies. Similarly, the resonant two-winding method [27] utilizes resonant circuits to minimize measurement errors and achieve better resolution in certain regimes.

However, these alternative techniques often involve significant calibration effort – such as establishing thermal equilibrium or tuning resonant tanks – and are typically less amenable to automation. Consequently, they are not well suited for high-throughput, large-scale database generation. The choice of the two-winding method in this system thus reflects a balance between measurement accuracy, automation feasibility, and dataset scalability. By operating within a carefully constrained measurement range and implementing rigorous quality control procedures (discussed in Section 2.3), the MagNet platform achieves both efficient data acquisition and reliable measurement accuracy at scale.

2.3 Data Quality Control

In data-driven modeling, the accuracy of the results heavily depends on both the size and quality of the dataset. The model accuracy is inherently bounded by the precision and reliability of the data collected during experiments. When measuring the B – H loops and core losses of magnetic materials across a broad range of operational conditions, it is crucial to account for a variety of error sources. These errors can arise from several factors including parasitics, oscilloscope limitations, timing skew between

channels, the behavior of microcontrollers, electrical noise, quantization noise, and temperature fluctuations. The real-time measured voltage and current signals can be described as:

$$\begin{aligned} v_L(t) &= G_V(V_0 + V_{DC} + v_{AC}(t)) \\ i_L(t) &= G_I(I_0 + I_{DC} + i_{AC}(t - \theta)) \end{aligned} \quad (2.4)$$

Here, G_V and G_I represent the gain factors for voltage and current measurements, respectively. V_0 and I_0 are the constant offsets in the voltage and current signals. V_{DC} and I_{DC} represent the dc components in the voltage and current, while v_{AC} and i_{AC} are the ac components in the steady state. The term θ indicates any time skew between the voltage and current measurements. These variables account for all the discrepancies that can influence the measurement accuracy, especially in the context of power loss calculations.

Based on Eq. (2.1), the average power loss across N cycles can be expressed as:

$$\begin{aligned} P_{loss} &= \frac{1}{NT} \int_{t_0}^{t_0+NT} v_L(t) \cdot i_L(t) dt \\ &= G_V G_I (V_0 I_0 + V_0 I_{DC} + V_{DC} I_0) \\ &\quad + G_V G_I V_{DC} I_{DC} \\ &\quad + \frac{G_V G_I}{NT} \int_{t_0}^{t_0+NT} v_{AC}(t) \cdot i_{AC}(t - \theta) dt \end{aligned} \quad (2.5)$$

Equation (2.5) provides insight into the errors associated with various factors such as gain (G_V and G_I), offsets (V_0 and I_0), dc and ac components, and the timing skew. Errors in these variables can lead to significant discrepancies in core loss estimation. For example, as illustrated in Fig. 2.5, even minor errors in voltage or current mea-

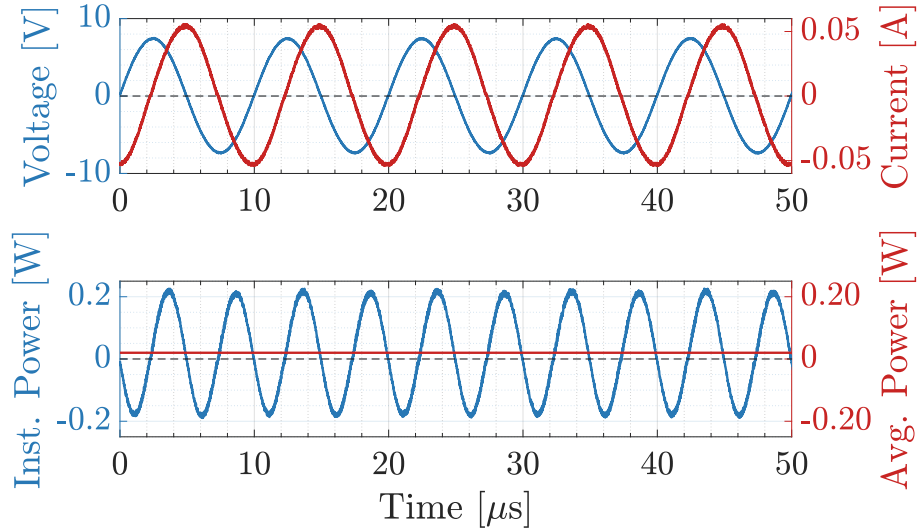


Figure 2.5: Example measured voltage, current, and power waveform of TDK N87 ferrite material at 100 kHz.

surements, or a phase mismatch between them, can result in substantial errors in the calculated power loss.

All equipment used in the data acquisition system undergoes extensive calibration to minimize these errors. For instance, the oscilloscope is calibrated against a digital multi-meter, with a relative error of 0.25% for dc voltage and 0.67% for RMS ac voltage. Before each measurement iteration, auto-calibration of the oscilloscope ensures that zero-drift offsets are minimized, and the voltage and current channels are deskewed. Additionally, parasitic elements introduced by the power stage and cable connections are minimized, by carefully laying out the PCB boards and configuring the measurement platform, to reduce the potential time skew between voltage and current measurements. More details are provided in Appendix B.

A model-driven method that combines physics-based virtual measurements and Monte Carlo simulations is employed to quantify the measurement error and estimate its distribution. The analysis of the systematic and statistical errors helps to refine the measurement range and ensures high data quality. Specifically, the study identifies the significant impact of geometry variations on core loss, as described in [6], where

the maximum geometry-to-geometry variation of core loss density can exceed 10%, a larger influence than most other sources of error.

Moreover, a data-driven algorithm is developed to detect and remove anomalous outliers from the collected dataset. Given the large scale of data collected in an automated fashion, it is inevitable that some erroneous data points will be present. The algorithm evaluates the smoothness of the measured data points within a specified range of flux density and frequency by curve-fitting the local Steinmetz Equation. For each data point, an expected value of core loss is inferred from adjacent points, and the discrepancy between the expected and measured values is computed. Data points that exhibit significant discrepancies are flagged and removed from the dataset. This process ensures that the dataset remains clean and reliable for model training. Further details on the data quality control process can be found in Appendix B.

By incorporating these rigorous data quality control measures, the database developed for power magnetics research remains highly accurate, reliable, and suitable for training robust machine learning models.

2.4 Database Construction

The fully automated data acquisition system allows for the rapid and efficient measurement of B - H loop data, capturing the magnetic material's behavior under different excitation waveforms. Figure 2.6 shows four examples of measured voltage and current waveforms, which include sinusoidal, triangular, symmetric trapezoidal, and asymmetric trapezoidal waveforms, all measured with N87 ferrite material at 100kHz. The sampling time step for each waveform sequence is set to 8 ns, and each sequence contains 10,000 sampling points for a 100 μ s measurement period.

Accurate and well-documented data is essential for making effective use of the collected information. Figure 2.7 illustrates the current data format of the MagNet database, which is structured into three main data domains:

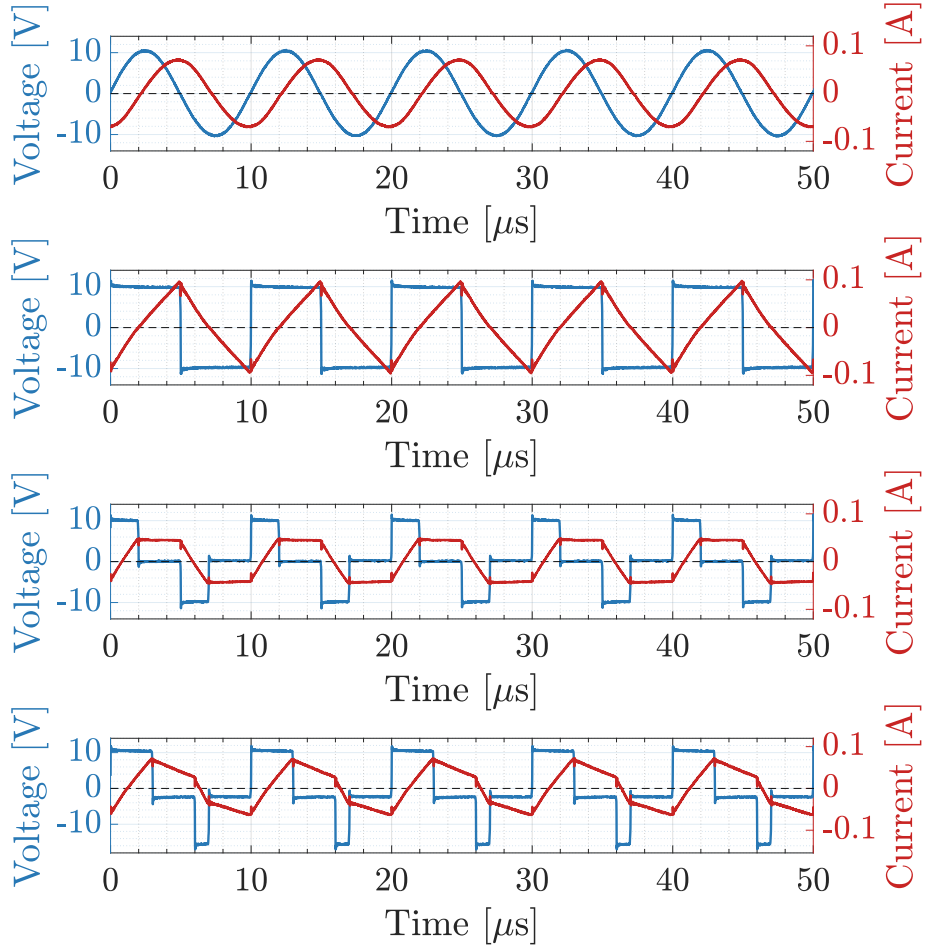


Figure 2.6: Example voltage and current waveforms of sinusoidal, triangular, symmetric trapezoidal, and asymmetric trapezoidal excitations.

- DUT Information: This includes the material type and geometry parameters of the device under test (DUT).
- Raw Measured Data: This domain contains the voltage, current, and the corresponding time stamps of the measured time-series data.
- Post-processed Data: This includes derived quantities such as the frequency, peak flux density, dc bias, duty ratio, temperature, volumetric power loss, and the single-cycle B - H loop sequences.

	Field	Value
DUT Information	Date_processing	'2022-08-10'
	Material	'N87'
	Core_Shape	'R34.0X20.5X12.5'
	Effective_Area	8.2600e-05
	Effective_Volume	6.7780e-06
	Effective_Length	0.0821
	Primary_Turns	5
	Secondary_Turns	5
Raw Time Series Data	Voltage	24773x10000 double
	Current	24773x10000 double
	Time	24773x10000 double
	Sampling_Time	1.0000e-08
	Frequency	24773x1 double
	Flux_Density	24773x1 double
Post-processed Data	Hdc	24773x1 double
	Duty_P	24773x1 double
	Duty_N	24773x1 double
	Temperature	24773x1 double
	Volumetric_Loss	24773x1 double
	B_Field	24773x100 double
	H_Field	24773x100 double

Figure 2.7: Data format of the MagNet database with four different types of contents.

Due to the resolution of the digital micro-controller, there might be slight deviations between the actual signal frequency and the configured frequency. To calculate the actual frequency of the signals, the data is processed using Welch's method [31], which estimates the power spectral density of the signal. The frequency with the highest power spectral density near the commanded frequency is identified as the fundamental frequency. The flux density is calculated by integrating the voltage signal, using the geometry parameters of the DUT. The duty ratio is detected based on the zero-crossing point for each section of the waveform.

The single-cycle B - H loop data is generated by averaging the different periodic sections of the waveform across the entire sequence, in order to mitigate the statistical error in the measurement. A 100-step interpolation is then applied to the averaged

Table 2.1: Number of Data Points Currently in the MagNet Dataset

Material	Sine	Tri.	Trap.	Total
TDK N27	1,612	13,480	27,856	42,948
TDK N30	741	4,254	9,139	14,134
TDK N49	1,392	13,591	26,185	41,168
TDK N87	3,495	46,973	92,403	142,871
Ferroxcube 3C90	4,008	34,833	69,653	108,494
Ferroxcube 3C94	5,130	35,442	73,119	113,691
Ferroxcube 3F4	925	18,210	31,495	50,630
Ferroxcube 3E6	503	2,045	44,48	6,996
Fair-Rite 77	1,115	9,316	19,555	29,986
Fair-Rite 78	1,000	7,437	15,654	24,091
Total	19,921	185,581	369,507	575,009

waveform, capturing the main shape of the B - H loop in the targeted frequency range with significantly reduced data size. Although this process homogenizes waveforms with different frequencies into sequences of equal length, it also reduces the resolution, particularly around switching events. Despite the loss of resolution, the single-cycle data provides a simplified representation of the B - H loop in periodic steady-state operation.

Further details regarding the data processing methods used in constructing the MagNet database can be found in [6].

Data are open-sourced in four different formats, including “.mat”, “.json”, “.hdf5”, and “.csv”. This data structure is designed to contain sufficient information that facilitates the research community to compare, verify and reproduce the core loss measurement, and trace the potential error mechanisms in the automatic data acquisition process.

Table 2.1 lists the size of the MagNet dataset in its current state. The sizes of the data for the ten materials are slightly different because of their various designated operation ranges for the parameter sweeping. Details about the range of measurement (e.g., flux density, frequency, dc bias, and temperature) are provided in Appendix A.

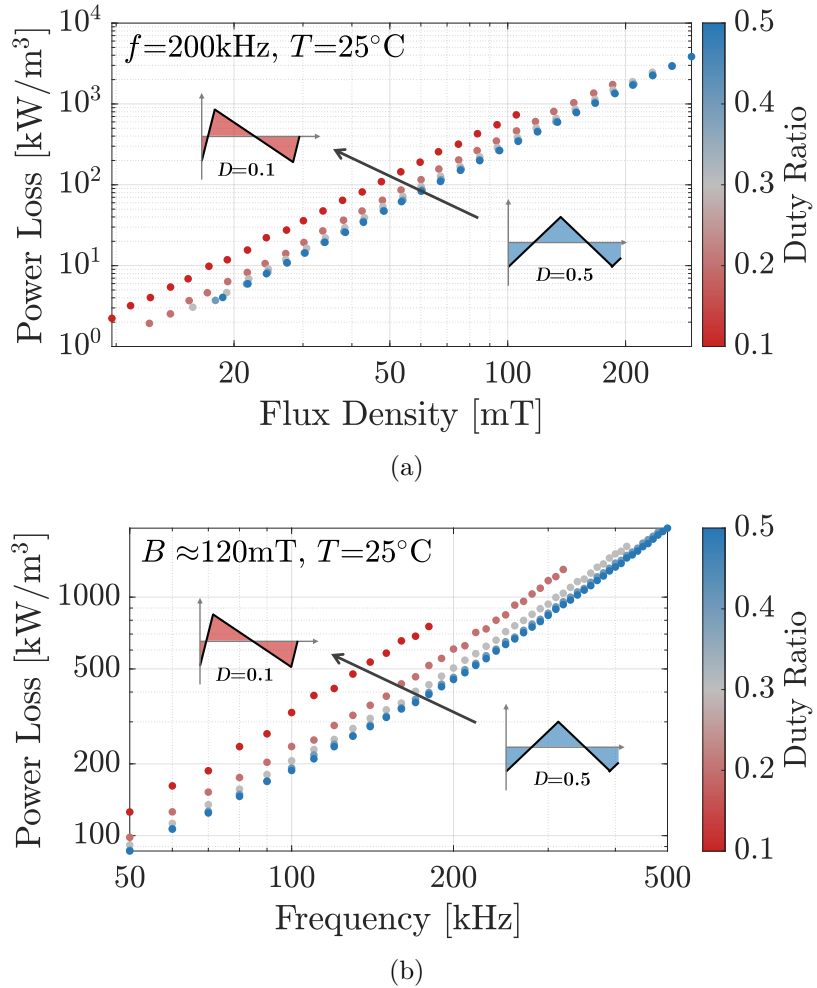


Figure 2.8: Data visualization of the measured core losses under triangular excitation for N87 material: (a) core loss versus peak flux density with frequency at 200 kHz; (b) core loss versus frequency with peak flux density around 120 mT;

The total number of data points is more than 500,000 so far. Measurements for other materials are in progress and the scale of MagNet dataset is expanding constantly.

Figure 2.8 and 2.9 illustrates the magnetic core loss density of N87 ferrite material, providing a visual example of the MagNet database. In this case, the magnetic core is excited with triangular waveforms at different duty ratios. Panel (a) of Figure 2.8 shows the core loss variation with respect to the peak flux density at a fixed frequency of 200 kHz. Panel (b) depicts the core loss variation with frequency, where the peak flux density is approximately fixed at 120 mT. Panel (a) of Figure 2.9 presents

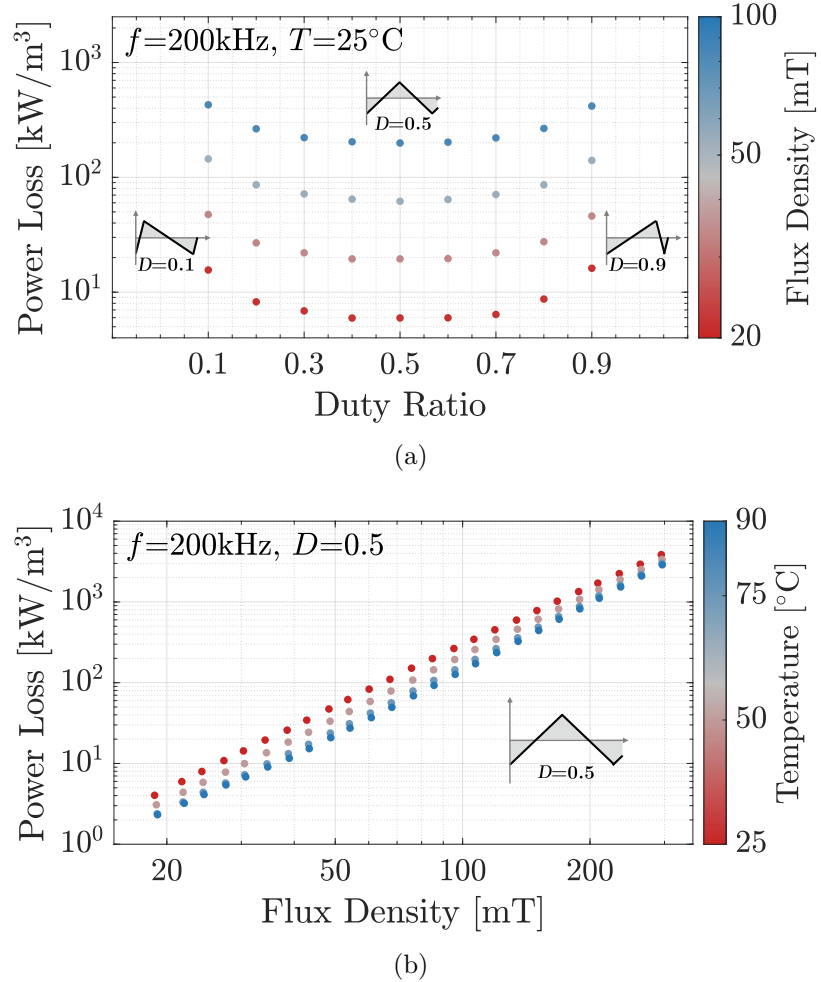


Figure 2.9: Data visualization of the measured core losses under triangular excitation for N87 material: (a) core loss versus duty ratios at different flux density level with frequency at 200 kHz; (b) core loss versus peak flux density at different temperature with frequency at 200 kHz and duty ratio at 0.5.

the variation in core loss with duty ratio at different flux density levels, with the frequency fixed at 200 kHz, all measured at 25°C . Finally, panel (b) shows the core loss variations at different temperatures, with the duty ratio fixed at 0.5 and the frequency at 200 kHz. Each panel demonstrates a unique nonlinear relationship in terms of varying factors, which are typically present together in real applications. A more in-depth discussion of these factors is available in [6]. The intricate nature of power magnetics characteristics, as evidenced by these plots, further highlights the necessity of utilizing machine learning techniques.

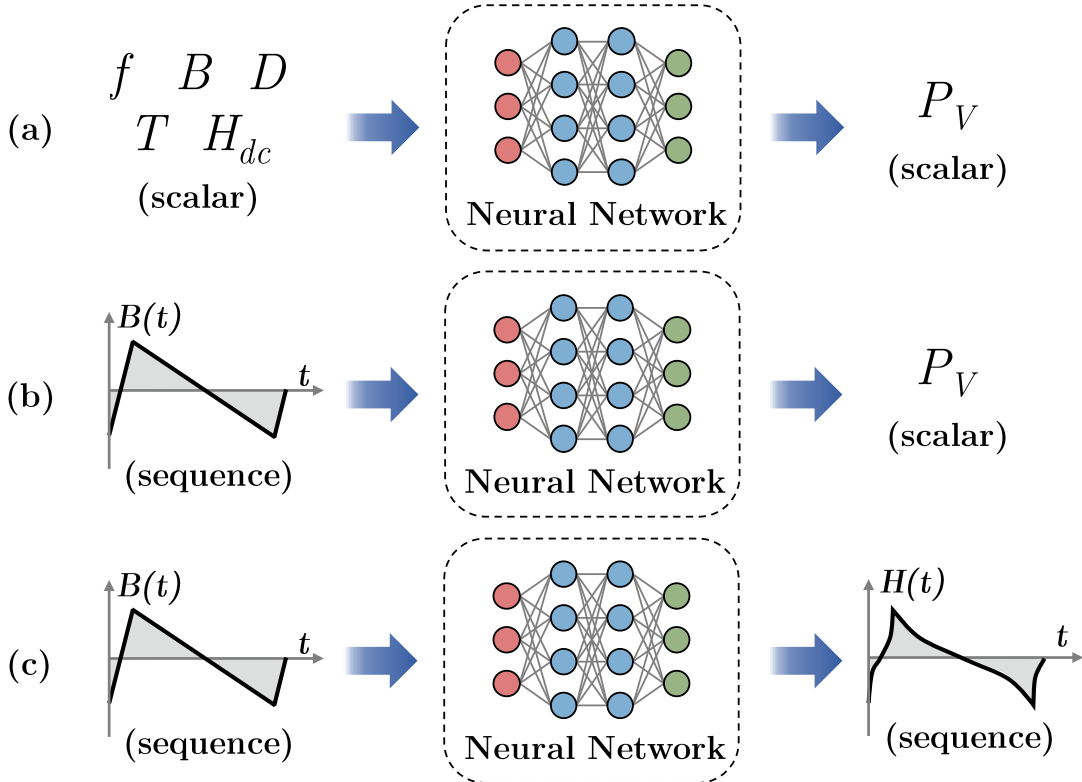


Figure 2.10: Three example ways of modeling the behavior of magnetic materials with neural networks: (a) scalar-to-scalar, (b) sequence-to-scalar, and (c) sequence-to-sequence.

To provide broader access to the data and tools, a webpage-based platform with a graphical user interface (GUI) – MagNet – has been developed. The MagNet platform allows users to search, visualize, and download all the aforementioned measured datasets. It also offers a user-friendly interface for calculating and simulating magnetic core loss using the neural network models introduced in Section 2.5, supported by a PLECS simulation engine. The platform, models, and datasets are open-sourced and accessible on GitHub¹.

2.5 Neural Network Models for Power Magnetics Modeling

The MagNet database provides a versatile foundation for modeling and designing power magnetics. It allows users to either plot the data directly to read core loss values under specific operating conditions or develop equation-based analytical models for magnetic core loss. These methods include identifying Steinmetz parameters, forming loss maps, or extracting parameters for models such as Jiles-Atherton. However, this thesis emphasizes the use of neural network modeling for power magnetics based on the MagNet database. As shown in Figure 2.10, we explore three approaches to modeling the behavior of magnetic materials using neural networks:

- **Scalar-to-Scalar Model:** This approach is akin to the traditional Steinmetz Equation where a neural network is used to map multiple scalar inputs, such as frequency, peak flux density, and duty ratio, to a scalar output representing the core loss. The primary advantage of using neural networks in this context is the ability to make more accurate predictions over a wider range of operating conditions. This is possible because neural networks can handle a significantly larger number of parameters than the traditional Steinmetz equation. Furthermore, the model can be easily extended, generalized, and retrained to incorporate additional influencing factors, such as temperature and dc bias.
- **Sequence-to-Scalar Model:** Similar to the improved Generalized Steinmetz Equation (iGSE), a neural network can be used in a sequence-to-scalar configuration. In this case, the entire excitation waveform (e.g., flux density) is input into the model, and the output is the scalar value of the core loss. This model is advantageous over the scalar-to-scalar model because it can predict core loss for arbitrary excitation waveforms without the need to extract parameters from the waveform, thereby reducing errors.

¹MagNet GitHub repo: <https://github.com/PrincetonUniversity/magnet/>

- **Sequence-to-Sequence Model:** This model is similar to the Jiles-Atherton model and is used to predict the magnetic responses (e.g., $B(t)$) based on the excitation waveform (e.g., $H(t)$). Sequence-to-sequence models are particularly useful for integration in time-domain circuit simulations, such as SPICE simulations. They can predict the magnetic material's behavior in response to varying excitation waveforms, providing a more comprehensive understanding of the material's dynamic performance.

In this dissertation, we focus solely on the sequence-to-sequence models. Other types of models can be found in [32]. The models discussed in this thesis are purely data-driven and do not incorporate existing physical knowledge about power magnetics. However, leveraging such existing physical understanding to enhance the neural network design is a promising future direction for improving model performance [33].

2.5.1 Encoder-Projector-Decoder Architecture

The encoder-projector-decoder neural network architecture proposed in this thesis is designed to model the complex behavior of magnetic materials, particularly the hysteresis loop, under varying operating conditions. This architecture allows the mapping of input time-series data into another time-series output while incorporating important scalar inputs such as frequency, temperature, and dc bias. These factors significantly influence the shape and characteristics of the B - H loop, making it essential to include them in the prediction process.

Figure 2.11 illustrates the structure and data flow of the encoder-projector-decoder architecture. In this setup, the input sequence consists of the flux density $B(t)$, and the output sequence corresponds to the field strength $H(t)$, which defines the core shape of the hysteresis loop. The architecture is built to consider both the time-series nature of the input and the additional scalar inputs that affect the material's response.

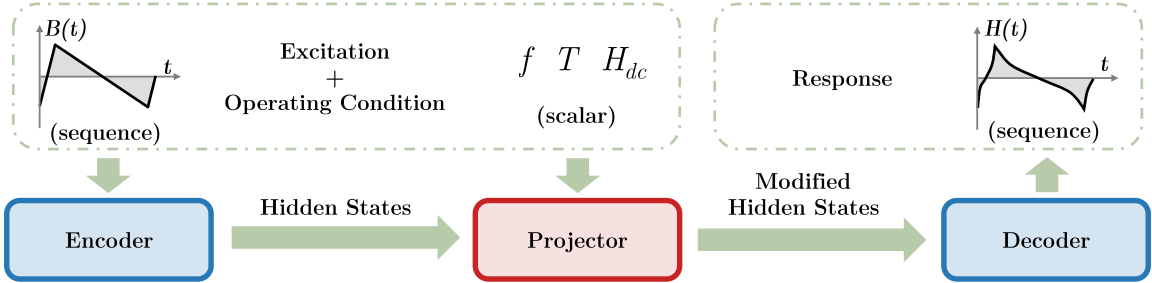


Figure 2.11: Architecture and data flow of the encoder-projector-decoder neural network architecture.

The encoder component processes the input flux density sequence $B(t)$ and compresses it into a fixed-dimensional vector. During this process, it captures important temporal correlations and sequential information, including the shape, amplitude, and rate of change of the excitation waveform. These hidden state vectors, which summarize the relevant information from the input sequence, are then passed through the projector.

The projector plays a crucial role by adjusting the hidden state vectors according to the scalar inputs, such as frequency (f), temperature (T), and dc bias (H_{dc}). This step ensures that the model accounts for the external conditions that influence the shape of the B - H loop.

Finally, the modified hidden state vectors are processed by the decoder to predict the output field strength sequence $H(t)$.

An important feature of this architecture is the auto-regressive nature of the model during inference. At each time step, the model not only uses the current hidden state vectors but also considers the previously generated predictions. This sequential generation preserves the temporal information of the sequence, ensuring that the output is consistently aligned with the input data and maintains hidden time causality.

The proposed model is focused on material-level modeling of magnetic components, specifically the hysteresis loop. Although this approach does not directly

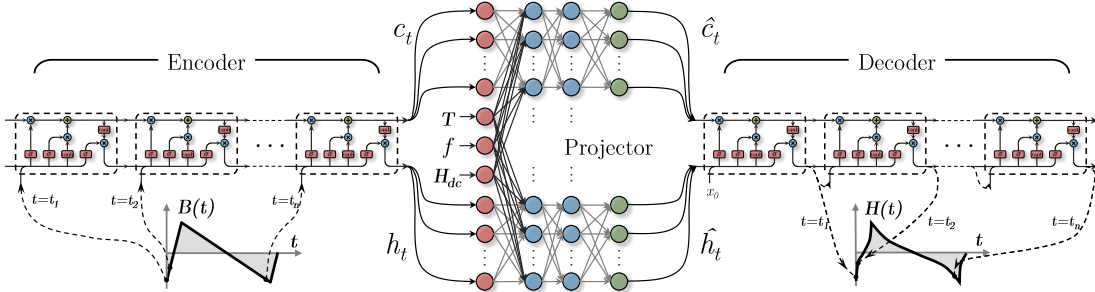


Figure 2.12: Neural network structure of the LSTM-based encoder-projector-decoder architecture. Temperature (T), frequency (f), and dc bias (H_{dc}) information are mixed with the waveform information in the FNN projector after the encoder and before the decoder.

incorporate the impact of component-level geometry, the encoder-projector-decoder architecture could be extended in future work to include geometric factors, which significantly affect the component-level behaviors of magnetic materials [34–36].

Different types of neural network architectures, such as recurrent neural networks (RNN) [37], attention-based networks (transformer), and convolutional neural networks (CNN) [38–40], can be used for the encoder and decoder modules. These architectures have proven effective in modeling sequences with complex temporal dependencies. A Wavelet-CNN-based neural network has already been applied to model core loss in [41]. In this work, we specifically investigate and provide guidance on using LSTM-based and transformer-based neural networks for the encoder-projector-decoder architecture, which is designed to map time-series input to output while incorporating external factors.

2.5.2 LSTM Neural Network Models

Long short-term memory is a specialized type of recurrent neural network that is well-suited for capturing the temporal relationships within time series data [42]. The effectiveness of LSTM networks in solving sequence-to-sequence tasks has been demonstrated, with the LSTM encoder-decoder architecture being one of the most widely

adopted implementations [43]. The LSTM-based encoder-decoder architecture has a well-established ecosystem in popular deep learning frameworks such as PyTorch and TensorFlow.

In the LSTM-based encoder-projector-decoder architecture depicted in Figure 2.12, both the encoder and the decoder are implemented as LSTM neural networks. At a given time step $t = t_i$, the input sequence of $B(t)$ is inputted to the LSTM network and processed through the input gate, forget gate, and output gate on the encoder side. The temporal information is stored in the cell states and the hidden states, which are fed back through the recurrent connections for processing the next input at $t = t_{i+1}$. By unwrapping the recurrent connections across the timeline, it is equivalent to passing the entire input sequence through a series of LSTM networks. Mathematically, the operation of the LSTM cell at time t can be described as:

$$\begin{aligned}
 f_t &= \sigma(W_{if}x_t + b_{if} + W_{hf}h_{t-1} + b_{hf}) \\
 i_t &= \sigma(W_{ii}x_t + b_{ii} + W_{hi}h_{t-1} + b_{hi}) \\
 g_t &= \tanh(W_{ig}x_t + b_{ig} + W_{hg}h_{t-1} + b_{hg}) \\
 o_t &= \sigma(W_{io}x_t + b_{io} + W_{ho}h_{t-1} + b_{ho}) \\
 c_t &= f_t \odot c_{t-1} + i_t \odot g_t \\
 h_t &= o_t \odot \tanh(c_t)
 \end{aligned} \tag{2.6}$$

where x_t is the sequential input at time t . Intermediate variables i_t , f_t , and o_t represent the value of the input gate, forget gate, and output gate, respectively. c_t and h_t refer to the cell states and the hidden states, which are the recurrent variables being fed back to the LSTM cell and thus providing the memorizing capability. The function $\sigma(x)$ is the Sigmoid function that operates as the activation function to provide the nonlinear learning capability. As in an FNN, W and b are the weights

Algorithm 1 LSTM-based Model

Input:

Flux Density $B(t)$, Frequency f , Temperature T ,
Dc bias H_{dc} ;

Output:

Magnetic Filed Strength $H(t)$;
 1: Initialize hidden states h_0 and cell states c_0 ;
 2: $x_1 \leftarrow B(t_1)$;
 3: **for** $i = 1$ to L **do**
 $h_i, c_i \leftarrow \text{LSTM}_1(h_{i-1}, c_{i-1}, B(t_i))$; **[Encoder]**
 4: $h'_0 \leftarrow \text{FNN}_1(h_L, f, T, H_{dc})$;
 $c'_0 \leftarrow \text{FNN}_2(h_L, f, T, H_{dc})$; **[Projector]**
 5: Initialize y_0 ;
 6: **for** $i = 1$ to L **do**
 $h'_i, c'_i, y_i \leftarrow \text{LSTM}_2(h'_{i-1}, c'_{i-1}, y(t_{i-1}))$; **[Decoder]**
 7: **return** $H(t) \leftarrow \{y_1, y_2, \dots, y_L\}$;

and biases, and the subscript refers to the source and target variables that they are applied to. The operator \odot stands for the Hadamard product, which performs an element-wise product for all the elements of two matrices.

Then, the cell states and the hidden states at the last time step are concatenated with the additional inputs, and fed into the projector, where these state vectors are modified using a feedforward neural network. The LSTM network in the decoder uses the modified states to predict the output $H(t)$ at $t = t_0$, which is then fed back as the input for the next prediction at $t = t_1$. The prediction continues until the entire output sequence is generated.

More details of the data flow in the LSTM model are described by the pseudo-codes in Algorithm 1. Models and example codes are available on MagNet GitHub repository².

2.5.3 Transformer Neural Network Models

²MagNet repository: <https://github.com/PrincetonUniversity/magnet/>

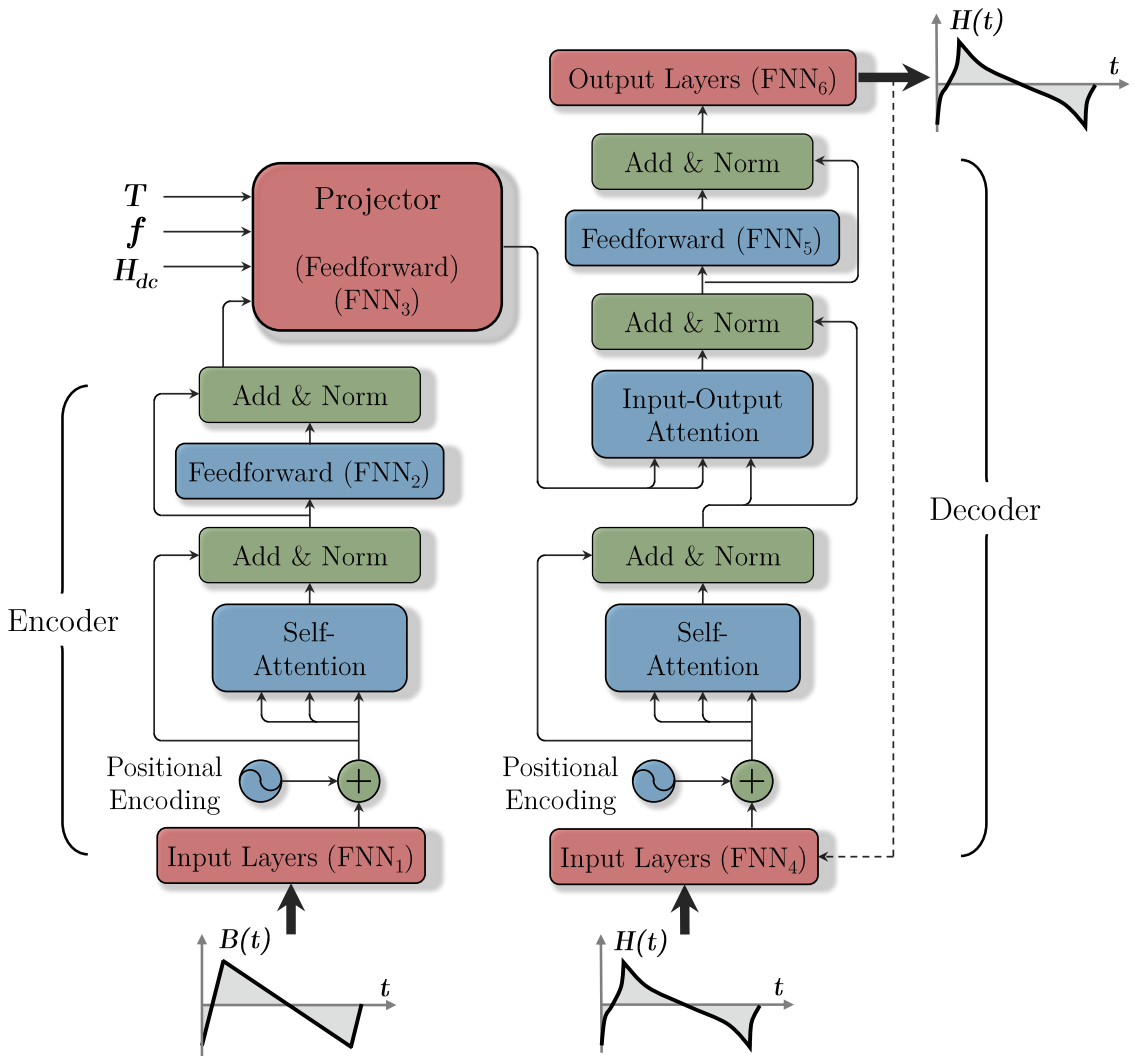


Figure 2.13: Network structure of the transformer-based encoder-projector-decoder architecture. $B(t)$ waveform is the sequence input of the encoder. T , f and H_{dc} are the scalar inputs of the projector. During the model training, the targeting $H(t)$ is directly fed to the decoder as a reference input. During the model inference, the predicted sequence is fed back to the decoder, generating the entire output sequence in an auto-regressive manner.

Transformer with the attention mechanism is another very successful network architecture that excels at modeling sequence-to-sequence problems, such as Large Language Models represented by ChatGPT. Unlike RNNs, the transformer eschews recurrent connections, but instead relies entirely on attention mechanisms to capture temporal dependencies between the input and output sequences. Modified from the

Algorithm 2 Transformer-based Model

Input:

Flux Density $B(t)$, Frequency f , Temperature T , Dc bias H_{dc} , Field Strength $H(t)$ (only available in training);

Output:

Magnetic Field Strength $H(t)$;

- 1: $X \leftarrow \text{FNN}_1(B(t))$; [Mapping]
- 2: $X \leftarrow X + \text{Positional Encoding}$;
- 3: $X \leftarrow \text{Norm}(X + \text{Self-Attention}_1(X))$;
 $X \leftarrow \text{Norm}(X + \text{FNN}_2(X))$; [Encoder]
- 4: $X' \leftarrow \text{FNN}_3(X, f, T, H_{dc})$; [Projector]
- 5: **if** training **then**
 - 5.1: $Y \leftarrow \text{FNN}_4(H(t))$; [Mapping]
 - 5.2: $Y \leftarrow Y + \text{Positional Encoding}$;
 - 5.3: $Y \leftarrow \text{Norm}(Y + \text{Self-Attention}_2(Y))$;
 - 5.4: $Y' \leftarrow \text{Norm}(Y + \text{Input-Output-Attention}(X', Y))$;
 - 5.5: $Y' \leftarrow \text{Norm}(Y' + \text{FNN}_5(Y'))$; [Decoder]
 - 5.6: $H(t) \leftarrow \text{FNN}_6(Y')$ [Mapping]
- 6: **else if** testing **then**
 - 6.1: Initialize $H_0(t) \leftarrow 0$;
 - 6.2: **for** $i = 1$ to L **do**
 - 6.2.1: $Y \leftarrow \text{FNN}_4(H_{i-1}(t))$; [Mapping]
 - 6.2.2: $Y \leftarrow Y + \text{Positional Encoding}$;
 - 6.2.3: $Y \leftarrow \text{Norm}(Y + \text{Self-Attention}_2(Y))$;
 - 6.2.4: $Y' \leftarrow \text{Norm}(Y + \text{Input-Output-Attention}(X', Y))$;
 - 6.2.5: $Y' \leftarrow \text{Norm}(Y' + \text{FNN}_5(Y'))$; [Decoder]
 - 6.2.6: $H_i \leftarrow \text{FNN}_6(Y')$ [Mapping]
 - 6.3: $H(t) \leftarrow H_L$;
- 7: **return** $H(t)$;

original structure in [44], we implement an encoder-projector-decoder architecture as shown in Fig. 2.13.

The data point at each time step in the input sequence $B(t)$ is firstly passed through a shallow feedforward neural network and transformed to a d -dimension vector, which sets the representation dimension of the model. Given that the attention mechanism used in the transformer model is essentially the dot-product of matrices, the time steps in the sequence are permutable. To ensure the model effectively captures temporal dependency, the input vector is combined with a positional encoding vector, providing information about the position of each time step in the sequence.

The resulting vector is then fed into the self-attention module, which analyzes and captures the temporal dependency within the input sequence itself. Further processed by a feedforward neural network, a set of hidden vectors encapsulating the information of the input sequence is generated and passed to the projector.

Next, the hidden vectors obtained from the encoder are similarly concatenated with the additional inputs, such as frequency f , temperature T , and dc bias H_{dc} , and the resulting vectors are passed through a feedforward neural network based projector. The projector modifies the hidden vectors by considering the influence of these additional inputs. The modified hidden vectors are then passed to the decoder for reconstructing the output sequence.

Besides the hidden vectors, the input of the decoder consists of a reference sequence. During the network training, it is the target output sequence; during the network testing, it is the sequence predicted by the model itself (initialized with zero), shown as the dashed line in Fig. 2.13. The reference sequence is similarly mapped to a d -dimension vector with a shallow feedforward neural network, summed with a positional encoding vector, and fed into the self-attention module to generate another set of hidden vectors. Both sets of hidden vectors from the projector and the self-attention module are further processed with the input-output attention module. Finally, the resulting output vectors are processed by a feedforward neural network to generate the desired output sequence $H(t)$.

More details of the data flow in the transformer model are described by the pseudo-codes in Algorithm 2. Models and codes are available on MagNet GitHub repository as well.

2.6 Data Processing and Augmentation

The accuracy of predictions made by a neural network model is intrinsically linked to the quality of the training data. In this study, the training data is derived from the

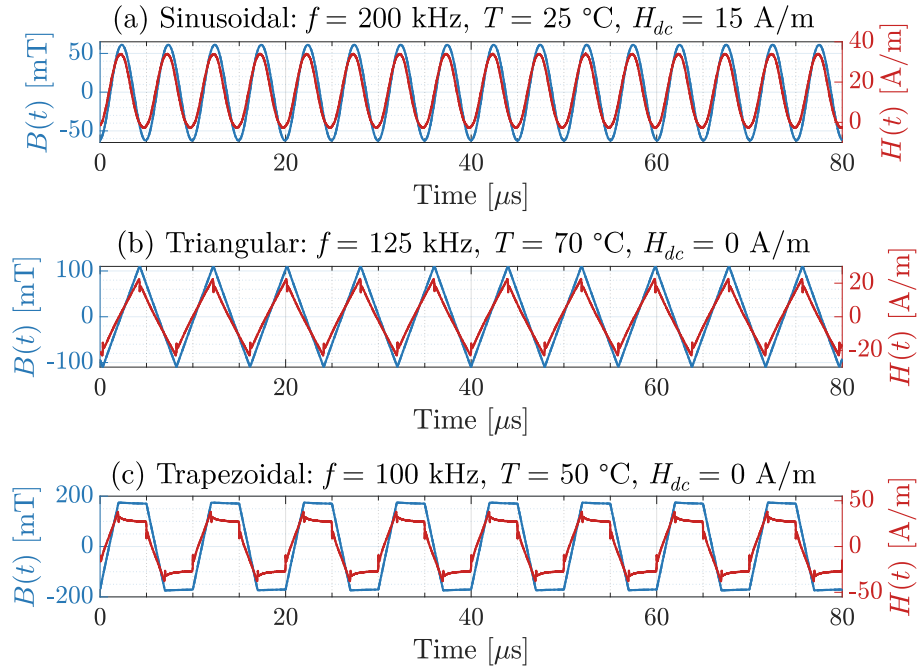


Figure 2.14: Examples of the full-length waveforms measured with N87 ferrite material under varying frequency, temperature, and dc bias conditions: (a) sinusoidal wave; (b) triangular wave; (c) trapezoidal wave.

extensive measured dataset in the MagNet database [32, 45]. The database contains B - H loop measurements for 10 different ferrite materials, captured across a wide array of excitation and operational conditions, all collected by an automated data acquisition system. The measurements are recorded during periodic steady-state operations.

The MagNet dataset consists of five key data fields: the flux density waveform $B(t)$, the field strength waveform $H(t)$, the fundamental frequency f , the temperature T , and the dc bias H_{dc} . The fundamental frequency is calculated using Welch's frequency domain method [46] based on the measured voltage waveform, while the other four data fields are directly obtained from the measurements. In the following sections, we present example results based on the dataset of N87 ferrite material, which includes 142,871 measured data points (B - H loops) covering a range of flux density amplitudes from 10 mT to 300 mT, fundamental frequencies from 50 kHz to

500 kHz, temperatures from 25°C to 90°C, and dc bias field strengths from 0 A/m to 60 A/m, with various waveform shapes and duty ratios. The measured waveform shapes are classified into three types: sinusoidal, triangular, and trapezoidal, based on the shape of the flux density waveform. Besides the amplitude, the duty ratio D for each segment in the triangular and trapezoidal waves can be independently adjusted. This dataset forms the foundation for a neural network model that predicts the hysteresis loop under varying operating conditions and excitation waveform shapes. Figure 2.14 provides examples of several waveforms contained in the dataset.

Due to the unknown permeability and relaxation effects, it is not possible to directly estimate B_{dc} from H_{dc} . The flux density $B(t)$ here represents only the ac component, which is derived from the voltage measurement, while $H(t)$ includes both ac and dc components, directly obtained from the current measurement. Consequently, the flux densities in the hysteresis loops presented below correspond only to the ac part, B_{ac} .

To enhance model convergence, all five data fields $B(t)$, $H(t)$, f , T , and H_{dc} are normalized prior to input into the neural network. This is achieved by subtracting the mean and scaling by the standard deviation for each data field. The parameters for this standardization are saved and reused during model testing and inference.

The two sequence inputs $B(t)$ and $H(t)$ require additional processing to ensure that the network achieves both accurate predictions and sufficient generalization. The most common preprocessing technique for preventing overfitting is the introduction of reasonable noise. In this study, both $B(t)$ and $H(t)$ waveforms are augmented with white noise, assuming a uniform distribution within the ranges of ± 0.1 mT and ± 0.05 A/m, respectively. Additionally, the sequence inputs undergo three further augmentation steps to improve the network's performance:

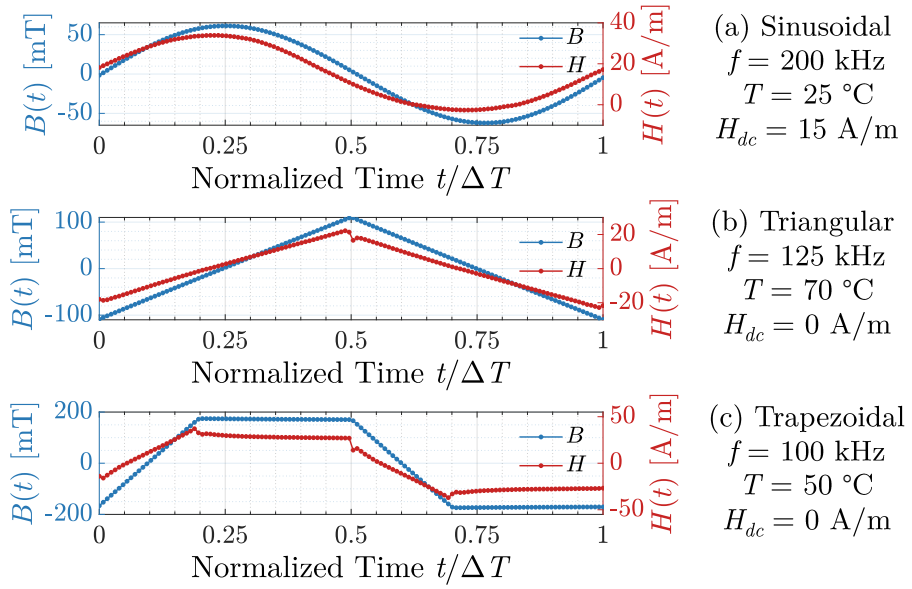


Figure 2.15: Examples of the single-cycle waveforms with a sequence length of 128, corresponding to the full-length waveforms shown in Fig. 2.14.

2.6.1 Single-Cycle Interpolation

In the original MagNet database, the $B(t)$ and $H(t)$ waveforms are directly derived from the raw voltage and current measurements. These waveforms consist of multiple cycles, all captured in the periodic steady state. Each waveform is represented as a $1 \times 10,000$ time sequence with a sampling rate of $f_s = 125 \text{ MHz}$. Since each waveform encompasses several cycles, training a neural network with these multi-cycle waveforms can present several challenges. On the one hand, the large number of data points significantly increases the computational load during both network training and inference. Moreover, since the waveform is captured in a periodic steady state, the repeated cycles offer little additional valuable information to the network. On the other hand, waveforms with different fundamental frequencies result in varying numbers of samples per cycle, causing discrepancies in the number of points on the B - H plane. This variation makes networks trained on these waveforms susceptible

to amplifying noise in low-frequency waveforms while neglecting sharp transitions in high-frequency waveforms.

To mitigate these challenges, a single-cycle interpolation algorithm is applied to all the $B(t)$ and $H(t)$ waveforms. Given the sampling rate f_s and the fundamental frequency f , the total number of cycles in each waveform can be computed as $N = 10,000 \times (f/f_s)$. The 10,000-sample waveform is then interpolated to $N \times 128$ samples using a spline algorithm. After interpolation, the waveform is divided into multiple sections, each containing a full cycle of the waveform, with exactly 128 sample points per section. These individual sections are then averaged to form a single-cycle waveform. Figure 2.15 presents the corresponding single-cycle waveform for each of the original waveforms shown in Fig. 2.14.

By employing the single-cycle interpolation method, the time stamps of the waveform are normalized by the period $\Delta T = 1/f$ into the interval $[0, 1]$. This ensures that the single-cycle waveforms for both $B(t)$ and $H(t)$ effectively capture the shape of the hysteresis loop in the periodic steady state, while maintaining a consistent sequence length across all frequencies. The process of single-cycle interpolation effectively removes the time stamp information from the original waveform. This is another key reason why the fundamental frequency f is included as one of the network inputs.

2.6.2 Phase-Shifting Augmentation

Through the single-cycle interpolation, we assume that the original waveform can be effectively reconstructed from the single-cycle waveform, as all waveforms are captured during the periodic steady state. Furthermore, we hypothesize that the predicted magnetic behaviors, such as the B - H loop and core loss, should remain unchanged regardless of where the waveform is segmented into sections, since they all reconstruct to the same original waveform. This assumption suggests that the predicted results should not be affected by the starting phase of the single-cycle waveform.

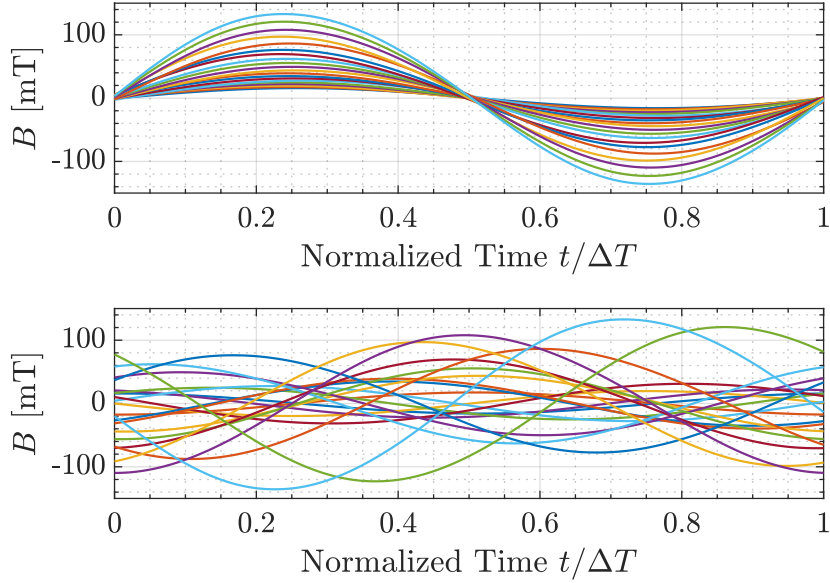


Figure 2.16: A set of example $B(t)$ waveforms of N87 ferrite before and after the phase-shifting augmentation. The waveforms are measured under sinusoidal excitations at 100 kHz, 25°C, and zero dc bias.

To mitigate the risk of the neural network misinterpreting the phase information, phase-shifting data augmentation is applied to the single-cycle waveforms. In this process, each pair of $B(t)$ and $H(t)$ waveforms is circularly shifted by a random phase, altering the starting phase of the waveform while maintaining the original phase difference between the $B(t)$ and $H(t)$ waveforms. Figure 2.16 demonstrates a set of example $B(t)$ waveforms of N87 ferrite before and after the phase-shifting augmentation.

Phase-shifting augmentation is also utilized to balance the dataset distribution. Given that waveforms with different shapes exhibit different degrees of freedom (e.g., amplitude, frequency, duty ratio), the amount of data available for each waveform shape in the original MagNet database varies significantly. For instance, the N87 ferrite material dataset contains 142,871 pairs of $B(t)$ and $H(t)$ waveforms, measured under varying frequency f , temperature T , and dc bias H_{dc} conditions. Of these, the sinusoidal wave, triangular wave, and trapezoidal wave contribute 3,495 (2.45%),

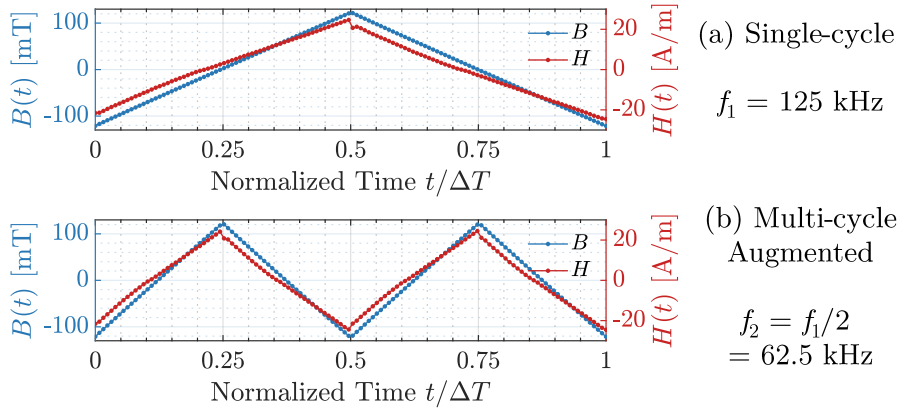


Figure 2.17: Examples of multi-cycle data augmentation: (a) the original single-cycle waveform at 125 kHz; (b) the augmented two-cycle waveform at an effective frequency of 62.5 kHz. A well-designed and well-trained neural network should be able to predict similar results for both cases.

46,973 (32.87%), and 92,403 (64.68%) pairs, respectively. Notably, the sinusoidal waveform has far fewer samples compared to the other two waveform shapes. As a result, training on this imbalanced dataset can lead to biased accuracy, especially for sinusoidal excitations. By applying phase-shifting augmentation, multiple phase values can be assigned to the sinusoidal waves, augmenting the data while ensuring that the augmented waveforms remain distinguishable from one another.

2.6.3 Multi-Cycle Augmentation

In addition to the phase, the frequency is another key factor that influences how the full-length waveform is divided into single-cycle sections. As described in Section 2.6.1, the waveform sequence is sliced based on the fundamental frequency, ensuring that each section contains a complete cycle of the waveform. Alternatively, the sequence can also be divided into sections based on $1/N$ of the fundamental frequency, with each section containing N cycles of the waveform. In theory, for any integer value of N , the sliced sections can always reconstruct the same full-length se-

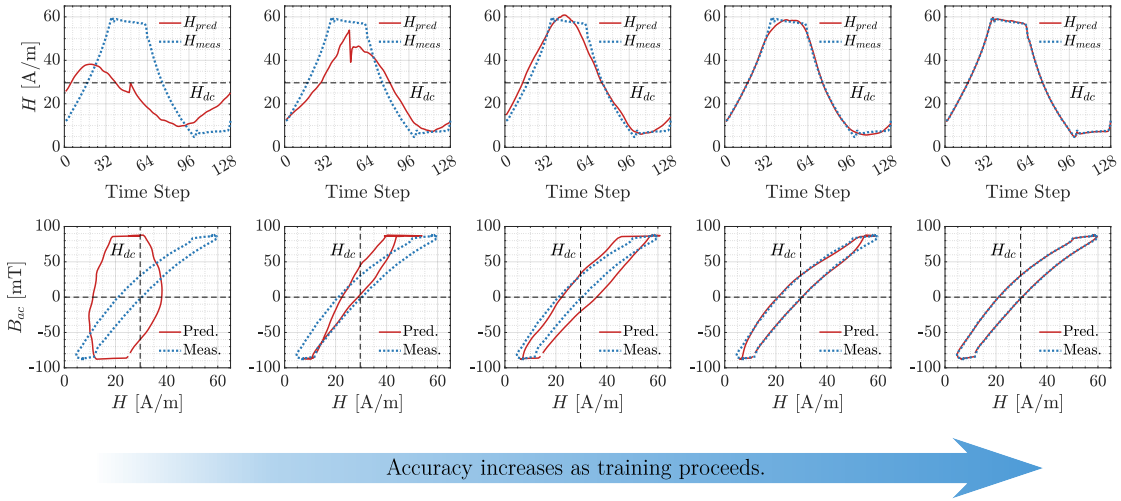


Figure 2.18: Prediction results of the $H(t)$ waveform and the B - H loop of an example testing point (trapezoidal, 140 kHz, 90°C, 30 A/m dc bias) at different stages of the training. The mismatch decreases progressively as the training advances, eventually achieving a close match between the predicted and measured waveforms.

quence and, consequently, the same B - H loop. However, the resolution within each cycle is reduced due to the fixed-length interpolation.

Building on this hypothesis, the dataset is further augmented by incorporating multi-cycle waveforms. Figure 2.17 illustrates an example of two-cycle data augmentation, where the augmented sequence consists of two cycles of the waveform, effectively halving the frequency. By leveraging multi-cycle augmentation, the neural network model is expected to predict approximately identical B - H loops and core losses, regardless of whether the input sequence consists of a single cycle or multiple cycles. This augmentation not only improves the model’s ability to generalize, but also enhances its performance for certain types of waveforms that are underrepresented in the original training dataset.

2.7 Model Training and Testing Results

The LSTM-based and transformer-based models are implemented using the PyTorch framework. Hyperparameters for both models are determined and optimized through

experimental training results. In the LSTM-based model, both the encoder and decoder are composed of a single-layer LSTM network with a 32-dimensional hidden state. For the transformer-based model, the model dimension is set to 24, with four attention heads. In both architectures, the projector is implemented as a 3-layer feed-forward neural network, each layer containing 40 hidden neurons. All these hyperparameters are optimized and determined using Optuna, an open-source automated hyperparameter optimization framework. These settings result in a total of 28,225 learnable parameters for the LSTM-based model and 28,481 learnable parameters for the transformer-based model.

The neural network model is trained for 5,000 epochs on Google Colab Pro GPU devices using the MagNet dataset. Following data augmentation, the size of the N87 ferrite dataset is expanded to 269,940 data points. These data points are randomly split into 70%, 20%, and 10% for the training, validation, and test sets, respectively. During the training process, the mean squared error (MSE) between the predicted sequence $H_{\text{pred}}(t)$ and the measured sequence $H_{\text{meas}}(t)$ is used as the loss function for backpropagation. The test dataset, which is not used for training, is employed to evaluate the model's performance. The Adam optimizer is utilized for model training, and an exponentially decaying learning rate strategy is implemented to improve convergence. The initial learning rate is set to 0.004, with a decaying rate of 90% every 150 epochs. The typical training time for each material is approximately 20 hours using Google Colab Pro, with the potential for further acceleration through parallel computing techniques.

2.7.1 Hysteresis B - H Loop Prediction

We evaluate the performance of the two trained models on the test set to assess their ability to predict the B - H hysteresis loop. Figure 2.18 shows a series of prediction results produced by the transformer-based model for an example testing point (trape-

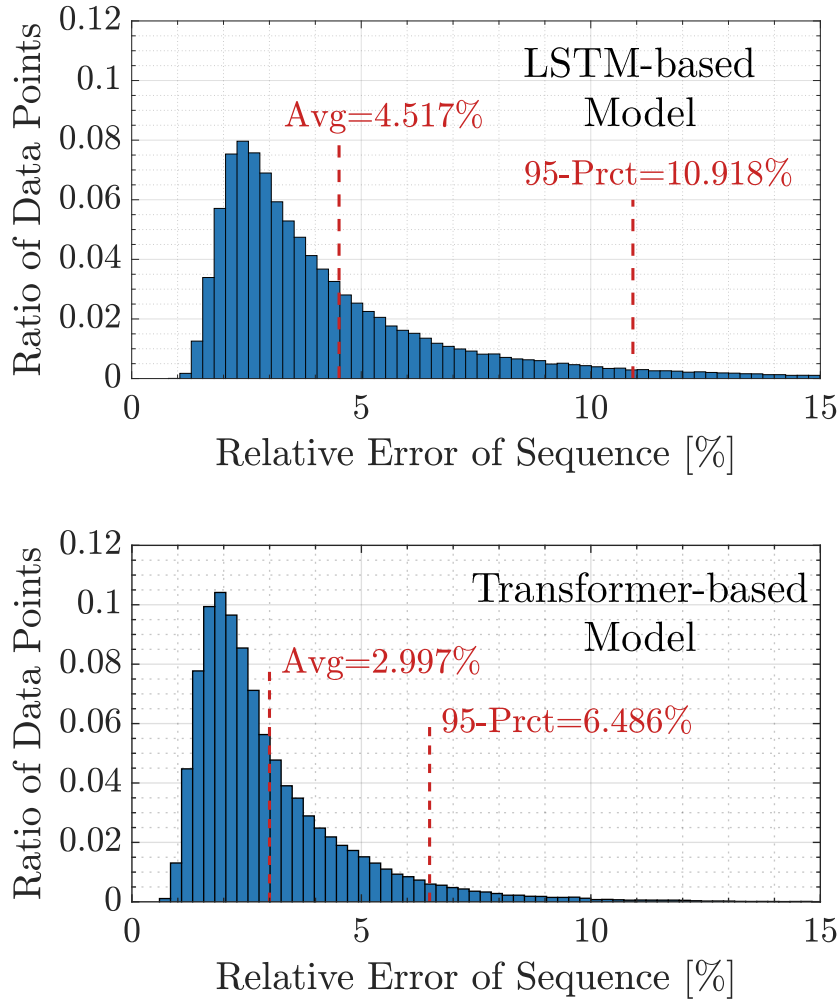


Figure 2.19: Relative error distributions of the predicted $H(t)$ sequence generated by the LSTM-based and transformer-based neural network models.

zoidal, 140 kHz, 90°C, 30A/m dc bias) at different stages of the training process. As the training progresses, the model gradually converges, minimizing the discrepancy between the predicted and measured hysteresis loops, eventually achieving a strong match.

To quantitatively assess the prediction accuracy of the models, we use the relative error between the predicted sequence $H_{\text{pred}}(t)$ and the measured sequence $H_{\text{meas}}(t)$ as the evaluation metric. The relative error is defined as follows:

$$\begin{aligned}
 \text{Relative Err. of Sequence} &= \frac{\text{rms}(H_{\text{pred}} - H_{\text{meas}})}{\text{rms}(H_{\text{meas}})} \\
 &= \frac{\sqrt{\frac{1}{n} \sum_{t=t_1}^{t_n} (H_{\text{pred}}(t) - H_{\text{meas}}(t))^2}}{\sqrt{\frac{1}{n} \sum_{t=t_1}^{t_n} (H_{\text{meas}}(t))^2}}
 \end{aligned} \tag{2.7}$$

Figure 2.19 illustrates the distribution of relative errors in the $H(t)$ predictions generated by both the LSTM-based and transformer-based models. As shown in the figure, both models demonstrate strong predictive accuracy for the $H(t)$ sequences. The average relative error for the LSTM-based model is 4.52%, while for the transformer model it is 2.99%. The 95th percentiles for the models are 10.92% and 6.48%, respectively, as summarized in Table 2.2. The test set encompasses data points from all three waveform shapes and spans the same ranges of frequency, temperature, and dc bias as those in the training set. These statistics confirm that both models can accurately predict the hysteresis loops under a variety of operating conditions. Under the given hyperparameter settings, the transformer-based model outperforms the LSTM-based model, as it demonstrates lower overall relative error in the prediction of the hysteresis loop.

2.7.2 Core Loss Prediction

We evaluate the performance of the two trained models to validate their ability to predict the core loss. Given the predicted B - H loop, the core loss P_V can be directly calculated using the following integral. The relative error between the predicted core loss $P_{V,\text{pred}}$ and the measured core loss $P_{V,\text{meas}}$ is then computed, serving as another metric for assessing model performance.

$$P_V = \frac{1}{T} \int_{B(0)}^{B(T)} H(t) dB(t) \tag{2.8}$$

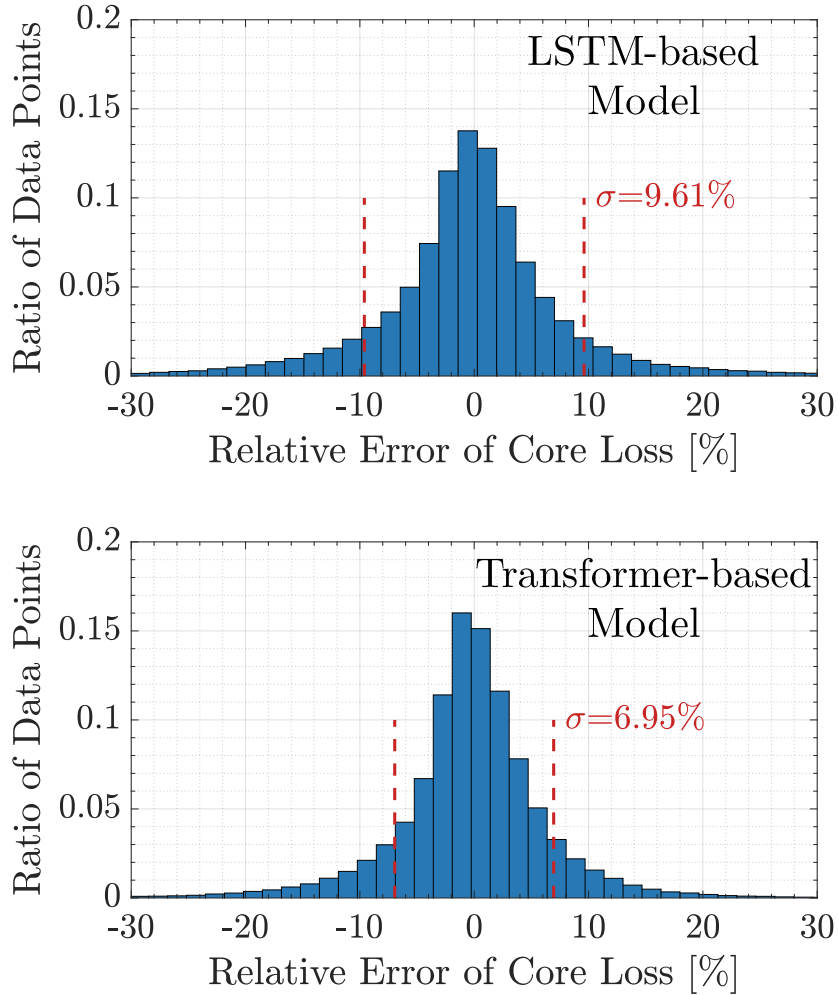


Figure 2.20: Relative error distributions of the predicted core loss generated by the LSTM-based and transformer-based neural network models.

$$\text{Relative Err. of Core Loss} = \frac{|P_{V,pred} - P_{V,meas}|}{P_{V,meas}} \quad (2.9)$$

Figure 2.20 shows the distribution of relative errors for the core loss predicted by both the LSTM-based and transformer-based models. As observed in the figure, the models are able to accurately predict the core loss for most of the data points in the test set. The standard deviation of the relative error for the LSTM-based model is 9.61%, while for the transformer model it is 6.95%. The 95th percentiles for the relative errors are 13.69% and 10.02%, respectively. These results indicate that the

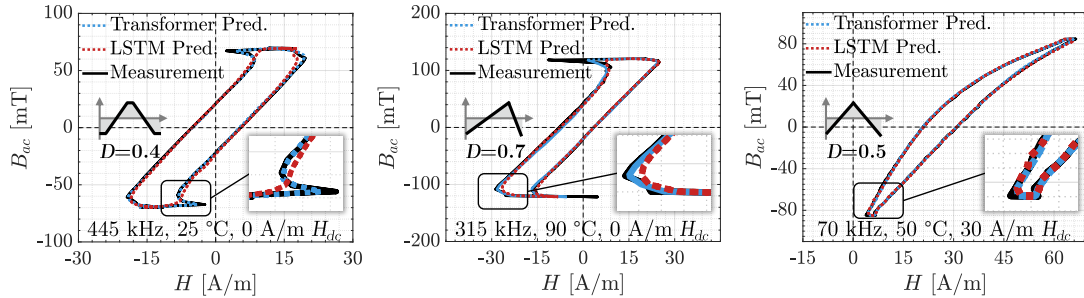


Figure 2.21: Examples of the predicted B - H loops under different frequency, temperature, and dc bias conditions, with multiple waveform shapes. Both the LSTM-based and the transformer-based models accurately predict the majority part of the B - H loops, while the sharp corners are better captured by the transformer-based model.

transformer-based model outperforms the LSTM-based model in core loss prediction, demonstrating lower overall relative error.

It is noteworthy that the overall relative error in core loss prediction is higher than that in hysteresis loop prediction. This discrepancy arises because, during training, the model is optimized to minimize the shape discrepancy between the predicted sequence $H_{\text{pred}}(t)$ and the measured sequence $H_{\text{meas}}(t)$, while core loss information is not directly available to the network. Core loss calculation, however, is highly sensitive to the phase mismatch between $H(t)$ and $B(t)$, meaning that an approximately matched sequence does not necessarily yield an accurate core loss prediction. To further enhance the accuracy of core loss prediction while maintaining high accuracy for hysteresis loop prediction, one could incorporate core loss information or phase information into the training loss function. However, this would likely increase the computational cost.

2.7.3 Comparison and Discussion

Table 2.2 presents a comparative analysis between the LSTM and transformer implementations in terms of their accuracy in predicting the hysteresis loop, model size,

Table 2.2: Comparison of the LSTM and Transformer implementation of the encoder-projector-decoder architecture.

Model Type	Average of Relative Error	95th Percentile of Relative Error	Number of Parameters	Elapsed Time of Model Inference
LSTM	4.52%	10.92%	28,225	0.017 ms/data point
Transformer	2.99%	6.48%	28,481	2.584 ms/data point

and approximate computational cost. Both models were trained and tested using the same training and test sets for the same number of epochs.

With the given hyperparameter settings, the transformer-based model outperforms the LSTM-based model in terms of overall prediction accuracy. Figure 2.21 illustrates examples of predicted B - H loops generated by each model compared to the measured ones under various frequency, temperature, and dc bias conditions, with multiple waveform shapes. Both models successfully predict the shape and location of the majority of the B - H loop, while the sharp corners are better captured by the transformer-based model, which benefits from the attention mechanism.

Although the LSTM-based model requires less elapsed time for model inference, the transformer-based model provides superior accuracy. Table 2.3 provides a theoretical comparison of the computational complexity of both models [44], where n represents the sequence length and d is the model dimension. In our testing cases, both models have $n = 128$, with the LSTM model having $d = 32$ and the transformer model having $d = 24$. Despite the transformer-based model reducing sequential operations and the maximum path length by avoiding recurrent operations, it suffers from a higher complexity per layer, which results in longer training and execution times.

Considering the trade-off between prediction accuracy and execution time, the transformer-based model is selected for establishing the neural network-aided smart datasheet. All the results in the following sections are generated using the transformer-based model.

Table 2.3: Comparison of the theoretical computational cost between the LSTM and the self-attention (transformer).

Layer Type	Complexity per Layer	Sequential Operations	Maximum Path Length
Recurrent (LSTM)	$\mathcal{O}(n \cdot d^2)$	$\mathcal{O}(n)$	$\mathcal{O}(n)$
Self-Attention (Transformer)	$\mathcal{O}(n^2 \cdot d)$	$\mathcal{O}(1)$	$\mathcal{O}(1)$

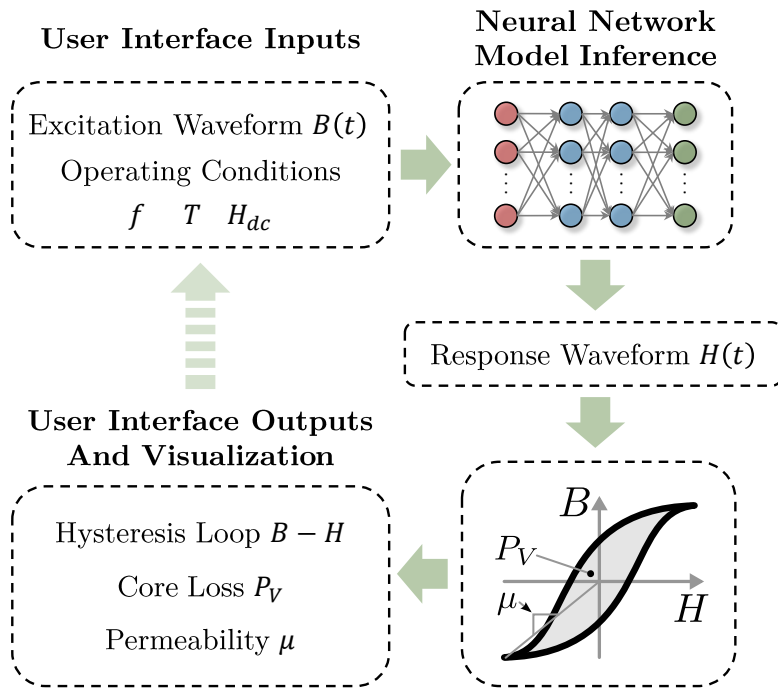


Figure 2.22: Flowchart of the neural network-aided smart datasheet. Users can specify the excitation waveform and the operating conditions through the user interface as the inputs to the neural network model. The model inference is executed to predict the response waveform. After post-processing, the prediction results, such as the hysteresis loop, core loss, and permeability, are visualized and provided to users.

2.8 Applications of Neural Network Models

2.8.1 MagNet-AI: A NN-aided Smart Datasheet

Evaluation results validate the neural network model's effectiveness in predicting the hysteresis loop and core loss under various operating conditions and excitation waveforms. To establish a neural network-aided smart datasheet, the neural network

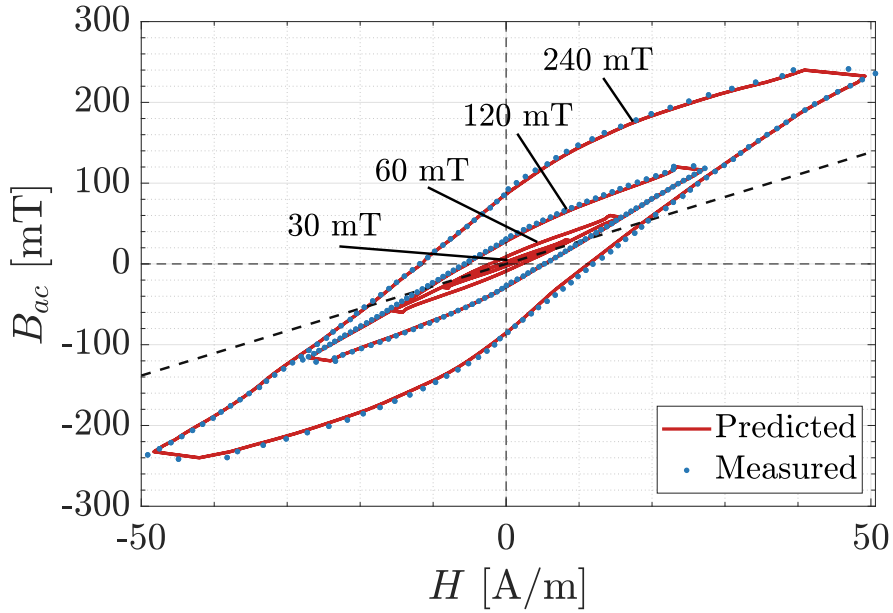


Figure 2.23: Predicted B - H loops with the manually generated model inputs using 50% duty ratio pure triangular waves, where the amplitude of flux density is swept from 30 mT to 240 mT. The frequency, temperature, and dc bias are fixed at 100 kHz, 25°C, and 0 A/m, respectively.

model is packaged into a function for rapid inference, where the inputs include the waveform of flux density $B(t)$, the frequency f , the temperature T , and the dc bias field strength H_{dc} , while the output is the waveform of the field strength $H(t)$. The flowchart of the neural network-aided smart datasheet is depicted in Fig. 2.22.

Here are several prediction examples to demonstrate different ways of using the NN-aided smart datasheet. In each example, a manually generated dataset is fed into the neural network model as the inputs, where the excitation waveforms are ideal shapes and the operating conditions are swept. It should be noted that the waveforms in the manually generated datasets are pure waves without any non-ideal effects, such as switching transitions, which naturally leads to slightly different prediction results compared to the measurements, despite their close resemblance.

- **Example 1: Predicting the hysteresis loop at different flux density amplitudes.** In this example, the excitation waveforms are a set of 50%

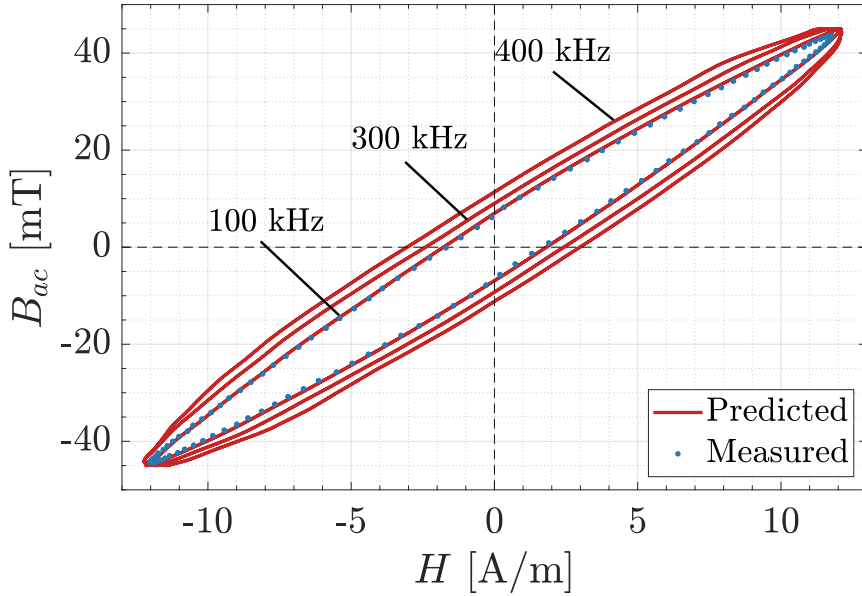


Figure 2.24: Predicted B - H loops with the manually generated model inputs using pure sinusoidal waves, where the fundamental frequency is swept from 100 kHz to 400 kHz. The amplitude, temperature, and dc bias are fixed at 45 mT, 25°C, and 0 A/m, respectively.

duty ratio pure triangular waves, where the amplitude is swept from 30 mT to 240 mT. The frequency, temperature, and dc bias are fixed at 100 kHz, 25°C, and 0 A/m, respectively. Figure 2.23 presents the predicted B - H loops with this manually generated dataset as model inputs. It is observed that the impact of the flux density amplitude on the hysteresis loop is well captured and predicted by the neural network model, achieving a good match with respect to the adjacent measured hysteresis loops. At small amplitude, the B - H loop approximately aligns with the straight line $B = \mu_i H$, where μ_i is the initial permeability of the material. As the amplitude increases, the B - H loop expands and gradually saturates, leading to a significantly larger core loss and a markedly different permeability.

- **Example 2: Predicting the hysteresis loop at different frequencies.** In this example, the excitation waveforms are a set of pure sinusoidal waves, with

an amplitude of 45 mT. The temperature and dc bias are fixed at 25°C and 0A/m, respectively, while the frequency is swept from 100 kHz to 400 kHz. Figure 2.24 presents the predicted B - H loops with this manually generated dataset as model inputs. It is observed that the impact of the fundamental frequency on the hysteresis loop is well captured and predicted by the neural network model, with a good match achieved with the adjacent measured hysteresis loops. As the frequency increases, the B - H loop enlarges, resulting in a larger core loss energy per cycle.

- **Example 3: Predicting the hysteresis loop at different levels of dc bias.** In this example, the excitation waveforms are a set of pure sinusoidal waves, with an amplitude of 30 mT. The frequency and temperature are fixed at 200 kHz and 25°C, respectively, while the dc bias is swept from 0 A/m to 30 A/m. Figure 2.25 presents the predicted B - H loops with this manually generated dataset as model inputs. The neural network model captures the impact of the dc bias on the hysteresis loop and achieves a good match with the adjacent measured hysteresis loops. As the dc bias increases, the B - H loop enlarges and tilts.
- **Example 4: Predicting the core loss under triangular waves with different duty ratios.** In this example, the excitation waveforms are a set of pure triangular waves, with an amplitude of 43.5mT, and the duty ratio is swept from 10% to 90%. The frequency, temperature, and dc bias are fixed at 315 kHz, 25°C, and 0A/m, respectively. Figure 2.26 presents the predicted core loss curves with this manually generated dataset as model inputs. The relationship between the duty ratio and the core loss is well captured and predicted by the neural network model, achieving a good match with the adjacent measured core loss. For triangular waves, the core loss reaches a minimum when the duty ratio

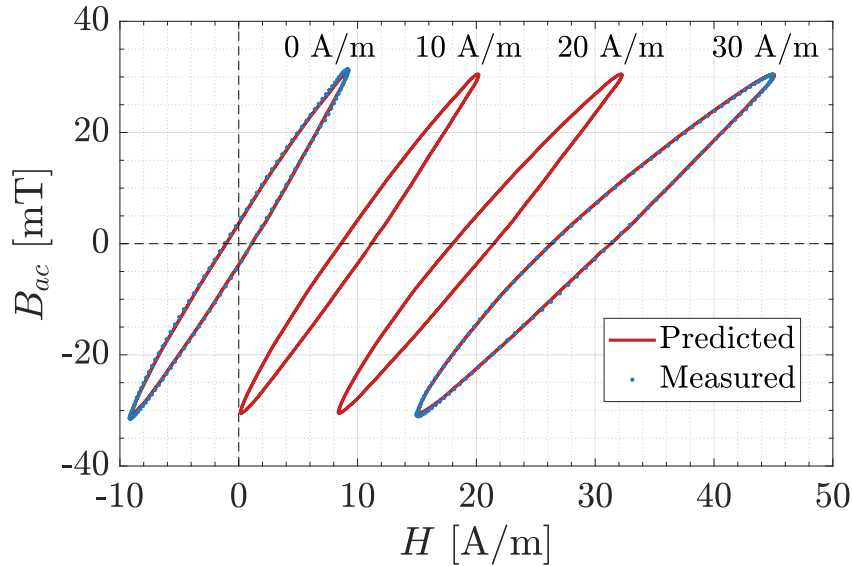


Figure 2.25: Predicted B - H loops with the manually generated model inputs using pure sinusoidal waves, where the dc bias is swept from 0 A/m to 30 A/m. The amplitude, frequency, and temperature are fixed at 30 mT, 200 kHz, and 25°C, respectively.

$D = 0.5$, and increases as it approaches 0 or 1. The core losses for duty ratios of D and $1 - D$ are approximately the same, resulting in a symmetric core loss curve versus duty ratio.

- **Example 5: Predicting the core loss at different temperatures.** In this example, the excitation waveforms are a set of pure trapezoidal waves, with duty ratios for rising and falling both at 20%. The amplitude of flux density is fixed at 35 mT, 70 mT, and 140 mT, respectively. The frequency and dc bias are fixed at 100 kHz and 0 A/m, while the temperature is swept from 25°C to 90°C. Figure 2.27 presents the predicted core loss curves with this manually generated dataset as model inputs. The relationship between temperature and core loss is well captured and predicted by the neural network model, with a good match achieved with the adjacent measured core loss. As the temperature rises, the core loss decreases.

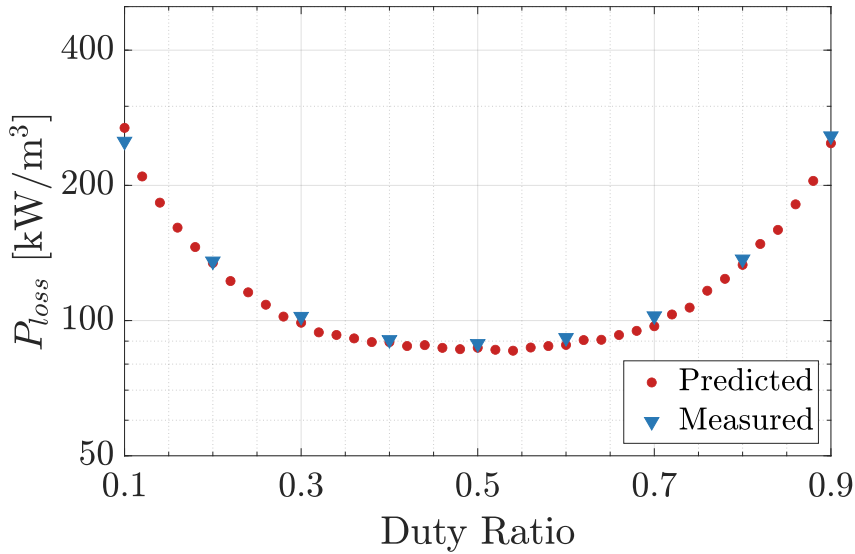


Figure 2.26: Predicted core loss curves with the manually generated model inputs, where the duty ratio of the triangular wave is swept from 10% to 90%. The amplitude, frequency, temperature, and dc bias are fixed at 43.5 mT, 315 kHz, 25°C, and 0 A/m, respectively.

With the capability to predict the hysteresis loop and core loss under various operating conditions, as demonstrated in the examples above, the proposed neural network model can serve as an alternative to conventional datasheets or measurement datasets. Notably, the neural network model can significantly reduce the size of the dataset with minimal loss of accuracy. For the N87 material in this work, the size of the post-processed dataset for model training is 3.8 GB, whereas the size of the transformer model is only 204 kB, which nearly equivalently describes the behaviors of magnetic materials and is much more comprehensive than the conventional datasheet of similar file size. Users of the neural network-aided datasheet can rapidly predict the behavior of magnetic materials, such as the hysteresis loop, permeability, and core loss, by specifying excitation waveforms and operational conditions, without the need for time-consuming data extraction and complex interpolation as required with conventional datasheets. In contrast to conventional datasheets, the neural network-aided smart datasheet is efficiently packaged into a function, making it feasible to

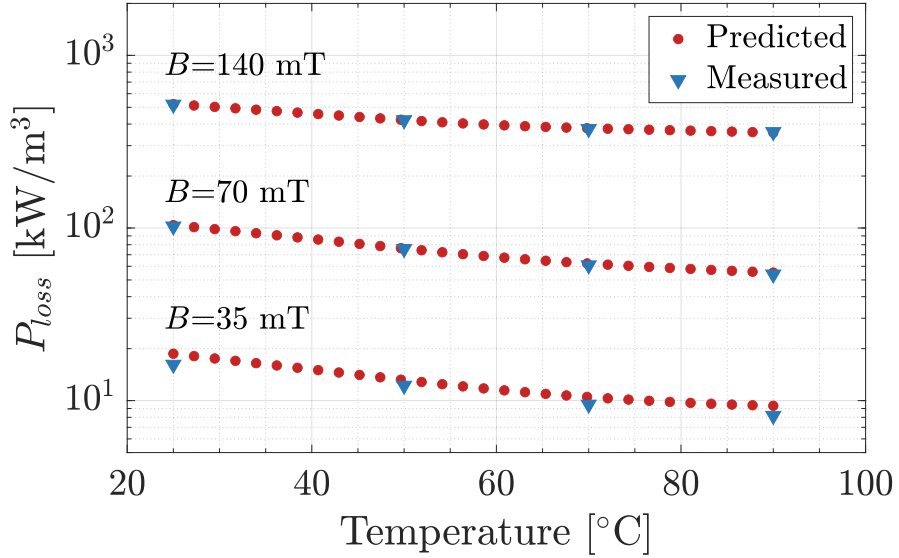


Figure 2.27: Predicted core loss curves with the manually generated model inputs, where the flux density is fixed at 35 mT, 70 mT, and 140 mT, and the temperature is swept from 25°C to 90°C. The frequency and dc bias are fixed at 100 kHz and 0 A/m, respectively.

integrate into other iterative calculations, such as multi-objective optimization algorithms or AI-mag [47].

2.8.2 NN-aided Material Recommendation

Benefiting from the fast model inference capabilities of neural networks, the proposed model can also assist in material comparison and selection for specific excitations and operating conditions. It can rapidly rank magnetic materials across a wide operational range. The transformer-based neural network model has been trained on all ten materials from the MagNet database, including TDKN27, N30, N49, N87, Ferroxcube3C90, 3C94, 3E6, 3F4, and Fair-Rite77, 78. The model was trained using a large measurement dataset similar to the one described in Section 2.4, with the same network hyperparameters and data augmentation techniques. When a specific operating condition is provided, these neural network models can be executed sequentially to sweep across all the materials and calculate the corresponding core loss for each

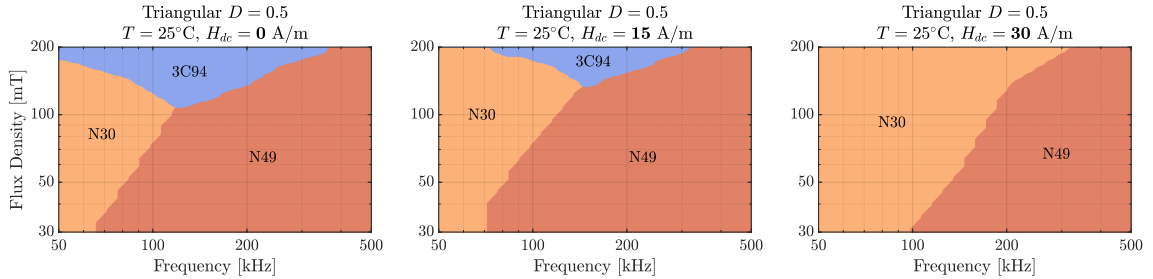


Figure 2.28: Material ranking map at different levels of dc bias across a wide range of flux density amplitude and frequency.

material. By sorting the core loss values among all candidate materials, MagNet-AI can recommend the best-performing material candidates for the given operating condition. Two examples of material ranking maps are provided here to illustrate the effectiveness of the neural network-aided material comparison.

- **Example 1: Selecting the optimal material at different levels of dc bias across a wide range of flux density and frequency.** In this example, the excitation waveforms consist of a set of 50% duty ratio pure triangular waves. The amplitude and frequency of the waveforms are swept from 30 mT to 200 mT and from 50 kHz to 500 kHz, respectively. The dc bias is selected from three different levels, namely 0 A/m, 10 A/m, and 20 A/m, while the temperature remains fixed at 25°C. Figure 2.28 presents the material ranking maps for each level of dc bias, where different colors represent different materials that achieve the lowest core loss under each operating condition. Each material exhibits its optimal operating range in terms of frequency, flux density, and dc bias. N30 ferrite demonstrates lower core loss at low frequencies, while N49 ferrite performs better at higher frequencies. The boundary shifts as the dc bias changes.
- **Example 2: Selecting the optimal material at different temperatures across a wide range of flux density.** In this example, the excitation wave-

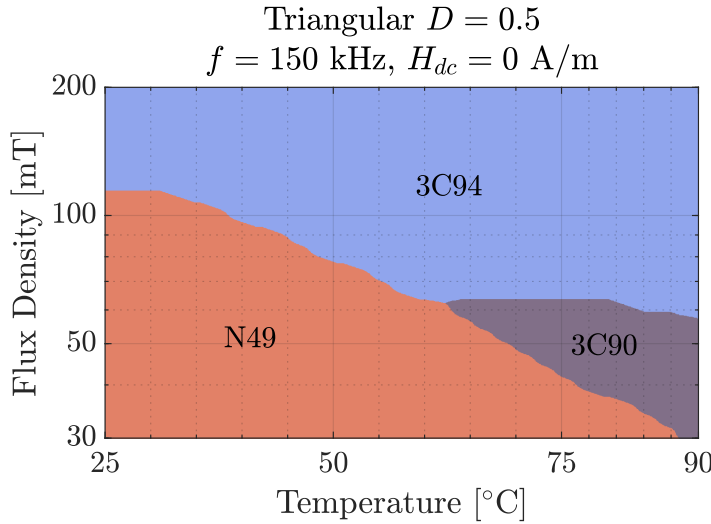


Figure 2.29: Material ranking map across a wide range of flux density amplitude and temperature.

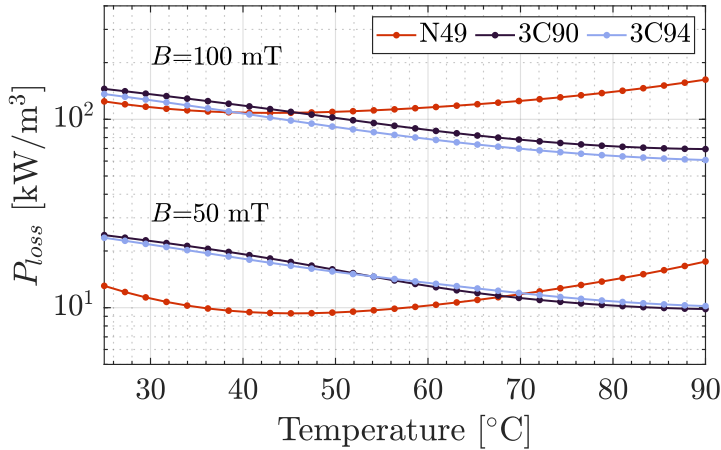


Figure 2.30: Core loss curve comparisons at different levels of flux density amplitude and temperatures.

forms consist of a set of 50% duty ratio pure triangular waves. The amplitude of the waveforms and the temperature are swept from 30 mT to 200 mT and from 25°C to 90°C, respectively. The frequency remains fixed at 150kHz, and the dc bias is set to zero. Figure 2.29 presents the corresponding material ranking map. As depicted, different materials have optimal operation ranges in terms of temperature. At low temperatures, the material map is dominated by N49

ferrite and 3C94 ferrite. As the temperature increases, 3C90 ferrite begins to show superior performance. More specifically, Figure 2.30 presents the predicted core loss curves for the three aforementioned materials across different temperatures. It is observed that N49 ferrite achieves its minimum core loss at relatively low temperatures, while the other two materials are more suitable for high-temperature applications.

As demonstrated, given a targeted operational range, the neural network model can effectively assist designers in determining which material offers the most desirable performance for the given operating conditions. With the constantly expanding material category, the neural network model provides design recommendations across various materials, with only a linearly increasing computational cost.

2.8.3 Online Smartsheet Platform

To enable interactive datasheet inference based on the proposed neural network model, an open-source webpage-based platform with a graphic user interface (GUI) has been designed and developed. Powered by Streamlit, an open-source Python framework for web app deployment, the platform is shared on GitHub and offers a variety of data visualization tools with a GUI for database access, magnetic core loss estimation, hysteresis loop prediction, circuit simulation, and access to download all measured data points. The neural network model and the circuit simulation engine are deployed on the website, allowing users to predict the hysteresis loop under user-defined conditions or simulation parameters. The website architecture and information flow of the platform are shown in Fig. 2.31.

Figure 2.32(a) presents an example screenshot of the smartsheet session of the neural network model. With the GUI, users can specify the type of magnetic material, operating conditions (temperature, frequency, and dc bias), and excitation waveform (either standard shapes or user-defined waves). The neural network engine rapidly

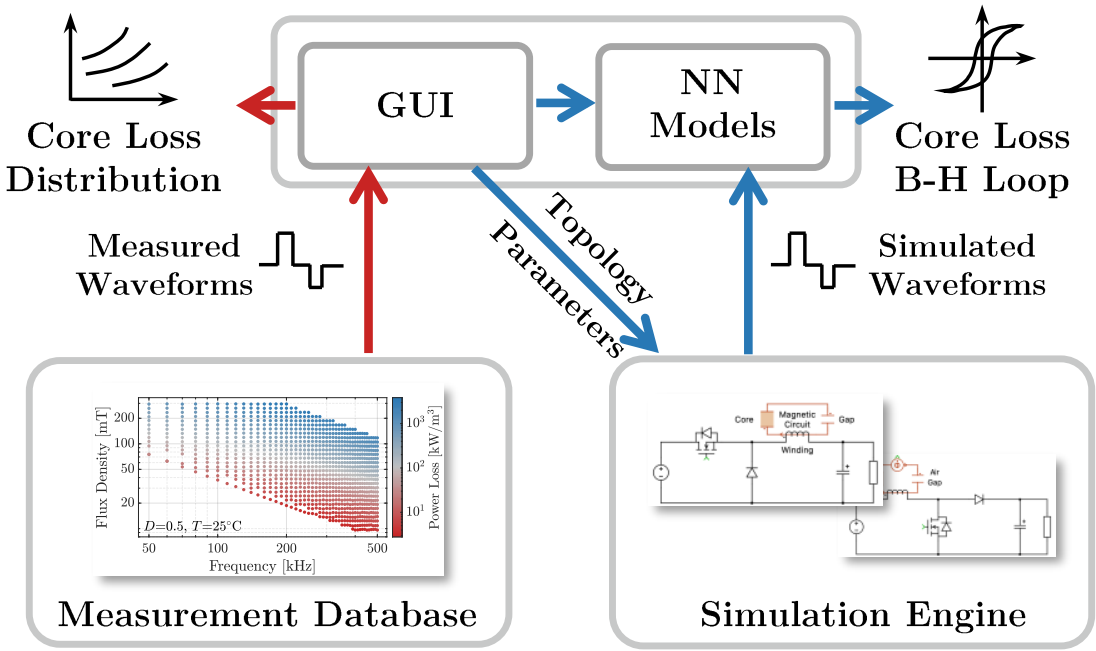


Figure 2.31: The website architecture and information flow of the MagNet webpage platform, which provides users with access to download and visualize the measured data in the MagNet core loss database, as well as analyze and simulate the magnetic behaviors with the deployed neural network models and the PLECS simulation engine.

predicts the B - H loop under the specified conditions, simultaneously generating a sequence of core loss curves around the operating point. This procedure provides a much more comprehensive dataset compared to conventional datasheets.

The webpage is also linked to a circuit simulation server hosted by Plexim. The webpage feeds information to the server, which returns inputs to the machine learning algorithms in combination with power converter operations, as shown in Fig. 2.32(b). Users can select from a pool of common topologies (Buck, Boost, Flyback, Dual Active Bridge), specify the circuit parameters, magnetic component specifications, and operating conditions. The simulation engine simulates and outputs the excitation waveform of the magnetic component. The MagNet server collects the waveform and predicts the core loss using the neural network models. Future iterations between the neural network model and simulation engine will enhance simulation accuracy by



Figure 2.32: An example screenshot of the MagNet-AI webpage-based magnetics analysis and prediction platform: (a) smartsheet session; (b) simulation session. MagNet-AI is available at: <https://mag-net.princeton.edu>, and open-sourced at: <https://github.com/PrincetonUniversity/magnet>.

capturing nonlinear effects. Note that the flux density is calculated based on specified geometric parameters, assuming a uniform flux distribution. The impact of geometry is not considered in this work, but the neural network models can be integrated with a circuit simulator to enable magnetic-in-circuit simulations.

In addition to the neural network-aided smart datasheet, the website provides a database section that allows the raw measurement dataset to be visualized in multiple ways, facilitating rapid comparison of core loss and B - H loop data across different materials. Users can specify the type of magnetic material, excitation waveforms, and operating conditions. The website backend searches the database for the requested data and visualizes it in the selected format. The platform also provides download access to the raw data collected from the equipment, including test conditions, and the post-processed dataset files for data-driven modeling applications.

The MagNet platform is continuously maintained and updated with new data and neural network models. Detailed information is available on the website to ensure trustworthy repeated measurements and cross-validation of the dataset.

2.9 Transfer Learning for Data Size Reduction

In the previous examples, the large-scale MagNet database serves as the foundation for training and testing the data-driven models. However, it may be unrealistic for designers to independently establish a core loss measurement platform and gather enough data for model training, particularly when dealing with new materials that have limited data available or when operating conditions lie outside the range of the existing database or equipment capabilities.

Transfer learning is a machine learning approach in which knowledge gained from solving one problem is applied to a similar problem. The central hypothesis behind using transfer learning in magnetic modeling is that similar physical principles govern how different magnetic materials respond to similar excitations. Thus, a general neu-

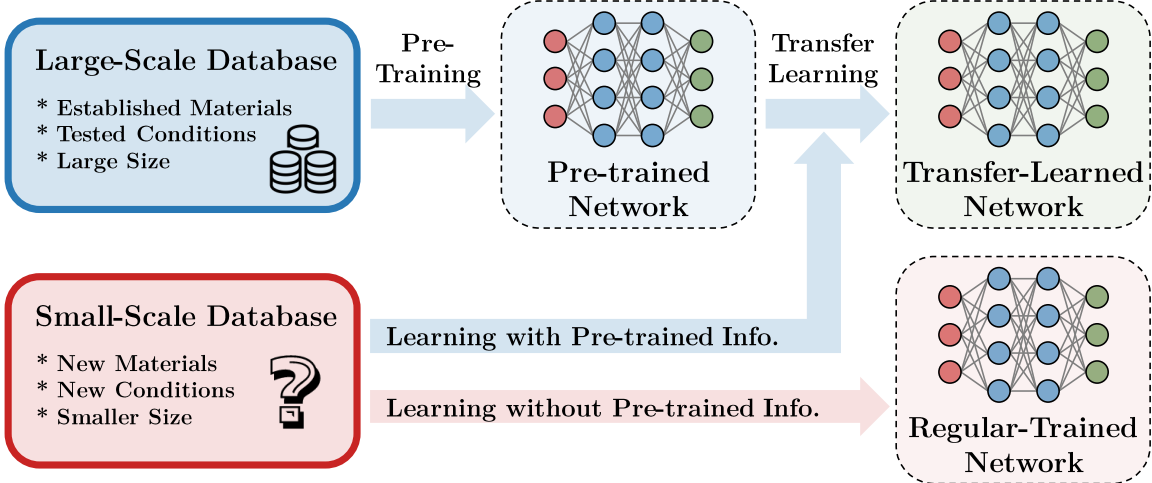


Figure 2.33: The core concept of transfer learning for magnetic core loss modeling.

ral network model can be trained to capture the common characteristics and patterns of various magnetic materials. This model can then be adapted for new materials, excitations, temperatures, or dc biases. Figure 2.33 illustrates the fundamental idea of transfer learning. We demonstrate both material-to-material and temperature-to-temperature transfer learning to explain the core principles.

2.9.1 Material-to-Material Transfer Learning

Material-to-material transfer learning is particularly useful when a model for a new material is needed, but only a small dataset is available for this material. Transfer learning can significantly reduce the amount of data required to achieve satisfactory accuracy in a neural network model.

Figure 2.34 illustrates the training process for material-to-material transfer learning. Three machine learning experiments are conducted to show the transfer learning principles: (1) Four materials from the MagNet database (N27, N49, 3C90, 3C94) are selected as the source materials, and a large dataset of their data is used to train a pre-trained model similar to the one used in [32]. The data from these four materials

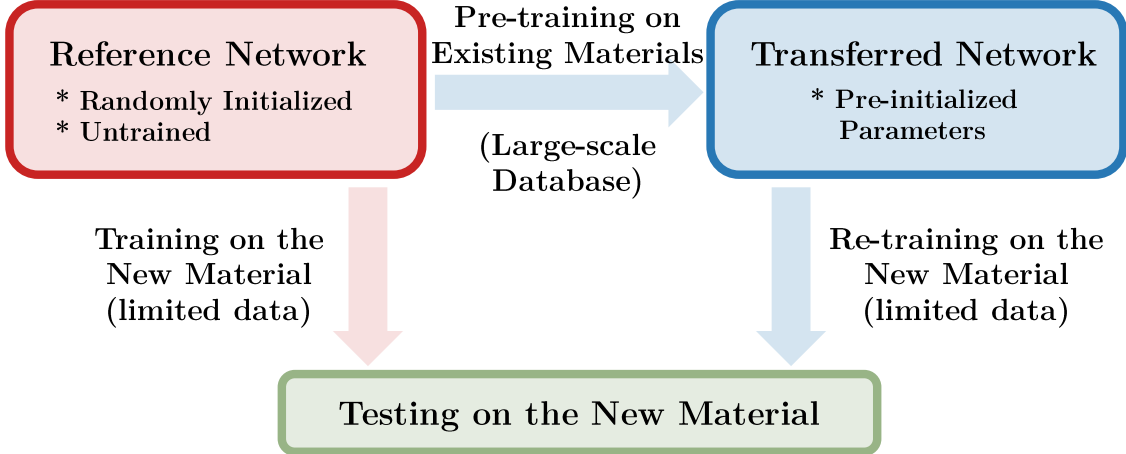


Figure 2.34: Network training process of the material-to-material transfer learning.

are combined into a larger dataset for network training, without using the material type as an input; (2) N87, a new material with limited core loss data, is selected as the target material. The pre-trained model is fine-tuned using only a small number of data points randomly selected from the N87 dataset; (3) For comparison, a randomly initialized neural network is trained directly on the same small dataset.

Figure 2.35 displays the material-to-material transfer learning results for triangular wave excitations at 180kHz and three different duty ratios. The pre-trained model is trained on the large dataset (30,705 data points) of the four existing materials (N27, N49, 3C90, 3C94). In Fig.2.35a, the pre-trained model is applied directly to the new material (N87) without re-training. The model captures some general patterns of the core loss, such as the exponential relationship between core loss and flux density, and the effect of duty ratio, but it fails to accurately predict the details.

The pre-trained model is then re-trained with 100 data points from N87. Figure 2.35b shows the updated prediction results. After re-training, the model performance significantly improves, as the new data fine-tunes the model, leading to much better accuracy. In contrast, Figure 2.35c shows the results of training a randomly

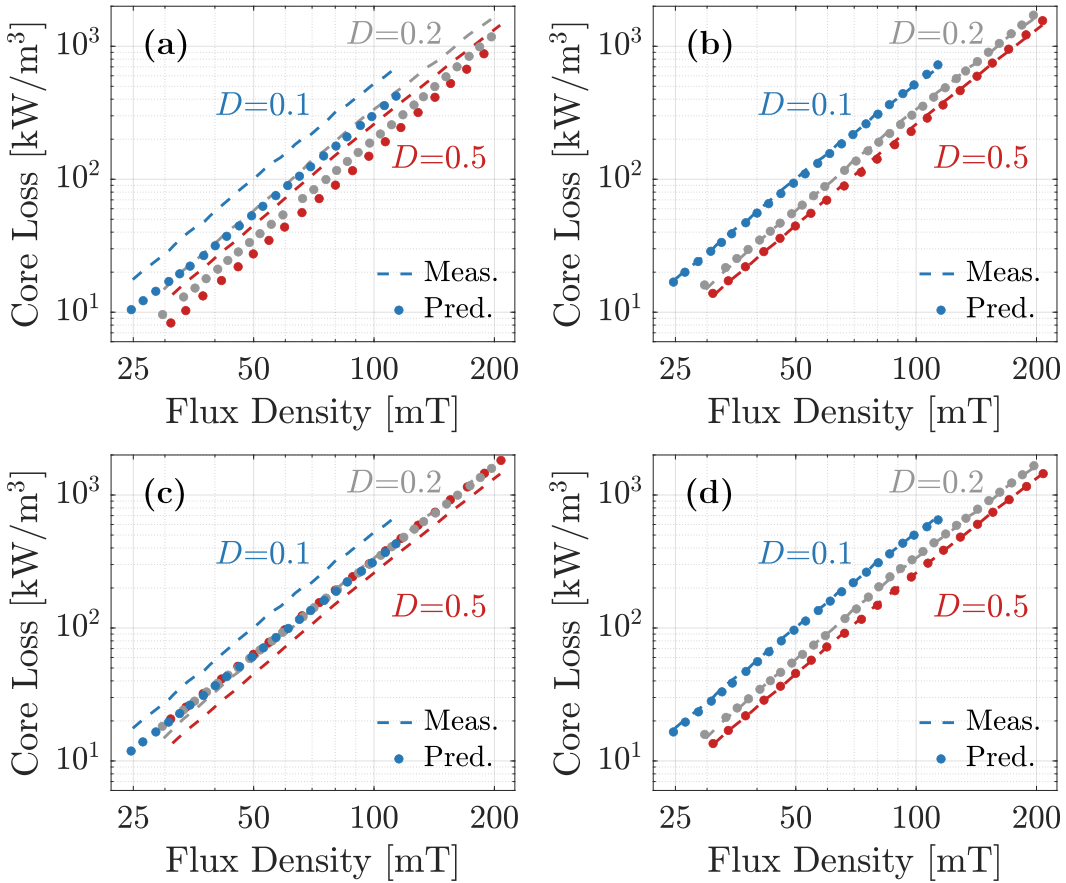


Figure 2.35: Prediction results: (a) applying a pre-trained model to the new material without re-training; (b) applying a pre-trained model to the new material after re-training with very few data points (100 randomly selected); (c) applying a randomly initialized model trained with very few data points (100 randomly selected); (d) applying a randomly initialized model trained with a large amount of data (100 data points).

initialized network with only 100 data points from the new material. This model performs poorly and fails to capture the core loss distribution accurately.

For comparison, the standard training process is also conducted, similar to the one described in [32], where a randomly initialized neural network is trained with 100 data points from the new material. This approach serves as a benchmark, and the results are shown in Figure 2.35d. The model achieves the highest accuracy in predicting core loss as expected, given the larger dataset.

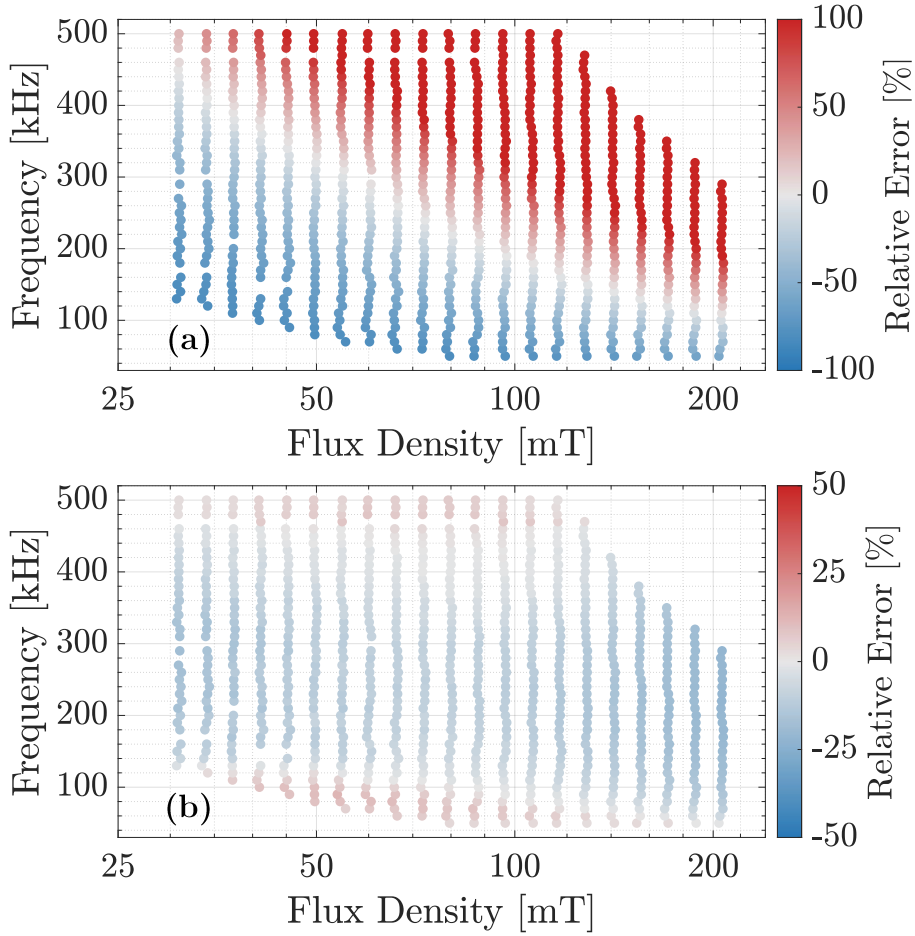


Figure 2.36: Error distribution of the prediction results: (a) using a randomly initialized model trained with only 100 data points from N87 (normal training); (b) using a pre-trained model from 4 existing materials re-trained with 100 data points from N87 (transfer learning). The data shown is a subset with a duty ratio of 0.5.

Figure 2.36 compares the overall error distribution between normal training (Fig. 2.35c) and transfer learning (Fig. 2.35b). The duty ratio is fixed at 0.5. Without pre-training, the model struggles to capture the core loss distribution due to limited data, resulting in an average relative error of more than 50

Further experiments were conducted by varying the number of data points used for re-training. Figure 2.37 shows the average testing relative errors as a function of the number of available data points, ranging from 25 to 3,600. The error rates are averaged over 10 trials for consistency. The pre-trained models consistently perform well, regardless of whether they are provided with 25 or 3,600 data points. In contrast,

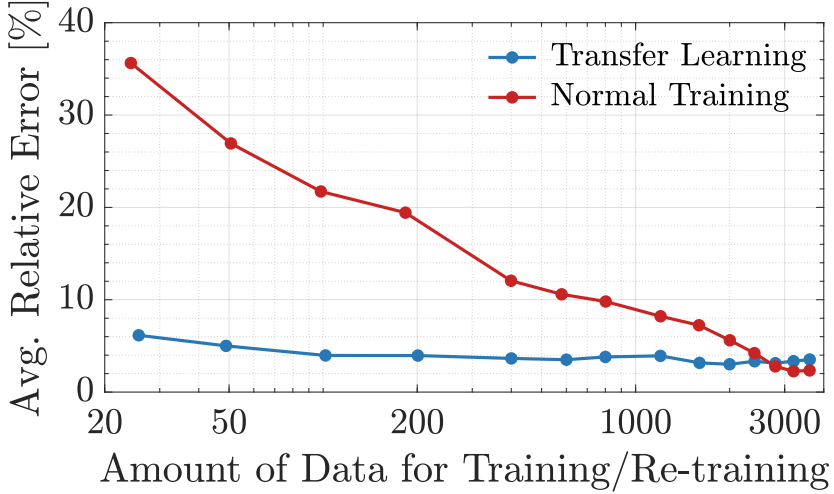


Figure 2.37: Testing average relative error rates after training a normal FNN and re-training a pre-trained FNN with varying amounts of data.

a randomly initialized FNN requires at least 2,400 data points to achieve comparable accuracy. These results confirm that transfer learning significantly reduces the data requirements for retraining a neural network for a new material.

2.9.2 Temperature-to-Temperature Transfer Learning

Temperature plays a crucial role in determining the behavior of magnetic materials. Using a model trained at one temperature to predict core loss at a different temperature can lead to substantial inaccuracies. Temperature-to-temperature transfer learning provides a solution for building neural network models that can predict core loss at various temperatures, especially when limited data is available for temperatures beyond the training set.

The principles behind temperature-to-temperature transfer learning are similar to material-to-material transfer learning. Figure 2.38 shows the training process of transferring a model trained at 25 °C to work at 90 °C. In this case, the neural network is first pre-trained for 500 epochs using data from N87 ferrite material at 25 °C with sinusoidal excitations, consisting of 800 data points. The model is then fine-tuned

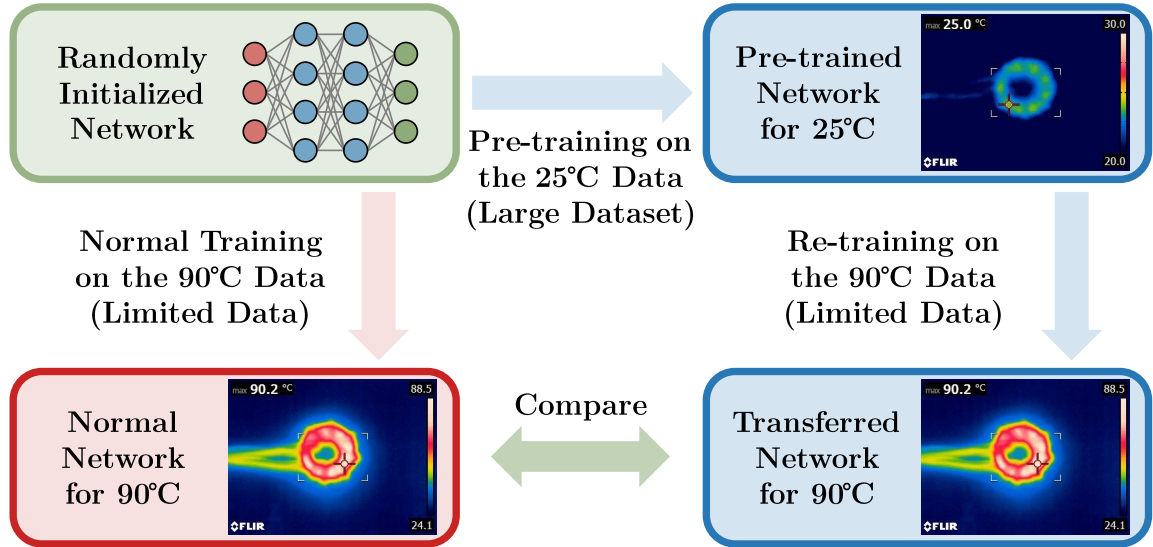


Figure 2.38: Training process of temperature-to-temperature transfer learning. Pre-training and fine-tuning can significantly reduce the data requirements for modeling magnetic core loss at different temperatures.

using a small number of data points from the 90 °C data, with 3,000 additional epochs of training. A randomly initialized model is trained from scratch on the 90 °C data for comparison.

Figure 2.39 demonstrates multiple core loss curves predicted by different network models. In Fig. 2.39a, the model pre-trained on 25°C data is evaluated on 90 °C data without re-training, resulting in poor predictions due to temperature differences. After fine-tuning with just 10 data points from 90 °C, the model performs significantly better, as shown in Fig. 2.39b. The prediction accuracy is comparable to that of a model trained with a larger dataset, as shown in Fig. 2.39d. In contrast, Fig. 2.39c shows the results of training a randomly initialized model with just 10 data points, which performs poorly.

Figure 2.40 shows the overall error distribution for both the normal training and transfer learning cases, corresponding to Fig. 2.39b and Fig. 2.39c, respectively. With transfer learning, the network achieves lower relative error across the entire evaluation range, resulting in an absolute average error of 7.94

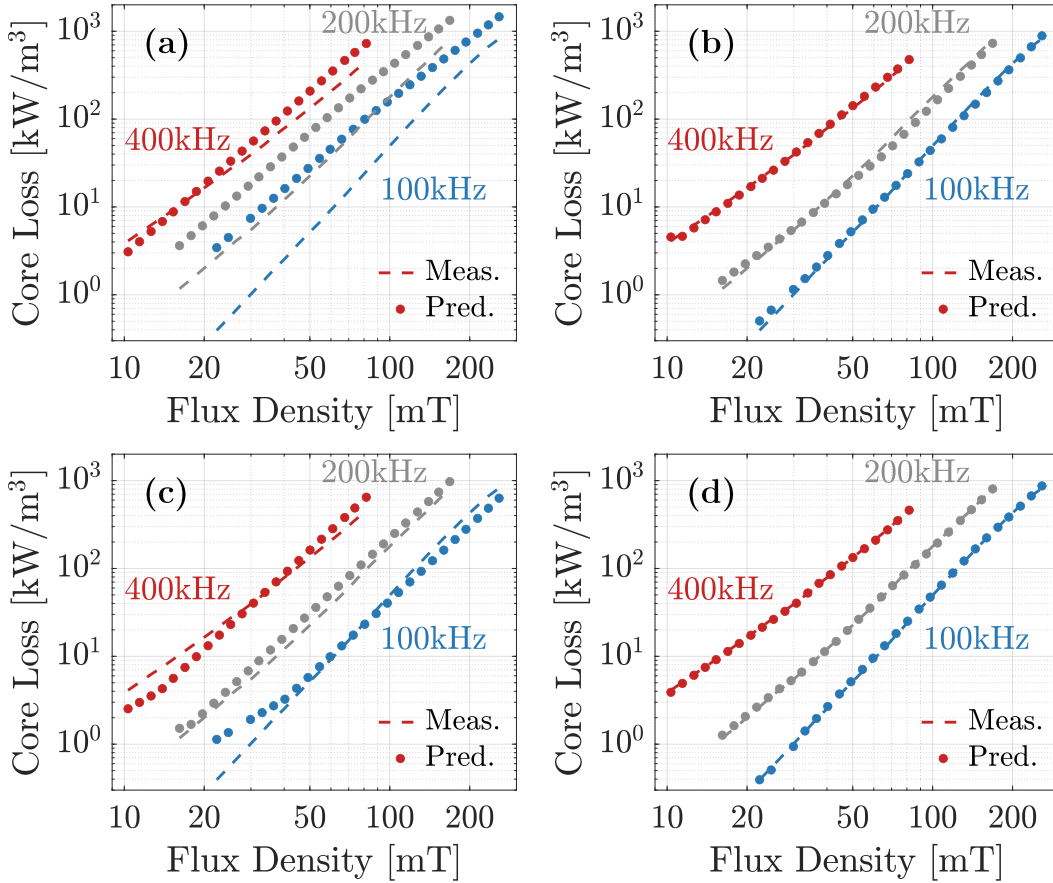


Figure 2.39: Prediction results: (a) applying a pre-trained 25 °C model to 90 °C data points without re-training; (b) applying a pre-trained 25 °C model to 90 °C data points after re-training with very few data points (10 randomly selected); (c) applying a randomly initialized model trained with very few data points (10 randomly selected); (d) applying a randomly initialized model trained with a large amount of data (800 data points).

Finally, the temperature-to-temperature transfer learning process was repeated with varying numbers of data points for training and fine-tuning. Figure 2.41 shows the average testing relative error as the number of data points increases, demonstrating that transfer learning significantly reduces the amount of data required to retrain a model for new temperature conditions.

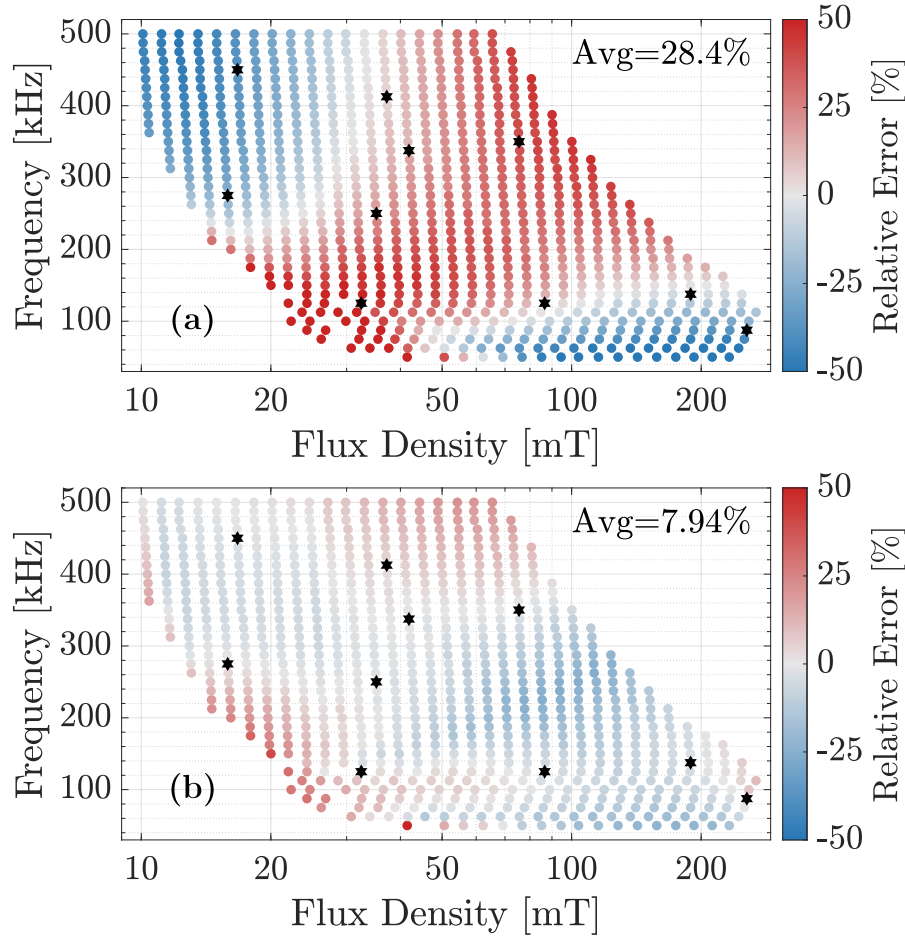


Figure 2.40: Error distribution of prediction results: (a) applying a randomly initialized model trained with 10 randomly selected 90 °C data points (normal training); (b) applying a pre-trained 25 °C model to the 90 °C data after re-training with 10 data points (transfer learning).

2.10 Chapter Summary

This chapter explores the application of machine learning in modeling power magnetics, with a particular focus on the development and use of the MagNet database for data-driven modeling of magnetic components. MagNet is an open-source, large-scale database specifically designed to support machine learning applications in the field of power magnetics. The data quality within the MagNet database is carefully curated and controlled to ensure its suitability for accurate model training and prediction, making it a reliable resource for researchers. The database contains a diverse set of

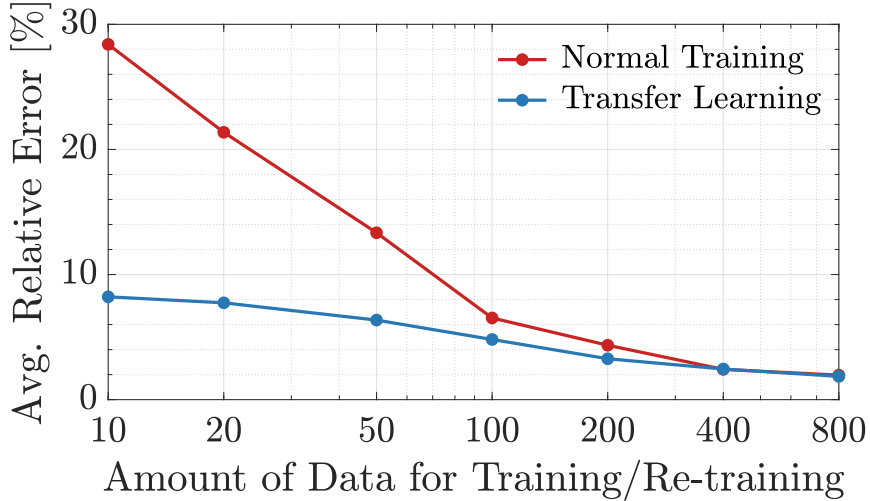


Figure 2.41: Testing average relative error rates of normal training and transfer learning as the number of data points increases.

measurements, encompassing a wide range of materials, operating conditions, and excitation waveforms, enabling robust model development.

Several neural network modeling applications based on the MagNet database are explored, including scalar-to-scalar, sequence-to-scalar, and sequence-to-sequence models. Additionally, the chapter investigates the use of transfer learning techniques to reduce data size requirements, demonstrating how pre-trained models can be adapted for new materials or operating conditions with minimal data. These applications showcase the effectiveness of neural networks in capturing and predicting the behavior of power magnetics, particularly in predicting the B - H loop and core loss for ferrite materials under various conditions.

The chapter introduces the novel concept of using neural networks as a “datasheet” for modeling magnetics across a wide operational range. To achieve this, the authors propose an encoder-projector-decoder neural network architecture for B - H loop modeling. This architecture combines both sequence-based inputs, such as excitation waveforms, and scalar inputs, such as operational conditions, to model hysteresis loops effectively. The network is implemented using both LSTM and transformer

architectures, leveraging the strengths of both approaches to handle the time-series nature of excitation waveforms and the static nature of operating conditions.

Experimental results demonstrate that the proposed neural network architecture can accurately predict the B - H loop and core loss for different ferrite materials, validating its effectiveness. Furthermore, the neural network model is integrated into a comprehensive, user-friendly webpage-based platform, which serves as a fully functional online smartsheet for magnetics analysis and prediction. This platform offers users an interactive tool to predict the B - H loop, core loss, and even recommend the best materials for given operating conditions, all with much greater convenience and accessibility compared to traditional datasheets.

Ultimately, this chapter shows that the neural network-aided datasheet not only provides much more detailed and comprehensive information than conventional datasheets but also maintains a significantly smaller file size, making it a highly efficient and scalable solution for modeling power magnetics. With the continuous growth of the MagNet database, including increased data scale, improved data quality, and greater waveform diversity, the proposed system offers unique opportunities for advancing research in power electronics, power magnetics, and data science, with wide-ranging applications in the field.

In particular, our research group launched the IEEE MagNet Challenge in 2023, aiming to further promote community engagement in data-driven research for power magnetics. This international competition was built upon the MagNet database, which was made publicly available to all participants. Teams were invited to develop their own core loss modeling methods based on the provided dataset, fostering innovation, collaboration, and benchmarking within the community. The challenge attracted 24 teams from 17 countries and led to the development of models that achieved both higher accuracy and smaller model size compared to those presented in this chapter. Further details can be found in [48] and Appendix C.

Related Publications

1. H. Li, D. Serrano, *et al.*, “**How MagNet: Machine Learning Framework for Modeling Power Magnetic Material Characteristics**,” *IEEE Transactions on Power Electronics* [First Prize Paper and Highlighted], vol. 38, no. 12, pp. 15829-15853, Dec. 2023.
2. H. Li, D. Serrano, *et al.*, “**MagNet-AI: Neural Network as Datasheet for Magnetics Modeling and Material Recommendation**,” *IEEE Transactions on Power Electronics*, vol. 38, no. 12, pp. 15854-15869, Dec. 2023.
3. D. Serrano, H. Li, *et al.*, “**Why MagNet: Quantifying the Complexity of Modeling Power Magnetic Material Characteristics**,” *IEEE Transactions on Power Electronics*, vol. 38, no. 11, pp. 14292-14316, Nov. 2023.
4. H. Li, D. Serrano, S. Wang, *et al.*, “**Predicting the B-H Loops of Power Magnetics with Transformer-based Encoder-Projector-Decoder Neural Network Architecture**,” *2023 IEEE Applied Power Electronics Conference and Exposition (APEC)*, Orlando, FL, USA, 2023, pp. 1543-1550.
5. H. Li, S. Wang and M. Chen, “**Compact Neural-Network Digital-Twin Models and Material Comparison for Power Magnetics**,” *2023 IEEE Energy Conversion Congress and Exposition (ECCE)*, Nashville, TN, USA, 2023, pp. 5624-5631.
6. H. Li, D. Serrano, T. Guillod, *et al.*, “**MagNet: An Open-Source Database for Data-Driven Magnetic Core Loss Modeling**,” *2022 IEEE Applied Power Electronics Conference and Exposition (APEC)*, Houston, TX, USA, 2022, pp. 588-595.
7. H. Li, S. R. Lee, *et al.*, “**MagNet: A Machine Learning Framework for Magnetic Core Loss Modeling**,” *2020 IEEE 21st Workshop on Control and Modeling for Power Electronics (COMPEL)*, Aalborg, Denmark, 2020, pp. 1-8.
8. D. Serrano, H. Li, T. Guillod, *et al.*, “**Neural Network as Datasheet: Modeling B-H Loops of Power Magnetics with Sequence-to-Sequence LSTM Encoder-Decoder Architecture**,” *2022 IEEE 23rd Workshop on Control and Modeling for Power Electronics (COMPEL)*, Tel Aviv, Israel, 2022, pp. 1-8.

9. E. Dogariu, **H. Li**, D. Serrano, *et al.*, “**Transfer Learning Methods for Magnetic Core Loss Modeling**,” *2021 IEEE 22nd Workshop on Control and Modelling of Power Electronics (COMPEL)*, Cartagena, Colombia, 2021, pp. 1-6.

Chapter 3

Via-Winding Magnetics: Ultra-Thin Multiphase Pinwheel Coupled Inductors

3.1 Background and Motivation

Advances in heterogeneous three-dimensional (3D) integration and power delivery architectures have enabled high-performance computing systems operating at sub-1 V core voltages and drawing over 1000 A of current [49–51]. Conventional voltage regulation modules (VRMs), typically placed on printed circuit boards (PCBs), struggle to meet these growing demands due to their large physical footprint and the limitations imposed by lateral power distribution. Delivering such massive currents through long, high-resistance lateral power delivery networks (PDNs) results in significant I^2R losses, electromagnetic interference (EMI), and degraded transient performance. Furthermore, the presence of bulky off-chip magnetics exacerbates the challenge of achieving efficient and compact VRM designs [2].

To address these issues, there has been increasing interest in vertical power delivery (VPD) schemes, where power conversion and distribution are aligned in the vertical direction – from the package substrate to the processor die [52,53]. This configuration shortens the lateral PDN path, significantly reduces conduction losses, and improves transient response. At the same time, emerging interconnect technologies

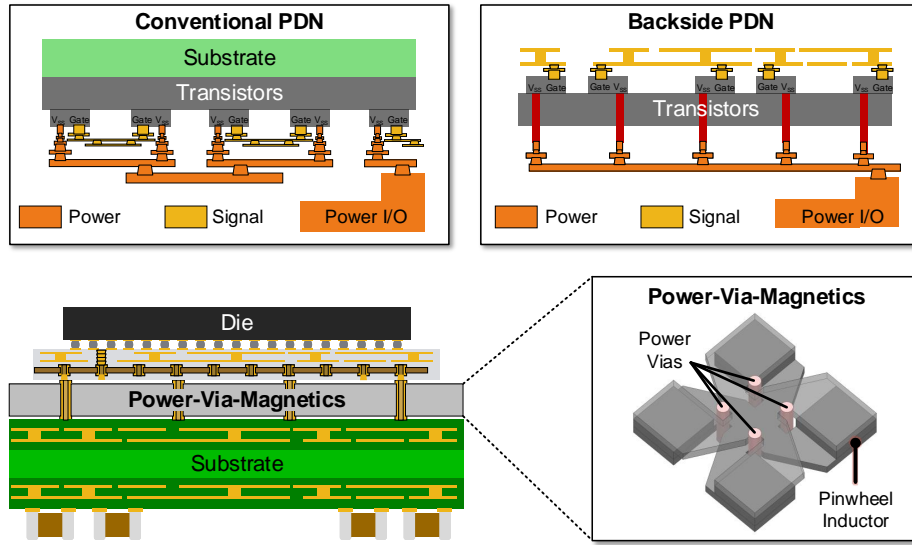


Figure 3.1: The vision of power-via magnetics. The power vias in packaging are surrounded by a pinwheel patterned magnetic layer as the substrate for minimizing the power distribution network (PDN) impedance, and connected with power vias in silicon to enable end-to-end vertical power delivery.

such as Cu-Cu direct bonding and micro-bumps offer higher interconnect densities than traditional solder-based methods [54–56], making VPD architectures more viable.

Among several VPD configurations, the in-packaging vertical stacked VRM architecture, as shown in Figure 3.1 has gained traction due to its ability to deliver high current with low vertical profile while remaining decoupled from the constraints of on-die integration. As illustrated in Fig. 1.1, this architecture distributes power through three vertically arranged functional layers: a capacitor layer for switched-capacitor (SC) power conversion, a semiconductor layer for power switching, and a magnetic layer for current filtering and modulation [57–59]. This heterogeneously integrated structure takes advantage of co-packaging flexibility to combine optimized semiconductor, capacitor, and magnetic technologies, enabling high current density and improved efficiency without sacrificing layout flexibility or compatibility with signal interconnects.

While the capacitor and semiconductor layers benefit from advanced integration and planar scaling, the magnetic layer remains a bottleneck due to its dominant contribution to system height and limited options for miniaturization. Traditional magnetic components are hard to scale vertically because they require core materials with sufficient cross-sectional area to support high current while maintaining low loss and acceptable inductance. Designing compact magnetics with high current capability and tight physical constraints poses a fundamental co-design challenge in modern power electronics [60].

To meet these challenges, three complementary strategies can be used to minimize the magnetic component footprint and improve performance:

- **Stage Partitioning:** Reduce the burden on magnetics by compressing the voltage conversion ratio using a preceding SC or transformer-based stage. For example, a 4:1 step-down SC stage followed by a multiphase buck converter minimizes duty ratio and associated magnetic stress.
- **Coupled Magnetics:** Leverage multiphase coupling to cancel dc flux components, enhance transient response, and reduce ripple current, thereby enabling smaller inductance values and reduced core sizes.
- **Volumetric Optimization:** Design intricate 3D magnetic structures that distribute flux efficiently within minimal vertical height while accommodating high current-carrying windings.

This chapter introduces a new magnetic design methodology tailored to vertical VRM integration: the *via-winding magnetics* approach. It presents the design and optimization of ultra-thin multiphase coupled inductors, where vertical conductor vias are embedded directly within the magnetic core structure. A key innovation is the *pinwheel coupled inductor* – a novel geometry that surrounds these vertical windings with intricately patterned magnetic material to achieve high coupling, minimized

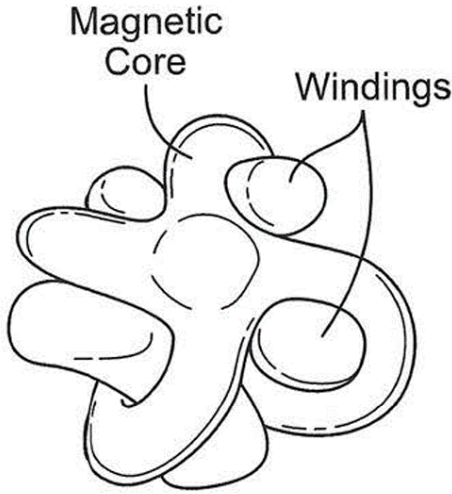


Figure 3.2: Rendering of the concept of pinwheel magnetics. The magnetic core forms a 3D structure that effectively contorts itself around vertical windings to achieve multiphase coupling with low resistance and height.

resistance, and compact height, as depicted in Figure 3.2. This approach represents a new development in the lineage of coupled magnetic technologies, including planar-flux inductors [59], twisted-core inductors [61], and vertical winding structures [62].

Ultimately, the core challenge is to strategically and optimally populate the available 3D volume with magnetic material, copper, and air to meet both electrical and physical constraints. Figure 3.3 illustrates a broader vision for approaching this challenge from a computational design perspective. The constrained design space can be discretized into a set of smaller “unit cubes,” each of which is assigned to one of three fundamental building blocks of a magnetic structure: (1) air, (2) magnetic material (e.g., soft ferrite), or (3) copper conductor. This conceptual framework provides a foundation for advanced layout synthesis, enabling the use of optimization algorithms – or even machine learning techniques – to iteratively refine and generate magnetic component structures layer by layer, with the goal of meeting specific performance metrics such as inductance, coupling, resistance, and height.

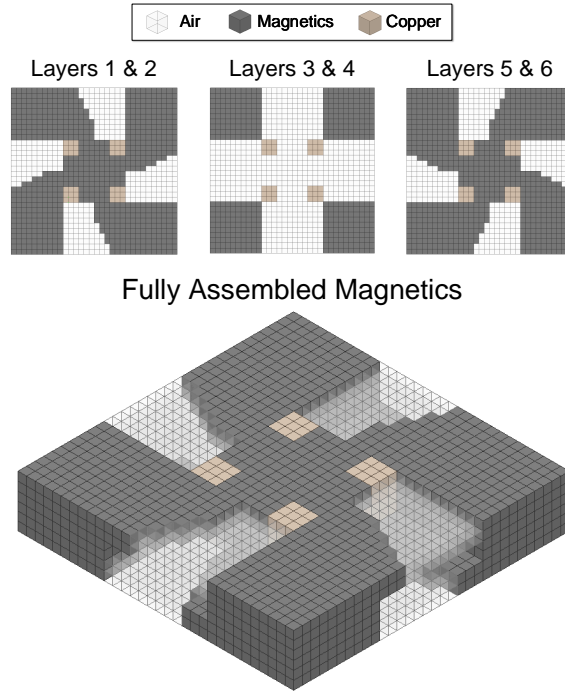


Figure 3.3: Assembly procedure for a four-phase pinwheel inductor. Two identical core pieces are used, with the top piece rotated 180° in the x-axis and placed on top of the bottom piece. Four vertical windings are inserted through the core assembly.

While such algorithmic synthesis represents a long-term direction, this work takes a more structured and systematic approach by proposing and evaluating several specific geometric forms of vertically coupled multiphase inductors. These designs are carefully parameterized, allowing for closed-form modeling, guided optimization, and physical prototyping. By studying these representative cases, we demonstrate the practicality and performance potential of vertical magnetics design, laying the groundwork for more automated methods in future VRM integration efforts.

The main contributions of this chapter are:

- The introduction of the *pinwheel via-winding* magnetic structure for efficient vertical VRMs, enabling strong phase coupling and compact 3D integration.

- A modeling and optimization framework for determining the optimal geometry, material distribution, and electrical parameters of the pinwheel structure under area and height constraints.
- Fabrication and experimental validation of two representative designs demonstrating 4 V to 1 V conversion at 120 A total current, achieving up to 93.5% efficiency and 3,960 W/in³ power density at 2 MHz switching frequency.

This work demonstrates how co-designing packaging, interconnects, and magnetics can push the limits of vertical VRM performance, paving the way toward high-density, low-impedance, and thermally manageable power delivery for next-generation computing platforms.

3.2 Modeling and Optimization Framework

3.2.1 Principles of Multiphase Coupling

Multiphase coupled inductors have been widely studied for their ability to break traditional trade-offs in magnetic design for VRMs. In a coupled structure, multiple windings share common magnetic flux paths – either through a unified magnetic core or via close-proximity air coupling. This configuration, when combined with interleaved phase operation, extends the current ripple cancellation benefits typically observed at the input and output nodes to each individual phase. As a result, a multiphase coupled inductor can reduce both the per-phase ripple current ($\Delta i_{p-p,\Phi}$) and the effective inductance observed during transient events (L_ℓ), compared to using discrete uncoupled inductors.

Theoretical analysis of multiphase coupled inductors has been well established in prior works [62–65], including recent explorations of air-coupled implementations [66]. In this section, we summarize key formulations critical to the optimization of the pinwheel-type multiphase coupled inductor introduced in this thesis.

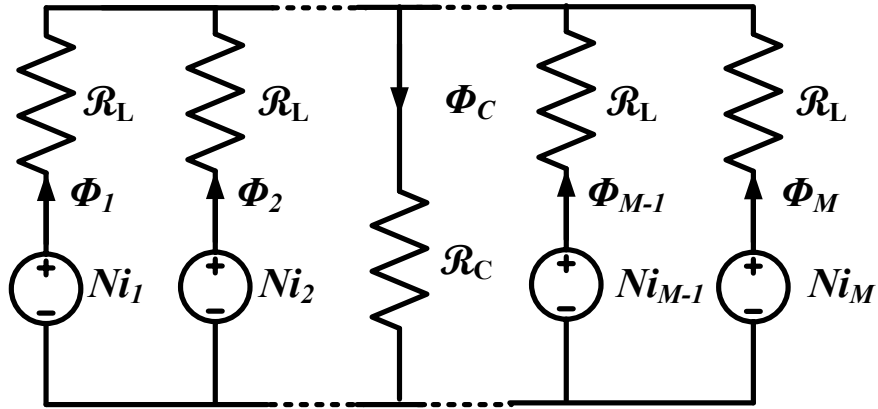


Figure 3.4: Generalized lumped reluctance model of an M -phase coupled inductor. The model captures the geometric structure with M leg reluctances representing the flux paths around each winding and a central reluctance representing the middle air gap. This formulation aligns closely with physical dimensions, allowing calculation of flux distribution and enabling evaluation of key design constraints such as inductance, coupling coefficient, and maximum flux density during optimization.

For any candidate magnetic structure, a corresponding lumped reluctance model can be constructed, where magnetic reluctance is defined as $\mathcal{R} = \frac{l}{\mu A}$, with l being the effective flux path length, A the cross-sectional area, and $\mu = \mu_r \mu_0$ the permeability of the magnetic material. This model allows estimation of flux and flux density in each region to prevent core saturation.

Figure 3.4 shows a generalized reluctance model for an M -phase coupled inductor. The per-phase leakage inductance, which determines transient response behavior, is derived as:

$$L_\ell = \frac{N^2}{\mathcal{R}_L + M\mathcal{R}_C} \quad (3.1)$$

where N is the number of turns per phase winding, and \mathcal{R}_L , \mathcal{R}_C are reluctances as shown in the figure.

With phase interleaving (i.e., $360^\circ/M$ phase shift), current ripple at the shared nodes is significantly reduced. The ripple reduction propagates into each phase due to magnetic coupling, quantified by the coupling coefficient $\beta = \frac{M\mathcal{R}_C}{\mathcal{R}_L}$. The resulting

per-phase ripple reduction ratio is defined as:

$$\gamma = \frac{1 + \beta\Gamma}{1 + \beta} \quad (3.2)$$

where the interleaving factor Γ is given by:

$$\Gamma = \frac{(k + 1 - DM)(DM - k)}{D(1 - D)M^2}, \quad (3.3)$$

with $D = \frac{V_{out}}{V_{in}}$, $T = 1/f_s$, M the number of phases, and k an integer such that $\frac{k}{M} < D < \frac{k+1}{M}$.

Based on these, the per-phase peak-to-peak current ripple is expressed as:

$$\Delta i_{p-p,\Phi} = \gamma \frac{V_{out}(1 - D)T}{L_\ell}. \quad (3.4)$$

These analytical relationships from [62] serve as the foundation for the optimization routine, enabling rapid evaluation of ripple behavior, transient response, and magnetic saturation for a given inductor geometry.

3.2.2 Optimization Framework

Using the coupled inductor model described above, a comprehensive optimization framework is developed to guide the design of vertical multiphase coupled inductors. The full process is illustrated in Fig. 3.5. Both inductor designs presented in this work follow this same optimization flow.

The framework begins with two types of inputs: (1) system-level parameters including V_{in} , V_{out} , switching frequency, per-phase current, and worst-case current imbalance; and (2) geometric constraints such as total footprint and height.

Given these, the optimizer selects geometry-defining parameters for a specific structure (e.g., the pinwheel inductor) and evaluates its performance. To do this

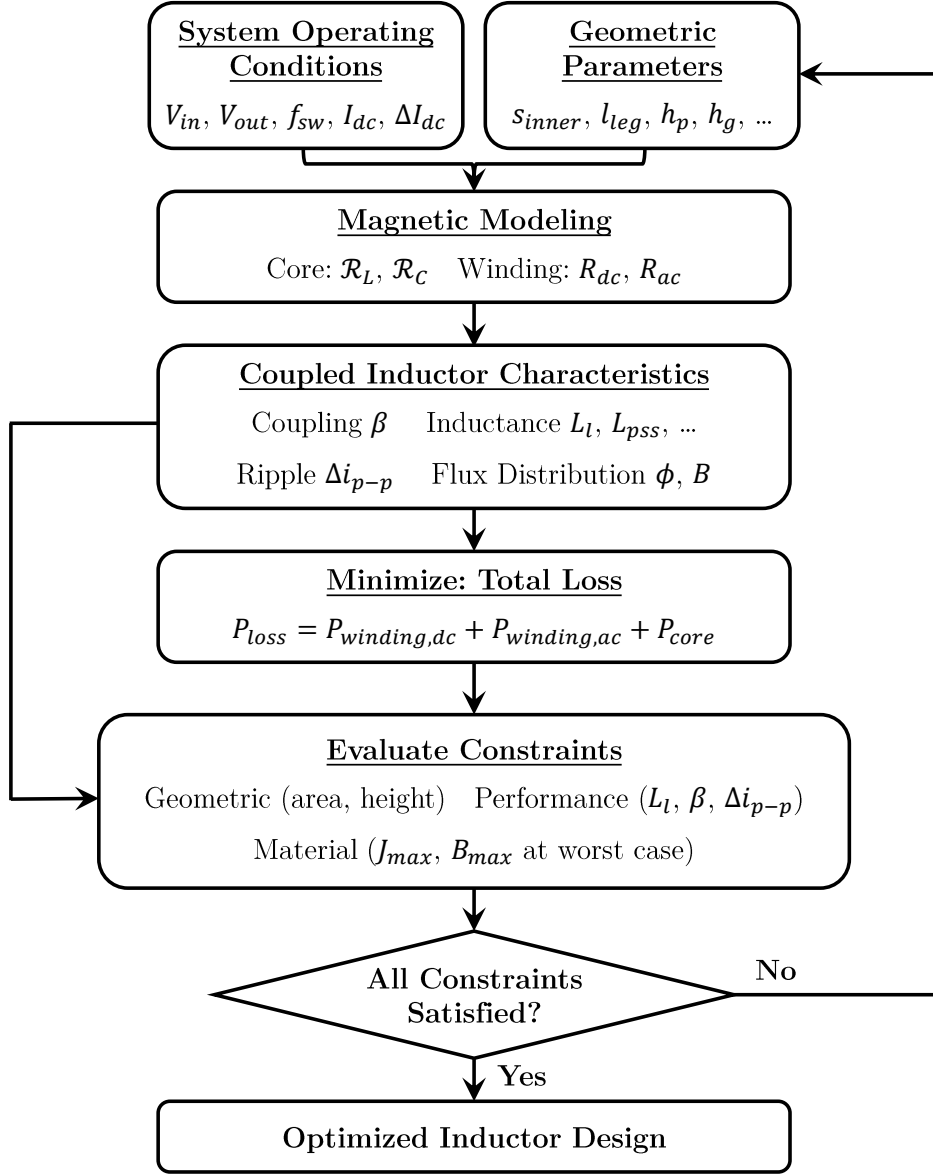


Figure 3.5: Flowchart of the optimization process for a multiphase coupled inductor. Given the system operating conditions and geometric parameters, the algorithm estimates the reluctance of each magnetic path and the winding resistance, then computes coupled inductor characteristics. The optimization minimizes the total loss of inductors while satisfying constraints on geometric limitations, coupled inductor performance, peak current and flux density.

efficiently, the magnetic core is discretized into segments, enabling localized flux density estimation without relying on full FEM simulation.

With the calculated reluctances and winding resistances, the key performance metrics – including coupling coefficient, leakage inductance, ripple current, and peak flux – are determined.

The optimization objective is to minimize total inductor loss, which includes:

- Dc copper loss, based on average current and winding resistance.
- Ac copper loss, derived from current ripple and ac resistance models.
- Core loss, computed using the iGSE model [26] based on peak and RMS flux in each segment, which, in the future, can be replaced and improved by neural network models shown in Chapter. 2.

Each iteration checks for constraint compliance, including physical feasibility, target inductance and ripple, and safety margins for peak current and flux density – even in worst-case imbalance scenarios.

Beyond identifying optimal geometries, this framework also enables design-space exploration via parameter sweeping. For example, by varying the core footprint or height while holding electrical conditions constant, one can trace Pareto curves of volume vs. loss, enabling co-optimization of performance and compactness.

3.3 Design Examples and Implementation of Pinwheel Coupled Inductors

To implement the concept of via-winding magnetics, both inductor designs presented in this work utilize vertically oriented, straight-through conductors that are magnetically coupled via a surrounding pinwheel-shaped ferrite core. In this core configuration, two identical ferrite components are employed – one rotated 180° about the x -axis and placed atop the other – to create closed magnetic paths encircling each

vertical conductor. This arrangement enables magnetic flux to flow from the central region of the top core, around each via, and return to the bottom core, thereby achieving strong interphase coupling while maintaining sufficient leakage inductance per phase.

To evaluate the flexibility of the proposed optimization methodology (detailed in Section 3.2), two distinct designs are explored, each following the same design flow but targeting different specifications. The first design, referred to as the *pinwheel inductor #1*, features a compact $8\text{ mm} \times 8\text{ mm}$ footprint and a total height of 1.8 mm. It is designed to support a rated current of 25 A per phase and accommodate up to 5% dc current imbalance among phases. The second design, termed the *expanded variant #2*, adopts a slightly larger $9\text{ mm} \times 9\text{ mm}$ footprint and a 2.5 mm height, allowing higher current operation at 40 A per phase with tolerance for up to 10% dc current mismatch.

Both inductors are designed for four-phase multiphase buck converters operating at 2 MHz, targeting a 4 V to 1 V voltage conversion. As derived in Eq.(3.3), the effectiveness of interleaved current ripple cancellation in multiphase coupled inductors is maximized when the converter duty cycle D is near k/M , where $k \in 0, 1, \dots, M - 1$. With $M = 4$, a target duty cycle of 25% aligns well with this optimal ripple reduction condition.

The core material used in both designs is DMR53 Mn-Zn ferrite, manufactured by Hengdian Group DMEGC Magnetics Co., which offers a relative permeability of 900 and a saturation flux density of 480 mT. These characteristics make it a suitable choice for compact, high-efficiency, and high-density magnetic integration in ultra-thin VRM applications.

A summary of the shared electrical specifications and design constraints for both inductor implementations is provided in Table 3.1.

Table 3.1: Electrical Parameters and Constraints

Electrical Parameters

Description	Symbol	Value
Input Voltage	V_{in}	4 V
Output Voltage	V_{out}	1 V
Switching Frequency	f_s	2 MHz

Electrical Constraints

Description	Symbol	Value
Dc Resistance	R_{dc}	$\leq 0.2 \text{ m}\Omega$
Full-Load Phase Current	$I_{out,\Phi}$	25 A or 40 A
Worst-case Current Imbalance	$\Delta I_{out,\Phi}$	5% or 10%
Per-Phase Current Ripple	$\Delta i_{p-p,\Phi}$	$\leq 3 \text{ A}$
Saturation Flux Density	B_{sat}	480 mT
Per-Phase Leakage Inductance	L_ℓ	$\leq 30 \text{ nH}$

3.3.1 Design #1: Pinwheel Coupled Inductor

Inductor Geometry

The structural design of the pinwheel coupled inductor is depicted in Fig. 3.6, which presents a three-dimensional view of the complete assembly alongside top and side projections that define all critical geometrical parameters.

As illustrated in Fig. 3.6(a), each phase winding follows a vertical trajectory, conducting current directly from the bottom to the top of the magnetic assembly. This through-hole winding strategy substantially reduces the effective length of the conductor, thereby lowering both resistance and conduction losses. The resulting magnetic flux generated by any given winding follows a loop within the core, entering from the top core section, circulating through the adjacent magnetic legs, and returning through the legs of the remaining three windings via the bottom core section. A small portion of the flux also travels across the central air gap between the core halves, completing the closed magnetic path. This arrangement ensures strong

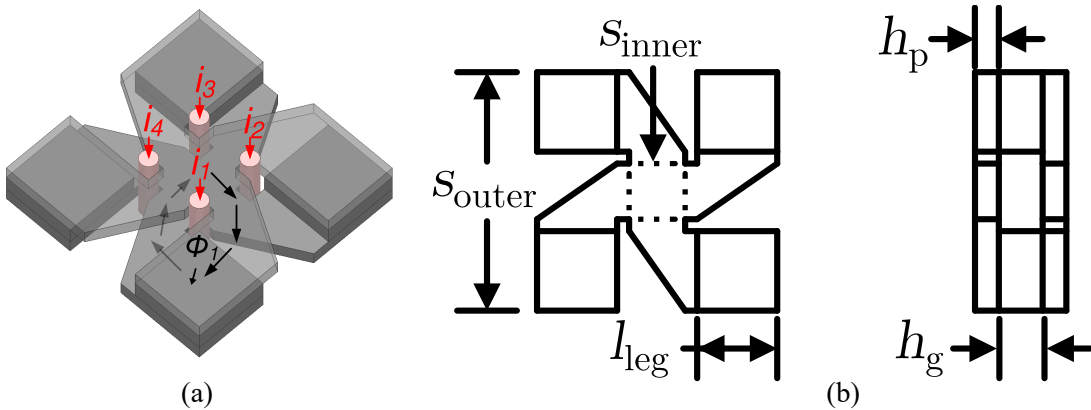


Figure 3.6: (a) 3D view of the four-phase pinwheel coupled inductor, illustrating the flux path associated with winding 1. The dc flux generated by this winding wraps around the winding and circulates from the top core piece to the bottom, with most of the flux continuing to the leg posts of the other three windings, while a small amount of the flux travels through the middle air gap, completing the magnetic path. (b) Parameterization of the pinwheel inductor geometry. The top view defines the key in-plane dimensions s_{inner} , s_{outer} , and l_{leg} , which determine the allocation of ferrite material for each leg and the central region, as well as the designated copper winding space. The side view illustrates the z -dimension parameters: core plate thickness h_g and air gap height h_p , and total assembled height. These geometric parameters serve as the basis for structural optimization and magnetic modeling.

magnetic coupling between phases while maintaining sufficient self-inductance in a compact form factor.

The top-down view of the core highlights two major ferrite domains: a central core region and four surrounding magnetic legs. The central region, with an area of s_{inner}^2 , serves as the convergence zone for magnetic flux from all windings. Each leg comprises a square ferrite post with an area of l_{leg}^2 , joined to the central area by angled flux-guiding arms. The intervening space, defined as $\frac{(s_{\text{outer}} - 2 \times l_{\text{leg}} - s_{\text{inner}})^2}{2}$, forms the winding window where vertical copper conductors are routed.

The side view presents the complete stacked assembly of the inductor, made of two identical ferrite plates. The vertical dimensions are governed by two key parameters: h_p , denoting the thickness of each ferrite layer, and h_g , representing the air gap height between the two plates. These dimensions, combined with the planar layout,

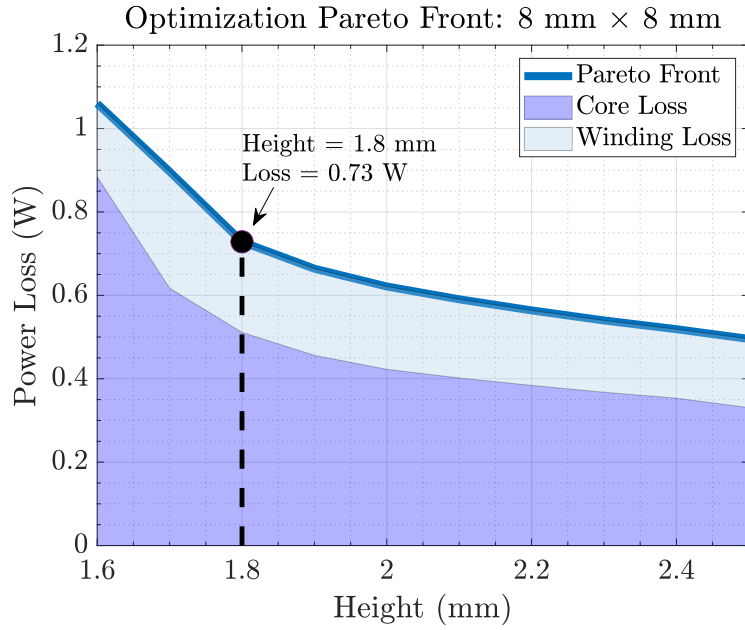


Figure 3.7: Pareto front of the pinwheel coupled inductor optimization. The “knee” of the curve, where the height is minimized while maintaining low loss, is at 1.8 mm. The design at 1.8 mm is selected for fabrication.

determine the total inductor volume and serve as the basis for material allocation in the optimization process.

Optimization and Simulation Results

Using the geometric framework illustrated in Fig. 3.6 and the modeling methodology detailed in Sec. 3.2, the pinwheel inductor was optimized to deliver high current-handling capability while maintaining a low vertical profile. The planar dimensions were fixed at $8 \times 8 \text{ mm}^2$ to comply with packaging constraints at the system level, while the vertical height was treated as a design variable and swept to evaluate trade-offs between overall thickness and power loss.

Figure 3.7 shows the resulting Pareto front, which captures the optimal loss achievable for each candidate inductor height, subject to the electrical and volumetric constraints defined in Table 3.1. As expected, increasing the height permits greater

Table 3.2: Geometric Parameters of Designed Pinwheel Inductor
Volumetric Constraints

Description	Symbol	Value
Length	s_{outer}	$\leq 8 \text{ mm}$
Width	s_{outer}	$\leq 8 \text{ mm}$
Total Height	$2 \times h_p + h_g$	1.6 – 2.5 mm
Optimization Results		
Description	Symbol	Value
Outer Side	s_{outer}	8 mm
Inner Side	s_{inner}	1.5 mm
Leg	l_{leg}	2.65 mm
Total Height	$2 \times h_p + h_g$	1.8 mm
Plate Height	h_p	0.6 mm
Gap Height	h_g	0.6 mm

accommodation of magnetic material, thereby lowering losses. However, the benefit of further increasing height becomes marginal past a certain point.

A total height of 1.8 mm was selected as the final design, as it corresponds to the “knee” of the Pareto curve – a point where further height increases result in minimal additional loss reduction. At this operating point, the inductor exhibits a total loss of 0.73 W under full-load conditions (25 A dc current per phase), while remaining within the targeted low-profile envelope required for vertical system integration.

The finalized inductor design, with geometric parameters summarized in Table 3.2, adopts a total height of 1.8 mm, where the vertical dimension is distributed as 0.6 mm for each ferrite plate and 0.6 mm for the central air gap. This partition balances magnetic performance and manufacturability within the constrained height profile.

To assess magnetic performance under realistic operating conditions, the structure was analyzed using ANSYS Maxwell 3D simulations. Figure 3.8 presents the simulated dc magnetic flux distribution under two loading conditions. In the balanced case, each winding carries 25 A of dc current. The resulting peak flux density reaches

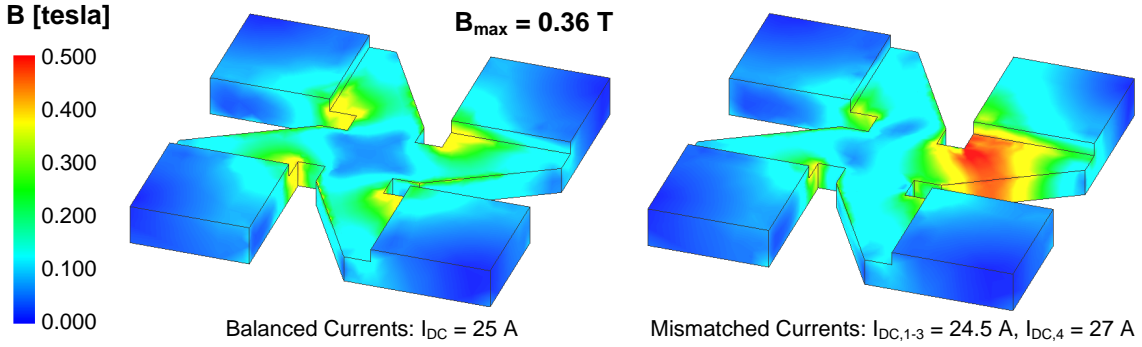


Figure 3.8: ANSYS Maxwell 3D dc flux density distribution with balanced phase currents of 25 A per phase (left) and a dc current mismatch where $I_{DC,1-3} = 24.5 \text{ A}$ and $I_{DC,4} = 27 \text{ A}$ (right). The maximum flux density in the core is 360 mT when all phases have balanced currents. For the dc current mismatch condition, the inductance of winding four drops by 20% of its zero dc bias inductance value, still providing sufficient inductance during full load unbalanced operation.

0.36 T near the ferrite corners adjacent to the copper conductors, which is well below the saturation threshold of the DMR53 ferrite, ensuring safe magnetic operation across all phases.

To further evaluate the impact of current imbalance – a critical consideration in coupled inductor designs – a second scenario introduces a deliberate 5% mismatch, where windings 1–3 each conduct 24.5 A and winding 4 carries 27 A. This induces localized magnetic stress in the vicinity of the higher-current phase. As a result, the self-inductance of winding 4 experiences a 20% reduction relative to its zero-bias value. Nevertheless, this drop remains within acceptable limits and does not compromise the inductor’s ability to satisfy ripple and transient performance specifications. These results confirm that the pinwheel structure maintains magnetic robustness under moderate imbalance, an important consideration for real-world current sharing among phases.

Performance Characterization and Evaluation

Physical prototypes of the pinwheel coupled inductor were fabricated based on the optimized dimensions detailed in Table 3.2. Manufacturing of the ferrite cores and

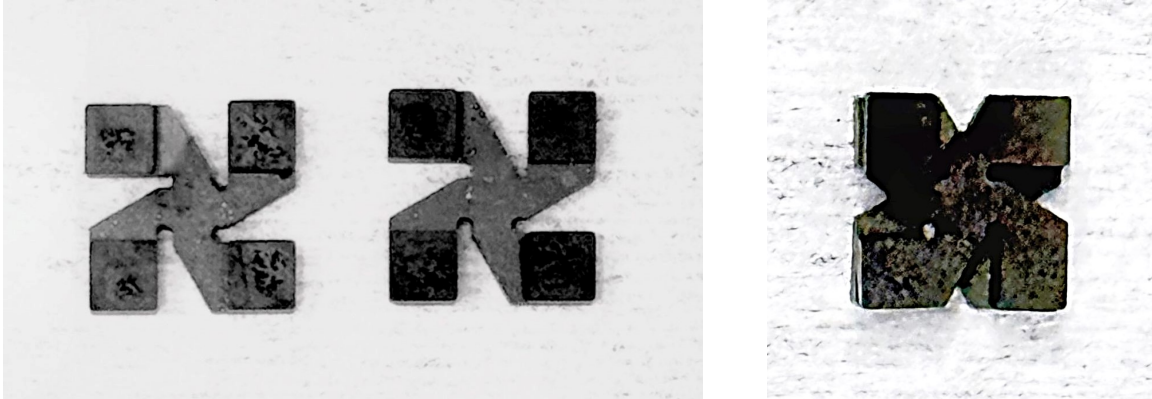


Figure 3.9: Photographs of the fabricated pinwheel core pieces and the fully assembled four-phase coupled inductor. The identical top and bottom core halves are shown alongside the final stacked assembly.

assembly of the complete inductor structure were carried out by ITG Electronics.

Figure 3.9 shows photographs of the fabricated components, including the identical top and bottom ferrite pieces and the fully assembled four-phase inductor. The inductor was integrated into a test platform consisting of a four-phase buck converter and its motherboard, which are described in more detail in Section 3.4, to facilitate electrical performance evaluation.

The inductance characteristics of the assembled inductor were measured using an Agilent 4395A Network Analyzer, following the procedure outlined in [58]. These measurements capture both the intrinsic behavior of the magnetic structure and the parasitic effects introduced by PCB layout and vertical ground return paths. At 2MHz, the self-inductance for each phase was found to be 189 nH, while the total leakage inductance measured 6.63 nH.

The resulting inductance matrix for the inductor integrated in the four-phase buck converter is:

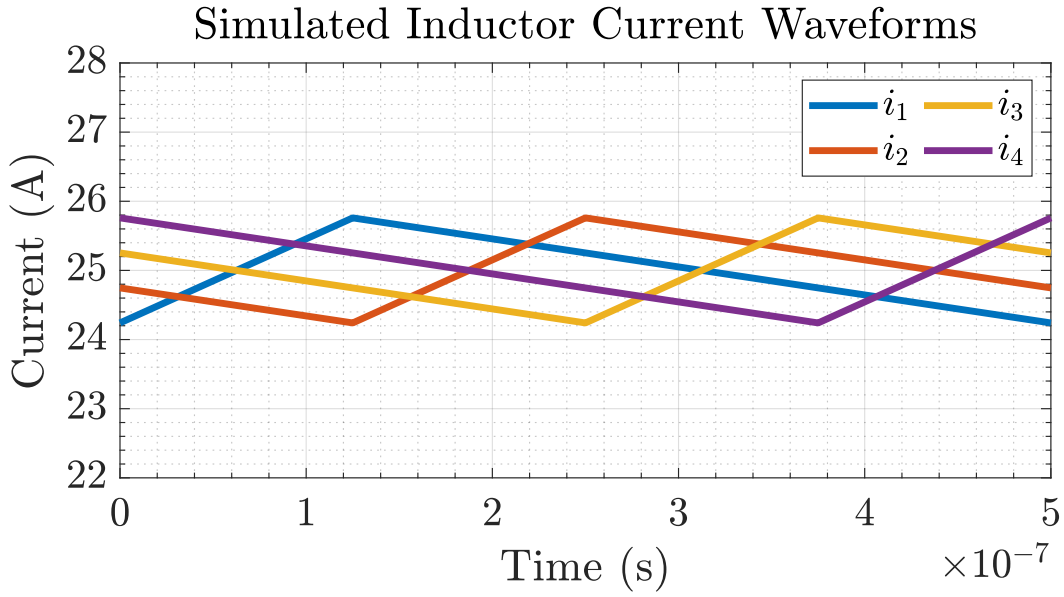


Figure 3.10: Simulated inductor current waveforms using the inductance matrix obtained from Ansys Maxwell 3D for a four-phase buck converter with $V_{in} = 4$ V, $V_{out} = 1$ V, and $f_s = 2$ MHz. The peak-to-peak current ripple is 1.52 A.

$$\mathbf{L} = \begin{bmatrix} 189 & -54.3 & -54.3 & -54.3 \\ -54.3 & 189 & -54.3 & -54.3 \\ -54.3 & -54.3 & 189 & -54.3 \\ -54.3 & -54.3 & -54.3 & 189 \end{bmatrix} \text{nH.} \quad (3.5)$$

This matrix reflects a high degree of symmetry and interphase coupling, with substantial mutual inductance between each phase pair. Based on this matrix, the effective steady-state per-phase inductance at a duty ratio of $D = 25\%$ is calculated to be 243 nH, and the effective leakage inductance is 26 nH.

Using these inductance values, a time-domain simulation was performed to evaluate inductor current ripple under nominal converter conditions ($V_{in} = 4$ V, $V_{out} = 1$ V, $f_s = 2$ MHz). As shown in Fig. 3.10, the resulting peak-to-peak current ripple per phase is 1.52 A, indicating strong ripple suppression enabled by the coupled inductor architecture.

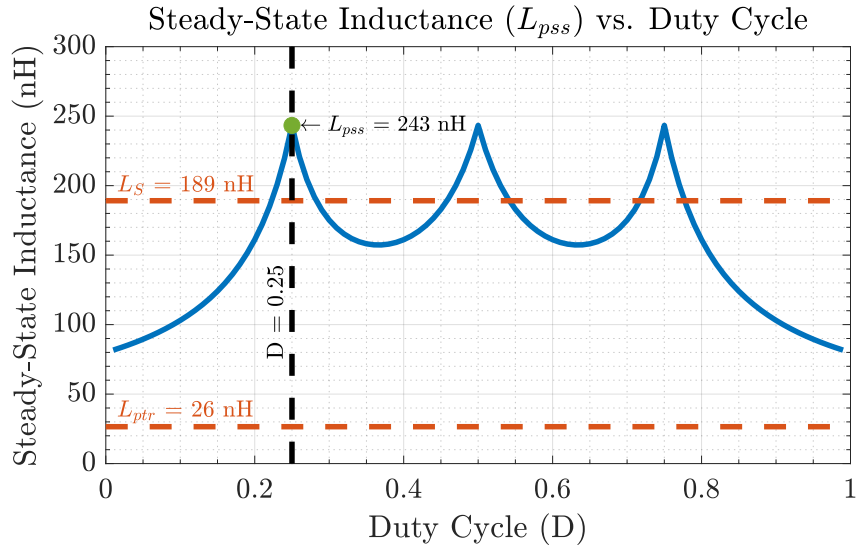


Figure 3.11: Plot of the steady-state inductance (L_{pss}) vs. duty cycle for the pinwheel coupled inductor assembly. At $D = 0.25$, $L_{pss} = 243 \text{ nH}$, exceeding L_S by a factor of 1.3 and exceeding L_{ptr} by a factor of 7.

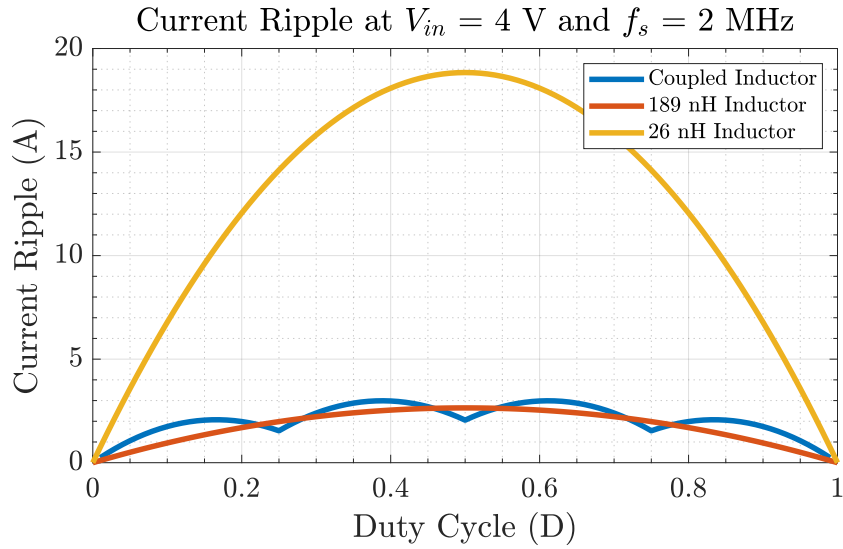


Figure 3.12: Plot of the peak-to-peak phase current ripple for the four-phase buck VRM when $V_{in} = 4 \text{ V}$ and $f_s = 2 \text{ MHz}$ compared to if four discrete inductors with values $L_{disc} = L_S$ and $L_{disc} = L_{ptr}$ were used. The peak-to-peak phase current ripple at $D = 0.25$ is 1.54 A for the coupled inductor, 1.98 A for the discrete inductor case where $L_{disc} = L_S$, and 14.13 A for the discrete inductor case where $L_{disc} = L_{ptr}$.

To further assess the inductor's dynamic behavior, Fig. 3.11 presents the variation of per-phase steady-state inductance L_{pss} and leakage inductance L_ℓ as functions of

the duty cycle $D = V_{out}/V_{in}$, calculated using Equations (3.4) and (3.1). Notably, at typical operating points such as $D = 25\%$, 50% , and 75% , L_{pss} exceeds the nominal self-inductance value, highlighting the benefit of interphase magnetic coupling in multiphase topologies. This increase in effective inductance leads to improved current ripple suppression under steady-state operation.

The ripple mitigation effect is quantitatively illustrated in Fig. 3.12, which compares the peak-to-peak phase current ripple of the pinwheel coupled inductor against that of two discrete inductor configurations. The first comparison case uses discrete inductors with the same self-inductance as the coupled inductor ($L_{disc} = L_S = 189 \text{ nH}$), while the second uses inductors with the same transient inductance ($L_{disc} = L_{ptr} = 26 \text{ nH}$). At a duty ratio of $D = 0.25$, the coupled inductor achieves a ripple of 1.54 A , representing a $1.3\times$ reduction compared to the L_S case and a $7\times$ improvement over the L_{ptr} case. This substantial reduction in ripple current reinforces the benefits of tight interphase coupling in achieving higher performance within compact footprints.

3.3.2 Design #2: Extended Pinwheel Coupled Inductor

Inductor Geometry

To accommodate increased load current requirements – raising the per-phase rating from 25 A to 40 A – and a more relaxed current mismatch tolerance of up to 10% , the extended pinwheel inductor adopts a slightly enlarged footprint and vertical profile compared to the baseline design.

As illustrated in Fig. 3.13, this variant adopts a restructured magnetic layout to more efficiently utilize the available 3D volume. The revised geometry improves the spatial partitioning between copper and magnetic material, allowing for increased core cross-sectional area and improved magnetic flux containment, which are both

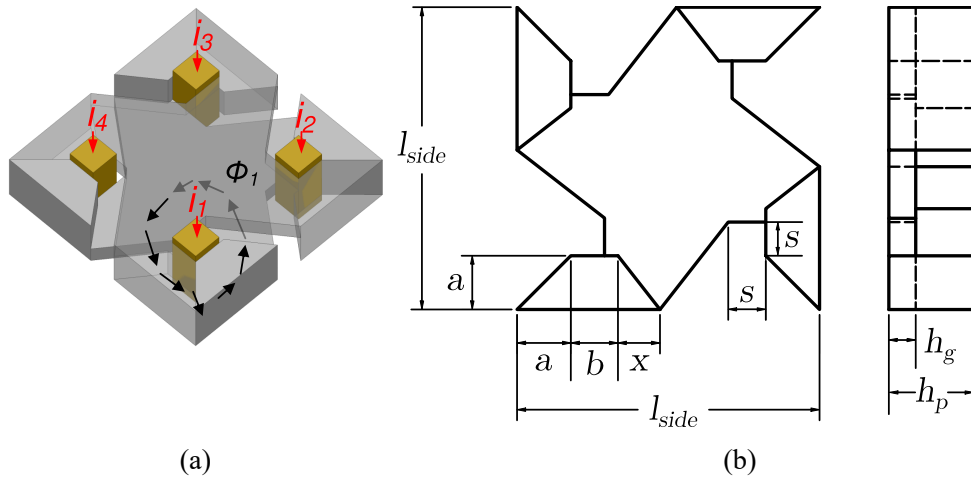


Figure 3.13: (a) 3D rendering of the extended pinwheel inductor, showing vertical current conduction and flux circulation paths. (b) Geometry parameterization highlighting key variables a , b , x , s , l_{side} , h_p , and h_g , which are used in modeling and optimization.

critical for handling higher energy levels while limiting core saturation and power loss.

Consistent with the previous design, each phase utilizes a vertically oriented conductor that runs straight through the core stack from bottom to top, as shown in Fig. 3.13(a). This straight-through configuration minimizes winding length and associated resistance, improving conduction efficiency under high current operation. The resulting magnetic flux path wraps through the top ferrite piece, down the outer leg posts, across the bottom ferrite plate, and back up through neighboring legs. A portion of the total flux also closes through the center air gap, enhancing interphase coupling and overall magnetic efficiency.

From the top view, the magnetic core can be divided into a central flux-converging region and four surrounding leg posts that serve as return paths for the coupled flux. Several variables govern this geometry: the offset parameter a defines the position of each winding aperture, b sets the width of the leg post, x controls the angular sector assigned to each leg, and s represents the size of the copper window. The full lateral

span of the structure is set by l_{side} , determining the outer boundary of the ferrite footprint.

In the vertical dimension, the structure consists of two core plates, each with height h_g , and vertical leg extensions of height h_p , as shown in the side view. These vertical dimensions determine the total volume available for magnetic and winding material, and are included as variables within the optimization process.

The overall structure is composed of two symmetric ferrite pieces. One is flipped 180° about the horizontal axis and stacked onto the other, enabling natural alignment of magnetic paths and winding windows. This assembly approach eliminates the need for additional magnetic fillers or bonding layers while forming a continuous closed magnetic loop around each winding, facilitating strong coupling and manufacturability.

Optimization and Simulation Results

Leveraging the geometric framework illustrated in Fig. 3.13 and the modeling methodology outlined in Section 3.2, the extended pinwheel inductor was optimized to accommodate higher phase currents while preserving a constrained vertical profile. For this design, the footprint was fixed at $9 \times 9 \text{ mm}^2$, ensuring compatibility with the system-level layout, while also offering sufficient core volume to handle the elevated magnetic flux demands of 40 A per-phase operation.

As with the prior design, the total height of the structure was treated as a sweep variable in the optimization process. This enabled the identification of the Pareto front, capturing the trade-off between magnetic loss and structural height. The final design point was selected to balance minimal power loss with compact packaging. The resulting key geometrical parameters of the optimized structure are summarized in Table 3.3.

Table 3.3: Geometric Parameters of Designed Pinwheel Inductor
Optimization Results

Description	Symbol	Value
Total Length	l_{side}	9 mm
Total Width	l_{side}	9 mm
Winding Location	a	1.6 mm
Leg Post Width	b	0.4 mm
Window Size	s	1.0 mm
Angular Span	x	0.5 mm
Plate Thickness	h_g	0.8 mm
Leg Post Height	h_p	2.5 mm
Total Height	h_p	2.5 mm

Compared to the baseline 8×8 mm² configuration, the extended pinwheel design allocates a larger cross-sectional area to each winding window. This expanded area allows for the integration of thicker copper conductors, which is especially beneficial for reducing conduction losses under high-current operation. In parallel, the reconfigured geometry achieves better volumetric efficiency – enabling a higher fill factor for the ferrite material – which improves the inductive energy storage capability and reduces core losses.

Despite only moderate increases in footprint and vertical height, this optimized design significantly enhances the current handling capacity and robustness against dc current imbalance, achieving these improvements within the tight spatial constraints required for high-density integration.

To verify the magnetic safety margin of the optimized design, the extended pinwheel inductor was evaluated using 3D finite element simulations conducted in ANSYS Maxwell. These simulations help ensure that the magnetic core operates within safe flux density limits under expected operating conditions. Figure 3.14 illustrates the simulated dc flux distributions for two representative scenarios.

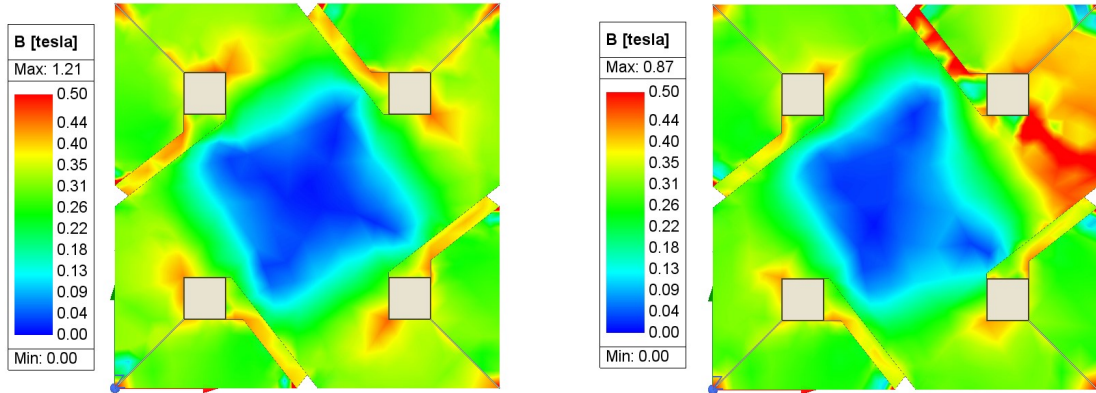


Figure 3.14: ANSYS Maxwell 3D simulation of dc flux density distribution in the extended pinwheel inductor under (left) balanced phase currents of 40 A and (right) a 10% dc current mismatch where $I_{DC,1-3} = 40$ A and $I_{DC,4} = 44$ A. The maximum flux density reaches 400 mT under balanced conditions. With the imbalance, localized flux increases are observed and the self-inductance of winding four decreases by 15%, while remaining sufficient for full-load operation.

Under nominal operation, each of the four phases conducts a balanced dc current of 40 A. The resulting flux density distribution reveals a peak value of approximately 0.40 T, primarily concentrated near the leg regions adjacent to the vertical winding conductors. This value remains comfortably below the saturation flux density of 460 mT for the DMR53 Mn-Zn ferrite, confirming that the core can safely handle elevated current levels without entering magnetic saturation.

To further evaluate the inductor's performance under real-world non-idealities, a second simulation scenario introduces a 10% dc current mismatch – winding 4 is driven at 44 A, while the other three carry 40 A. This imbalance induces localized flux intensification near the overloaded leg post, but the peak flux still remains below the ferrite's saturation threshold. According to the simulation results, the self-inductance of winding 4 decreases by roughly 15% relative to its zero-bias value. Nevertheless, this reduced inductance remains sufficient to ensure acceptable ripple suppression and transient response under full-load conditions. These findings demonstrate the

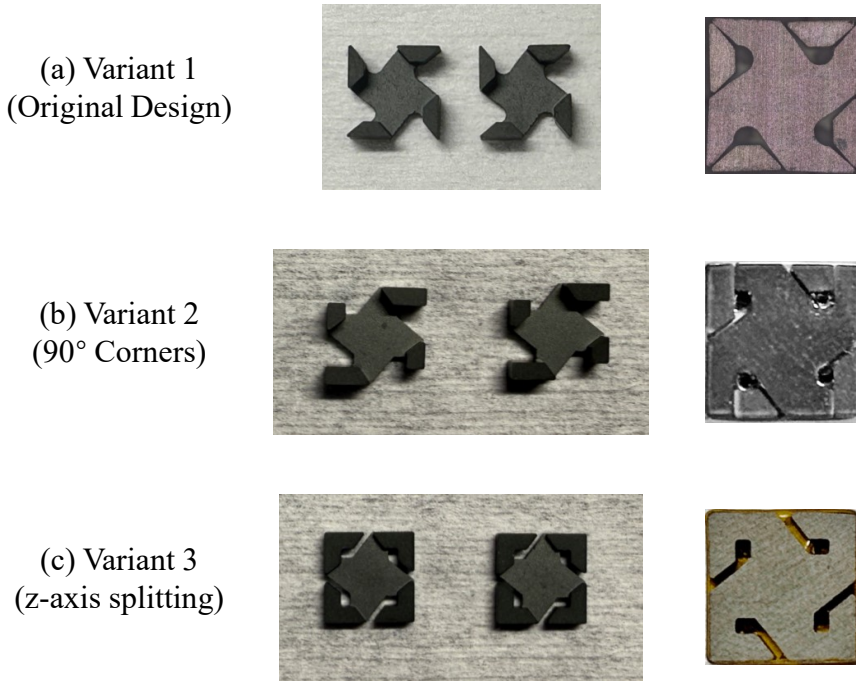


Figure 3.15: Three variants of the extended pinwheel coupled inductor design. (a) Variant #1 is fabricated based on the original extended pinwheel geometry, where two core halves with interleaved structures are assembled at 45° corner joints, resulting in unintended air gaps due to manufacturing limitations. (b) Variant #2 modifies the corner geometry to form complementary 90° angled faces, allowing easier machining and improved alignment. (c) Variant #3 introduces a horizontal split along the z -axis, forming two equal-thickness core halves with all contact surfaces lying in a single plane, enabling tighter assembly and reduced variation across phases.

extended design's resilience to practical current mismatches, highlighting its suitability for demanding multiphase applications.

Design Variants and Manufacturing Considerations

Following optimization, prototype samples of the extended pinwheel coupled inductor were fabricated by ITG Electronics according to the geometric specifications listed in Table 3.3. The first prototype – denoted as Variant #1 and shown in Fig. 3.15(a) – adhered closely to the original structural concept. However, inductance measurements revealed a substantial performance shortfall, with values falling 30% to 40% below simulated expectations and exhibiting significant inter-phase variation.

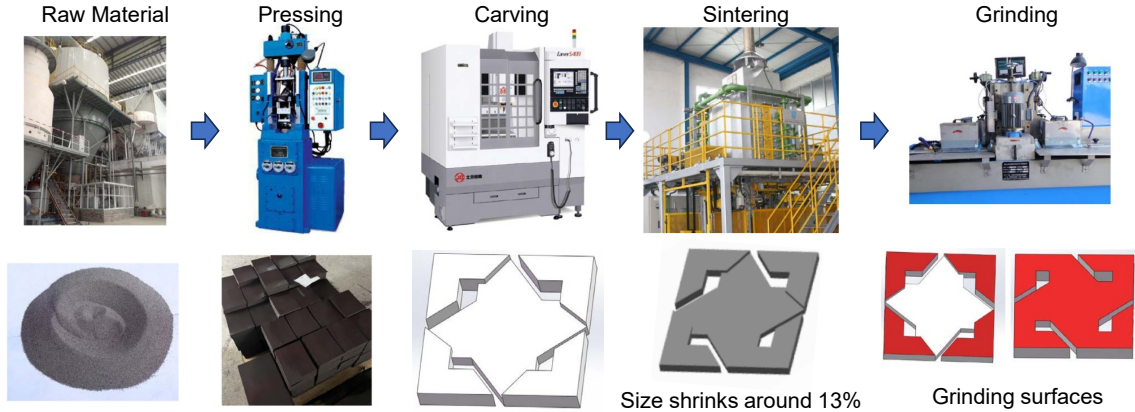


Figure 3.16: Conceptual manufacturing process of magnetic components with customized geometries, provided by ITG Electronics. The carving precision determines how closely the fabricated shape matches the intended design. During sintering, dimensional shrinkage occurs and must be accounted. The effectiveness of grinding directly impacts the flatness and quality of contact surfaces, which are critical for achieving tight assembly and minimizing unintended air gaps.

Subsequent analysis identified the root cause as unintended air gaps at the corner junctions between the two ferrite halves. The original design assumed ideal alignment of the angled corner faces, enabling low-reluctance magnetic flux closure across phases. In practice, however, fabrication tolerances and geometric complexity prevented these sharp 45° mating surfaces from achieving full contact during assembly. The resulting high-reluctance gaps disrupted the intended 3D magnetic paths, diminishing both inductance and interphase coupling effectiveness.

Figure 3.16 outlines the conceptual manufacturing process employed by ITG Electronics for customized ferrite components. Key fabrication stages – particularly carving, sintering, and grinding – play critical roles in defining the dimensional accuracy and structural integrity of the magnetic core. Intricate features such as narrow slots, sharp corners, and internal cavities are especially vulnerable to chipping, deformation, or misalignment due to the brittle nature of ferrite. Furthermore, surface flatness is paramount for minimizing magnetic reluctance at contact interfaces. While planar surfaces are straightforward to grind and align, the angled corner joints in Variant

#1 introduced complexity that exceeded standard tooling capabilities, leading to misalignment and variable assembly fit.

This experience underscores an important principle in vertically integrated magnetic design: while unconventional 3D geometries can offer superior electromagnetic performance, their real-world viability hinges on manufacturability and mechanical precision. Accordingly, magnetic component design must be informed by both performance objectives and practical fabrication constraints, especially in applications aimed at scalable production.

To overcome the shortcomings of Variant #1, two revised core geometries – Variant #2 and Variant #3, shown in Fig. 3.15(b) and (c), respectively – were developed. These designs preserve the overall footprint, form factor, and structural philosophy of the extended pinwheel inductor, while introducing localized geometric modifications to improve alignment and minimize assembly-induced air gaps:

- Variant #2 transforms the original 45° corner joint into a pair of complementary 90° faces by shifting the upper and lower edges of the mating surface in opposite directions. This modification allows for more reliable surface preparation using conventional grinding tools and improves mating accuracy during assembly. However, some sensitivity to y -axis misalignment remains, which may introduce slight asymmetries or residual air gaps.
- Variant #3 reorients the stacking direction by introducing a horizontal split along the z -axis. This results in two core halves with flat, co-planar contact surfaces, enabling uniform grinding and tighter assembly tolerances. The phase windings of all four channels now intersect a single horizontal plane, analogous to the approach used in the original pinwheel inductor. While this configuration simplifies assembly and improves phase-to-phase consistency, it requires high dimensional precision in the carved flux-guiding slots to preserve magnetic continuity across the vertical axis.

Both variants were fabricated and experimentally evaluated. In contrast to Variant #1, both revised designs demonstrated significantly improved inductance values, closely matching simulated predictions and exhibiting much lower variation across phases. The difference in electrical performance between the two was minimal. However, owing to its superior mechanical alignment and ease of surface finishing, Variant #3 was selected as the final implementation for all subsequent characterization and system-level integration.

Performance Characterization and Evaluation

The extended pinwheel coupled inductor, implemented using Variant #3, was fabricated and experimentally evaluated to validate its electrical performance. As with the previous design, the inductor was integrated into a custom four-phase buck converter test fixture, with the entire assembly mounted on a dedicated motherboard for measurement and evaluation.

To account for any asymmetries introduced during manufacturing, phase-by-phase inductance measurements were performed. Specifically, the self-inductance of each phase was measured between its input terminal and the common output node. In addition, mutual inductance between phase pairs was extracted through differential measurements. These data were used to construct the full inductance matrix, which captures the inter-phase coupling behavior of the physically realized inductor. The resulting inductance matrix, measured with the inductor installed in the four-phase vertical VRM assembly, is given as:

$$\mathbf{L} = \begin{bmatrix} 129.2 & -34.6 & -39.3 & -36.2 \\ -34.6 & 127.2 & -34.5 & -35.2 \\ -39.3 & -34.5 & 120.9 & -35.5 \\ -36.2 & -35.2 & -35.5 & 123.0 \end{bmatrix} \text{nH} \quad (3.6)$$

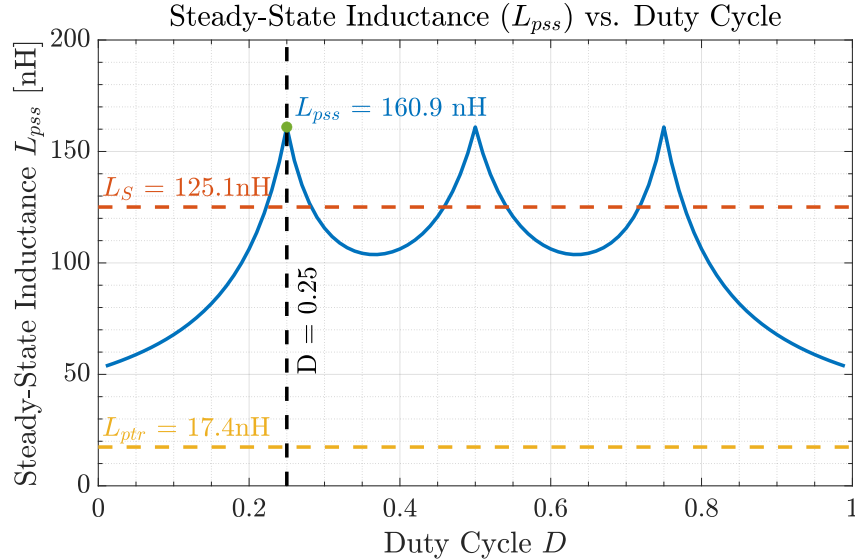


Figure 3.17: Steady-state inductance (L_{pss}) and leakage inductance (L_ℓ) vs. duty cycle, extracted from the measured inductance matrix. At $D = 0.25$, $L_{pss} = 160.9$ nH.

Using this experimentally obtained matrix in conjunction with the coupled inductor modeling framework outlined in Section 3.2, key performance metrics were derived. At a duty cycle of $D = 25\%$, the steady-state effective inductance per phase (L_{pss}) is calculated to be 160.9 nH, and the corresponding leakage inductance (L_ℓ) is 17.4 nH. These values yield a simulated peak-to-peak phase current ripple of 2.33 A under full-load conditions.

Figure 3.17 shows how L_{pss} and L_ℓ vary with duty ratio, based on the measured inductance matrix. As observed in previous designs, L_{pss} peaks at $D = 25\%$, 50% , and 75% – duty cycles where the interleaved phase operation maximally reinforces ripple cancellation. These benefits are further illustrated in Fig. 3.18, which compares the current ripple performance of the coupled inductor against two discrete inductor configurations.

At $D = 25\%$ with $V_{in} = 4$ V and $f_s = 2$ MHz, the peak-to-peak ripple of the coupled inductor is reduced by $1.3\times$ compared to a discrete inductor with $L_{disc} = L_S = 125.1$ nH, and by $9.2\times$ compared to a low-inductance discrete case of $L_{disc} = L_{ptr} = 26$ nH. These results reaffirm the efficacy of vertical magnetic integration and

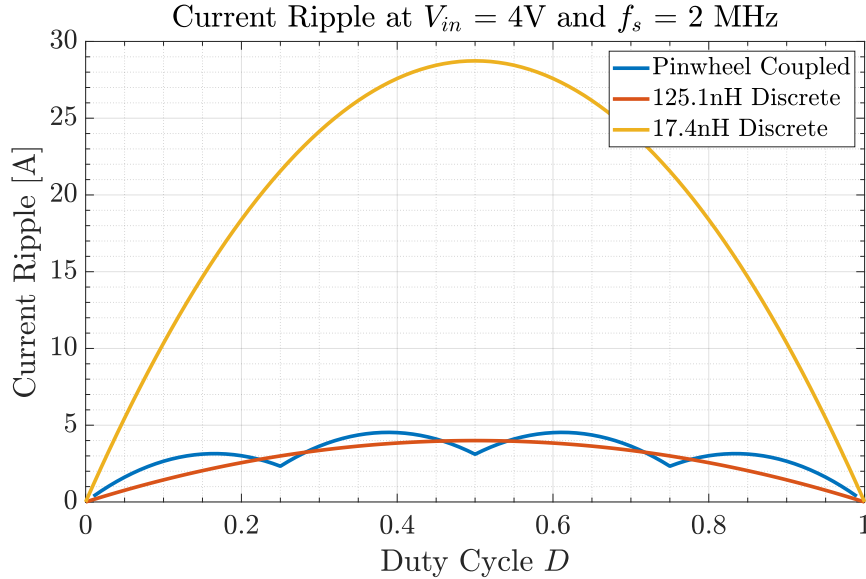


Figure 3.18: Comparison of peak-to-peak phase current ripple at $V_{in} = 4$ V, $f_s = 2$ MHz, $D = 0.25$ for three inductor configurations: coupled inductor, discrete inductor with L_S , and discrete inductor with L_{ptr} .

interphase coupling in reducing ripple and enhancing transient behavior in compact VRM designs.

3.4 Experimental Verification

3.4.1 Four-Phase Buck Voltage Regulator Design

To experimentally validate the electrical performance of the proposed vertically coupled inductor designs, a four-phase synchronous buck voltage regulator was developed. This converter is specifically designed to interface directly with the vertical windings of the inductor, enabling efficient vertical power delivery in a compact layout.

Figure 3.19 shows the top-layer PCB layout of the buck converter. The four power stages are symmetrically arranged around the center of the board, with each phase featuring a dedicated switching node routed through vertical vias that directly interface with the corresponding inductor winding. This via-connected layout ensures

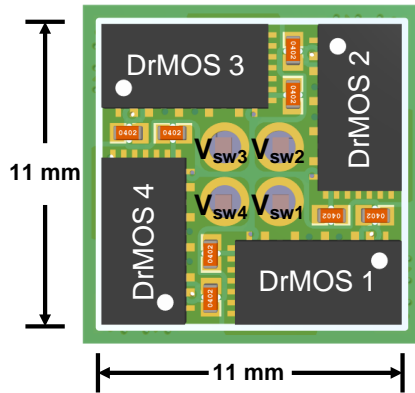


Figure 3.19: Top-layer layout of the four-phase buck converter power stage, highlighting the symmetrical placement of each MP86936 DrMOS device and associated passive components. Switch nodes are routed vertically through vias for direct connection to the coupled inductor.

a minimal path between the switch nodes and inductor terminals, thereby reducing parasitic inductance and improving transient performance.

The assembly process is illustrated in Fig. 3.20. The vertically coupled inductor is surface-mounted onto the buck converter PCB, with its vertical conductors soldered to plated through-holes on both the buck board and a supporting base board. The base board serves as an interconnect platform that delivers input power to the buck stage and routes the regulated output from the inductor terminals to the load or measurement interface. Output capacitors are strategically placed on the underside of the base board to minimize loop inductance and optimize output filtering.

The complete bill of materials (BOM) for the four-phase buck converter is provided in Table 3.4. Each power stage employs an MP86936 DrMOS device, chosen for its high current handling capability, integrated driver and bootstrap circuit, and compact 3mm×6mm package. With careful layout and vertical integration, the total power stage footprint is constrained to 11mm×11mm with a maximum component height of only 0.8 mm, making it well suited for high-density, low-profile power delivery applications.

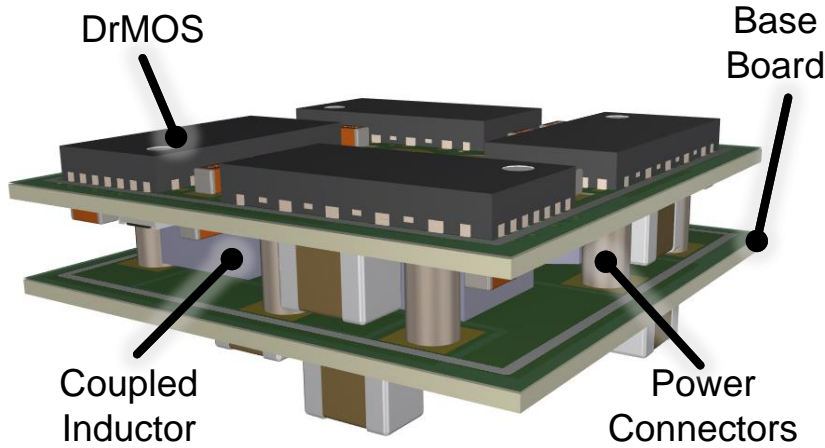


Figure 3.20: 3D view of the fully assembled power stage. The vertically coupled inductor is mounted by soldering its through-windings to the via pads of both the power stage PCB and the motherboard. Power connectors on the baseboard supply input voltage and ground return paths.

Table 3.4: Bill-of-Materials for Four-Phase Buck VRM

Description	Component	Quantity
DrMOS Devices	MPS MP86936GRJT-P	4
Bootstrap Capacitors	Kemet 0402 25 V 0.1 μ F	4
Input Capacitors	Kemet 0402 25 V 4.7 μ F TDK 0805 25 V 22 μ F	4 8
Output Capacitors	TDK 0805 6.3 V 100 μ F	12

3.4.2 Converter Efficiency

A four-phase buck VRM is assembled with the four-phase pinwheel coupled inductor as shown in Fig. 3.21. A signal board is used to provide the PWM signals, gate drive power, and house test points for probing. Signals are generated using a TMS320F28388D microcontroller from Texas Instruments. Cooling was performed with one 36 CFM dc fan.

To benchmark the performance of the proposed pinwheel coupled inductors, a baseline four-phase buck VRM was assembled using off-the-shelf discrete inductors from the Coilcraft SLR4040 series. Each inductor in this series measures

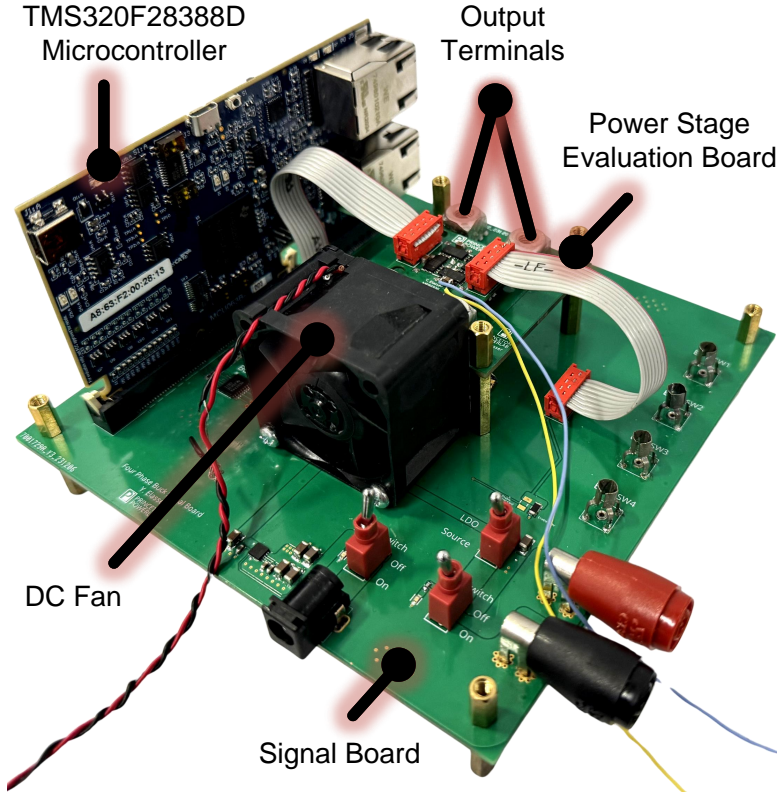


Figure 3.21: Test fixture setup for the four-phase buck VRM. The power stage evaluation board contains the four-phase buck power stage, including the pinwheel coupled inductor, as well as the base motherboard which hosts the input and output power terminals. A TMS320F28388D microcontroller is connected to a signal board, which generates the PWM signals, provides the gate drive power, and houses test points. System cooling is provided by a 36 CFM dc fan.

4 mm × 4 mm × 4 mm, and when arranged in a 2 × 2 configuration, the overall footprint becomes 8 mm × 8 mm – identical to that of the pinwheel coupled inductor design #1, and only slightly smaller than the 9 mm × 9 mm footprint of design #2.

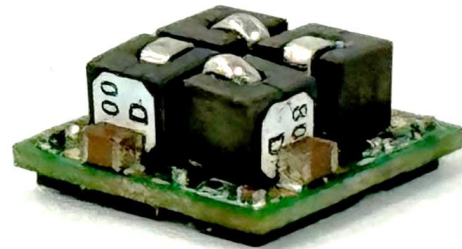
Figure 3.22 visually compares the fully assembled VRM systems using either the integrated pinwheel coupled inductor or the four discrete inductors. The height of the pinwheel inductors is 1.8 mm for design #1 and 2.5 mm for design #2, while the discrete inductors are each 4 mm tall. After accounting for board stack-up and mechanical clearances, the total system heights are 3.4 mm, 4.1 mm, and 5.6 mm, respectively. This illustrates that the pinwheel approach achieves up to 40% reduction

**Pinwheel Coupled
Inductor**



Height: 3.4 mm

**Coilcraft SLR4040
Discrete Inductors**



Height: 5.6 mm

Figure 3.22: Power stage of the four-phase buck VRM in Fig. 3.19, assembled with the pinwheel coupled inductor design #1 (left) and four discrete Coilcraft SLR4040 inductors (right). The pinwheel-based assembly achieves a total system height of 3.4 mm, reducing the height by over 2 mm compared to the 5.6 mm height of the system using discrete inductors.

in vertical profile – critical for enabling low-profile power modules in dense system environments.

The Coilcraft SLR4040 series supports several inductance options, including 22 nH, 50 nH, 65 nH, 80 nH, and 100 nH. For representative comparison, two configurations were selected:

- 22 nH, which closely matches the per-phase leakage inductance (L_ℓ) of the coupled inductor, thus serving as a baseline for ripple comparison under similar transient response.
- 100 nH, the highest available inductance in this form factor, which offers better ripple suppression but may limit transient performance due to slower current ramp-up.

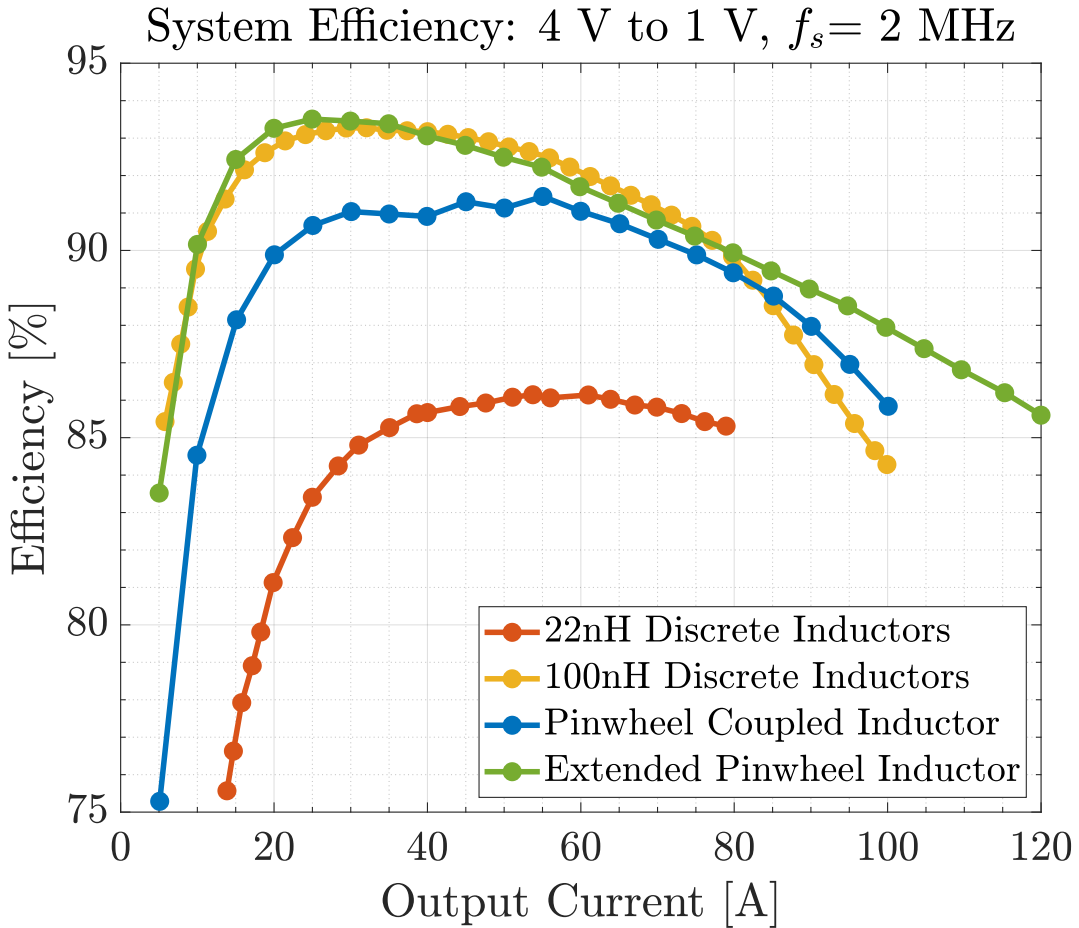


Figure 3.23: Measured system efficiency of the four-phase buck VRM using the pinwheel coupled inductor (design 1), extended pinwheel inductor (design 2), and Coilcraft SLR4040 discrete inductors with 22 nH and 100 nH values. All data points correspond to DrMOS junction temperatures below 100°C. Design 1 achieves a peak efficiency of 91.5%, while design 2 reaches 93.5%. Both coupled inductor configurations outperform the 22 nH discrete inductors by a large margin, which offer comparable transient performance. Compared to the 100 nH discrete inductors, design 1 exhibits slightly lower peak efficiency, whereas design 2 matches or exceeds efficiency across the full load range.

These configurations allow a direct performance comparison between the coupled inductor and industry-standard discrete implementations, highlighting the trade-offs in ripple control, height reduction, and magnetic efficiency enabled by the pinwheel architecture.

Figure 3.23 plots the measured system efficiency for all tested configurations under a 4 V input, 1 V output, and 2 MHz switching frequency. Gate drive losses –

approximately 0.43 W at 2 MHz – are excluded for consistency. Thermal conditions were controlled by limiting operation to a maximum DrMOS junction temperature of 100°C, as monitored by onboard temperature sensors.

The $8 \times 8\text{mm}^2$ pinwheel coupled inductor (design1) achieved a peak efficiency of 91.5% at a 55 A load, maintaining 85.9% efficiency at 100 A full load. The extended $9 \times 9\text{mm}^2$ variant (design2) reached an even higher peak efficiency of 93.5% at 25 A and sustained 85.4% efficiency at 120 A. Though the inductor is rated for up to 160 A, testing was capped at 120 A due to the thermal limitations of the DrMOS devices.

In contrast, the VRM using 22 nH discrete inductors reached its thermal limit at 80 A, with a peak efficiency of 86.2% at 60 A and only 85.2% at full load. The low inductance results in significant ripple current, which amplifies conduction, core, and switching losses across the system.

When 100 nH discrete inductors were used, peak efficiency increased to 93.2% at 40 A. However, these components suffer from limited saturation current due to the lack of dc flux cancellation. At elevated temperatures (100°C), the saturation threshold per inductor drops to 17 A, leading to rapid efficiency degradation at higher currents. Full-load efficiency fell to 87% at 90 A.

These experimental results highlight two distinct advantages of the multiphase coupled inductor architecture:

- **Improved Efficiency at Comparable Transient Performance:** When matched against 22 nH discrete inductors, which offer similar dynamic response due to comparable leakage inductance, the pinwheel designs deliver substantially higher efficiency. This stems from enhanced ripple suppression via multiphase coupling, which lowers conduction, core, and switching losses.
- **Superior Transient Response at Comparable Steady-State Inductance:** When compared with 100 nH discrete inductors – selected to match the effective L_{pss} of the coupled design – the pinwheel inductor provides similar

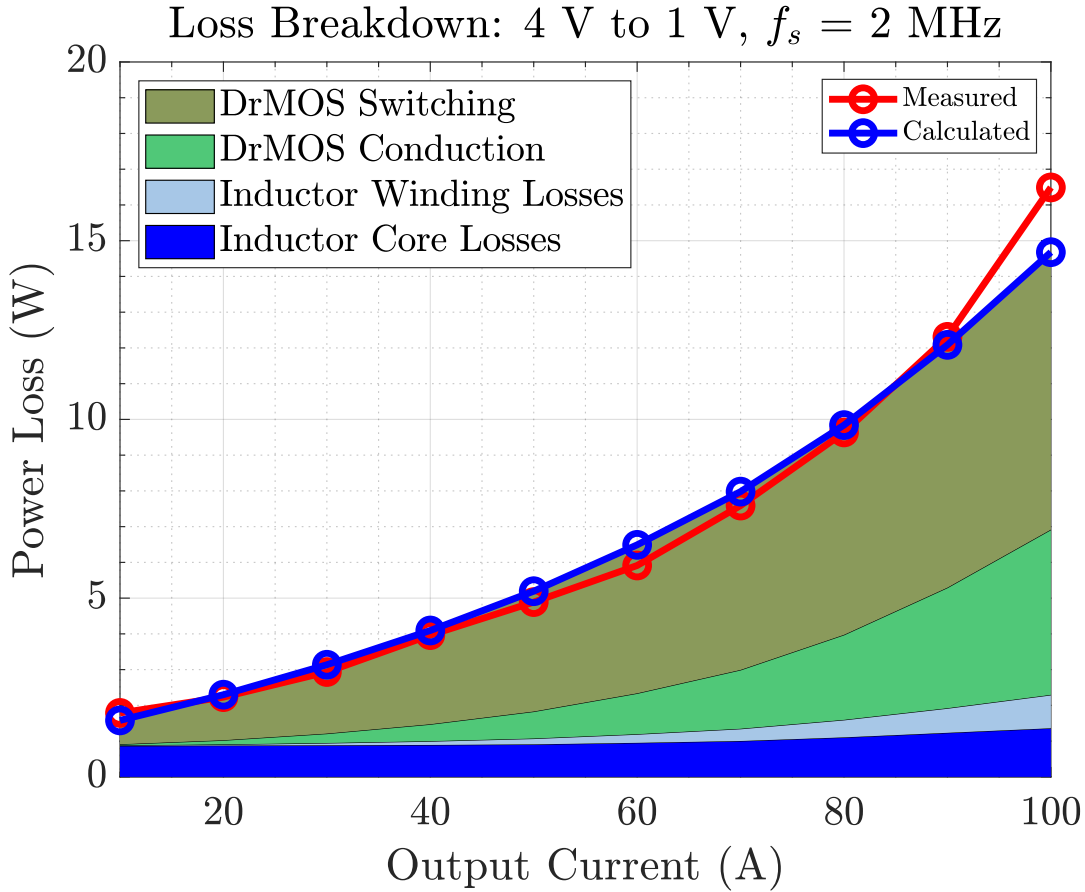


Figure 3.24: Loss breakdown for the four-phase buck VRM with the pinwheel coupled inductor (design 1). Measured and calculated values are compared. DrMOS switching and conduction losses dominate the total system loss, while inductor losses remain minimal due to low dc resistance and vertically integrated layout.

or better efficiency while maintaining superior transient behavior, thanks to its low leakage inductance.

Between the two pinwheel designs, the extended variant (design #2) consistently delivers higher efficiency. This advantage is attributed to its larger cross-sectional area for windings, improved copper utilization, and better flux path distribution due to enhanced 3D geometry. These attributes reduce both copper and core losses, justifying the slight increase in volume.

Figure 3.24 shows a breakdown of the major power loss components in the VRM system using the pinwheel coupled inductor (design1). As expected, DrMOS devices contribute the majority of total power loss due to significant switching losses at 2MHz.

Winding losses are minimized by the inductor’s vertical straight-through conductor layout, resulting in low dc resistance – 0.09 mΩ per phase for design #1 and 0.12 mΩ for design #2. However, the compact design and higher flux concentration increase magnetic core losses. At 55 A load, core loss alone accounts for a 1.4% drop in peak efficiency. This trade-off underscores the design tension between ultra-low profile and magnetic efficiency. Thinner form factors push flux density higher, increasing core losses unless compensated with advanced magnetic design.

These results emphasize the importance of accurate core loss modeling – especially in geometrically complex, non-uniform flux structures like coupled inductors. Traditional estimation techniques may not capture localized saturation or hysteresis behaviors. Thus, geometry-aware and data-driven modeling methods – such as those discussed in [67] – will be critical to future optimization of compact, high-efficiency magnetics for power delivery applications.

3.4.3 Converter Transient Performance

To evaluate the transient performance of the system, open-loop step response tests were conducted on three configurations: the pinwheel coupled inductor VRM (design #1), the extended pinwheel coupled inductor VRM (design #2), and the four-phase VRM utilizing 100 nH discrete inductors. A synchronized common-mode duty cycle step \tilde{d} was applied simultaneously to all four phases, and the corresponding output voltage change \tilde{v}_o was measured to assess the system’s dynamic response. The resulting small-signal transfer function, $G_{vd} = \tilde{v}_o/\tilde{d}$, characterizes the impact of the inductor’s effective leakage inductance on transient behavior, as lower L_ℓ typically yields faster voltage settling [68, 69].

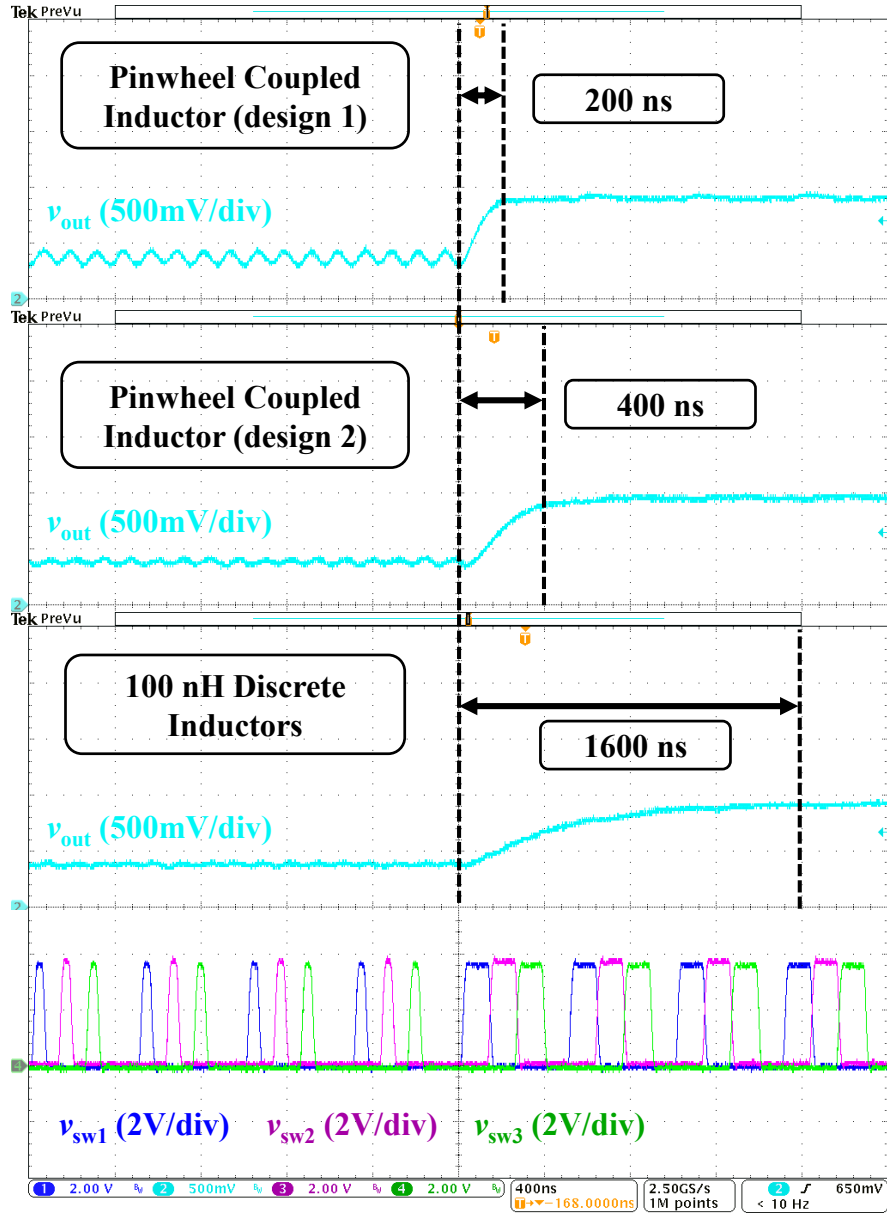


Figure 3.25: Output voltage response to a common-mode duty cycle step from 10% to 25% at $V_{in} = 4$ V and $f_s = 2$ MHz. From top to bottom: the pinwheel coupled inductor (design #1) settles within 200 ns; the extended pinwheel coupled inductor (design #2) settles within 400 ns; the VRM with 100 nH discrete inductors requires approximately 1600 ns to reach its new steady state.

All three configurations were tested under identical passive and load conditions to ensure comparability. The output stage included 22 units of Kemet 0805 C0G capacitors (47 nF, 10 V), totaling 1.13 μ F of ceramic output capacitance. A 50 m Ω

resistive load was implemented using twenty parallel $1\ \Omega$, $1\ \text{W}$, 1% 1206 chip resistors. The applied duty cycle was stepped from 10% to 25%, which shifted the converter's output voltage from 0.4 V to 1 V, and the corresponding load current from 8 A to 20 A, assuming continuous conduction mode at $V_{in} = 4\ \text{V}$ and $f_s = 2\ \text{MHz}$.

The measured results are shown in Fig. 3.25, displaying the output voltage response and three representative switch node waveforms for each configuration. The VRM with design #1 settles within 2% of the new voltage level in just 200 ns. Design #2 follows closely, settling within 400 ns. In comparison, the system using discrete 100 nH inductors takes roughly 1600 ns to reach the same settling threshold.

These results demonstrate an $8\times$ improvement in transient speed for design #1 and a $4\times$ improvement for design #2 relative to the discrete inductor baseline. While the observed settling times do not exactly match theoretical predictions based on L_ℓ , such discrepancies are attributed to small variations in the effective output capacitance across test samples, which can arise from the tolerance spread inherent to multilayer ceramic capacitors.

In summary, these measurements validate a critical advantage of the proposed vertically integrated multiphase coupled inductor structures: they enable fast dynamic response through low leakage inductance, without sacrificing steady-state ripple suppression. This dual benefit makes the design well suited for next-generation voltage regulators that must simultaneously meet stringent efficiency and transient regulation demands under fast load transitions.

3.4.4 Tolerance to Dc Current Imbalance

In the extended $9\times 9\ \text{mm}^2$ pinwheel inductor design, particular emphasis was placed on verifying its resilience to dc current imbalance across phases – a common real-world scenario in multiphase voltage regulators. Ideally, multiphase coupled inductors achieve nearly complete dc flux cancellation when phase currents are balanced

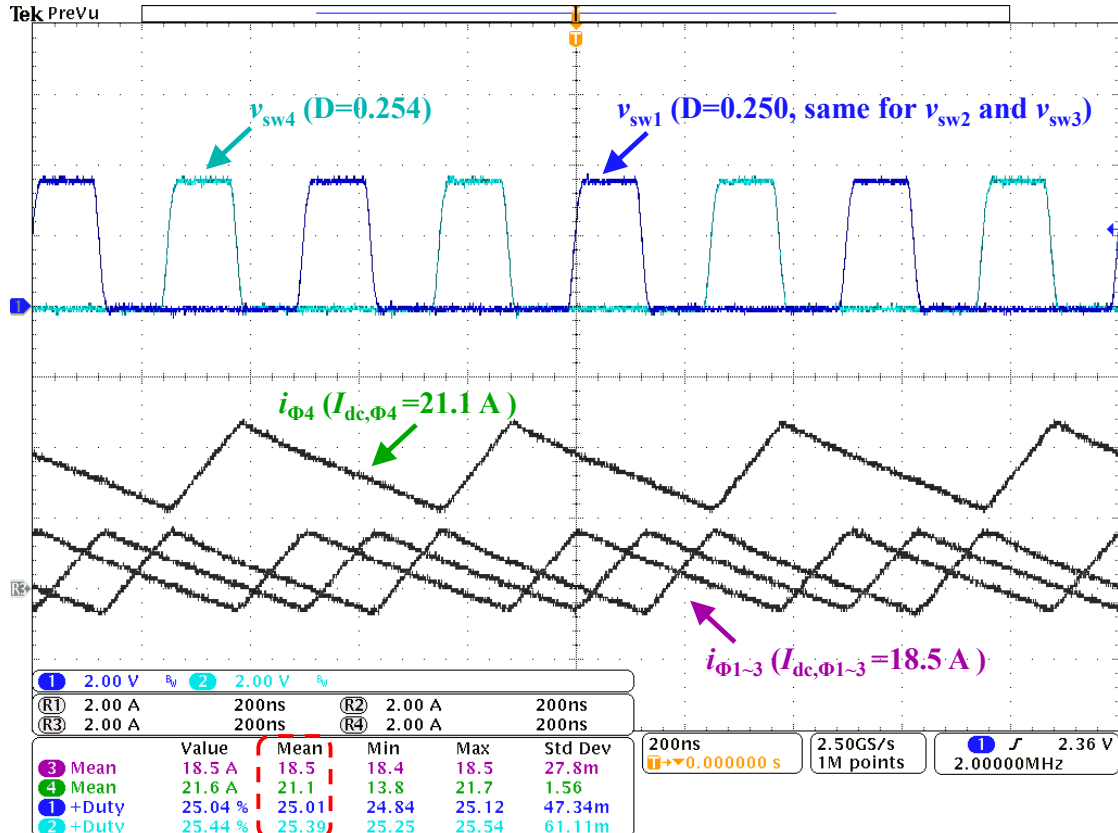


Figure 3.26: Current waveforms and corresponding switch node voltages for the four-phase buck VRM under intentional duty cycle mismatch. Phase 4 operates at a duty ratio of 25.4% with a measured dc current of 21.1 A, while the other three phases operate at nominal 25% duty ratio with approximately 18.5 A dc current. Despite an approximately 13% current imbalance, all four phases exhibit clean, undistorted current waveforms, indicating that the magnetic core remains unsaturated and maintains linear behavior.

and interleaved. However, in practical systems, control imperfections, PCB layout asymmetries, or transient disturbances can introduce non-negligible mismatches in current sharing, which may lead to residual net flux buildup in the magnetic core.

This residual flux increases localized flux density and can push specific regions of the core toward or into saturation. In such cases, the self-inductance of the overloaded phase tends to drop significantly, and core loss increases due to elevated hysteresis and eddy current effects. Consequently, both efficiency and regulation performance

may suffer. Therefore, ensuring robust tolerance to such imbalance is essential for the safe and reliable operation of coupled inductors in high-current applications.

To experimentally assess this behavior, a controlled duty cycle deviation was introduced in one phase of the four-phase buck converter. Specifically, the duty ratio of phase 4 was incremented from the nominal 25% to 25.4%, while the remaining three phases retained a nominal 25% setting. Given the fixed input and output voltages, this small change results in a measurable increase in average current through phase 4 relative to the others.

As shown in Fig. 3.26, the measured phase currents indicate a dc current of approximately 21.1 A through phase 4, compared to 18.5 A through each of the remaining phases – amounting to a 13% current mismatch. Despite this imbalance, all four phases exhibit well-formed triangular current waveforms with no discontinuities, distortion, or waveform clipping. Likewise, the switch node voltages remain clean and periodic. These results confirm that the magnetic core stays well below its saturation threshold under this imbalance scenario, and retains linear behavior.

Due to thermal constraints of the DrMOS components in the test platform, experiments could not be extended to larger imbalance levels (e.g., $40\text{ A} \pm 10\%$) without exceeding safe temperature limits. Nevertheless, the results provide a strong indication that the extended pinwheel design offers substantial headroom against core saturation and can maintain stable operation under realistic load mismatches.

In practical systems, perfect current sharing is difficult to maintain continuously. Inductor designs that only perform well under balanced excitation may exhibit dramatic performance degradation under modest mismatch, posing risks in dynamic or fault-tolerant environments. The demonstrated robustness of the proposed vertically coupled inductor structure against dc current imbalance supports its deployment in high-performance, high-reliability multiphase VRMs.

Table 3.5: Performance Comparison between Coupled and Discrete VRM Implementation (Operating Condition: 4 V-to-1 V, and $f_s = 2$ MHz)

Inductor	Efficiency		Density		L_ℓ
	Peak	Full Load	Area	Volume	
Pinwheel #1 Coupled	91.5% @ 55 A	85.9% @ 100 A	0.83 A/mm ²	3760 W/in ³	26.5 nH
Pinwheel #2 Coupled	93.5% @ 25 A	85.4% @ 120 A	1.00 A/mm ²	3960 W/in ³	17.4 nH
22 nH Discrete	86.2% @ 60 A	85.2% @ 80 A	0.67 A/mm ²	1930 W/in ³	22 nH
100 nH Discrete	93.2% @ 40 A	87% @ 90 A	0.75 A/mm ²	2180 W/in ³	100 nH

3.5 Chapter Summary

3.5.1 Performance Benchmarking

As shown in Table 3.5, the coupled inductor designs provide a comprehensive performance advantage across key metrics. While maintaining the same or slightly increased lateral footprint, they reduce total system height by over 30% and boost power density, demonstrating the effectiveness of 3D magnetic integration.

In transient behavior, the coupled inductors achieve sub-500 ns settling times – representing 4× to 8× improvement over the discrete implementations. This stems from the low leakage inductance characteristic of coupled structures, which directly enhances transient bandwidth without sacrificing steady-state inductance or increasing ripple.

The efficiency comparison highlights another dimension of benefit. Despite their compact vertical form factor and added inter-phase coupling, both coupled inductor variants match or exceed the peak efficiency of the discrete 100 nH design, while offering significantly improved thermal headroom and supporting higher peak current operation.

Table 3.6: Comparison of the Pinwheel Coupled Inductor Against Other Magnetics Solutions for VRMs

Year	Inductor Reference	Size			Inductance		Winding Resistance	Phase Current*	Phase Count	Operation Frequency
		Length	Width	Height	Inductance Density	$\gamma _{D=0.25} \dagger$				
This Work	Pinwheel Design #1	8 mm	8 mm	1.8 mm	6.56 $\frac{\text{nH}}{\text{mm}^3}$	0.107	0.09 mΩ	25 A	4	2 MHz
This Work	Pinwheel Design #2	9 mm	9 mm	2.5 mm	2.47 $\frac{\text{nH}}{\text{mm}^3}$	0.108	0.12 mΩ	40 A	4	2 MHz
2022	Integrated Series Asymmetrical [70]	5.21 mm	3.36 mm	0.54 mm	9.7 $\frac{\text{nH}}{\text{mm}^3}$	0.521	3.1 mΩ	3 A	4	20 MHz
2023	LC Two-Phase [71]	8 mm	14 mm	1.3 mm	0.82 $\frac{\text{nH}}{\text{mm}^3}$	0.580	0.15 mΩ	25 A	2	1.6 MHz
2024	MSC-PoL [72]	28.9 mm	13 mm	3.9 mm	1.67 $\frac{\text{nH}}{\text{mm}^3}$	0.126	0.06 mΩ	28.1 A	4	400 kHz
2024	Mini-LEGO [58]	8 mm	8 mm	2.5 mm	7.93 $\frac{\text{nH}}{\text{mm}^3}$	0.025	0.185 mΩ	20 A	4	1.5 MHz
2024	Switching Bus [73]	18 mm	5 mm	5 mm	4.62 $\frac{\text{nH}}{\text{mm}^3}$	0.331	0.48 mΩ	31.3 A	2	150 kHz
2024	Twisted Core [61]	9.3 mm	8.6 mm	2 mm	0.98 $\frac{\text{nH}}{\text{mm}^3}$	0.436	0.03 mΩ	65 A	2	1.5 MHz

† Inductance density is calculated using the sum of the self inductances of all of the phases divided by the overall box volume of the inductor: $\Sigma_i (L_{S,i}) / l \times w \times h$.

‡ $\gamma|_{D=0.25}$ is equal to the per-phase leakage inductance over the per-phase steady state inductance evaluated at D=0.25: $L_\ell / (L_{pss}|_{D=0.25})$. A lower number indicates higher magnetic coupling.

* The per-phase current denotes the maximum phase current that was experimentally achieved in the testing of the inductor.

Importantly, the extended design (design #2) validates the scalability of the pinwheel topology. With only marginal increases in footprint and height, it delivers higher current capability, better thermal distribution, and improved efficiency, without compromising manufacturability.

In conclusion, these results establish the vertical multiphase coupled inductor as a high-performance, compact, and scalable solution for emerging VRM applications. Its combination of high efficiency, fast dynamics, excellent tolerance to imbalance, and structural simplicity makes it a strong candidate for next-generation power delivery in space-constrained and performance-critical environments such as AI accelerators and high-end GPUs.

Additionally, the pinwheel coupled inductors are benchmarked against a broad set of state-of-the-art magnetic integration solutions for VRMs, as summarized in Table 3.6. These include integrated magnetics, coupled inductor arrays, and fully embedded power stages reported in recent literature. While each prior work offers specific trade-offs tailored to distinct application constraints, the pinwheel structures

introduced in this thesis demonstrate consistently strong performance across multiple critical metrics.

Targeting the demanding regime of high-current and high-frequency operation (typically 100 kHz to 5 MHz), the proposed inductors achieve among the smallest magnetic volumes reported, while supporting one of the highest switching frequencies. This is enabled by the vertical via-winding structure and compact pinwheel magnetic geometry, which allow dense magnetic integration without compromising thermal or electrical performance.

Both designs exhibit high inductance density and strong interphase coupling, resulting in significantly enhanced steady-state inductance compared to the individual winding self-inductance. The ratio $\gamma|_{D=0.25} = L_{pss}/L_\ell$ reaches 0.107 and 0.108 for design #1 and design #2, respectively – indicating a 10× increase in ripple attenuation relative to using discrete inductors with equivalent leakage. This confirms the ability of multiphase coupling to suppress ripple without degrading transient response. Furthermore, the measured dc resistance values of 0.09 mΩ and 0.12 mΩ are among the lowest reported, achieved through direct vertical windings with optimized copper cross-sections, which effectively minimize conduction losses at high load.

Through this benchmarking, the two designs – optimized for compact ($8 \times 8 \text{ mm}^2$) and high-current ($9 \times 9 \text{ mm}^2$) operation – are shown to deliver competitive or superior performance in terms of efficiency, ripple suppression, dynamic response, and volumetric utilization. More importantly, they validate the pinwheel-based ultra-thin coupled inductor architecture as a compelling approach for next-generation VRMs. Building upon prior concepts in [59, 61], the proposed structures provide a scalable solution with low profile, high current capability, and reduced loss – characteristics essential for future vertically integrated power delivery systems in advanced computing platforms.

3.5.2 Conclusion

This chapter presents the concept of via-winding magnetics through the development of the pinwheel coupled inductor – an ultra-thin, high-performance multiphase magnetic structure tailored for vertical power delivery in modern VRMs. A quantized magnetic design methodology and systematic optimization framework were introduced to enable compact, high-current coupled inductor implementations with strong interphase coupling and minimal vertical profile.

Two prototypes were demonstrated: an $8 \times 8 \text{ mm}^2$, 1.8 mm-high version supporting up to 100 A, and a $9 \times 9 \text{ mm}^2$, 2.5 mm-high variant capable of 160 A. Integrated into four-phase buck VRMs operating at 2 MHz, the proposed inductors achieved up to 93.5% peak efficiency, 1.00 A/mm² current density, and 3,960 W/in³ power density – while maintaining sub-400 ns transient settling and robust tolerance to over 10% dc current imbalance. These results demonstrate the effectiveness of the pinwheel architecture in balancing ripple suppression, dynamic response, and thermal reliability within a compact form factor.

Overall, the vertical via-winding structure offers a promising path forward for scalable, low-profile magnetic integration in next-generation high-power computing platforms employing 3D heterogeneous packaging and vertically stacked VRMs.

Related Publications

1. **H. Li**, Y. Elasser, *et al.*, “**Via-Winding Magnetics: Optimal Design for Ultra-Thin Multiphase Coupled Inductors for Vertical Power Delivery**,” *TechRxiv*, June 2025.
2. Y. Elasser, **H. Li**, P. Wang, *et al.*, “**Circuits and magnetics co-design for ultra-thin vertical power delivery: A snapshot review**,” *MRS Advances*, vol. 9, pp. 12–24, Dec. 2023.

Chapter 4

Air-LEGO: Air-Coupled Inductors for Ultra-thin Power Delivery

4.1 Background and Motivation

In the preceding chapters, we have explored the modeling of magnetic materials and the design of vertically integrated coupled inductors, both of which aim to address the pressing challenges of integrating magnetics into high-density power delivery systems. These solutions, while effective, still fundamentally rely on the presence of magnetic core materials, which impose constraints in terms of size, thermal limits, and loss mechanisms. An alternative and increasingly attractive direction is to eliminate magnetic cores entirely and instead utilize air-coupled inductors. This chapter delves into such an approach and investigates the design, implementation, and validation of a magnetic-free voltage regulation module (VRM) architecture.

Driven by the relentless demand for computational performance in CPUs and GPUs, modern power delivery systems must deliver high current at low voltages within ever-tightening spatial constraints. These requirements stretch the capabilities of conventional VRMs, which typically rely on ferrite-core inductors. Fig. 4.1 illustrates one such emerging concept: an ultra-thin Air-LEGO VRM designed to fit directly into a CPU or GPU package, maintaining a total system height below 3 mm.

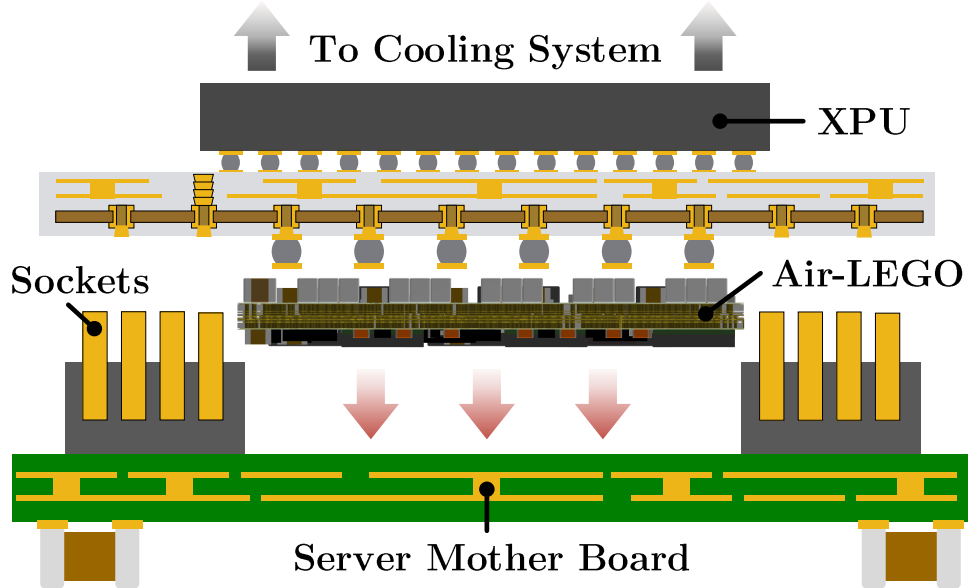


Figure 4.1: Ultra-thin Air-LEGO VRM embedded into a CPU or GPU package for compact in-package integration. The air-coupled inductor enables a system height under 3 mm while mitigating thermal constraints.

This compact design not only satisfies form-factor requirements but also relaxes thermal constraints by eliminating core losses entirely.

Magnetic-core inductors, while traditionally central to VRM functionality, present significant limitations in advanced packaging. These include high core losses, limited thermal tolerance, and relatively bulky dimensions, all of which hinder integration and reliability [2, 57, 58]. Magnetic materials are especially vulnerable to temperature variations, often experiencing performance degradation or failure beyond 100°C, while modern semiconductors routinely operate at temperatures exceeding several hundred degrees Celsius [74]. Core-dependent properties like permeability and hysteresis losses vary significantly with operating conditions, further complicating the co-design of power, thermal, and mechanical aspects in compact systems.

In contrast, air-core inductors offer complete immunity to such thermal instabilities. Without saturation, hysteresis, or frequency limitations inherent to magnetic cores, air-core designs can support operation at very high frequencies with excellent

thermal performance [1, 75]. This not only simplifies thermal management but also opens new opportunities in packaging flexibility, especially for applications where vertical stacking and thin form factors are paramount.

Furthermore, air-core inductors are particularly well-suited for multiphase configurations. Their open magnetic path allows magnetic field cancellation through proper interleaving and placement of adjacent phases, leading to reduced ac losses, diminished ripple currents, and improved transient response [62, 66]. Designs such as origami inductors have demonstrated the benefits of flux cancellation and enhanced dynamics even without the assistance of magnetic cores.

This chapter introduces and evaluates the Air-LEGO architecture, an ultra-thin, magnetic-free VRM operating at high switching frequencies. The converter utilizes air-coupled inductors arranged in a modular and extendable structure to achieve a low-profile solution suitable for in-package integration. Through analytical modeling, finite element simulation, and experimental validation, we demonstrate the feasibility and benefits of air-core solutions while addressing the key design challenges they introduce.

- The design and realization of an ultra-thin air-core VRM module that meets the demanding current and voltage requirements of high-performance computing;
- Analysis of the performance trade-offs between different winding configurations and their impact on loss mechanisms and EMI;
- Experimental verification of the proposed architecture in a high step-down application, validating the practical viability of air-core inductors for future-generation power delivery.

The rest of this chapter is organized as follows: Section 4.2 introduces the circuit topology and operating principles of the Air-LEGO architecture. Section 4.3 discusses the design considerations and simulation results of air-coupled inductors.

Section 4.4 presents the experimental results of the Air-LEGO prototype, highlighting both the feasibility and limitations of adopting air-coupled inductors in practical VRM applications. Finally, Section 4.5 summarizes the findings and insights of this chapter.

4.2 LEGO Architecture and Operation Principles

The Air-LEGO voltage regulator module (VRM) adopts the Linear-Extendable Group Operated (LEGO) framework [57, 76], as shown in Fig. 4.2. This architecture is characterized by a series-connected input stage and a parallel-connected output stage, making it particularly advantageous for high-current applications that demand large voltage step-down ratios. The LEGO system is composed of two major components: a front-end 2:1 switched-capacitor (SC) array configured in a series-stacked manner, and a backend multi-phase buck stage employing coupled inductors.

In the Air-LEGO implementation, the first stage takes an input of 24 V and steps it down to three 4 V intermediate voltages through three series-stacked 2:1 SC submodules. This stacked configuration ensures equal voltage sharing among the submodules, reduces the voltage stress on each unit, and allows for the use of lower-voltage-rated components. As a result, the reliability of the system is enhanced, and the component selection is simplified.

The second conversion stage is responsible for further stepping down each 4 V intermediate node to the target output, such as 1 V. This is achieved through three buck converter submodules, each implementing two interleaved phases. The duty cycle for each phase is approximately 25%, which allows for high current capability and helps suppress output voltage ripple. The interleaving of the two phases in each submodule promotes thermal distribution, minimizes electromagnetic interference (EMI), and enhances the overall power delivery efficiency. Each individual phase can deliver up to 20 A, allowing the full system to supply a total of 120 A output current.

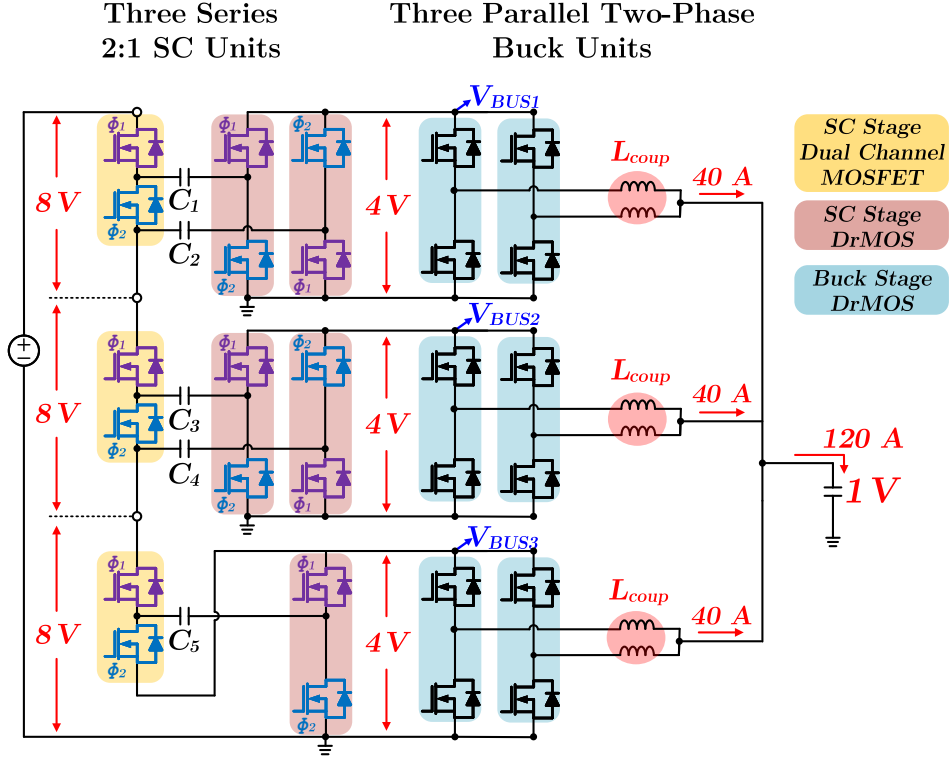


Figure 4.2: Principles of LEGO architecture, consisting of three series-stacked switched-capacitor submodules and three paralleled multi-phase buck submodules with coupled inductors. LEGO architecture provides large voltage conversion ratio and high current capacity with reduced switch stress for high current VRM applications.

The modular and scalable design of the LEGO architecture also enables easy adaptation to varying power requirements. By adding more series-stacked SC units or parallel buck submodules, the system can be extended to support a wider range of input-output conversion ratios or increased current demands, providing flexibility for various power delivery applications in modern computing platforms.

The gate-driving method for the LEGO architecture is illustrated in Fig. 4.3. The 2:1 SC units operate at relatively low frequency (on the order of hundreds of kHz), using two gate signals (ϕ_1 and ϕ_2) that alternate with a 50% duty cycle and 180° phase shift. This low-frequency operation reduces switching losses in the SC stage. In contrast, the buck stage operates at a much higher frequency with interleaved

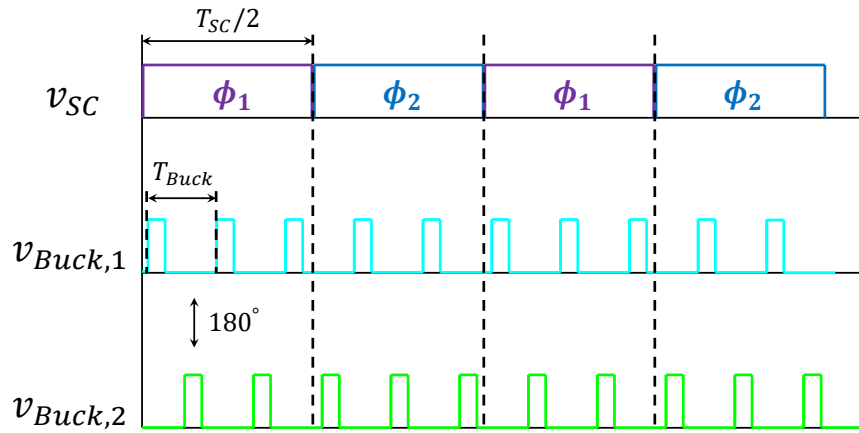


Figure 4.3: Theoretical gate drive modulation strategy of LEGO architecture. The switched-capacitor unit is driven by low frequency 50% duty ratio square waves with 180° phase difference. The two-phase buck unit is driven by a higher frequency sequence with desired duty ratio, where two phases are 180° interleaved. Soft-charging of capacitors, zero-current switching of SC unit, and phase current balancing through phase rotation are achieved.

control between its two phases, which helps suppress output ripple and improves transient response and control bandwidth.

An important innovation of this architecture lies in the seamless integration of the SC and buck stages. Unlike traditional two-stage converters, there is no need for either a resonant inductor in the SC stage or a bulky decoupling capacitor between stages. The SC and buck units work in tandem: the buck stages behave like programmable current sources that softly charge the capacitors in the SC units. The capacitors are dynamically charged and discharged by the current supplied from the buck stages. By carefully synchronizing the gate drive signals, the inductor current from the buck stage flows through the SC network only when the high-side switches are on. This coordinated timing ensures that the switching of SC transistors happens during the zero-current periods, achieving Zero-Current Switching (ZCS) and thereby minimizing switching losses in the SC stage.

To further enhance system-level efficiency and robustness, the architecture also incorporates automatic current balancing among buck phases. The absence of a large dc-link capacitor leads to greater ripple in the intermediate voltages, which may cause phase current imbalance. To address this, a passive phase-rotation mechanism is used [57]. If the switching frequency of the buck stage satisfies:

$$f_{Buck} = (2k + 1) \cdot f_{SC}, \quad k = 1, 2, 3\dots \quad (4.1)$$

where f_{Buck} and f_{SC} denote the switching frequencies of the buck and SC stages, respectively, the buck phase switches cycle through different positions within the SC switching period. As an example, if $f_{Buck} = 5f_{SC}$, then five buck switching events occur per SC cycle, enabling each phase to encounter a different portion of the intermediate bus ripple. This dynamic phase rotation ensures balanced average input conditions across the phases and promotes even current sharing, improving performance and reducing thermal stress.

4.3 Air-Coupled Inductor Design

Designing the air-coupled inductors used in the Air-LEGO architecture involves careful optimization of winding geometry to achieve an effective balance among self-inductance, mutual inductance, and winding resistance. As illustrated in Fig. 4.4, the basic structure of the two-phase air-core inductor includes two turns per phase and is defined by three key parameters: l_1 , l_2 , and l_3 . These dimensions collectively determine the inductor's electromagnetic performance. The region defined by the product $l_2 \times l_3$ determines the area of overlap between the two phases, which directly influences the mutual coupling coefficient. Higher coupling improves ripple cancellation and energy transfer but can also introduce parasitic coupling effects. The segment represented by l_1 is primarily decoupled and contributes to the self-inductance, of-

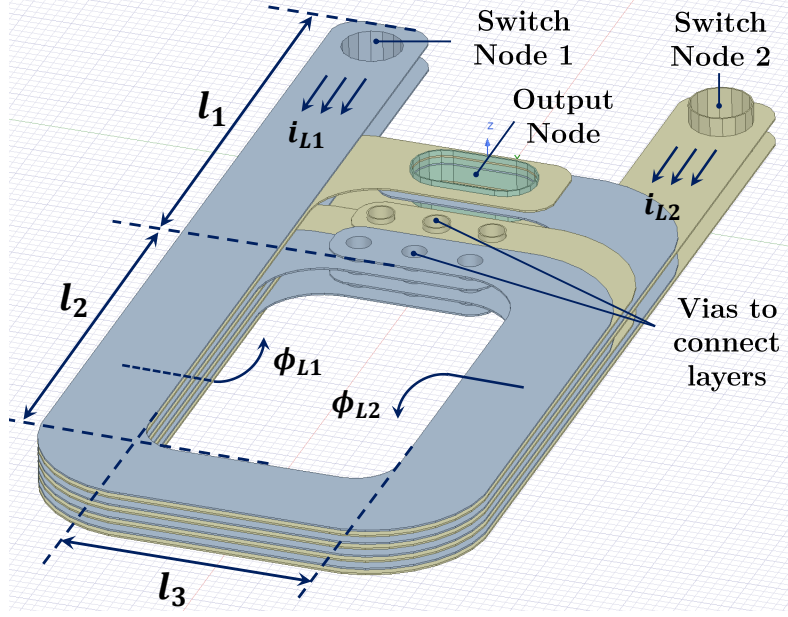


Figure 4.4: Basic geometry of the two-phase air-coupled inductor. Three parameters need to be determined, where the coupling factor between two phases is mostly determined by l_2 and l_3 , while l_1 provides additional self-inductance.

fering design flexibility. In contrast, l_3 is constrained by the spatial footprint of the power components and cannot be significantly modified without impacting layout. Therefore, tuning l_1 and l_2 becomes essential in optimizing the inductor design for performance and efficiency. To explore this design space, extensive simulations were performed, sweeping l_1 and l_2 values to evaluate resulting changes in self-inductance, mutual inductance, and dc resistance. The results are summarized in Fig. 4.5.

From the parameter sweep results, an optimal geometry was selected with l_1 set to 12 mm and l_2 set to 8 mm. This configuration achieves a practical trade-off by delivering sufficient self-inductance and coupling, while maintaining manageable winding resistance and enabling overall system performance.

For designs using PCB windings, implementing layer interleaving is an essential strategy to combat frequency-dependent losses such as the skin and proximity effects [5]. Figure 4.6 shows the simulated current density in an 8-layer PCB with and without interleaving. The interleaved layout demonstrates a significantly lower ac

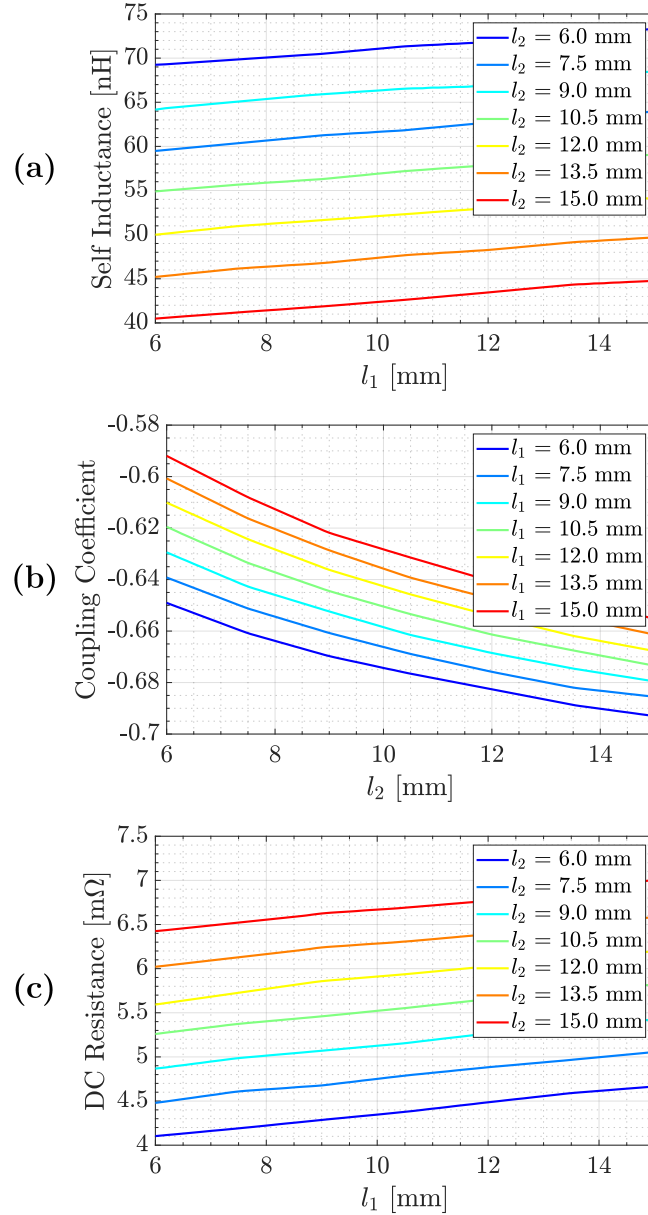


Figure 4.5: Simulation results with parameter sweeping for different l_1 and l_2 combinations: (a) self inductance per phase; (b) coupling coefficient between phases; and (c) Dc resistance per phase.

resistance (R_{ac}), as the current distribution becomes more uniform across layers. In comparison, the non-interleaved structure suffers from severe crowding effects, leading to an ac resistance approximately 2.25 times higher. Interleaving reduces these losses, contributing directly to improved efficiency.

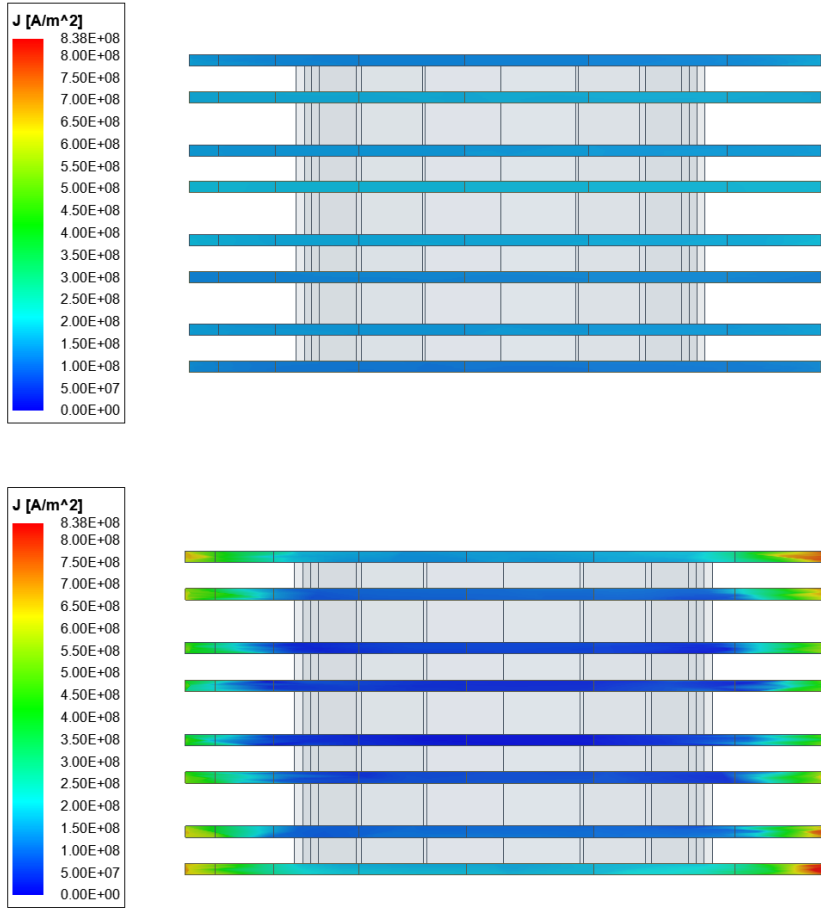


Figure 4.6: Simulated current density distributions for interleaved structure (top) and non-interleaved structure (bottom), where interleaving greatly mitigates the skin effect and proximity effect, and reduces the winding ac resistance.

In addition to reducing losses, interleaving also plays a significant role in limiting fringing magnetic fields. Air-core inductors inherently pose challenges in terms of EMI due to unconfined stray flux. However, by carefully arranging conductors in an interleaved pattern, opposing magnetic fields can partially cancel each other. As shown in Fig. 4.7, this cancellation effect confines most of the flux to the vicinity of the winding plane, reducing electromagnetic emissions. This is particularly advantageous in compact, high-density VRMs where EMI compliance is a critical concern. The use of interleaving thus not only boosts efficiency but also improves system compatibility.

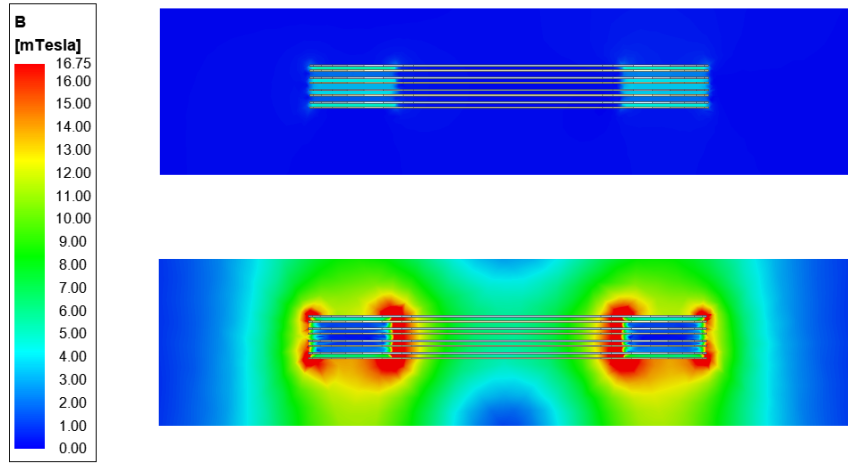


Figure 4.7: Simulated flux density distributions for interleaved structure (top) and non-interleaved structure (bottom), where interleaving effectively minimizes fringing flux and confines it around the winding plane.

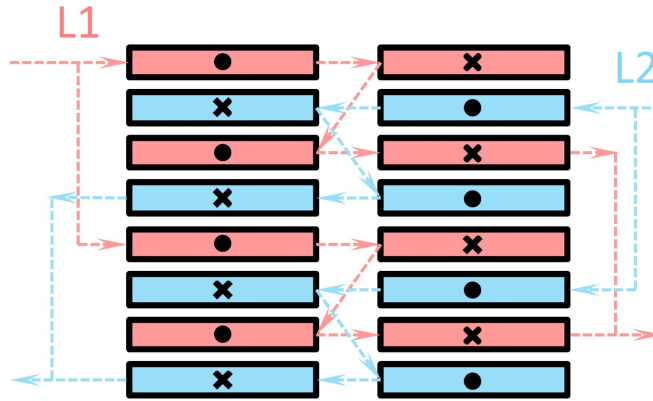


Figure 4.8: The interleaved winding structure in this design, where each phase contains two sets of parallel windings, and the two phases are fully interleaved in an 8-layer PCB stack.

Additional magnetic shielding sheets can also be applied to further suppress stray fields and enhance EMI performance.

The chosen interleaving structure is shown in Fig. 4.8, where each phase consists of two parallel winding sets and is fully interleaved with the opposite phase across an 8-layer PCB stack. This approach enhances coupling, reduces both dc and ac resistance,

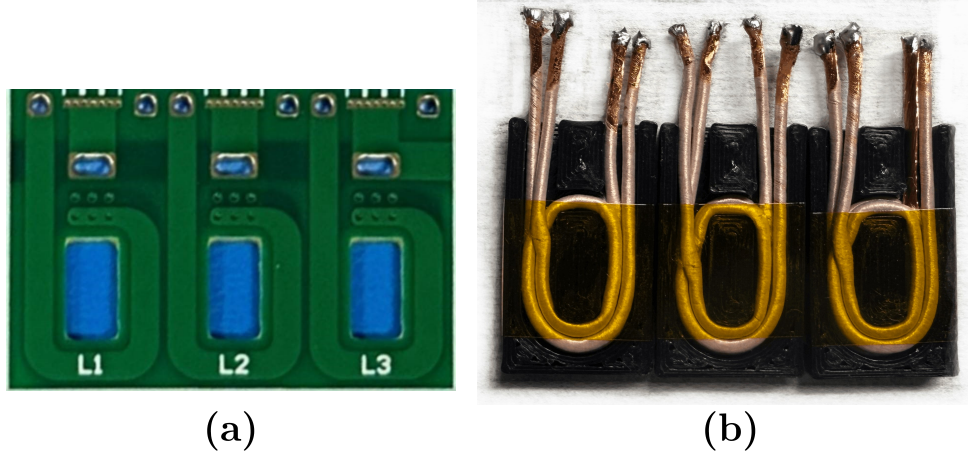


Figure 4.9: Pictures of the air-coupled inductors: (a) PCB traces as windings; (b) Litz-wire as windings.

Table 4.1: Comparison of PCB-winding inductor and Litz-wire inductor.

Winding Type	R_{dc} [mΩ]	R_{ac} [mΩ] @2MHz	L_s [nH]	L_m [nH]
PCB Traces	4.46	17.9	47.56	-27.83
Litz Wire	3.51	11.8	60.21	-34.85

and minimizes EMI as discussed. Importantly, the added parasitic capacitance from such interleaving did not introduce observable issues in practical testing.

For Litz-wire inductors, a similar geometry was employed to match the PCB counterpart in terms of dimensions and electromagnetic characteristics. The selected wire bundle has a thickness close to that of the PCB stack, helping preserve the converter’s low-profile mechanical design. A custom bobbin and frame were fabricated to hold the Litz windings in place, ensuring good alignment and consistent inductance.

As depicted in Fig. 4.9, the final inductor designs include both PCB-based and Litz-wire implementations. The PCB version uses a pair of 8-layer PCBs with 1 oz copper, producing a combined thickness of 2.1 mm. The Litz-wire version is composed of 300 strands of 46 AWG wires, pressed to a similar total thickness. The comparison table (Table 4.1) summarizes key electrical parameters. While PCB windings support better manufacturability and integration, the Litz version shows lower ac resistance

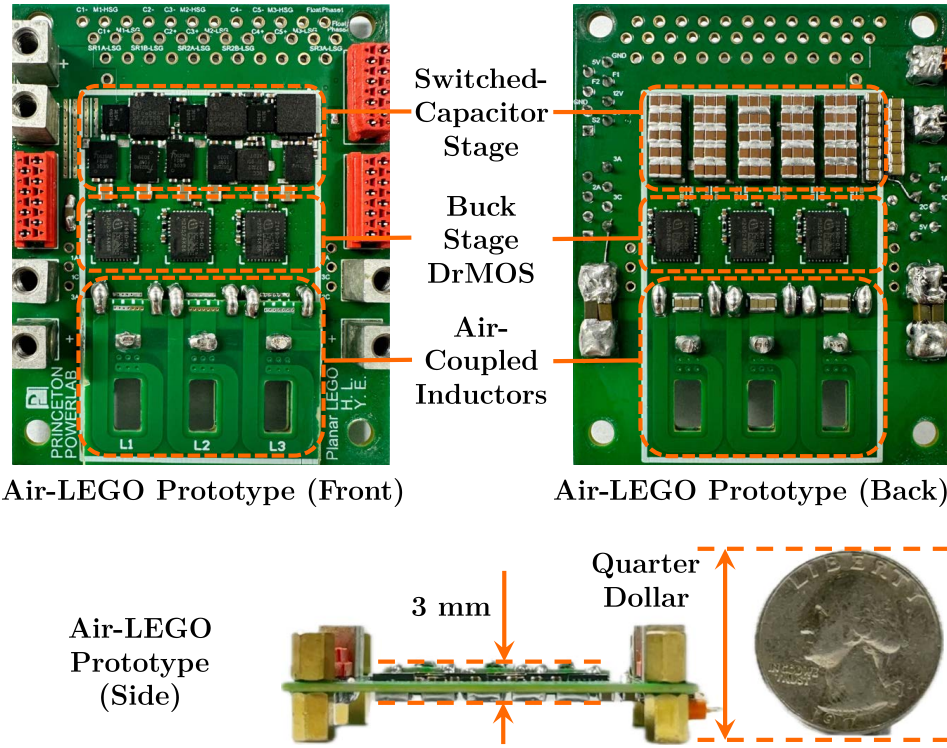


Figure 4.10: Pictures of the Air-LEGO prototype (with PCB-trace inductors) from front, back, and side views, achieving a low profile of 3 mm.

and superior high-frequency efficiency. Consequently, the decision between the two options depends on application priorities – space and consistency versus performance and loss minimization. Both designs demonstrate the importance of careful magnetic layout and integration in advanced VRMs.

4.4 Experimental Results

To verify the practicality and performance of the Air-LEGO converter, a fully assembled prototype was developed and subjected to comprehensive testing. In the switched-capacitor (SC) stage, the floating switches are realized using Onsemi NT-TFD2D8N03P1E dual-channel MOSFETs, driven by Infineon 2EDF7275K isolated gate drivers. To supply the required gate voltage for the floating switches, a TI UCC27212 charge pump is employed. The remaining switches in the SC stage utilize



Figure 4.11: Pictures of the testing platform, including dc power supplies, electronic loads, digital multimeters with current shunts for power measurement, and an oscilloscope.

Onsemi FDMF3039 DrMOS modules, selected for their compact integration and efficiency. All buck-stage switches are implemented using Infineon TDA21490 DrMOS modules, known for supporting high-frequency operation and low conduction losses. The SC and buck stages operate at switching frequencies of 400 kHz and 2 MHz, respectively.

Figure 4.10 displays the completed prototype using PCB-based inductors. The image highlights the compact and flat integration of the air-coupled inductors, which contribute significantly to the converter's thin profile. The air-core design not only removes the thermal constraints typically imposed by magnetic cores but also introduces design flexibility. Additionally, a second prototype with Litz-wire inductors was

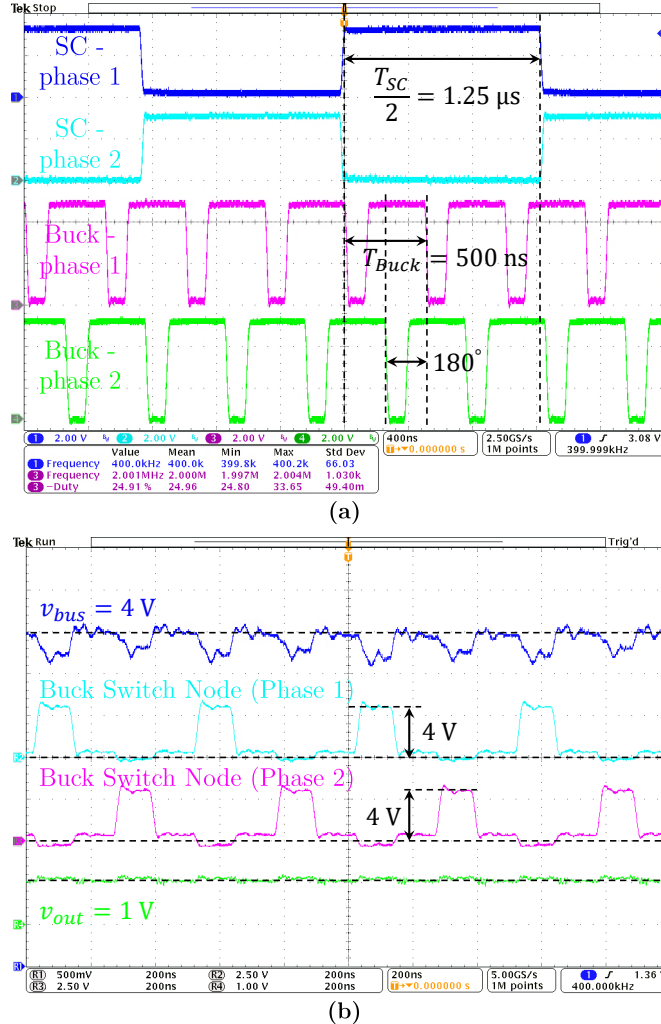


Figure 4.12: Key experimental waveforms of the Air-LEGO prototype: (a) switched-capacitor stage 400 kHz gate drive signals, with 50% duty ratio and 180° phase shift; 2 MHz two-phase gate drive signals for one of the buck submodules, with 180° phase interleaving. (b) 4 V intermediate bus voltage, two-phase interleaved buck stage switch node voltage, and 1 V output voltage.

fabricated using the same overall design. The interface compatibility between the two types of inductors allows direct performance comparison under identical conditions.

The testing platform setup is shown in Fig. 4.11, featuring a dc power supply, electronic load, precision shunt-based multimeters for power monitoring, and an oscilloscope for waveform analysis. During the evaluation, cooling was provided using a single dc fan without any heat sink, demonstrating the converter's inherent thermal efficiency. The flat inductor design enables direct attachment of a heat sink, which

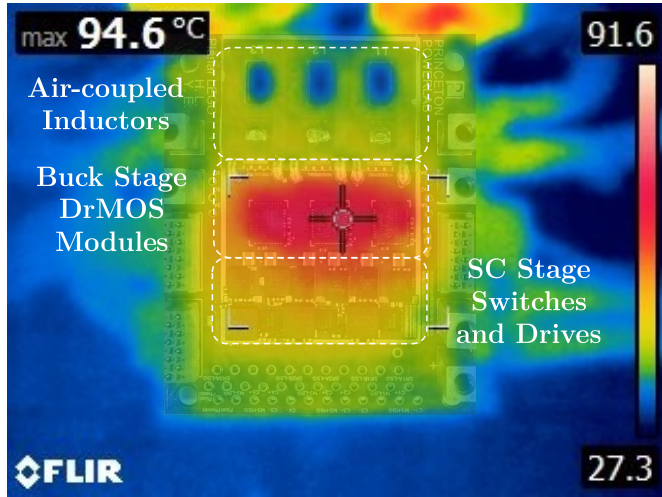


Figure 4.13: Thermal image of the Air-LEGO prototype with PCB windings at 24-to-1 V operation and 120 A output current. The DrMOS modules in the buck stage shows the highest temperature.

can simultaneously cool both the inductors and semiconductor devices. This co-thermal solution simplifies heat management and enhances system reliability during high-power operation.

Representative waveforms are presented in Fig. 4.12, confirming correct operation and expected switching patterns. Fig. 4.13 shows a thermal snapshot of the prototype under full-load operation (120 A at 1 V), where the buck-stage DrMOS devices exhibit the highest temperature, aligning with expectations from power dissipation analysis.

Efficiency testing was carried out across various input voltages and buck-stage switching frequencies, as summarized in Fig. 4.14. The Litz-wire inductor variant consistently outperformed the PCB version, achieving a peak efficiency of 85.9% compared to 75.8%. Under full-load conditions, the efficiencies dropped to 73.1% and 62.5%, respectively.

The following observations offer deeper insights:

- **Impact of inductor implementation:** The higher efficiency of the Litz-wire version is attributed to significantly lower resistive losses, as detailed in Table 4.1. Despite similar geometries, PCB windings suffer from high resistance

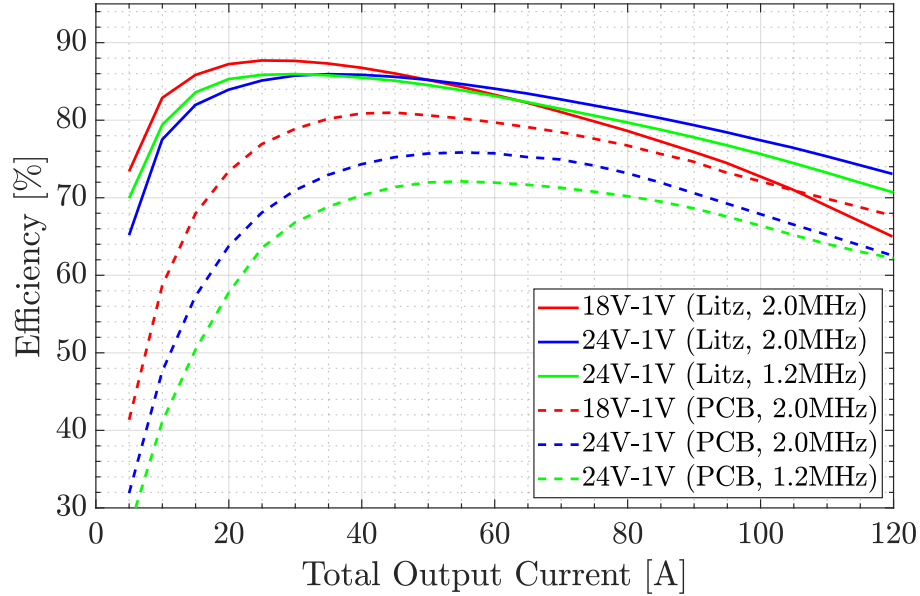


Figure 4.14: Measured efficiency of the Air-LEGO prototype with either the Litz-wire inductors or PCB winding inductors, at different input voltages and different buck stage switching frequencies, excluding consumption of gate drives. Prototype with Litz-wire air-coupled inductors demonstrates higher efficiency.

due to limited copper thickness, particularly in dc conditions. Moreover, the Litz-wire design more effectively suppresses skin and proximity effects, especially at MHz-level switching frequencies. However, PCB windings offer advantages in manufacturability and consistency, while Litz wire solutions are more challenging to scale due to manual winding variations. Minor differences in inductance values also influence performance, but the dominant factor is resistive loss.

- **Effect of switching frequency:** Although higher switching frequencies generally incur more switching loss, in this design, the use of air-core inductors – having relatively low inductance – leads to significant ripple current. At lower frequencies (e.g., 1.2 MHz), this ripple increases resistive losses, offsetting the benefits of reduced switching loss. Therefore, 2 MHz operation yields better ef-

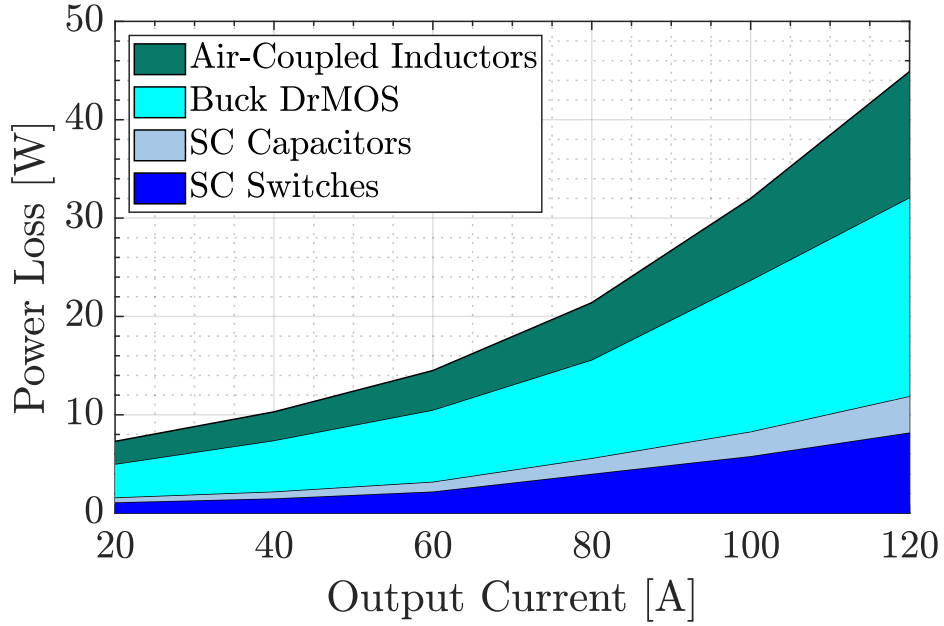


Figure 4.15: Calculated loss breakdown of the Air-LEGO prototype during 24 V-to-1 V operation at 2 MHz with PCB-winding inductors. The switched capacitor stage loss is split into switching and conduction losses due to the switches, losses due to the capacitors. In the buck stage, the loss is divided into the device switching and conduction losses and the winding from the air-coupled inductors.

ficiency under most conditions, except under light load, where switching losses dominate and lower frequency slightly improves performance.

- **Influence of input voltage:** Larger conversion ratios typically reduce efficiency, and results confirm this trend. At higher input voltages (e.g., 48 V), the buck stage must operate at very low duty cycles (e.g., 12.5%), increasing ripple and losses. For this reason, the prototype is optimized for 24 V and 18 V input. However, using over-rated devices for these lower voltages adds unnecessary conduction and switching losses due to higher $R_{DS(on)}$ and C_{oss} . At 18 V, efficiency degradation at high load is caused by the SC stage losing its ZCS operation and transitioning into hard-switching mode, significantly increasing switching losses.

Figure 4.15 provides a breakdown of loss components during 24 V to 1 V conversion at 2 MHz. The dominant losses originate from the DrMOS devices in the buck stage, consistent with the thermal profile shown in Fig. 4.13. These losses stem from conduction losses due to $R_{DS(on)}$, as well as capacitive switching losses related to C_{oss} .

The air-coupled inductors also contribute significantly to total loss due to their large dc and ac resistances, as well as increased current ripple from their limited inductance. Beyond 60 A of output current, the SC stage begins losing its soft-switching condition and enters hard-switching mode, exacerbating switching losses and further lowering efficiency.

These findings inform several optimization directions for future Air-LEGO designs. Improvements include selecting appropriately rated switching devices for lower voltage operation, redesigning the air-core inductors to increase inductance while minimizing resistance, and preserving the system's low-profile geometry. Such refinements will be crucial for enhancing both efficiency and thermal management in next-generation VRM systems.

4.5 Chapter Summary

This chapter has demonstrated the feasibility and potential of integrating air-coupled inductors into voltage regulator module (VRM) designs, achieving ultra-thin profiles and high levels of integration. By removing magnetic cores, the proposed architecture eliminates the thermal constraints and core losses typically associated with conventional magnetic materials. This design choice not only simplifies thermal management but also expands the flexibility of VRM placement and cooling strategies, enabling novel integration opportunities for advanced power delivery systems.

Experimental validation confirmed that Litz-wire windings outperform PCB-based windings, primarily due to their lower ac and dc resistance at the targeted 2 MHz switching frequency. The benefits of Litz wire become especially pronounced under

high-current operation, where resistive losses dominate. Additionally, proper winding interleaving was shown to be essential not only for reducing high-frequency ac losses but also for suppressing fringing flux, thereby addressing electromagnetic interference (EMI) concerns. These findings emphasize the importance of careful geometric design and layout when implementing air-core inductors.

Nonetheless, the prototype also revealed several efficiency bottlenecks. Both the switched-capacitor (SC) stage and the buck stage incurred considerable power losses within their switching devices. Furthermore, the winding losses of the air-coupled inductors – driven by their relatively large resistance and low inductance – constitute a non-negligible portion of the total power loss. These results underscore a fundamental trade-off in air-core inductor-based VRM designs: while compactness and thermal simplicity are significantly improved, they often come at the cost of reduced electrical efficiency.

Future efforts will focus on optimizing the device selection, refining the air-core inductor geometry, and further reducing parasitic losses to enhance the overall system performance. Through these improvements, the Air-LEGO architecture may become a promising solution for high-current, high-density power delivery in next-generation computing platforms.

Related Publications

1. **H. Li, W. Zeng, Y. Elasser and M. Chen, “Air-LEGO: A Magnetic-Free Ultra-Thin 24V-to-1V 120A VRM with Air-Coupled Inductors,” 2025 IEEE Applied Power Electronics Conference and Exposition (APEC), Atlanta, GA, USA, 2025, pp. 510-5178.**

Chapter 5

Conclusion

5.1 Conclusion

This dissertation presents a comprehensive exploration of data-driven and hybrid approaches for modeling and designing magnetic components in power electronics. In response to the growing demands of high-density computing platforms and the limitations of traditional magnetics, this work addresses fundamental challenges across the modeling, optimization, and integration of power magnetics, aiming to unlock new levels of performance, compactness, and adaptability.

Magnetic components play a pivotal role in power conversion systems, serving as energy buffers, current regulators, and EMI filters. Yet they remain the most bulky, lossy, and difficult-to-model elements in modern power converters. With the advent of vertical power delivery (VPD) architectures and chiplet-based packaging, the miniaturization and co-design of magnetics have become more urgent than ever. This dissertation introduces data-driven techniques and hybrid design methodologies to break existing bottlenecks, leveraging machine learning and structural innovations to overcome long-standing modeling and design challenges.

The contributions of this thesis are structured into three core directions:

1. **Data-driven Modeling of Power Magnetics:** Chapter 2 presents a data-centric framework for modeling the nonlinear behavior of magnetic materials. A high-resolution experimental platform is developed to measure the B - H response and core losses across a wide range of operating conditions. The resulting database, MagNet, enables the training of neural network models – including LSTM and Transformer architectures – that serve as “neural datasheets” capable of accurate prediction and generalization. Transfer learning methods are also proposed to reduce the data burden for new materials. These models can compress, extrapolate, and recommend material behavior with high fidelity, offering a transformative tool for magnetic material evaluation and system-level optimization.
2. **Design of Ultra-thin Multiphase Coupled Inductors:** Chapter 3 focuses on the design and optimization of ultra-compact, high-current magnetics for vertical VRM integration. A novel via-winding structure combined with vertically coupled pinwheel cores is proposed to facilitate low-impedance current delivery with minimal vertical height. A co-optimization framework accounts for current balancing, thermal constraints, and core material selection. Two high-performance prototypes are demonstrated, supporting up to 160 A in a footprint below 9×9 mm² and achieving power densities exceeding 3,900 W/in³. These results validate the feasibility of scalable magnetic integration for next-generation PoL converters.
3. **Magnetic-Free Power Delivery with Air-Coupled Inductors:** Chapter 4 explores an alternative route – air-core magnetics – for achieving ultra-thin VRMs with minimal EMI and excellent thermal profiles. The Air-LEGO architecture adopts stacked switched-capacitor and buck stages, using PCB or Litz-based air-coupled inductors in each phase. This design eliminates lossy

magnetic cores while retaining performance, with each phase capable of delivering 20 A. A complete 24-to-1 V, 120 A prototype demonstrates the practicality of magnetic-free designs in compact, modular, and EMI-conscious systems.

Collectively, these contributions form a cohesive advancement in the modeling and design of magnetic components for high-performance power electronics. By bridging the gap between empirical modeling and data-driven inference, and between discrete magnetics and co-designed integration, this thesis offers new pathways for efficient, scalable, and miniaturized power delivery systems.

5.2 Future Work

Building on the foundations laid in this dissertation, several compelling future research directions emerge that could further enhance the modeling, design, and integration of power magnetic components. These directions aim to deepen the interaction between data-driven intelligence and physical constraints, improve co-design methodologies, and enable adaptive and scalable system-level implementation.

- 1. Circuits–Magnetics–Thermal Co-Design:** While this work has emphasized the electrical and magnetic design dimensions, thermal constraints remain a critical limiting factor for high-density power electronics. Future research should explore unified co-design frameworks that simultaneously consider circuit performance, magnetic coupling, and thermal dissipation. Such frameworks can incorporate thermally-aware magnetic layout, 3D heat spreading models, and active cooling strategies to optimize total system performance. Machine learning methods may be leveraged to predict hotspot locations or optimize winding patterns for uniform heat distribution, especially in tightly stacked VPD environments.

2. **In-situ Characterization and Adaptive Modeling:** As power electronics systems become increasingly dynamic, static models built from offline measurements may no longer suffice. Future magnetics modeling frameworks should incorporate *in-situ characterization* – using embedded sensors or real-time current/voltage monitoring – to adaptively update core loss predictions and hysteresis behavior under actual operating conditions. Coupling this with neural models that support online learning or lightweight re-training would enable real-time adaptation to changes in temperature, aging, or input waveform distortion, enabling more resilient and efficient systems.
3. **Physics-Informed Neural Networks (PINNs):** A promising direction is to incorporate domain knowledge into neural network architectures via *physics-informed neural networks* (PINNs). For power magnetics, this could include embedding Maxwell’s equations, hysteresis constraints, or core saturation boundaries directly into the training loss functions. Such hybrid modeling approaches can improve generalization, reduce required training data, and ensure physically plausible predictions. Additionally, PINNs may help resolve long-standing issues in extrapolation or data-sparse regimes, which are common in exotic materials or rare operating conditions.
4. **Integration with EDA Tools and Design Automation:** Neural magnetic models developed in this thesis are currently used in standalone workflows. Future work should focus on integrating these models into mainstream electronic design automation (EDA) tools, enabling automated magnetics-aware optimization in circuit simulators and layout engines. With APIs or plug-ins for SPICE, LTspice, or Cadence tools, designers could query neural models directly to evaluate material trade-offs, predict ripple and loss behavior, or synthesize inductor

geometries, greatly streamlining the magnetic co-design process in power electronics.

5. **Standardized Datasets and Benchmarking:** The absence of publicly available, high-fidelity datasets for magnetic materials remains a key obstacle. Building on the open-source MagNet database, a standardized community effort is needed to benchmark modeling methods under consistent protocols. This would accelerate research reproducibility, facilitate fair comparison between empirical and machine learning models, and foster collaborative tool development across academia and industry. An open evaluation suite could include diverse materials, excitation conditions, and core geometries to benchmark accuracy, speed, and data efficiency.
6. **Cross-Domain Transfer and Generalization:** Finally, expanding the scope of learned models beyond magnetics into adjacent domains – such as capacitors, thermal interface materials, or EMI shielding – opens the door to unified component modeling. Transfer learning techniques could be explored to allow models trained on ferrite materials to generalize to amorphous cores, or even extrapolate from one frequency range to another. Combining these approaches with generative design and topology optimization frameworks could yield fully automated power module generation from specification to layout.

Appendix A

Detailed Implementation of Automated Data Acquisition System

Here we introduce more details about the design and implementation of the data acquisition system in the following aspects:

A.1 Excitation

The data acquisition system supports multiple excitation waveforms, including sinusoidal, triangular, and trapezoidal shapes, enabling comprehensive characterization of power magnetics under realistic operating conditions. These excitations are essential for accurately assessing magnetic behavior, especially core loss and hysteresis, which are strongly waveform-dependent.

For sinusoidal excitation, the system employs a function generator (Rigol DG4102) coupled with a power amplifier (Amplifier Research 25A250AM6). The frequency and amplitude of the waveform are programmatically controlled via the host PC, which communicates with the function generator to sweep through a range of operating points. Due to the non-constant gain of the power amplifier – especially under varying load impedance and magnetic nonlinearity – calibration is performed for each excitation point to ensure measurement accuracy. When large B_{ac} excitations are

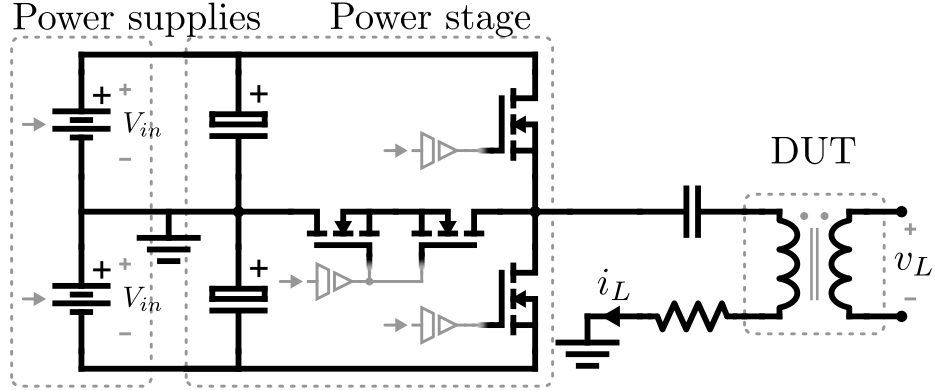


Figure A.1: Circuit schematic of the power stage for generating the excitations and measuring the magnetic component behaviors in the data acquisition system of Mag-Net.

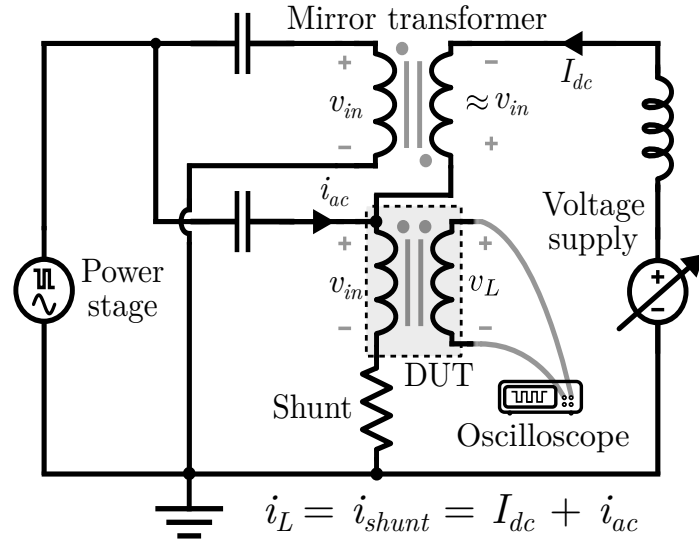


Figure A.2: Circuit schematic of the auxiliary dc-bias current injection circuitry for the measurements under dc-bias conditions.

used, the amplifier may enter a nonlinear regime, resulting in waveform distortion. This distortion affects both the voltage and current measurements, particularly at low impedance conditions or near magnetic saturation. Consequently, waveform quality is closely monitored, and points with excessive distortion are either discarded or replaced.

For piece-wise linear waveforms such as triangular and trapezoidal signals, the excitation is synthesized using a T-type inverter topology powered by two programmable dc supplies (B&K Precision XLN60026), as illustrated in Fig. A.1. This topology allows the generation of three voltage levels $[V_{in}; 0; -V_{in}]$ to approximate linear transitions in the magnetic excitation. High-speed GaN devices (GaN Systems GS66508B) are used in the switching stage to achieve fast and clean transitions. The waveform generation is controlled by a microcontroller (Texas Instruments F28379D control-CARD), which issues precise PWM signals to the gate drivers. All parameter sweeps – including duty cycle, frequency, and amplitude – are synchronized and iterated automatically via the host PC.

A blocking capacitor is inserted in series with the DUT to eliminate any unwanted dc bias originating from either the switching stage or the power amplifier. This ensures that only the intended excitation waveform is applied. The capacitor must have a sufficiently large value to avoid low-frequency voltage droop that could distort the excitation waveform. In this implementation, a 100 μF , 100 V film capacitor is used to ensure minimal impedance at the lowest operating frequencies.

To enable characterization under dc bias, an auxiliary injection circuit is included in the setup (see Fig. A.2). Rather than using a separate third winding – which may introduce unwanted ac ripple due to coupling – the dc bias is injected directly into the primary winding, downstream of the blocking capacitor. This topology isolates the dc current path from the ac excitation. A mirror transformer and a filter inductor are employed to prevent voltage disturbances from the DUT reflecting back to the dc source. The bias current is supplied by a programmable voltage source (Siglent SPD3303X-E), with its current limit automatically set by the host PC. This approach allows flexible and stable dc biasing without interference with the main excitation.

It is important to note that dc bias is defined and controlled in terms of magnetic field strength (H_{dc}), not magnetic flux density (B_{dc}). This is because the initial

magnetization state (B_0) of the core is generally unknown and cannot be easily reset or controlled between measurements. As explained in [24], the mapping between H_{dc} and B_{dc} is nonlinear and path-dependent, making B_{dc} an unreliable metric for repeatable experimental conditions. Therefore, B_{dc} is not reported in this study, and all dc bias levels are expressed in terms of H_{dc} for consistency and clarity.

A.2 Device Under Test

The Device Under Test (DUT) is composed of a toroidal magnetic core with a pair of windings: a primary winding responsible for excitation and a secondary winding used for sensing. The primary winding is connected to the power stage to deliver the required excitation waveform, while the secondary winding remains open-circuited and is used to infer the time-varying magnetic flux density $B(t)$ by numerically integrating the voltage induced across its terminals. This approach conforms to the standard two-winding (voltamperometric) characterization method.

In this work, the majority of DUTs are fabricated using toroidal cores with dimensions approximately $R34.0 \times 20.5 \times 12.5\text{mm}$, which aligns with typical form factors found in commercial magnetic material datasheets. While it is acknowledged that core geometry can influence the measured magnetic characteristics – particularly the flux distribution and eddy current paths – these geometric effects are outside the scope of the current study. For more detailed discussions on geometry-induced variation in B - H loop shape and core loss, we refer the reader to [6].

The number of turns for the DUT windings is carefully selected to balance several competing design constraints. On one hand, the number of turns must be sufficiently large to enable a broad operating range of flux density and frequency within the voltage and current ratings of the system. On the other hand, increasing the turns elevates the inductance of the DUT, which may result in excessive current demand and violate the current limits of the excitation stage. As a practical design example,

for characterizing a TDK N87 toroidal core in this system, both the primary and secondary windings are configured with 5 turns. The primary winding uses 22 AWG Litz wire, composed of 40 strands of 38 AWG filaments, optimized for minimum ac resistance at around 100 kHz. The secondary winding, which ideally carries zero current, is wound with standard 18 AWG solid copper wire.

As recommended in [77], ungapped toroidal cores are employed in this study, as they provide a closed magnetic path that minimizes external field leakage and enables more reliable measurements of intrinsic magnetic behavior.

A.3 Measurement and Acquisition

Voltage and current waveforms are simultaneously recorded using a high-speed 8-bit oscilloscope (Tektronix DPO4054), configured to acquire 10,000 samples per measurement window at a sampling interval of 10 ns, yielding a total time span of 100 μ s per trace. Depending on the frequency of the excitation, this duration captures multiple switching cycles, thereby enabling accurate reconstruction of both steady-state behavior and waveform-dependent losses. To suppress high-frequency switching noise – especially in triangular and trapezoidal excitations – the oscilloscope bandwidth is limited to 20 MHz via built-in filtering.

For voltage measurements, a low-capacitance passive probe (Tektronix P6139A) is used to minimize capacitive loading and preserve waveform fidelity. The current flowing into the DUT’s primary winding is measured using a precision coaxial shunt resistor (T&M Research W-5-10-1STUD) with a resistance of 0.983 Ω , chosen for its superior frequency response and minimal phase error compared to conventional current probes [24, 25, 78]. The oscilloscope input channel connected to the shunt is terminated with 50 Ω , and this termination is explicitly accounted for during current calculation to ensure measurement accuracy [24].

This acquisition configuration ensures accurate and reproducible extraction of $B(t)$ and $H(t)$ waveforms across a wide range of operating conditions. These waveforms serve as the foundation for computing core loss, hysteresis characteristics, and training data for machine learning models.

A.4 Temperature Control

Temperature is a critical factor in magnetic characterization, as magnetic core losses are highly sensitive to thermal variations. Even small changes in temperature can lead to significant deviations in the measured B - H loop and core loss, especially in high-frequency applications. However, controlling temperature during measurements is inherently difficult, since the DUT naturally heats up due to internal power dissipation during excitation.

To achieve stable and repeatable temperature conditions, a dedicated thermal control system is employed. The DUT is submerged in a mineral oil bath, which offers both electrical insulation and excellent thermal conductivity. This oil bath is itself enclosed in a larger water tank, whose temperature is regulated using a precision water heater (ANOVA AN400). To ensure thermal equilibrium between the oil and water, the tank is sealed to prevent heat loss, and sufficient time is allowed for thermal settling. A magnetic stirrer (INTLLAB) is placed under the oil bath to ensure continuous fluid circulation, which prevents localized hot spots and maintains the DUT at a temperature close to that set by the water heater.

This setup allows accurate control of the DUT temperature over extended measurement sessions, thereby improving the consistency and reproducibility of the magnetic characterization process across different thermal conditions.

A.5 Software System

A Python-based software interface running on the host PC manages the coordination of all hardware subsystems and enables fully automated control, measurement, and data collection. The system is specifically designed to facilitate large-scale, unattended data acquisition across multidimensional parameter sweeps.

The software performs three main functions:

- **Excitation Configuration:** It communicates with the power stage – including power supplies, the function generator, and a microcontroller unit – to configure and transmit the waveform properties for each test condition. These properties include waveform shape (e.g., sinusoidal, triangular, trapezoidal), frequency, and amplitude. This allows the power stage to generate the correct excitation for each test case.
- **Measurement Execution:** It communicates with the oscilloscope to configure the acquisition settings, including sampling rate and bandwidth filtering. The system can also trigger calibration routines as needed and retrieve the digitized voltage and current waveforms for post-processing.
- **Data Storage and Formatting:** It processes the acquired waveforms and stores them in a standardized format, ready for downstream use in machine learning models or physics-based analysis. The software handles data parsing, compression, and metadata tagging for each measurement.

To implement these functionalities, the communication with the microcontroller is handled via the UART (Universal Asynchronous Receiver-Transmitter) protocol, while interaction with external lab instruments – such as the oscilloscope, function generator, and programmable power supplies – is managed through the VISA (Virtual Instrument Software Architecture) standard.

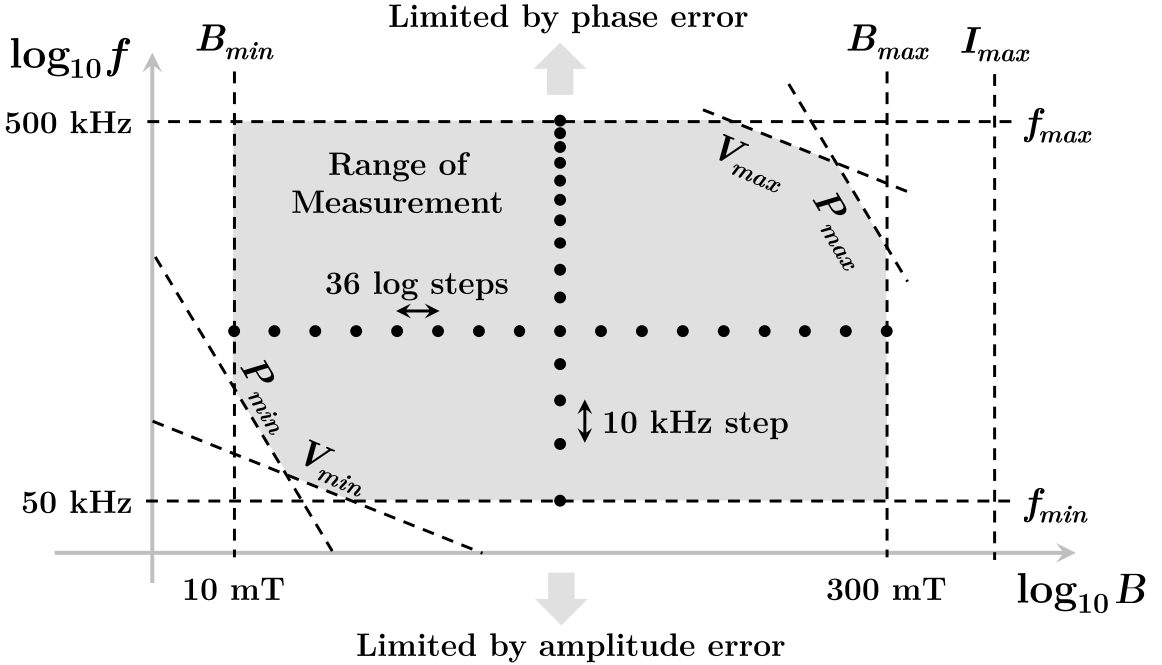


Figure A.3: Range of measurement for the flux density amplitude and the frequency.

These operations are executed within a hierarchical control loop structure that systematically iterates over the full multidimensional parameter space – spanning frequency, flux density, waveform shape, temperature, and dc bias – without the need for human intervention. Only three manual operations are occasionally required: (1) switching between sinusoidal and piecewise-linear excitation modes, (2) changing the DUT, and (3) setting the desired bath temperature for thermal control.

A.6 Range of Measurement

The operational range of the data acquisition system must be carefully defined to ensure the quality, relevance, and accuracy of the collected data. This range is constrained by the physical limitations of the hardware, the thermal properties of the materials under test, and the measurement accuracy under various excitation conditions. The coverage of flux density amplitude and frequency for the measurements in this work is summarized in Fig. A.3.

Flux Density Amplitude and Frequency Flux density amplitudes (B_{ac}) are swept from 10 mT to 300 mT in 36 logarithmically spaced steps. The use of a logarithmic scale allows for more uniform coverage of the core loss response, which tends to exhibit exponential dependence on B_{ac} . The upper bound of 300 mT is chosen to remain sufficiently below the saturation flux density specified in manufacturer datasheets, thereby preventing waveform distortion and ensuring safe operating conditions. The lower bound of 10 mT is selected to ensure a sufficient signal-to-noise ratio during low-amplitude measurements.

For frequency, measurements are taken from 50 kHz to 500 kHz with fixed 10 kHz steps. These steps are selected such that each acquired waveform contains an integer number of cycles within the 100 μ s sampling window (10,000 points at 10 ns resolution), ensuring accurate frequency-domain representation and integration-based calculations. This frequency range is aligned with the typical switching frequencies of modern power electronic converters using ferrite cores.

However, as discussed in Sec. 2.3 and Appendix B, the accuracy of measurements degrades under conditions of very low B_{ac} or very high frequency. These data points are either carefully filtered or excluded to maintain the integrity of the database.

Dc Bias Range Dc bias is swept using a linear ramp of H_{dc} from 0 to 60 A/m in 15 A/m steps, based on the excitation current injected through the auxiliary dc bias circuit. For each level of dc bias, the maximum allowable B_{ac} is adjusted downward to avoid material saturation, using the maximum amplitude permeability curves provided in material datasheets. This ensures that the combined impact of dc and ac excitation remains within the linear or weakly nonlinear regime of the core material, thus avoiding irreversible magnetization or thermal damage.

Voltage Constraints and Excitation Window The excitation voltage applied to the DUT is bounded by the ratings of the power amplifier and the T-type inverter. For

sinusoidal excitations, the voltage sweep ranges from 1 V to 50 V; for triangular and trapezoidal PWM excitations, the sweep extends from 5V to 80V. These limitations define an upper bound for the $B_{ac} \cdot f$ product of the measured waveforms and constrain the achievable combinations of flux density and frequency, particularly under extreme duty cycles or high-frequency operation.

Thermal Constraints and Data Pruning To prevent excessive temperature rise in the core during high-loss measurements, points with estimated losses exceeding 5,000 kW/m³ (estimated using iGSE) are excluded. Such high losses would not only affect thermal equilibrium but also compromise measurement accuracy and potentially damage the DUT. Conversely, extremely low-loss points below 1 kW/m³ are also skipped to avoid unnecessary measurement overhead and focus data collection within the range of practical interest for design and modeling applications.

Temperature Range The temperature range for characterization is set from 25°C (room temperature) to 90°C, covering the most relevant conditions encountered in real-world power electronics applications. This range is determined by the capabilities of the thermal control system described earlier. While the system can accommodate controlled submersion heating, extending the range above 100°C would require the use of advanced thermal environments such as temperature-controlled ovens, which are considered outside the scope of this study.

Appendix B

Data Quality Control of Large-Scale Measurement

Here we introduce more details about the measures to control the data quality in the following aspects:

B.1 Equipment Evaluation and Calibration

The accuracy of the large-scale data acquisition system heavily depends on the careful evaluation and calibration of the equipment used. To ensure high data quality, the experimental setup, including all measurement instruments, has been designed and implemented following the guidelines outlined in [24, 28, 29]. Special attention is paid to understanding and mitigating the limitations of each piece of equipment, as these limitations directly affect the measurement precision and, consequently, the overall quality of the data.

One of the key components in the system is the oscilloscope (Tektronix DPO4054), which is responsible for capturing the voltage and current waveforms during the measurements. To evaluate its performance, the oscilloscope was calibrated against an Agilent 34401A $6\frac{1}{2}$ -digit multimeter, measuring both dc and ac voltage signals under the same conditions. The relative errors for dc and ac measurements were calculated

by averaging measurements taken over the full measurement range (0 V to 80 V and 50 kHz to 500 kHz). The relative error for the mean dc voltage was found to be 0.25%, and for the RMS ac voltage, it was 0.67%. These results confirm the oscilloscope's accuracy in measuring V_{DC} , I_{DC} , v_{AC} , and i_{AC} , which are critical to the core loss calculation in Eq. (2.5). According to the oscilloscope's specifications, the gain accuracy is rated at $\pm 1.5\%$, which directly affects the measurement of the gain factors G_V and G_I . In addition, prior to each measurement iteration, the oscilloscope's signal path is reset and re-calibrated, which eliminates any undesired zero-drift offsets (V_0 and I_0) and ensures that any time skew between voltage and current measurements (θ) is minimized.

The current measurement is performed using a wide-band coaxial shunt (T&M W-5-10-1STUD), which is known for its low parasitic inductance and stable performance under varying temperatures. The coaxial shunt is connected to the DUT and the circuit board through a BNC connector, which has a parasitic terminal capacitance of less than 10 pF. Additionally, efforts are made to minimize parasitic capacitances on the circuit board to ensure the accuracy of the current measurement. The low parasitic inductance and minimized capacitance significantly reduce errors in I_{DC} and i_{AC} , particularly mitigating time skew (θ), which is essential for precise core loss calculations.

To further ensure high data accuracy, all equipment calibration and measurement processes are fully automated, reducing the possibility of human error during the setup and acquisition phases. Automated calibration also contributes to the consistency of measurements over time. Repeated measurements on the same DUT demonstrate that the core loss values can be reproduced with a relative discrepancy of less than 3% between trials in the worst case, validating the reliability and consistency of the acquired data.

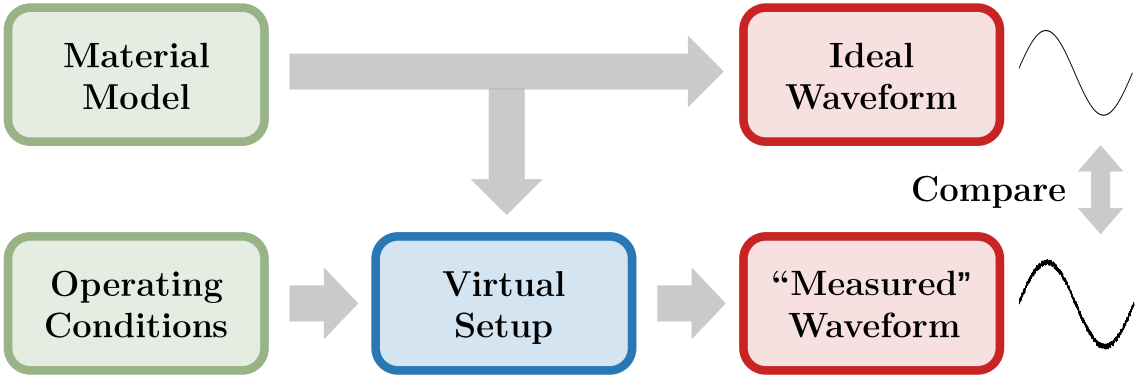


Figure B.1: Workflow of the virtual measurement simulation. The virtual measurement setup numerically simulates the impact of various sources of measurement error. The virtually measured waveform is compared against the ideal waveform to estimate the measurement accuracy.

This rigorous calibration process, combined with the automated equipment setup, guarantees high measurement precision and consistency, essential for building a reliable large-scale dataset for power magnetics research.

B.2 Model-driven Method for Quantifying the Error

The accuracy of data-driven models is directly tied to the quality of the underlying data. To assess the potential error in the measured results and estimate the distribution of such errors, we adopt a model-driven approach that combines physics-based simulations with virtual measurements. This method helps quantify the impact of various measurement errors, and by leveraging Monte Carlo experiments, it allows for an in-depth analysis of the uncertainty associated with the measurements. This error analysis provides a benchmark for setting accuracy targets when employing machine learning models or curve-fitting techniques.

Figure B.1 illustrates the workflow of the virtual measurement simulation. In this approach, a reference waveform is generated based on the material model and passed into the virtual measurement setup. The setup then incorporates various sources

of error, such as system parasitics, signal distortion, and calibration uncertainties. By simulating the effects of these errors, the setup generates a virtually measured waveform, which is then compared to the ideal waveform. This comparison allows for the evaluation and estimation of measurement uncertainty.

The parameters in the virtual measurement setup are determined either from datasheets of equipment, components, and materials, or estimated based on real experimental results. The key sources of measurement error that are considered in this setup include:

- **Systematic error:** This includes parasitic effects from the power stage circuit, cables, and the DUT itself. Other factors, such as timing skew between passive probes (± 1.6 ns), uncertainties in probe gains ($\pm 1.5\%$), and probe offsets ($\pm 0.5\%$), also contribute to systematic errors. Additionally, manufacturing tolerances in the core geometry (e.g., assuming area and length with a variation of $\pm 2.5\%$, typically) affect the accuracy of calculating the magnetic field $B(t)$ and field strength $H(t)$.
- **Statistical error:** Statistical errors arise from environmental factors such as electrical noise, quantization errors, and sampling noise introduced by the oscilloscope. Temperature variations in the DUT, which can lead to a deviation of $\pm 1.6\%$ in power loss (P_V), also contribute to the overall statistical error.

By modeling these sources of error, we can quantify the uncertainty in the data collection process and establish confidence intervals for the measured values. This model-driven approach allows for a more accurate and systematic understanding of the sources of error, providing valuable insights into the overall accuracy of the measurement system and guiding the improvement of data collection methods. Additionally, the insights gained from this method can inform the calibration and optimization of the data-driven models, ensuring that the results are both reliable and precise.

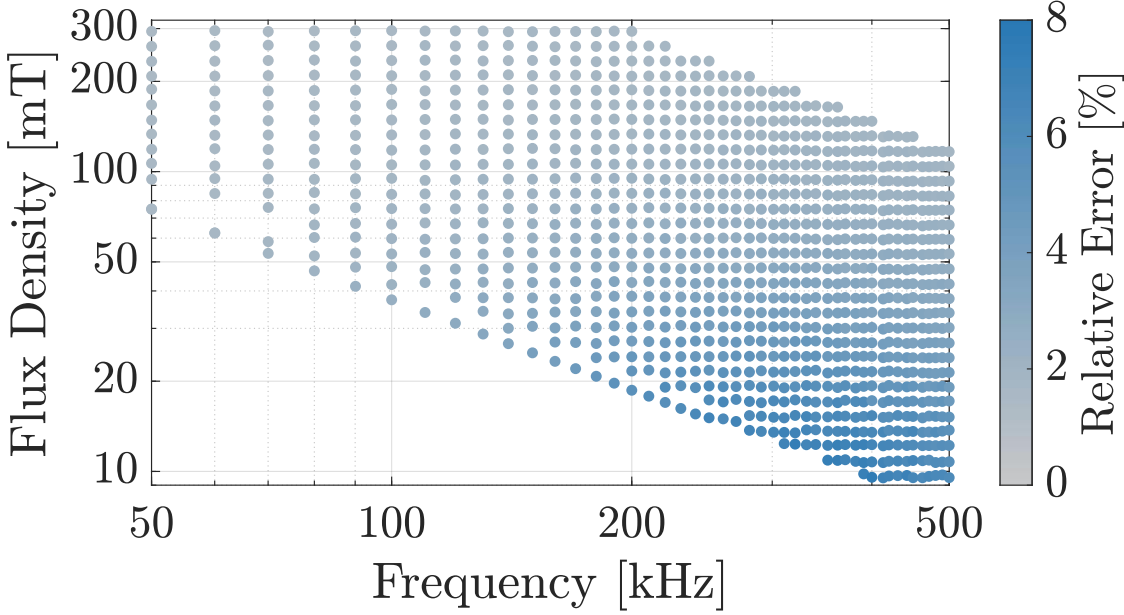


Figure B.2: Example simulation results for TDK N87 material with the virtual measurement setup and Monte Carlo experiments, where the measurement uncertainties introduced by the probe and scope are taken into consideration. Colors depict the discrepancy between the virtually measured core loss and the expected core loss.

Using the virtual measurement setup, a series of Monte Carlo simulations were performed to quantify the measurement uncertainty and error distribution. The uncertain variables in the system, including parasitic components, oscilloscope limitations, and temperature variations, were assumed to follow either Gaussian or uniform distributions, with the respective 2σ deviations. Figure B.2 shows the simulation results for the TDK N87 material, where the impact of measurement uncertainties introduced by the oscilloscope probes and scope settings is included.

In the simulation, the discrepancy between the virtually measured core loss and the expected core loss is evaluated. The values displayed in Figure B.2 correspond to the 95th percentile of the Monte Carlo distribution, which represents the upper bound of the measured error across various trials. As the figure demonstrates, most of the sample points in the measured range show relatively low error rates, with errors less than 6%. However, the highest error levels are found in the regions with high

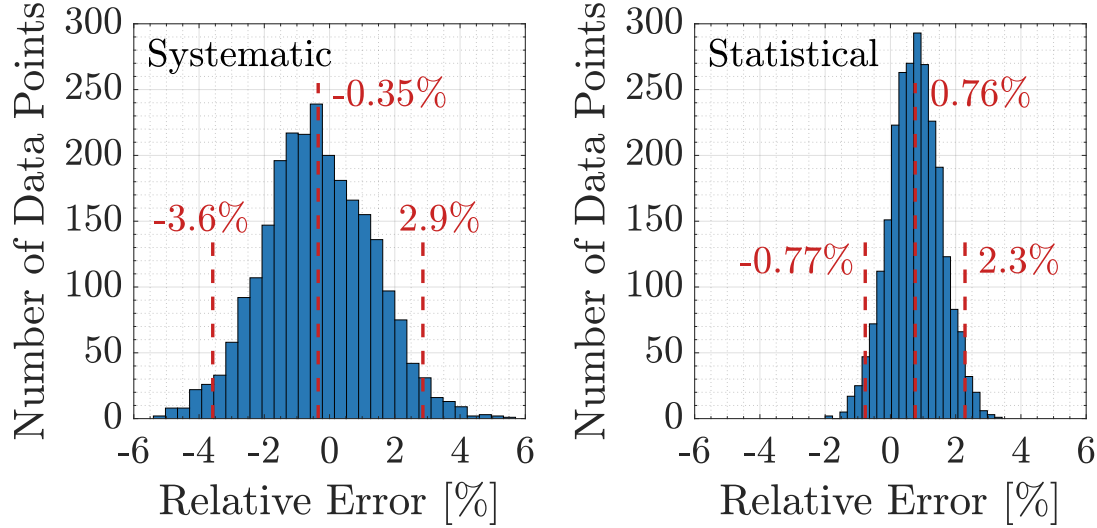


Figure B.3: Error distribution of an example point (300 kHz, 50 mT, 50% duty ratio triangular wave with zero dc bias measured at 25°C), where the measurement uncertainties introduced by the circuit parasitics, scope and probe, temperature variation, and geometry variations are considered. Both the systematic error and the statistical error are less than 4% for the majority of trials in the Monte Carlo experiments. The spread of systematic error is larger than that of statistical error.

frequency and low flux density. In these regions, the measurements are more susceptible to electrical noise and the inherent inaccuracies of the measurement equipment, as expected.

Further refinement of the error analysis is presented in Figure B.3, which shows the error distribution for a specific measurement point – 300 kHz, 50 mT flux density, 50% duty cycle triangular waveform, and zero dc bias, measured at 25°C. The uncertainties introduced by circuit parasitics, oscilloscope probe inaccuracies, temperature variations, and core geometry fluctuations are taken into account in the Monte Carlo simulation. The results show that for the majority of trials (95%), both the systematic error and the statistical error remain within 4%. Specifically, the systematic error is generally less than 3.6%, while the statistical error is below 2.3%. These results indicate that systematic errors have a more significant impact on the overall measurement accuracy than statistical errors.

Geometry variation, especially in the core material, contributes significantly to systematic error. Although geometry fluctuations are inherent to material production and cannot be avoided in the design phase, equipment upgrades and reducing parasitic effects (such as minimizing time skewing between voltage and current signals) can help to improve measurement accuracy marginally. Additionally, temperature variations contribute substantially to statistical error, underlining the importance of precise temperature control during measurements.

Overall, the high measurement accuracy is maintained within the typical operating range of the data acquisition system. However, measurements for materials with a high quality factor, particularly at high frequencies or low flux densities, are more prone to error. By combining model-driven error analysis with material datasheet specifications, we can confidently determine a reliable measurement range where the data quality remains high, as indicated in Figure A.3 in Appendix A. This error map can be similarly generated for each material in the database to assess the quality of the collected data.

B.3 Data-driven Methods for Data Quality Control

In large-scale automated data collection, outliers are inevitable due to rare anomalous operations. To address this, an algorithm was developed to detect and remove outlier data points based on smoothness analysis. As illustrated in Fig. B.4, for each data point in the dataset, the estimated power losses are calculated using the Steinmetz parameters inferred from the neighboring data points, which are close in terms of frequency and flux density. The other variables are kept constant for these points. If the measured losses of a given data point significantly deviate from the estimated value, it can be flagged as an outlier.

More specifically, for a given data point, a weight reflecting the closeness to other data points is assigned. This weight is defined as:

$$w_i = \max \left\{ 1 - \frac{\sqrt{(\log f_i - \log f_0)^2 + (\log B_i - \log B_0)^2}}{w_{max}}, 0 \right\} \quad (\text{B.1})$$

Here, (f_0, B_0) are the frequency and flux density of the considered data point, while (f_i, B_i) refer to the values of each other data point in the dataset. The square root term quantifies the distance between two data points on the logarithmic f - B plane. The parameter w_{max} can be tuned to determine the size of the neighboring area under consideration. Based on this weight definition, the closer (f_i, B_i) are to (f_0, B_0) , the closer w_i is to 1. Conversely, any (f_i, B_i) that are farther from (f_0, B_0) will have a smaller w_i value, eventually reaching 0 if the distance exceeds w_{max} . Fig. B.4 shows an example distribution of the weights for a considered data point, with the color of the points reflecting the normalized distance between any given data point and the considered data point.

Based on the weight w_i , a weighted least square regression is performed to calculate the local Steinmetz parameters:

$$\min_{k,\alpha,\beta} \sum_{i \neq 0} \left[(kf_i^\alpha B_i^\beta)^2 - P_{meas,i}^2 \right] w_i^2 \quad (\text{B.2})$$

The local Steinmetz parameters for a given data point are computed using the nearby data points, allowing the expected core loss value to be estimated according to the Steinmetz equation. The outlier factor is then defined as the relative discrepancy between the expected loss and the measured loss:

$$\text{Outlier Factor} = \frac{kf^\alpha B^\beta - P_{meas}}{P_{meas}} \times 100 \quad (\text{B.3})$$

Figure B.5 illustrates an example of the discrepancies between the expected core loss, based on the local Steinmetz parameters of nearby points, and the measured losses for different data points. A data point with a high outlier factor is considered a low-quality measurement and is subsequently removed from the dataset.

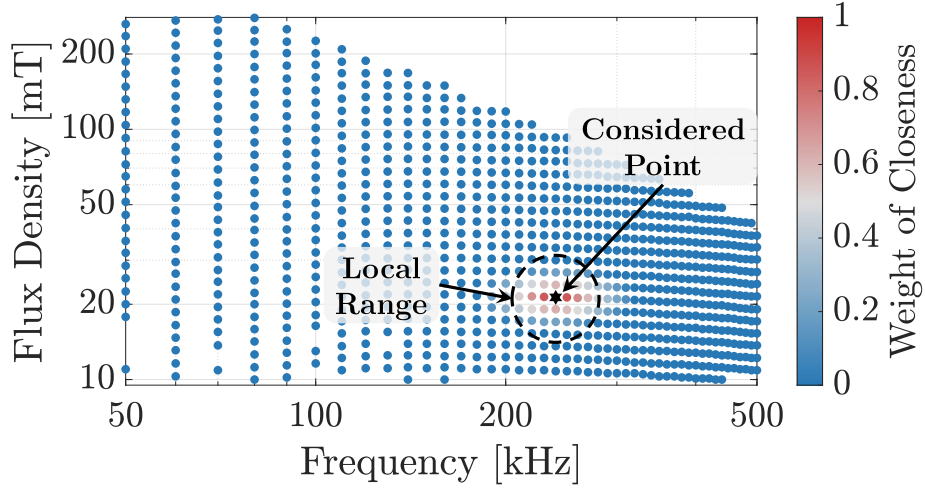


Figure B.4: Example distribution of the defined weight of closeness for a specific considered data point. The local Steinmetz will be performed within the local range that is close enough to the considered data point.

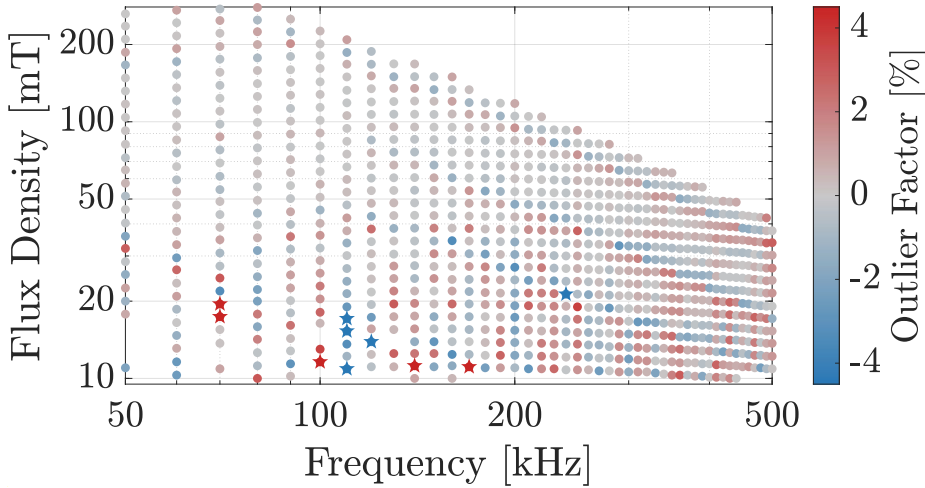


Figure B.5: Example of outlier data points in a dataset for the material N87 under sinusoidal excitation. For each point, data up to 0.1 decades far in terms of flux density and frequency are used to generate the local Steinmetz parameters. The data points discarded because the error compared to the estimation is above $\pm 4\%$ are marked as solid stars.

Outlier detection is crucial for maintaining high data quality. This outlier detection algorithm is one approach for evaluating data quality and removing abnormal data. While it has several strengths, it also has limitations, such as its inability to detect systematic errors and the potential to miss unusual material characteristics that do not fit typical patterns.

Appendix C

MagNet Challenge for Data-Driven Power Magnetics Modeling

Here we provide an introduction on the IEEE MagNet Challenge 2023. More details about this competition can be found in [48].

C.1 Background and Motivation

Magnetic components play a pivotal role in power electronics, often contributing over 30% to both total cost and system losses. As modern applications increasingly demand higher efficiency, density, and dynamic performance, magnetics have emerged as a critical bottleneck. The design and analysis of these components are complicated by their nonlinear behavior, geometry-dependent properties, and sensitivity to dc bias, temperature, and frequency. These influences result in highly complex performance characteristics that are difficult to capture using traditional modeling techniques, which often rely on empirical equations, lookup tables, or simplified loss maps. While circuit-level simulation tools and numerical field solvers have seen significant advancement, the modeling of magnetic materials themselves – especially under real operating conditions – has progressed much more slowly.

One of the most widely adopted methods for core loss modeling is the Steinmetz equation (SE), originally proposed in the 1890s. While the SE and its numerous variants (e.g., iGSE, i^2 GSE) have been extended to handle arbitrary waveforms, they are inherently limited by their low parameter count and empirical nature. These models lack the ability to generalize across operating conditions or account for complex dependencies such as thermal variation and dc bias. Despite being ubiquitous in practice, even the most advanced Steinmetz-based models struggle to offer sufficient accuracy for modern high-performance magnetic design.

Beyond core loss estimation, another essential task in magnetic modeling is capturing the B - H hysteresis loop, which serves as a fingerprint of material behavior and is key to analyzing effects like saturation, inductance variation, and coupling. Traditional frameworks – such as the Preisach [79] and Jiles-Atherton [10] models – are built upon semi-empirical formulations and face similar limitations in scalability and accuracy. As modern power magnetics are increasingly shaped by data complexity and nonlinearity, there is a compelling opportunity to leverage machine learning techniques, particularly neural networks, to upgrade both core loss and B - H modeling approaches [80, 81]. Doing so would enable a unified, data-driven framework capable of capturing the full range of nonlinear, frequency-dependent, and thermal effects in power magnetics, while maintaining compatibility with modern simulation workflows.

Inspired by the success of the ImageNet Challenge in the computer vision domain [82], the MagNet Challenge was conceived to establish a collaborative, open-source platform for advancing magnetic component modeling in power electronics. Its primary objective was to transcend the limitations of the traditional Steinmetz equation-based framework by leveraging a large-scale, high-fidelity dataset that spans a wide array of magnetic materials, excitation waveforms, frequencies, and temperatures. As shown in Fig. C.1, the challenge aimed to catalyze the development of

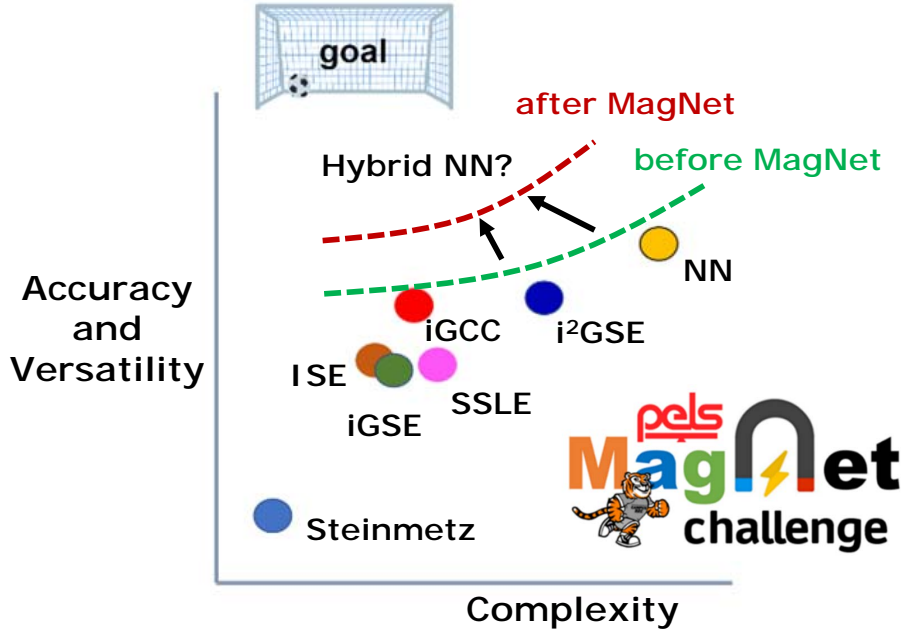


Figure C.1: The vision and mission of the MagNet Challenge in 2023. The open-source initiative aims at developing less complex, more versatile, and more accurate data-driven power magnetics models.

new modeling paradigms that are not only more accurate but also significantly more compact, versatile, and scalable.

At its core, the MagNet Challenge sought to identify and promote data-driven techniques that are efficient in computation, memory, and training data requirements, while offering robust generalization across diverse material behaviors. In designing the challenge framework, we formulated a set of fundamental questions to guide the community’s exploration of next-generation modeling approaches:

- Should we adopt a unified modeling architecture (e.g., a generalized Steinmetz-based framework), or allow for multiple specialized models tailored to different materials and applications?

- What level of accuracy is practically sufficient, given the inherent variations in material batches, core geometry, temperature fluctuations, and manufacturing inconsistencies? Can we distinguish modeling error from measurement noise?
- What is the minimal parameter set needed to describe a magnetic material across its full operational envelope without sacrificing predictive capability?
- Which modeling paradigm is best suited for various use cases – such as core loss estimation, B - H loop prediction, analytical design, SPICE-level simulation, or finite element integration?
- How can we visualize model behaviors and data distributions to enhance interpretability and deepen our physical insight into magnetic phenomena?
- What is the optimal data requirement and sampling strategy for training models that remain accurate and efficient across a wide operation space?

To investigate these challenges systematically, the competition was organized into three complementary tracks:

- Model Performance Track: Focused on building predictive models that generalize well across both known and unseen materials, utilizing large datasets to extract meaningful patterns.
- Concept Novelty Track: Encouraged the introduction of new theoretical frameworks, modeling philosophies, and signal processing techniques that could reframe our understanding of magnetic behavior.
- Software Engineering Track: Aimed at creating practical tools with clean, modular code, user-friendly interfaces, and open-source readiness to support widespread adoption and community growth.

Through these tracks, the MagNet Challenge established a benchmark platform to not only evaluate model performance but also promote innovation, reproducibility, and deeper engagement with the fundamental science of power magnetic materials.

Specifically, MagNet Challenge 2023 concentrated on the problem of modeling core losses under periodic steady-state excitation. Participants were provided with measured B - H loop data as training input, and were tasked with developing models capable of accurately predicting core losses across a wide range of materials and operating conditions. While the scope of the 2023 challenge was intentionally focused to enable direct comparisons of modeling techniques, future iterations may expand to encompass additional tasks such as transient magnetic behavior modeling or direct B - H loop prediction.

Rather than simply benchmarking existing literature, the MagNet Challenge was conceived as a forward-looking, open-access research platform aimed at critically evaluating both established and emerging modeling approaches under standardized conditions. The competition format provided a unique opportunity to assess model accuracy, generalization, efficiency, and usability in a transparent and reproducible manner. The full challenge timeline is illustrated in Fig. C.2. The event attracted contributions from more than 220 researchers worldwide, including academic and industry participants, who engaged as developers, reviewers, judges, and organizers.

To promote openness and foster future collaboration, all submitted reports, source code, and models were released publicly [48]. This ensured that the intellectual contributions of each team were disclosed in full, enabling reproducibility, peer review, and potential re-use within the broader research community. The MagNet Challenge thereby served not only as a benchmarking campaign, but also as a catalyst for community building and open scientific advancement in the domain of data-driven power magnetics modeling.

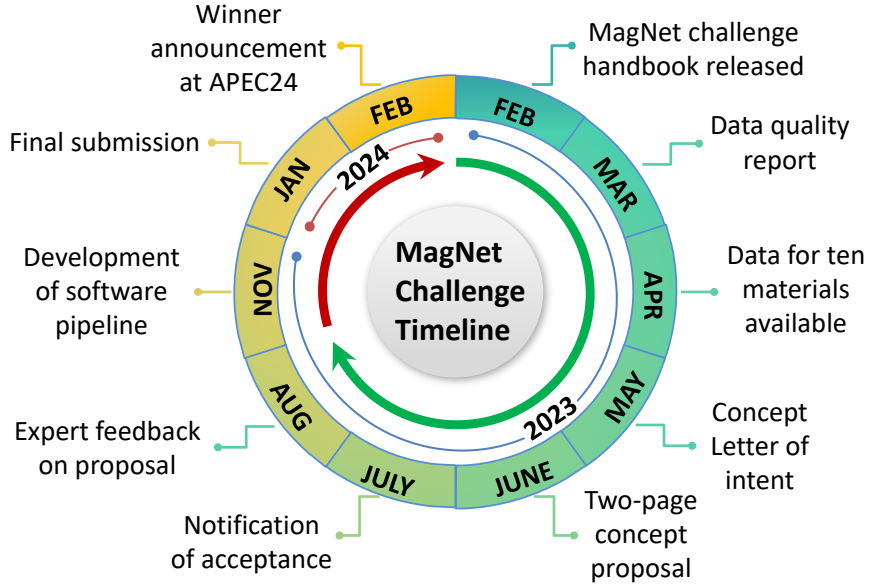


Figure C.2: The 1-year timeline of the MagNet Challenge in 2023, spanning from February 2023 to February 2024.

The contributions of MagNet Challenge include both advancing the technology and fostering a more collaborative research community in power electronics by:

- 1. Advancing the state-of-the-art:** Through collaborative and competitive multi-objective optimization, the challenge has pushed the boundaries of what is possible in power magnetics modeling.
- 2. Developing guidelines for data-driven research:** The challenge has established practical rules and useful guidelines for conducting data-driven research in power electronics.
- 3. Fostering an open-source research community:** It has set examples for creating a transparent, open-source international research community, promoting collaboration on key topics.

4. Exploring future research directions: By providing a fair performance benchmark, it offers new insights that can guide future research in power magnetics modeling towards the most promising approaches.

C.2 Goals, Task Setup, and Evaluation Criteria

The goal of the MagNet Challenge in 2023 is to develop intelligent software tools that can learn and predict core loss information with efficient data usage, based on the MagNet database as demonstrated in Chapter 2. For each magnetic material of interest, student teams were asked to develop a MATLAB or Python function that takes the following three inputs for modeling power magnetic materials in steady state:

- A single-cycle arbitrary flux density waveform in 1024 steps: $B(t)$ (unit: T).
- An operation frequency: f_{sw} (unit: Hz).
- A temperature: T (unit: degrees C).

and produce the following output:

- An average volumetric core loss estimation (floating point): P_v (unit: W/m³).

The training data includes the B - H loop time sequences, frequency f_{sw} , and temperature T . The final outcome of the model is a callable function:

$$P_v = f(B(t), f_{sw}, T). \quad (\text{C.1})$$

Although measurement data with dc bias conditions was made available through the MagNet database, such effects were not formally included in the 2023 MagNet Challenge evaluation. This exclusion was primarily due to limitations in the availability of high-quality, bias-dependent data and the lack of a rigorous understanding of

measurement accuracy under these conditions. Similarly, the impact of magnetic core geometry on loss characteristics – while known to be significant – was also omitted from the official evaluation framework due to comparable challenges in data consistency and interpretability. Nevertheless, teams were encouraged to explore the use of dc bias data as an optional enhancement to their modeling approaches. Incorporating such factors is expected to be a key direction for future iterations of the MagNet Challenge, as improved datasets and more refined measurement methodologies become available.

The challenge included two rounds of competitions: a pre-test round which allowed the teams to get familiar with the data and the competition rules, and a final-test round which determined the teams' final ranking. Each training data point is offered as a pair of single-cycle $B(t)$ and $H(t)$ time sequences, with 1024 steps at different frequencies f_{sw} and temperatures T . The area of the B - H loop determines the volumetric core loss P_v . Note that different numerical integration algorithms for calculating the B - H loop areas may result in very different core loss estimation results, especially if the B - H curve is not smooth (e.g., due to non-sinusoidal excitation or nonlinear material behavior). The testing data points include $B(t)$, f_{sw} , and T , but do not include $H(t)$ or P_v . The datasets used for the pre-test phase and the final-test phase were:

- Round #1 Training: A large amount of training data for 10 materials dedicated for training: {**3C90, 3C94, 3E6, 3F4, 77, 78, N27, N30, N49, N87**}.
- Round #1 Testing: Separate, randomly sampled testing data for the same 10 materials: {**3C90, 3C94, 3E6, 3F4, 77, 78, N27, N30, N49, N87**}.
- Round #2 Training: Strategically sampled training data for 5 materials: {**3C92, T37, 3C95, 79, ML95S**}.

- Round #2 Testing: The remaining data for the same 5 materials used in Round #2 training: {**3C92, T37, 3C95, 79, ML95S**}.

Particularly, to ensure fairness during the second round of the MagNet Challenge, the identities of the magnetic materials used were kept confidential. Their datasets were strategically sampled to evaluate model performance under a variety of scenarios. Each material was designed to represent a different type of modeling challenge:

- **Material A (3C92): Tiny Data Challenge** This material exhibits characteristics similar to those of the 10 materials provided in the first-round training set. It was used to assess model generalization under data-scarce conditions, where only a limited amount of training data was provided, while the majority of the dataset was reserved for testing.
- **Material B (T37): New Material Challenge** As a broadband material significantly different from the first-round materials, T37 was introduced to test the ability of models to adapt to unfamiliar material properties. In this case, a large training set was provided, but only a small test set was released.
- **Material C (3C95): Temperature Challenge** This material was selected to evaluate the temperature dependence of core loss models. The test dataset included temperature ranges not covered in the training data, enabling assessment of a model's ability to interpolate or extrapolate across thermal variations.
- **Material D (79): Waveform Challenge** This material was used to examine the model's sensitivity to excitation waveform shape. The training set included only limited data points with trapezoidal waveforms, whereas the test set was enriched with a diverse set of trapezoidal excitation conditions.
- **Material E (ML95S): Frequency and Flux Density Challenge** This material was used to test a model's capability to capture frequency and flux density

dependencies. The training set included sparse data over a narrow operating range, while the testing set featured a wide range of unseen frequency and flux density conditions.

Through these five targeted tracks, the round #2 evaluation aimed to systematically challenge model robustness, generalization, and versatility under realistic and diverse operating conditions.

MagNet Challenge 2023 primarily focused on the task of predicting magnetic core losses under periodic steady-state excitation. To evaluate prediction accuracy, the relative error ϵ between predicted and measured volumetric core loss was defined as:

$$\epsilon = \frac{|P_{v,\text{meas}} - P_{v,\text{pred}}|}{P_{v,\text{meas}}} \times 100 \quad (\text{C.2})$$

Here, $P_{v,\text{meas}}$ denotes the measured volumetric core loss, while $P_{v,\text{pred}}$ represents the corresponding predicted value. The 95th percentile error was selected as the primary metric for ranking the prediction accuracy of submitted models. Based on prior evaluations of sample-to-sample variability in magnetic components [83], a 95th percentile error below 10% was considered a competitive benchmark for core loss prediction. It is worth noting that the normalization in (C.2) may lead to biases – particularly for samples with extremely low absolute losses – since the prediction error (numerator) does not necessarily scale linearly with the loss magnitude (denominator). Therefore, extreme low-loss or high-loss operating points may have limited practical relevance in typical power magnetic design. This observation suggests that alternative performance metrics may be explored in future iterations of the challenge.

In addition to accuracy, model compactness was also evaluated. Model size was defined as the total number of stored parameters required to describe each material. This metric excluded algorithmic complexity – such as the number of computational layers, iteration structures, or model depth – and instead focused solely on memory

requirements. This design choice aimed to incentivize the development of models that are parameter-efficient and computationally scalable, aligning with real-world constraints in embedded and hardware-constrained applications.

C.3 Final Evaluation Results

In April 2023, the MagNet Challenge officially launched with the registration of 39 teams from 17 countries. By the end of the competition, 24 teams from these countries successfully submitted their final results, marking a strong international engagement.

The MagNet Challenge provided a platform for teams to investigate a broad spectrum of modeling approaches, encompassing both equation-based and data-driven techniques for characterizing power magnetic materials. Through this open benchmarking effort, the results quantitatively revealed a fundamental trade-off between model compactness and prediction accuracy, offering new insights into the complexity-accuracy balance in magnetics modeling.

While the majority of participating teams adopted modern machine learning strategies – including neural networks and other advanced data-driven algorithms – a smaller number of teams pursued physics-informed or traditional equation-based frameworks. The strategic structure of the MagNet dataset enabled a fair and systematic comparison of these diverse approaches. This in turn contributed to a deeper understanding of the advantages and limitations inherent to each modeling strategy under real-world constraints such as waveform diversity, data sparsity, and operating condition variation.

Designing a high-performing, data-driven power magnetics model involves multi-objective optimization, balancing accuracy, compactness, and generalization. By aggregating the final submissions, the competition effectively constructed a Pareto frontier representing the current state-of-the-art. This collective outcome offers both

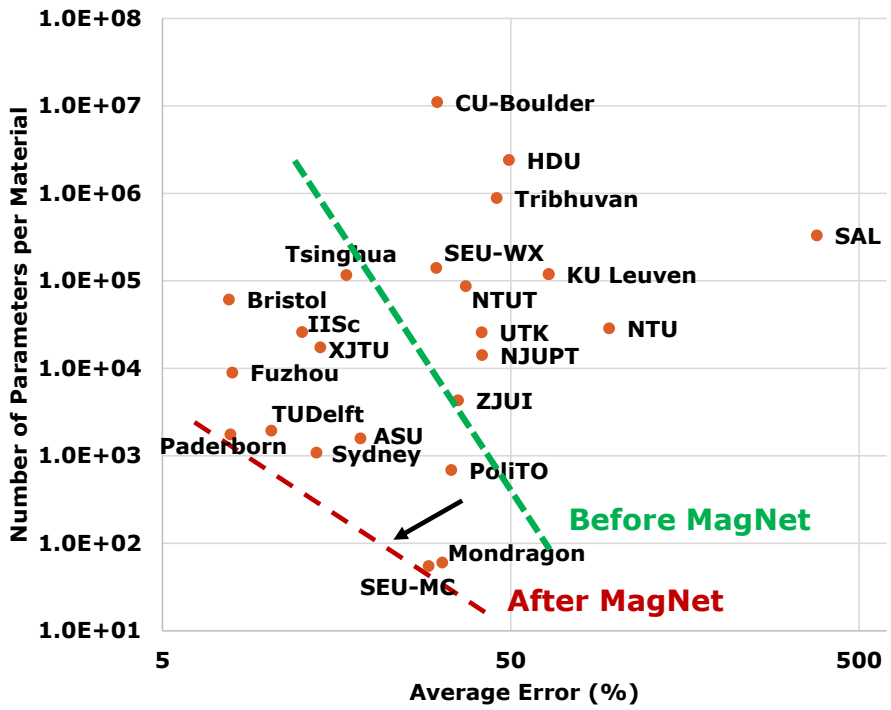


Figure C.3: Average 95th percentile error across the 5 materials, and average model number of parameters (size) of the 24 final submissions, together with the state-of-the-art (SOTA) Pareto fronts before and after the MagNet Challenge, estimated using the results reported in [80] as a benchmark. The minimum average 95th percentile error reaches 7 %, and the smallest model parameter size reaches 60. Both the model sizes and average errors are greatly reduced as a result of the community effort in the MagNet Challenge.

a quantitative benchmark and a qualitative perspective for future research directions in power magnetics modeling.

Figure C.3 presents the average 95th percentile error versus model size for all final submissions. Notably, the top-performing models achieved less than 10% average 95th percentile error while using approximately 1,000 parameters, highlighting impressive advances in model efficiency and precision.

Thanks to the concerted efforts of all participating teams, significant improvements have been achieved in both the accuracy and compactness of magnetic core loss models. Detailed documentation of the complete list of participating teams, in-

dividual models and technical approaches adopted by each team, and final evaluation results can be found in [48].

C.4 Conclusion and Future Roadmap

The ultimate objective of the MagNet Challenge is to establish a comprehensive framework for modeling power magnetic components by evaluating and advancing a wide spectrum of modeling strategies, with the long-term goal of enabling the optimization and automation of magnetic component design. Drawing from the insights gained through the 2023 competition, we envision the next-generation MagNet models to possess the following key characteristics:

- **Accuracy:** Models should achieve high fidelity in predicting magnetic behavior, matching the precision of experimental data and accounting for sample-to-sample variation. They must also reflect the inherently multi-scale and multi-physics nonlinear nature of magnetic phenomena, to be applicable across the entire design, development, and manufacturing process.
- **Compactness:** To support efficient training, fast simulation, and effective optimization, models should remain lightweight in size. Given the large design space (e.g., materials, geometries) and operating space (e.g., frequency, waveform, temperature), compact models with minimal parameters are critical, especially when measurement data is limited.
- **Generality, Consistency, and Versatility:** Models should be broadly applicable across various applications, consistent with other electronic component models (e.g., for semiconductors and capacitors), and flexible enough to accommodate diverse design objectives – such as prioritizing either accuracy or simplicity.

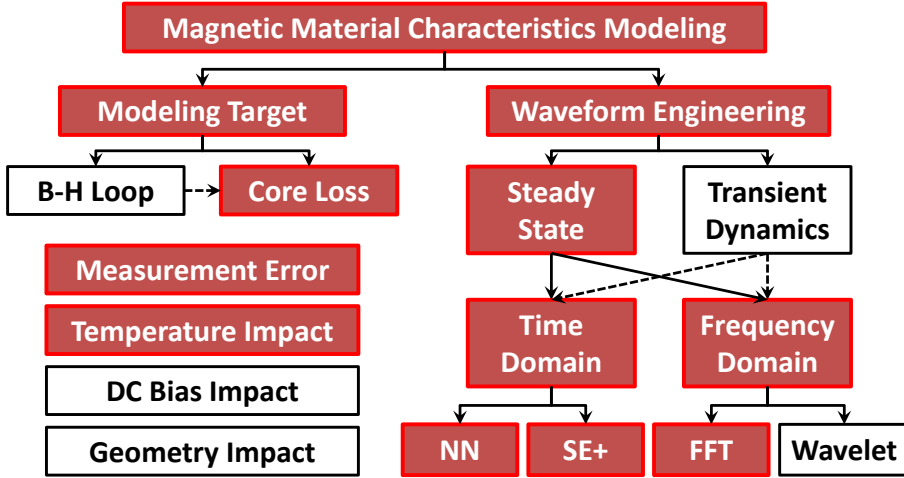


Figure C.4: Roadmap of the MagNet challenge with addressed topics marked in red boxes, and example future topics marked in white boxes.

The 2023 MagNet Challenge revealed that both equation-based and data-driven approaches offer distinct strengths and weaknesses. There remains substantial room for improvement in both camps, as well as opportunities to combine them into hybrid methods capable of addressing more sophisticated design needs. As illustrated in Fig. C.4, the future roadmap of the MagNet Challenge aligns with the aforementioned objectives, with a particular emphasis on expanding model generality.

For instance, the 2023 Challenge focused on major-loop steady-state excitation with zero DC bias, within a limited frequency range (tens to hundreds of kHz) and sparse temperature conditions. Future challenges are expected to cover more complex excitation conditions, such as transient waveforms, minor loops, and non-zero DC bias, as well as wider frequency bands, geometry dependence, and mixed-mode operation (e.g., magnetics used in ac-dc switched-mode converters).

While the top-performing models in 2023 demonstrated strong results under the specific evaluation settings, they may not generalize well to unseen conditions or broader application scenarios. Continued progress will require new modeling

paradigms and deeper understanding. In this context, several promising research directions for future MagNet Challenges include:

- **Data Engineering:** Future challenges should move toward community-driven, open-source data acquisition frameworks, with standardized measurement protocols and cross-validation among institutions and manufacturers. As the fidelity of a model is ultimately bounded by the quality of the input data, a transparent and sustainable data infrastructure will be vital.
- **Model Framework:** In 2023, teams explored a range of modeling paradigms including black-box (data-driven), white-box (equation-based), and gray-box (hybrid) approaches. Most relied on time-domain modeling, while frequency-domain approaches remain underexplored and warrant further attention. Future frameworks should support scalable, updatable architectures that can accommodate multiple materials under a unified representation, and possibly interface with large language models to enhance adaptability and accessibility.
- **Data Visualization:** The high-dimensional nature of magnetic material data necessitates robust visualization tools for filtering, compressing, and interpreting results. Enhancing the human–data interface will be crucial to unlocking new insights and applications.
- **Physical Insights and Better Materials:** While the primary focus of the 2023 Challenge was not on improving physical theories, several teams attempted to close the loop between data-driven modeling and material physics. With better datasets, more expressive models, and improved visualization, the MagNet Challenge holds the potential to deepen physical understanding and guide the design of novel magnetic materials and components.

In summary, the MagNet Challenge sets a precedent for community-driven advancement in power magnetics modeling. By fostering collaboration and benchmark-

ing progress across disciplines, it is poised to drive both technological innovation and scientific discovery in the years to come.

Related Publications

1. M. Chen, **H. Li**, S. Wang, T. Guillod, D. Serrano *et al.*, “**MagNet Challenge for Data-Driven Power Magnetics Modeling**,” in *IEEE Open Journal of Power Electronics*, vol. 6, pp. 883-898, 2025.

Bibliography

- [1] D. J. Perreault, J. Hu, J. M. Rivas, Y. Han, O. Leitermann, R. C. Pilawa-Podgurski, A. Sagneri, and C. R. Sullivan, “Opportunities and challenges in very high frequency power conversion,” in *2009 Twenty-Fourth Annual IEEE Applied Power Electronics Conference and Exposition*, pp. 1–14, 2009.
- [2] C. R. Sullivan, B. A. Reese, A. L. F. Stein, and P. A. Kyaw, “On size and magnetics: Why small efficient power inductors are rare,” in *2016 International Symposium on 3D Power Electronics Integration and Manufacturing (3D-PEIM)*, pp. 1–23, 2016.
- [3] Y. Han, G. Cheung, A. Li, C. R. Sullivan, and D. J. Perreault, “Evaluation of magnetic materials for very high frequency power applications,” *IEEE Transactions on Power Electronics*, vol. 27, no. 1, pp. 425–435, 2012.
- [4] A. J. Hanson, J. A. Belk, S. Lim, C. R. Sullivan, and D. J. Perreault, “Measurements and performance factor comparisons of magnetic materials at high frequency,” *IEEE Transactions on Power Electronics*, vol. 31, no. 11, pp. 7909–7925, 2016.
- [5] M. Chen, M. Araghchini, K. K. Afidi, J. H. Lang, C. R. Sullivan, and D. J. Perreault, “A systematic approach to modeling impedances and current distribution in planar magnetics,” *IEEE Transactions on Power Electronics*, vol. 31, no. 1, pp. 560–580, 2016.
- [6] D. Serrano, H. Li, S. Wang, T. Guillod, M. Luo, V. Bansal, N. K. Jha, Y. Chen, C. R. Sullivan, and M. Chen, “Why magnet: Quantifying the complexity of modeling power magnetic material characteristics,” *IEEE Transactions on Power Electronics*, pp. 1–25, 2023.
- [7] C. Steinmetz, “On the law of hysteresis,” *Proceedings of the IEEE*, vol. 72, no. 2, pp. 197–221, 1984.
- [8] J. Goodenough, “Summary of losses in magnetic materials,” *IEEE Transactions on Magnetics*, vol. 38, no. 5, pp. 3398–3408, 2002.
- [9] J. Li, T. Abdallah, and C. Sullivan, “Improved calculation of core loss with nonsinusoidal waveforms,” in *Conference Record of the 2001 IEEE Industry Applications Conference. 36th IAS Annual Meeting*, vol. 4, pp. 2203–2210 vol.4, 2001.

- [10] D. Jiles and D. Atherton, “Theory of ferromagnetic hysteresis,” *Journal of Magnetism and Magnetic Materials*, vol. 61, pp. 48–60, 1986.
- [11] Y. LeCun, Yann Bengio and G. Hinton, “Deep learning,” *Nature*, vol. 521, p. 436–444, 2015.
- [12] J. Schmidhuber, “Deep learning in neural networks: An overview,” *Neural Networks*, vol. 61, pp. 85–117, jan 2015.
- [13] B. Widrow and M. Lehr, “30 years of adaptive neural networks: perceptron, Madaline, and backpropagation,” *Proceedings of the IEEE*, vol. 78, no. 9, pp. 1415–1442, 1990.
- [14] J. Deng, W. Dong, R. Socher, L.-J. Li, K. Li, and L. Fei-Fei, “ImageNet: A large-scale hierarchical image database,” in *2009 IEEE Conference on Computer Vision and Pattern Recognition*, pp. 248–255, 2009.
- [15] H. Saliah, D. Lowther, and B. Forghani, “A neural network model of magnetic hysteresis for computational magnetics,” *IEEE Transactions on Magnetics*, vol. 33, no. 5, pp. 4146–4148, 1997.
- [16] C. Serpico and C. Visone, “Magnetic hysteresis modeling via feed-forward neural networks,” *IEEE Transactions on Magnetics*, vol. 34, no. 3, pp. 623–628, 1998.
- [17] E. Fallah, J. Moghani, and H. Talebi, “Modeling of magnetic hysteresis using counter propagation neural network,” in *2003 IEEE International Magnetics Conference (INTERMAG)*, pp. DP–07, 2003.
- [18] H. Saliah, D. Lowther, and B. Forghani, “Modeling magnetic materials using artificial neural networks,” *IEEE Transactions on Magnetics*, vol. 34, no. 5, pp. 3056–3059, 1998.
- [19] F. Sixdenier, R. Scorretti, R. Marion, and L. Morel, “Quasistatic hysteresis modeling with feed-forward neural networks: Influence of the last but one extreme values,” *Journal of Magnetism and Magnetic Materials*, vol. 320, no. 20, pp. e992–e996, 2008.
- [20] Z. Zhao, F. Liu, S. L. Ho, W. N. Fu, and W. Yan, “Modeling magnetic hysteresis under dc-biased magnetization using the neural network,” *IEEE Transactions on Magnetics*, vol. 45, no. 10, pp. 3958–3961, 2009.
- [21] F. Riganti Fulginei and A. Salvini, “Neural network approach for modelling hysteretic magnetic materials under distorted excitations,” *IEEE Transactions on Magnetics*, vol. 48, no. 2, pp. 307–310, 2012.
- [22] C. Grech, M. Buzio, M. Pentella, and N. Sammut, “Dynamic ferromagnetic hysteresis modelling using a Preisach-recurrent neural network model,” *Materials*, vol. 13, no. 11, p. 2561, 2020.

- [23] S. Quondam Antonio, F. Riganti Fulginei, A. Laudani, A. Faba, and E. Cardelli, “An effective neural network approach to reproduce magnetic hysteresis in electrical steel under arbitrary excitation waveforms,” *Journal of Magnetism and Magnetic Materials*, vol. 528, p. 167735, 2021.
- [24] E. Stenglein, B. Kohlhepp, D. Kübrich, M. Albach, and T. Dürbaum, “GaN-half-bridge for core loss measurements under rectangular ac voltage and dc bias of the magnetic flux density,” *IEEE Transactions on Instrumentation and Measurement*, vol. 69, no. 9, pp. 6312–6321, 2020.
- [25] V. Thottuveilil, T. Wilson, and H. Owen, “High-frequency measurement techniques for magnetic cores,” *IEEE Transactions on Power Electronics*, vol. 5, no. 1, pp. 41–53, 1990.
- [26] J. Li, T. Abdallah, and C. Sullivan, “Improved calculation of core loss with nonsinusoidal waveforms,” in *Conference Record of the 2001 IEEE Industry Applications Conference. 36th IAS Annual Meeting (Cat. No.01CH37248)*, vol. 4, pp. 2203–2210 vol.4, 2001.
- [27] M. Mu, Q. Li, D. J. Gilham, F. C. Lee, and K. D. T. Ngo, “New core loss measurement method for high-frequency magnetic materials,” *IEEE Transactions on Power Electronics*, vol. 29, no. 8, pp. 4374–4381, 2014.
- [28] E. Stenglein, D. Kuebrich, M. Albach, and T. Duerbaum, “Guideline for hysteresis curve measurements with arbitrary excitation: Pitfalls to avoid and practices to follow,” in *PCIM Europe 2018; International Exhibition and Conference for Power Electronics, Intelligent Motion, Renewable Energy and Energy Management*, pp. 1–8, 2018.
- [29] M. Luo, D. Dujic, and J. Allmeling, “Test setup for characterisation of biased magnetic hysteresis loops in power electronic applications,” in *2018 International Power Electronics Conference (IPEC-Niigata 2018 -ECCE Asia)*, pp. 422–427, 2018.
- [30] P. Papamanolis, T. Guillod, F. Krismer, and J. W. Kolar, “Transient calorimetric measurement of ferrite core losses up to 50 MHz,” *IEEE Transactions on Power Electronics*, vol. 36, no. 3, pp. 2548–2563, 2021.
- [31] P. Welch, “The use of fast Fourier transform for the estimation of power spectra: A method based on time averaging over short, modified periodograms,” *IEEE Transactions on Audio and Electroacoustics*, vol. 15, no. 2, pp. 70–73, 1967.
- [32] H. Li, D. Serrano, T. Guillod, E. Dogariu, A. Nadler, S. Wang, M. Luo, V. Bansal, Y. Chen, C. R. Sullivan, and M. Chen, “MagNet: An open-source database for data-driven magnetic core loss modeling,” in *2022 IEEE Applied Power Electronics Conference and Exposition (APEC)*, pp. 588–595, 2022.

- [33] M. Raissi, P. Perdikaris, and G. E. Karniadakis, “Physics-informed neural networks: A deep learning framework for solving forward and inverse problems involving nonlinear partial differential equations,” *Journal of Computational Physics*, vol. 378, pp. 686–707, 2019.
- [34] G. Skutt and F. Lee, “Characterization of dimensional effects in ferrite-core magnetic devices,” in *PESC Record. 27th Annual IEEE Power Electronics Specialists Conference*, vol. 2, pp. 1435–1440 vol.2, 1996.
- [35] A. Nabih, F. Jin, R. Gadelrab, F. C. Lee, and Q. Li, “Characterization and mitigation of dimensional effects on core loss in high-power high-frequency converters,” *IEEE Transactions on Power Electronics*, pp. 1–20, 2023.
- [36] M. Kacki, M. S. Rylko, J. G. Hayes, and C. R. Sullivan, “Analysis and experimental investigation of high-frequency magnetic flux distribution in mn-zn ferrite cores,” *IEEE Transactions on Power Electronics*, vol. 38, no. 1, pp. 703–716, 2023.
- [37] A. Sherstinsky, “Fundamentals of recurrent neural network (RNN) and long short-term memory (LSTM) network,” *CoRR*, vol. abs/1808.03314, 2018.
- [38] K. O’Shea and R. Nash, “An introduction to convolutional neural networks,” *CoRR*, vol. abs/1511.08458, 2015.
- [39] J. Wang, Q. Liu, Z. Liu, and S. Wu, “Towards accurate and interpretable sequential prediction: A cnn & attention-based feature extractor,” in *Proceedings of the 28th ACM International Conference on Information and Knowledge Management*, pp. 1703–1712, 2019.
- [40] Y. LeCun and Y. Bengio, *Convolutional networks for images, speech, and time series*. MIT Press, 1995.
- [41] H. Li, S. R. Lee, M. Luo, C. R. Sullivan, Y. Chen, and M. Chen, “MagNet: A machine learning framework for magnetic core loss modeling,” in *2020 IEEE 21st Workshop on Control and Modeling for Power Electronics (COMPEL)*, pp. 1–8, 2020.
- [42] S. Hochreiter and J. Schmidhuber, “Long short-term memory,” *Neural Computation*, vol. 9, no. 8, pp. 1735–1780, 1997.
- [43] H. Sak, A. W. Senior, and F. Beaufays, “Long short-term memory recurrent neural network architectures for large scale acoustic modeling,” in *INTERSPEECH*, pp. 338–342, 2014.
- [44] A. Vaswani, N. Shazeer, N. Parmar, J. Uszkoreit, L. Jones, A. N. Gomez, L. Kaiser, and I. Polosukhin, “Attention is all you need,” in *Advances in Neural Information Processing Systems*, vol. 30, 2017.

- [45] H. Li, D. Serrano, T. Guillod, S. Wang, E. Dogariu, A. Nadler, M. Luo, V. Bansal, N. Jha, Y. Chen, C. R. Sullivan, and M. Chen, “How magnet: Machine learning framework for modeling power magnetic material characteristics,” in *TechRxiv. Preprint*, 2022. <https://doi.org/10.36227/techrxiv.21340998.v3>.
- [46] P. Welch, “The use of fast fourier transform for the estimation of power spectra: A method based on time averaging over short, modified periodograms,” *IEEE Transactions on Audio and Electroacoustics*, vol. 15, no. 2, pp. 70–73, 1967.
- [47] T. Guillod, P. Papamanolis, and J. W. Kolar, “Artificial neural network (ANN) based fast and accurate inductor modeling and design,” *IEEE Open Journal of Power Electronics*, vol. 1, pp. 284–299, 2020.
- [48] M. Chen, H. Li, S. Wang, T. Guillod, D. Serrano, N. Förster, W. Kirchgässner, T. Piepenbrock, O. Schweins, O. Wallscheid, Q. Huang, Y. Li, Y. Dou, B. Li, S. Li, E. Havugimana, V. T. Chacko, S. Radhakrishnan, M. Ranjram, B. Sauter, S. Reese, S. Sinha, L. Zhang, T. McKeague, B. Cui, N. Rasekh, J. Wang, S. Liu, A. Martinez, X. Liu, C. Mei, R. Zhao, G. Wu, H. Wu, R. Zhang, H. Song, L. Zhang, Y. Lu, L. Hang, N. Rajput, H. B. Sandhibigraha, N. Agrawal, V. M. Iyer, X. Shen, F. Tian, Q. Sui, J. Kong, W. Martinez, A. Arruti, B. Alberdi, A. Agote, I. Aizpuru, M. Zhang, X. Chen, Y. Dong, D. Wang, T. Shen, Y. Zhou, Y. Li, S. Wang, Y. Wu, Y. Jiang, Z. Xiao, Y. Tang, Y.-S. Hsieh, J.-D. Li, L.-C. Yu, T.-C. Hsu, Y.-C. Liu, C.-H. Hsia, C. Chen, A. Giuffrida, N. Lombardo, F. Marmello, S. Morra, M. Pasquale, L. Solimene, C. S. Ragusa, J. Reynvaan, M. Stoiber, C. Li, W. Qin, X. Ma, B. Zhang, Z. Wang, M. Cheng, W. Xu, J. Wang, Y. Hu, J. Xu, Z. Shi, D. B. Sapkota, P. Neupane, M. Joshi, S. Khan, B. Su, Y. Xiao, M. Yang, K. Sun, Z. Li, R. Mirzadarani, R. Liu, L. Wang, T. Luo, D. Lyu, M. G. Niasar, Z. Qin, S. I. A. Meerza, K. Froehle, H. Cui, D. Costinett, J. Liu, Z. Liu, C. Zhan, Y. Dang, Y. Zhang, N. Wang, Y. Chen, Y. Zhang, C. Li, Y. Yao, T. Hu, L. Xu, Y. Wang, S. Wang, S. Jiang, D. Shumacher, D. Maksimović, R. S. Y. Hui, J. W. Kolar, D. J. Perreault, and C. R. Sullivan, “Magnet challenge for data-driven power magnetics modeling,” *IEEE Open Journal of Power Electronics*, vol. 6, pp. 883–898, 2025.
- [49] S. Borkar and A. A. Chien, “The Future of Microprocessors,” *Commun. ACM*, vol. 54, p. 67–77, May 2011.
- [50] K. Radhakrishnan, M. Swaminathan, and B. K. Bhattacharyya, “Power Delivery for High-Performance Microprocessors—Challenges, Solutions, and Future Trends,” *IEEE Transactions on Components, Packaging and Manufacturing Technology*, vol. 11, no. 4, pp. 655–671, 2021.
- [51] J. Sun, J.-Q. Lu, D. Giuliano, T. P. Chow, and R. J. Gutmann, “3D Power Delivery for Microprocessors and High-Performance ASICs,” in *APEC 07 - Twenty-Second Annual IEEE Applied Power Electronics Conference and Exposition*, pp. 127–133, 2007.

- [52] S. Krishnakumar and I. Partin-Vaisband, "Vertical Power Delivery for Emerging Packaging and Integration Platforms - Power Conversion and Distribution," in *2023 IEEE 36th International System-on-Chip Conference (SOCC)*, pp. 1–6, 2023.
- [53] Y. Safari and B. Vaisband, "A Robust Integrated Power Delivery Methodology for 3-D ICs," *IEEE Transactions on Very Large Scale Integration (VLSI) Systems*, vol. 31, no. 3, pp. 287–295, 2023.
- [54] M. A. Akram, I.-C. Hwang, and S. Ha, "Power Delivery Networks for Embedded Mobile SoCs: Architectural Advancements and Design Challenges," *IEEE Access*, vol. 9, pp. 46573–46588, 2021.
- [55] M. O. Hossen, B. Chava, G. Van der Plas, E. Beyne, and M. S. Bakir, "Power Delivery Network (PDN) Modeling for Backside-PDN Configurations With Buried Power Rails and μ TSVs," *IEEE Transactions on Electron Devices*, vol. 67, no. 1, pp. 11–17, 2020.
- [56] G. Sisto, B. Chehab, B. Genneret, R. Baert, R. Chen, P. Weckx, J. Ryckaert, R. Chou, G. van Der Plas, E. Beyne, and D. Milojevic, "IR-Drop Analysis of Hybrid Bonded 3D-ICs with Backside Power Delivery and μ - & n- TSVs," in *2021 IEEE International Interconnect Technology Conference (IITC)*, pp. 1–3, 2021.
- [57] J. Baek, Y. Elasser, K. Radhakrishnan, H. Gan, J. P. Douglas, H. K. Krishnamurthy, X. Li, S. Jiang, C. R. Sullivan, and M. Chen, "Vertical Stacked LEGO-PoL CPU Voltage Regulator," *IEEE Transactions on Power Electronics*, vol. 37, no. 6, pp. 6305–6322, 2022.
- [58] Y. Elasser, J. Baek, K. Radhakrishnan, H. Gan, J. P. Douglas, H. K. Krishnamurthy, X. Li, S. Jiang, V. De, C. R. Sullivan, and M. Chen, "Mini-LEGO CPU Voltage Regulator," *IEEE Transactions on Power Electronics*, vol. 39, no. 3, pp. 3391–3410, 2024.
- [59] J. Baek, Y. Elasser, and M. Chen, "MIPS: Multiphase Integrated Planar Symmetric Coupled Inductor for Ultrathin VRM," *IEEE Transactions on Power Electronics*, vol. 38, no. 5, pp. 5609–5614, 2023.
- [60] Y. Elasser, H. Li, P. Wang, J. Baek, K. Radhakrishnan, S. Jiang, H. Gan, X. Zhang, D. Giuliano, and M. Chen, "Circuits and magnetics co-design for ultra-thin vertical power delivery: A snapshot review," *MRS Advances*, vol. 9, pp. 12–24, 2024.
- [61] A. M. Naradhipa, F. Zhu, and Q. Li, "Ultra-Low-Profile Twisted Core Inductor for Vertical Power Delivery Voltage Regulator," in *2024 IEEE Applied Power Electronics Conference and Exposition (APEC)*, 2024.

- [62] M. Chen and C. R. Sullivan, "Unified Models for Coupled Inductors Applied to Multiphase PWM Converters," *IEEE Transactions on Power Electronics*, vol. 36, no. 12, pp. 14155–14174, 2021.
- [63] P.-L. Wong, P. Xu, P. Yang, and F. Lee, "Performance improvements of interleaving VRMs with coupling inductors," *IEEE Transactions on Power Electronics*, vol. 16, no. 4, pp. 499–507, 2001.
- [64] J. Li, C. Sullivan, and A. Schultz, "Coupled-inductor design optimization for fast-response low-voltage DC-DC converters," in *APEC. Seventeenth Annual IEEE Applied Power Electronics Conference and Exposition (Cat. No.02CH37335)*, vol. 2, pp. 817–823 vol.2, 2002.
- [65] A. Ikriannikov and T. Schmid, "Magnetically coupled buck converters," in *2013 IEEE Energy Conversion Congress and Exposition*, pp. 4948–4954, 2013.
- [66] T. Sen, Y. Elasser, and M. Chen, "Origami inductor: Foldable 3-d polyhedron multiphase air-coupled inductors with flux cancellation and faster transient," *IEEE Transactions on Power Electronics*, vol. 39, no. 6, pp. 7312–7328, 2024.
- [67] H. Li, D. Serrano, S. Wang, and M. Chen, "MagNet-AI: Neural Network as Datasheet for Magnetics Modeling and Material Recommendation," *IEEE Transactions on Power Electronics*, vol. 38, no. 12, pp. 15854–15869, 2023.
- [68] M. Xu, J. Zhou, K. Yao, and F. C. Lee, "Small Signal Modeling of a High Bandwidth Voltage Regulator Using Coupled Inductors," *IEEE Transactions on Power Electronics*, vol. 22, no. 2, pp. 399–406, 2007.
- [69] D. H. Zhou, Y. Elasser, J. Baek, and M. Chen, "Reluctance-Based Dynamic Models for Multiphase Coupled Inductor Buck Converters," *IEEE Transactions on Power Electronics*, vol. 37, no. 2, pp. 1334–1351, 2022.
- [70] F. Zhu and Q. Li, "A Novel PCB-Embedded Coupled Inductor Structure for a 20-MHz Integrated Voltage Regulator," *IEEE Journal of Emerging and Selected Topics in Power Electronics*, vol. 10, no. 6, pp. 7452–7463, 2022.
- [71] W. Huang and B. Lehman, "Inversely Coupled Inductors With Small Volume and Reduced Power Loss for Switching Converters," *IEEE Transactions on Power Electronics*, vol. 38, no. 6, pp. 6779–6783, 2023.
- [72] P. Wang, Y. Chen, G. Szczeszynski, S. Allen, D. M. Giuliano, and M. Chen, "MSC-PoL: Hybrid GaN–Si Multistacked Switched-Capacitor 48-V PwrSiP VRM for Chiplets," *IEEE Transactions on Power Electronics*, vol. 38, no. 10, pp. 12815–12833, 2023.
- [73] Y. Zhu, T. Ge, N. M. Ellis, L. Horowitz, and R. C. N. Pilawa-Podgurski, "The Switching Bus Converter: A High-Performance 48-V-to-1-V Architecture with Increased Switched-Capacitor Conversion Ratio," *IEEE Transactions on Power Electronics*, pp. 1–20, 2024.

- [74] D. Serrano, H. Li, S. Wang, T. Guillod, M. Luo, V. Bansal, N. K. Jha, Y. Chen, C. R. Sullivan, and M. Chen, “Why magnet: Quantifying the complexity of modeling power magnetic material characteristics,” *IEEE Transactions on Power Electronics*, vol. 38, no. 11, pp. 14292–14316, 2023.
- [75] E. A. Burton, G. Schrom, F. Paillet, J. Douglas, W. J. Lambert, K. Radhakrishnan, and M. J. Hill, “Fivr — fully integrated voltage regulators on 4th generation intel® core™ socs,” in *2014 IEEE Applied Power Electronics Conference and Exposition - APEC 2014*, pp. 432–439, 2014.
- [76] Y. Elasser, J. Baek, K. Radhakrishnan, H. Gan, J. P. Douglas, H. K. Krishnamurthy, X. Li, S. Jiang, V. De, C. R. Sullivan, and M. Chen, “Mini-lego cpu voltage regulator,” *IEEE Transactions on Power Electronics*, vol. 39, no. 3, pp. 3391–3410, 2024.
- [77] E. Stenglein, D. Kübrich, M. Albach, and T. Dürbaum, “Influence of magnetic history and accommodation on hysteresis loss for arbitrary core excitations,” in *2019 21st European Conference on Power Electronics and Applications (EPE '19 ECCE Europe)*, pp. P.1–P.10, 2019.
- [78] A. Brockmeyer, “Experimental evaluation of the influence of dc-premagnetization on the properties of power electronic ferrites,” in *Proceedings of Applied Power Electronics Conference. APEC '96*, vol. 1, pp. 454–460 vol.1, 1996.
- [79] F. Preisach, “Über die magnetische nachwirkung,” *Zeitschrift für Physik*, vol. 94, pp. 277–302, May 1935.
- [80] H. Li, D. Serrano, T. Guillod, S. Wang, E. Dogariu, A. Nadler, M. Luo, V. Bansal, N. K. Jha, Y. Chen, C. R. Sullivan, and M. Chen, “How magnet: Machine learning framework for modeling power magnetic material characteristics,” *IEEE Transactions on Power Electronics*, vol. 38, no. 12, pp. 15829–15853, 2023.
- [81] H. Li, D. Serrano, S. Wang, and M. Chen, “Magnet-ai: Neural network as datasheet for magnetics modeling and material recommendation,” *IEEE Transactions on Power Electronics*, vol. 38, no. 12, pp. 15854–15869, 2023.
- [82] O. Russakovsky, J. Deng, H. Su, J. Krause, S. Satheesh, S. Ma, Z. Huang, A. Karpathy, A. Khosla, M. Bernstein, A. C. Berg, and L. Fei-Fei, “Imagenet large scale visual recognition challenge,” *International Journal of Computer Vision*, vol. 115, pp. 211–252, Dec 2015.
- [83] D. Serrano, H. Li, S. Wang, T. Guillod, M. Luo, V. Bansal, N. K. Jha, Y. Chen, C. R. Sullivan, and M. Chen, “Why magnet: Quantifying the complexity of modeling power magnetic material characteristics,” *IEEE Transactions on Power Electronics*, vol. 38, no. 11, pp. 14292–14316, 2023.